



HAL
open science

ADER scheme on Overset Grids with Compact Transmission and Hyper-reduction: Application to Incompressible Navier-Stokes Equations

Michele Giuliano Carlino

► **To cite this version:**

Michele Giuliano Carlino. ADER scheme on Overset Grids with Compact Transmission and Hyper-reduction: Application to Incompressible Navier-Stokes Equations. Numerical Analysis [cs.NA]. Université de Bordeaux, 2021. English. NNT : 2021BORD0370 . tel-03499022

HAL Id: tel-03499022

<https://theses.hal.science/tel-03499022>

Submitted on 21 Dec 2021

HAL is a multi-disciplinary open access archive for the deposit and dissemination of scientific research documents, whether they are published or not. The documents may come from teaching and research institutions in France or abroad, or from public or private research centers.

L'archive ouverte pluridisciplinaire **HAL**, est destinée au dépôt et à la diffusion de documents scientifiques de niveau recherche, publiés ou non, émanant des établissements d'enseignement et de recherche français ou étrangers, des laboratoires publics ou privés.



THÈSE PRÉSENTÉE
POUR OBTENIR LE GRADE DE
DOCTEUR
DE L'UNIVERSITÉ DE BORDEAUX

École doctorale de mathématiques et informatique

Mathématiques appliquées et calcul scientifique

Par **Michele Giuliano CARLINO**

ADER Scheme on Overset Grids with Compact Transmission
and Hyper-reduction: Application to Incompressible
Navier-Stokes Equations

Sous la direction de : **Michel BERGMANN**
(Co-directeur : **Angelo IOLLO**)

Soutenue le 15 décembre 2021

Membres du jury :

M. Michel BERGMANN	Chargé de Recherche	INRIA Bordeaux Sud-Ouest	Directeur
M. Michael DUMBSER	Professeur	Univ. Trento	Rapporteur
M. Alexandre ERN	Professeur	Ponts ParisTech & Polytechnique	Rapporteur
M. Angelo IOLLO	Professeur	Univ. Bordeaux	Co-directeur
M. Raphaël LOUBÈRE	Directeur de Recherche	CNRS	Président
M. Haysam TELIB	PhD et CEO	Optimad Engineering	Invité
Mme. Marie-Hélène VIGNAL	Maître de Conférence	Univ. Toulouse 3	Examinatrice

« *Entia non sunt multiplicanda praeter necessitatem.* »

Ockham's razor

Schéma ADER sur des Maillages Overset avec Transmission Compacte et Hyper-réduction : Application aux Équations de Navier-Stokes Incompressibles

Résumé : Dans cette thèse, nous proposons un schéma éléments finis (FEM) / volumes finis (FVM) spatio-temporel sur des grilles Chimera mobiles pour un problème général d'advection-diffusion linéaire et non linéaire. Une attention particulière est accordée aux zones de superposition des grilles afin de concevoir un stencil de discrétisation compact et précis pour échanger des informations entre les différents patches de maillage. Comme dans la méthode ADER, les équations sont discrétisées sur un maillage spatio-temporel. Ainsi, au lieu de conditions de transmission spatiale dépendant du temps entre des blocs en mouvement relatif, nous définissons des polynômes d'interpolation sur des cellules spatio-temporelles se croisant arbitrairement aux frontières des blocs. Grâce à ce schéma, une approche FEM-prédicteur/FVM-correcteur mesh-free est utilisée pour représenter la solution. Dans ce cadre de discrétisation, une nouvelle vitesse de stabilisation locale de Lax-Friedrichs (LLF) spatio-temporelle est définie en considérant à la fois la nature advective et diffusive de l'équation. Les illustrations numériques pour les systèmes linéaires et non linéaires montrent que les mailles mobiles de background et foreground n'introduisent pas de perturbations parasites dans la solution, atteignant uniformément le deuxième ordre de précision en espace et en temps. Il est démontré que plusieurs mailles du foreground, pouvant se superposer et ayant des déplacements indépendants, peuvent être utilisées grâce à cette approche.

La principale application de ce schéma concerne les équations de Navier-Stokes afin de simuler des écoulements visqueux incompressibles dans un domaine évolutif. Dans ce cas, les grilles évolutives spatio-temporelles utilisées sont capables de prendre en compte à la fois les objets éventuellement en mouvement et l'évolution du domaine. Puisqu'une méthode classique à pas fractionnaire est adoptée, un problème de Poisson pour la pression doit être résolu numériquement. Ainsi, pour la discrétisation de l'opérateur de gradient, une technique hybride est définie afin d'encoder automatiquement la configuration locale particulière de superposition aux interfaces de deux blocs. Ceci évite une étape ultérieure d'interpolation à l'interface pour échanger des informations entre différents blocs. La méthode qui en résulte est précise au second ordre pour la vitesse et la pression en espace et en temps. La précision et l'efficacité de la méthode sont testées par des simulations de référence.

Enfin, un schéma ADER réduit et hyper-réduit pour les équations d'advection-diffusion générales sur des grilles overset est présenté. Ce schéma, basé sur l'approche de la Décomposition Orthogonale Propre (POD), permet de réduire les coûts de calcul à la fois pour trouver la solution numérique et pour calculer les intégrales impliquées dans la définition des matrices au niveau discret. Dans une étape d'apprentissage offline, on construit un sous-espace réduit approprié sur lequel la solution réduite est ensuite projetée. Successivement, dans l'étape online, une solution réduite numérique est trouvée par rapport à un paramètre définissant l'évolution du domaine. Afin de réduire les coûts de calcul des intégrales numériques via la règle de quadrature, une étape supplémentaire d'apprentissage offline est effectuée. Elle permet de définir un ensemble largement réduit de nœuds de quadrature pour tout mouvement admissible du maillage. L'approche se situe dans un cadre de décomposition de domaine (DD) : par conséquent, sur le maillage de foreground, la solution réduite est récupérée alors que dans le maillage de background, la solution est haute-fidélité. La performance du schéma proposé est testée sur des problèmes linéaires et non linéaires pour différents mouvements du domaine de calcul. Les résultats montrent que les coûts de calcul sont réduits à $\mathcal{O}(1)$ degrés de liberté en préservant la précision de la solution.

Mots-clés : Maillage Chimera, Maillage Overset, Volumes Finis, Éléments finis, ADER, Transmission compacte, Advection-Diffusion instationnaire, Navier-Stokes Incompressible, POD, Modèles Réduits, Hyper-réduction, Décomposition de Domaine

ADER Scheme on Overset Grids with Compact Transmission and Hyper-reduction: Application to Incompressible Navier-Stokes Equations

Abstract: In this thesis, we propose a space-time Finite Element (FEM) / Finite Volume (FVM) scheme on moving Chimera grids for a general linear and nonlinear advection-diffusion problem. Special care is devoted to grid overlapping zones in order to devise a compact and accurate discretization stencil to exchange information between different mesh patches. Like in the ADER method, the equations are discretized on a space-time slab. Thus, instead of time-dependent spatial transmission conditions between relatively moving blocks, we define interpolation polynomials on arbitrarily intersecting space-time cells at the block boundaries. Through this scheme, a mesh-free FEM-predictor/FVM-corrector approach is employed for representing the solution. In this discretization framework, a new space-time Local Lax-Friedrichs (LLF) stabilization speed is defined by considering both the advective and diffusive nature of the equation. The numerical illustrations for linear and nonlinear systems show that background and foreground moving meshes do not introduce spurious perturbations to the solution, uniformly reaching second order of accuracy in space and time. It is shown that several foreground meshes, possibly overlapping and with independent displacements, can be employed thanks to this approach.

The main application of the scheme is for the Navier-Stokes equations in order to simulate incompressible viscous flows in an evolving domain. In this case, the employed evolving space-time overset grids are able to take into account both possibly moving objects and the evolution of the domain. Since a classical fractional step method is adopted, a Poisson problem for the pressure needs to be numerically solved. For this reason, for the discretization of the gradient operator, a hybrid technique is defined which is able to automatically encode the particular local overlapping configuration at the interfaces of two blocks. This avoids a subsequent interpolation step at the interface to exchange information between different blocks. The resulting method is second order accurate for both velocity and pressure in space and time. The accuracy and efficiency of the method are tested through reference simulations.

Finally, a reduced and hyper-reduced ADER scheme for general advection-diffusion equations on overset grids is presented. This scheme, based on the Proper Orthogonal Decomposition (POD) approach, allows to reduce the computational costs for both finding the numerical solution and for computing the integrals involved in the definition of the matrices of the algebraic counterpart. In an offline training stage it is built a proper reduced subspace onto which the reduced solution is later projected. Successively, in the online step, a numerical reduced solution is found with respect to a parameter defining the evolution of the domain. In order to alleviate the computational costs for performing the numerical integrals via quadrature rule, a further offline training stage is computed. It allows to define a largely small set of quadrature nodes for any admissible movement of the mesh. The approach is in a Domain Decomposition (DD) frame: consequently over the background mesh the reduced solution is recovered while in background the solution is high-fidelity. The performance of the proposed scheme is tested on both linear and nonlinear problem for different movement of the computational domain. Results show that the computational costs reduce to $\mathcal{O}(1)$ degrees of freedom by preserving the accuracy of the solution.

Keywords: Chimera mesh, Overset grid, Finite Volume, Finite Element, ADER, Compact Transmission, Unsteady Advection-Diffusion, Incompressible Navier-Stokes, POD, Reduced Order Model, Hyper-reduction, Domain Decomposition

**Équipe MEMPHIS (INRIA Bordeaux Sud-Ouest) et Institut de Mathématiques de
Bordeaux (IMB)**

UMR 5251 Université de Bordeaux, 351, Cours de la Libération, F-33405, TALANCE,
France.

Résumé détaillé

Background

Une des principales difficultés pour la simulation d'un phénomène modélisé par une équation différentielle partielle (EDP) est la modélisation géométrique du domaine de calcul avec un seul bloc de maillage. Ce problème est particulièrement pertinent lorsque le domaine est complexe ou que sa forme et sa topologie évoluent au cours de la simulation. Les approches classiques pour résoudre ce problème comprennent la méthode Lagrangienne-Eulérienne Arbitraire (ALE), les approches de domaine fictif et les maillages Chimera.

Les méthodes ALE [61] permettent un certain degré de déformation et d'adaptation du maillage grâce à une reformulation appropriée des équations gouvernantes et à des algorithmes de déplacement de grille sophistiqués et efficaces. En 1969, Harlow a dressé la liste des principaux schémas de résolution des problèmes de dynamique des fluides en fonction de leur formulation en coordonnées lagrangiennes ou eulériennes [54]. Lorsque la méthode utilise des mailles dont les nœuds se déplacent en fonction du mouvement du fluide, elle est dite lagrangienne. Au contraire, si le maillage est toujours fixe (c'est-à-dire qu'il ne change pas par rapport au mouvement du fluide), la méthode est eulérienne. La première tentative de formulation d'une méthode utilisant un maillage dont le mouvement est indépendant de la dynamique du fluide a été proposée par Trulio en 1966 pour les écoulements compressibles [113]. La méthode proposée est explicite, ainsi le mouvement du maillage est lié au mouvement du fluide par une condition de stabilité. Successivement, dans les articles de Hirt en 1970 [60] et Hirt *et al.* en 1974 [61], une méthode ALE aux différences finies a été définie. Dans ces travaux, du fait d'une formulation implicite, la vitesse du maillage est découplée de la vitesse du fluide. Cependant, lorsque la déformation du maillage conduit à des cellules excessivement étirées, une étape délicate (et coûteuse en calcul) de remaillage global peut être nécessaire. A son tour, cette opération peut introduire des irrégularités d'approximation qui sont causées par l'interpolation de la solution de l'ancienne grille à la nouvelle.

Dans les approches par domaine fictif, notamment les méthodes de frontière fantôme [47], de frontière immergée [78] ou de pénalisation [4] le problème original est discrétisé sur un maillage simple, généralement structuré et cartésien, constant dans le temps [48, 88, 4].

Fedkiw *et al.* dans [45] a proposé pour la première fois une méthode des frontières fantômes (GBM). Dans le but de simuler des problèmes de dynamique des gaz, la GBM combine la robustesse des schémas eulériens avec une méthode d'interface multimatérielle caractéristique d'un schéma lagrangien. En suivant l'interface avec une fonction d'ensemble de niveaux [82, 106], un problème de Riemann approximatif est résolu à l'emplacement de l'interface. Cette technique s'avère donc utile lorsqu'une onde de choc ou une discontinuité se déplace dans le domaine de calcul. Dans sa thèse de doctorat de 1972, Peskin a proposé la méthode Immersed Boundary

(IBM) afin de simuler la mécanique cardiaque associée à l'écoulement du sang [89]. Dans ce travail antérieur, l'auteur propose l'utilisation d'un seul bloc cartésien non conforme à la forme réelle du cœur (c'est-à-dire le domaine) ; ainsi une frontière immergée est intégrée dans le bloc cartésien pour simuler les effets du flux sanguin. Aujourd'hui, IBM est lié à une *méthode de grille cartésienne* développée à l'origine pour simuler des écoulements inviscides avec des frontières immergées complexes sur des grilles cartésiennes [15, 34]. Successivement, ces méthodes ont été étendues aux écoulements visqueux instationnaires [114, 119]. Aujourd'hui, les IBM s'adressent non seulement aux interactions fluide-structure mais aussi aux interactions liquide-liquide et liquide-gaz [2, 97].

Pour l'étude des écoulements incompressibles, une autre approche est fournie par les méthodes de pénalisation (PM). Cette méthode vise également à éviter de construire des maillages non structurés adaptés au corps afin d'utiliser des schémas numériques rapides et efficaces (par exemple, des méthodes spectrales, de différences finies ou de volumes finis) sur des maillages cartésiens. Pour ce faire, on ajoute un terme de vitesse de pénalisation dans l'équation de la quantité de mouvement pour les équations incompressibles de Navier-Stokes. Dans les travaux antérieurs [86, 87] de Peskin sur l'écoulement du sang dans le cœur et dans certaines autres formulations revues (comme dans [51]), une intégrale temporelle de la vitesse et un terme de pénalisation de la vitesse sont ajoutés uniquement à la surface définissant l'obstacle. Successivement, Saiki et Biringen [96] ont étendu la pénalisation à l'ensemble du domaine afin de prendre en compte les grands nombres de Reynolds. Les premiers à étendre la pénalisation à un volume d'un milieu poreux ont été Arquís et Caltagirone [6]. Enfin, Angot et Caltagirone [5, 3] ont étendu la pénalisation afin de traiter les systèmes solides fluides-poreux. En particulier, que le sous-domaine de calcul soit $\Omega \subset \mathbb{R}^d$, avec $d = 2, 3$, et qu'il contienne un certain nombre d'obstacles solides irréguliers dont l'union est définie par Ω_s et dont la vitesse possible est \mathbf{u}_s . Par conséquent, le sous-domaine restant $\Omega_f = \Omega / \Omega_s$ est occupé par le fluide. Les équations incompressibles de Navier-Stokes pour ce problème sont les suivantes : Trouver la vitesse $\mathbf{u} : \Omega_f \times \mathbb{R}_+ \rightarrow \mathbb{R}^d$ et la pression $p : \Omega_f \times \mathbb{R}_+ \rightarrow \mathbb{R}$ du fluide telles que :

$$\begin{aligned} \partial_t \mathbf{u} + \mathbf{u} \cdot \nabla \mathbf{u} &= \nabla p + \frac{1}{\text{Re}} \Delta \mathbf{u} && \text{in } \Omega_f \times \mathbb{R}_+ \\ \nabla \cdot \mathbf{u} &= 0 && \text{in } \Omega_f \times \mathbb{R}_+ \\ \mathbf{u} &= \mathbf{u}_s && \text{in } \partial\Omega_s \times \mathbb{R}_+ \end{aligned} \quad (1)$$

correctement fermé avec des conditions initiales et des conditions aux limites sur la partie restante de la frontière $\partial\Omega$ du domaine. Le PM résout les équations incompressibles de Navier-Stokes en substituant la première ligne du problème (1) par

$$\partial_t \mathbf{u} + \mathbf{u} \cdot \nabla \mathbf{u} = \nabla p + \frac{1}{\text{Re}} \Delta \mathbf{u} + \frac{\chi_s}{K} (\mathbf{u}_s - \mathbf{u}) \quad \text{in } \Omega_f \times \mathbb{R}_+, \quad (2)$$

où χ_s est la fonction indicatrice sur Ω_s et K est la constante de pénalisation. Pour les résultats théoriques de la convergence, dans la limite de vanité de K , de la solution pour (2) vers la solution pour (1), le lecteur est prié de se reporter à [4].

Pour ces approches de domaines fictifs brièvement présentées, le maillage ne correspond pas nécessairement aux limites physiques et un soin particulier doit être apporté pour atteindre un degré de précision suffisant aux limites. De plus, la présence de fines couches limites peut réduire de manière significative les avantages de calcul découlant d'un algorithme de maillage simple, en raison du rapport d'aspect uniforme du maillage. Des techniques hybrides employant des méthodes de

frontières immergées avec des adaptations de maillage anisotrope peuvent être employées pour contourner ce problème [1].

Maillage Chimera

Nous concentrons nos recherches sur les grilles Chimera [116, 14, 75, 90]. Les grilles de chimères consistent en de multiples blocs de mailles qui se chevauchent et qui définissent ensemble une grille sur-étendue utilisée pour discrétiser spatialement une EDP [104, 105, 103]. En général, on dispose d'un maillage de background qui comprend un ou plusieurs patches de maillage de foreground qui sont ajustés aux bords du domaine physique. Cette approche de génération de maillage simplifie considérablement la tâche d'adaptation du maillage dans le cas de couches limites, de géométrie changeante pour un problème instable (par exemple, les problèmes d'interaction fluide-structure en dynamique des fluides) et pour les domaines instables à connexions multiples [10, 8, 98, 9, 30]. Une fois que les multiples patches de maillage sont générés, ils sont assemblés afin d'obtenir une zone de recouvrement appropriée entre les blocs voisins [75].

L'utilisation des mailles Chimera est essentiellement basée sur des techniques d'intégration de grille pour discrétiser le domaine de calcul qui peut évoluer. Une grille principale (*bloc de background*) est d'abord construite. Elle est non-conforme par rapport à la forme complexe du domaine. Des grilles mineures successives (*blocs de foreground*) sont construites afin de décrire précisément les formes particulières des régions où se trouvent les obstacles. Comme les blocs mineurs superposent le bloc majeur, une région de superposition est définie entre tous les blocs. Le long des régions de superposition, les informations de la solution doivent être mutuellement échangées d'un bloc à l'autre. Dans cette thèse, une condition de transmission compacte est recherchée afin de limiter les communications entre les grilles. A savoir, un stencil compact composé uniquement de la première couche de cellules est défini autour de toute cellule.

Le choix du schéma d'interpolation à l'interface se situe entre deux possibilités : les approches non-conservatives et conservatives. Les schémas non-conservatifs (les plus utilisés) sont définis sur l'étude locale de la configuration particulière de cellules superposées utilisée pour définir l'interpolation elle-même. Des références sur l'ordre de précision affectant le schéma numérique global peuvent être trouvées dans [30]. Les interpolations conservatrices impliquent des interfaces patchées [16, 94] ou des régions arbitrairement superposées [81, 118]. En général, ces schémas ne sont pas attrayants car s'ils sont relativement faciles à mettre en œuvre en deux dimensions, ils deviennent encombrants ou impossibles à appliquer en trois dimensions. De plus, même si une conservation globale des flux est assurée entre les frontières superposées ou sur la frontière des trous, la conservation des flux locaux ne peut être préservée.

Dans cette thèse, nous proposons un schéma d'éléments finis - volumes finis spatio-temporels sur des grilles Chimera. Notre objectif est de combiner certains aspects de l'approche ALE, notamment sa flexibilité par rapport au déplacement et à la déformation de la grille, à la stratégie de discrétisation multi-blocs des grilles overset. En particulier, nous accordons une attention particulière aux zones de recouvrement de la grille afin de concevoir un stencil de discrétisation compact et précis permettant d'échanger des informations entre les différents patches de maillage, dans l'esprit des travaux précédents sur les grilles cartésiennes hiérarchiques [93]. Nous appliquons ensuite cette approche à l'intégration d'équations aux dérivées partielles

d'Advection-Diffusion linéaires et non linéaires et montrons comment la méthode peut exploiter la polyvalence des mailles Chimera pour atteindre une précision du second ordre dans des domaines instationnaires à connexions multiples.

La solution numérique sur les grilles Chimera est obtenue en échangeant des données à travers les cellules de frange au niveau de la zone de chevauchement. Par exemple, dans [32, 53, 117, 74], les cellules marginales (à savoir *donor*) d'un bloc à proximité de la zone de superposition fournissent les informations aux cellules marginales (c'est-à-dire *receptor*) d'un autre bloc par interpolation polynomiale. Dans [58], une grille grossière est automatiquement générée et une connexion des informations d'interpolation au niveau de la zone de superposition est présentée par le biais d'une approche multigrille.

Une autre façon de faire communiquer les différents blocs consiste à utiliser des méthodes de décomposition de domaine (DD) appropriées (par exemple, les méthodes de Schwartz, Dirichlet/Neumann ou Dirichlet/Robin). En particulier, chaque bloc de maillage est considéré comme une décomposition du domaine et les zones de chevauchement sont les interfaces permettant de coupler les différents blocs. En fonction de ces approches, des méthodes discrètes typiquement itératives sont employées. Pour cette communication à double sens, le lecteur est renvoyé à [62] pour plus de détails.

Dans le même cadre, d'autres approches connectent les mailles de background et de foreground, comme les grilles DRAGON [65] pour lesquelles la zone de chevauchement est remplacée par une grille non structurée lors d'une étape ultérieure en préservant les avantages de l'adaptation au corps des mailles Chimera. Enfin, une grille Dragon consiste à créer une grille de blocs unique à partir d'une configuration Chimera. Cependant, les coûts de calcul pour la réalisation d'une grille Dragon pour un domaine évolutif augmentent considérablement, car il est possible qu'à chaque instance, un nouveau maillage DRAGON doit être créé.

En revanche, nous dérivons ici une condition de transmission compacte du second ordre en définissant correctement un ensemble de cellules, c'est-à-dire le *stencil*, qui appartient aux maillages de background et de foreground, sur lequel la solution est interpolée dans l'espace et le temps par un polynôme approprié. Ce stencil hybride permet une transition continue de discrétisation d'un bloc à l'autre. En particulier, une solution FEM discontinue sans maillage est d'abord récupérée, puis une correction MVF est effectuée dans n'importe quelle cellule en utilisant les informations fournies par les cellules voisines. Ainsi, pour les cellules à franges, la solution est obtenue en combinant des valeurs provenant de différentes grilles.

Schéma ADER

La méthode Arbitrary high order DERivatives (ADER) constitue un cadre idéal pour poursuivre notre objectif. Dans [41, 109, 108, 29], les auteurs ont présenté une méthode permettant de récupérer une solution précise pour des EDP hyperboliques avec un ordre de précision arbitraire sur un seul bloc de maillage. Plus récemment, dans [28], les auteurs ont présenté un schéma ADER de Galerkin discontinu avec *a posteriori* un limiteur de volume fini à sous-cellules sur des grilles fixes et mobiles telles que des mailles cartésiennes AMR adaptatives spatio-temporelles. Le schéma numérique traite la variable temporelle indistinctement par rapport aux variables spatiales en définissant la solution sur une dalle spatio-temporelle. Cette approche de discrétisation nous permet donc de reconsidérer le problème des conditions de transmission des grilles de Chimera : au lieu de conditions de transmission spatiale

dépendant du temps entre des blocs de grille en mouvement relatif, nous définissons des polynômes d'interpolation sur des cellules spatio-temporelles se croisant arbitrairement aux frontières des blocs.

Dans le schéma ADER, une solution locale spatio-temporelle faible du problème entre les temps génériques t et $t + \Delta t$ est calculée dans chaque cellule spatio-temporelle. Cette solution est définie comme le *prédictrice*. L'étape de prédiction est locale et donc parallélisable, car la solution est calculée indépendamment des informations des cellules voisines. Ensuite, dans l'étape suivante de *correction*, le calcul d'un flux numérique spatio-temporel entre les cellules voisines fournit la stabilisation appropriée du schéma d'intégration. Nous étendons cette méthode de prédiction-corrrection aux EDP d'Advection-Diffusion sur des grilles surdimensionnées et proposons un flux spatio-temporel entre les cellules spatio-temporelles qui fournit une stabilisation et une précision améliorées car il prend en compte la nature advective et diffusive de l'opérateur local (éventuellement non linéaire).

Le schéma ADER, dans sa première formulation, peut être considéré comme une évolution d'un schéma classique de type Godunov pour les lois de conservation hyperboliques [49, 50]. Ce type de méthode utilise l'autosimilarité de la solution du problème de Riemann local avec des données initiales constantes par morceaux pour calculer le flux upwind numérique. Par la suite, la méthode a été étendue en employant une reconstruction linéaire par morceaux non oscillante pour le problème de Riemann généralisé local à l'interface des cellules avec lesquelles l'espace est discrétisé [68, 115]. La résolution numérique du problème de Riemann généralisé est généralement lourde et il peut être impossible de l'obtenir pour des équations d'Euler compliquées (par exemple, les problèmes de magnéto-hydro dynamique). La méthode ADER est une tentative pour surmonter cette difficulté. Il s'agit d'une méthode de précision d'ordre élevé dans l'espace et le temps. Afin d'évaluer le flux numérique, pour la méthode ADER, le problème de Riemann généralisé est résolu avec une condition initiale définie par des fonctions lisses en utilisant une méthode semi-analytique [110]. La solution approximative est donnée par une expansion de Taylor locale (c'est-à-dire à l'interface ou entre les cellules) en temps jusqu'à un ordre de précision quelconque.

Maillages surdimensionnées pour les écoulements incompressibles et les problèmes d'interaction fluide-structure

Un des objectifs de cette thèse est de développer un schéma de résolution des équations incompressibles de Navier-Stokes (1) où le domaine éventuellement déformable $\Omega(t)$ est discrétisé par des grilles overset. En particulier, le domaine $\Omega(t)$ peut être considéré comme l'espace géométrique dans lequel le fluide effectue sa dynamique. Par conséquent, le maillage Chimera se déforme en fonction d'une déformation de l'espace solide représenté et discrétisé par une surface interne des mailles de foreground. Historiquement, le premier à proposer des grilles overset a été Volkov dans les années 70 [116]; les premières implémentations d'importance scientifique sont celles de Starius pour les équations hyperboliques [105]. Successivement, parmi tous, nous mentionnons Atta [7] pour l'étude de l'interfaçage adaptatif des grilles, Kreiss [70] pour l'introduction de grilles curvilignes se superposent, Benek *et al.* [13, 14] et Rai [94], pour l'équation d'Euler, et Cheshire et Henshaw [30], pour une généralisation des maillages chimériques pour une large gamme d'EDP.

Tous les travaux cités utilisent plusieurs méthodes pour résoudre numériquement

les différents problèmes différentiels. Il est possible de les regrouper en deux catégories principales : Les méthodes à pas fractionnés (FSM) et les approches de décomposition de domaine (DD). Dans le contexte des écoulements incompressibles et de l'interaction fluide-structure, parmi les travaux utilisant une FSM, nous citons un article récent de Meng *et al.* [76]. Dans ce travail, les auteurs atteignent une précision de quatrième ordre. En ce qui concerne les approches DD, l'un des derniers travaux est celui de Mittal, Dutta et Fischer [77], dans lequel une approche Schwarz-spectrale est utilisée en décomposant le domaine par rapport aux différents blocs de la grille overset. Malgré les différentes méthodes, tous les travaux ont en commun le fait que les cellules marginales, à savoir les cellules à la limite des régions de recouvrement, échangent l'information par une interpolation appropriée. En général, un effort particulier est consacré à la définition d'une interpolation rapide et efficace garantissant l'ordre de précision requis pour la solution finale. Par exemple, dans le cas de [76], une interpolation polynomiale BWENO est employée, alors qu'une parallélisation efficace du processus d'interpolation dans les régions de superposition est proposée dans le cas de [77]. L'un des travaux les plus récents de Sharma *et al.* [100] définit la différenciation suivante des nœuds d'une grille overset :

- **Points de champ** : nœuds du maillage auxquels les équations de gouvernance sont résolues ;
- **Points de frontières** : points de maillage où les informations sont transférées entre les mailles superposées ;
- **Points de trou** : points de maillage pour lesquels la solution n'existe pas.

Ce classement classique des nœuds nous donne l'occasion de souligner les différences de la méthode proposée dans cette thèse par rapport à l'état actuel de la technique. Puisque nous utilisons une approche ADER et que nous dépensons une partie des coûts de calcul globaux pour trouver un stencil compact aux interfaces qui se superposent, nous n'avons jamais besoin d'échanger des informations par interpolation. En particulier, comme il apparaîtra clairement au cours de la thèse, l'étape de prédiction d'ADER définit une approche à mailles libres pour laquelle tous les nœuds ne sont pas différenciés par rapport au clustering classique ; ainsi, leur appartenance à un bloc spécifique n'est plus importante ; successivement, dans l'étape de correction suivante, en raison de la définition d'un stencil hybride composé de nœuds appartenant à des mailles différentes, l'approche par volumes finis permet d'échanger automatiquement les informations de l'étape précédente. La méthode ne considère pas les nœuds comme faisant partie d'un bloc mais plutôt leurs distances euclidiennes dans la définition du stencil. En d'autres termes, la configuration de superposition spécifique au problème est gérée sans effort. L'interpolation effectuée n'est obligatoire que lorsqu'une cellule de trou devient une cellule active en raison du mouvement de la maille de foreground.

La méthode proposée pour les équations incompressibles de Navier-Stokes étant fractionnaire, la pression est résolue via un problème de Poisson. Dans ce cas également, les cellules marginales ne sont plus exploitées comme donneurs ou récepteurs d'informations. En fait, une discrétisation appropriée de l'opérateur de gradient est proposée aux interfaces en utilisant toutes les informations du stencil hybride compact. Par conséquent, les relations décrites par la matrice de rigidité résultant de la discrétisation de l'opérateur de Laplace gèrent automatiquement l'échange d'informations sans passer par une étape d'interpolation ultérieure.

L'état actuel de l'art considère les grilles Chimera comme une discrétisation de l'espace. Grâce à la méthode ADER, les grilles overset proposées dans la thèse discrétisent le continuum espace-temps et, par conséquent, définissent des mailles chimères espace-temps. Ceci est un avantage qui permet de faire évoluer le domaine ainsi que la grille overset (avec une dépendance possible de la solution elle-même) et, en même temps, de calculer la solution sur cette structure de calcul évolutive.

Réduction et hyper-réduction de l'approche ADER

Dans la dernière partie de la thèse, une version réduite et hyper-réduite de l'approche ADER est introduite. Les méthodes de réduction de l'ordre du modèle (MOR) sont formulées afin de réduire de manière significative les coûts de calcul pour obtenir une approximation numérique de la solution d'une EDP. En particulier, quand on veut une solution qui est paramétrique par rapport à un ensemble donné de paramètres variables (comme les paramètres géométriques ou les variables de diffusion, etc.), les méthodes MOR donnent la possibilité d'évaluer facilement cette solution le long de l'instance spécifique des paramètres. Ce type de méthodes consiste typiquement en une étape d'apprentissage offline (éventuellement onéreuse en termes de coûts de calcul) et une étape online qui permet de reconstruire la nouvelle solution requise avec un grand avantage en termes de coûts et de temps de calcul.

La méthode réduite proposée pour obtenir la solution approchée est la Proper Orthogonal Decomposition (POD) [102, 22]. Les solutions haute-fidélité collectées via ADER pour certaines instances des paramètres sont réarrangées hiérarchiquement afin de définir une base couvrant le sous-espace V_M , de dimension M , d'un espace fonctionnel propre V sur lequel la solution réduite est projetée dans l'étape online. Nous sommes intéressés par la recherche de solutions dépendant de paramètre(s) conduisant à la déformation du domaine. Pour cette raison, une approche DD est appliquée à la réduction. Cela signifie que dans certaines régions particulières qui sont affectées par l'évolution du domaine, la solution est réduite et que dans les autres sous-régions, la solution est toujours de haute fidélité. En particulier, la décomposition est définie par la grille overset elle-même. L'approche de réduction donne l'opportunité de redéfinir le schéma ADER en considérant une macro-cellule identifiée par la grille de foreground.

Comme la nouvelle reformulation d'ADER sur une macro-cellule nécessite une légère modification par rapport à sa formulation classique (c'est-à-dire haute fidélité), les matrices qui en découlent dans la contrepartie algébrique du schéma doivent être calculées à chaque instance temporelle. En fait, l'espace de projection V est composé de fonctions qui ne sont assurées que d'une continuité locale (et non globale) le long des coordonnées spatiales. Pour cette raison, une approche d'hyper-réduction est proposée afin d'intégrer et de calculer facilement les matrices en utilisant des nœuds de quadrature beaucoup plus petits que ceux nécessaires pour obtenir une approximation intégrale à l'ordre de précision fixé.

Acknowledgements

I would like to express my deep gratitude to Dr. **Michel Bergmann** and Prof. **Angelo Iollo**, my research supervisors, for their patient guidance, enthusiastic encouragement and useful critiques of this research work. From both of them I have learnt several lessons about the researcher's job and I will definitely take inspiration from them for my future career. Among the most valuable lessons, I would like to mention three : 1) a thought, no matter how complex, is best expressed with the right words because a mathematician never uses too many or too few words ; 2) mathematics is a language that must not limit the objective but must help to solve the problem ; 3) having a social life helps to see even the most difficult mathematical problems from a decisively solving point of view.

One year of my PhD was at **Optimad Engineering** in Turin. Special thanks therefore go to Dr. **Haysam Telib**, CEO of the company, who welcomed me during the difficult period of the pandemic. That experience gave me an insight into how useful mathematics can be at an industrial level and gave me a real understanding of the mathematics that exists outside the academic environment.

The final result of this manuscript would not have been the same without the valuable contribution of reviewers Prof. **Michael Dumbser** and Prof. **Alexandre Ern**. The fair critique of what has been written and the ensuing debate has been an important moment of growth for me.

During my PhD years, an important guide and point of reference within INRIA was Mme. **Anne-Laure Gautier**, to whom I extend my warmest thanks for the many emails and the very quick and always useful replies.

Research is made up of people, and I was lucky enough to meet some of them between the IMB, INRIA and the University of Bordeaux. Many everyday moments have become special, from afternoons spent together debating different questions to many laughs, meals and drinks all together. Among all, I want to mention my office-mates **Antoine, Floriane, Guillaume, Beatrice, Alexis** and **Nishant**. All people from teams MEMPHIS and MONC turned out to be friends even before being colleagues.

Despite the hard times of the pandemic and the many restrictions of these years, I was able to have a life outside the walls of the university, both in Bordeaux and in Turin. And "out there" I actually found a "in here" made up of people who are now my friends and with whom a strong relationship began. I cannot mention them all because it would not be enough to write another thesis. My memory now has milestones made up of parties, walks, go-outs, eating, drinking or simply chatting with many of them. Among all, I would like to thank my flatmate **Snigdha** because of the great support given to me during this last year of my PhD and the sometimes "dramatic" and hard time of writing the manuscript.

Finally, I want to thank my family because they are always there. No matter how far I go, in the end it is never so far that I don't feel their support there.

The author of this thesis is a human being. I should thank for this a number of artists, scientists, poets, writers, dancers, painters, composers, psychologists, ... For

the sake of brevity, I will quote a poet, **Simonides of Keos**, as distant in time as he is close in perception of what he is saying :

«Ὁ λόγος τῶν πραγμάτων εἰκῶν ἐστίν».

The translation in English is by **Anne Carson**, the most powerful writer I read during my PhD, from her essay *Economy of the Unlost : Reading Simonides of Keos with Paul Celan* :

«The word is a picture of things».

My viewpoint in one sentence.

Myself in a fragment. . .

Bordeaux - Turin - Bordeaux
October 1st, 2018 - December 15th, 2021

Contents

Résumé	v
Abstract	vii
Résumé détaillé	ix
Acknowledgements	xvii
List of Figures	xxiv
List of Tables	xxvi
List of Abbreviations	xxvii
1 Introduction and state of the art	1
2 The one dimensional case	11
2.1 The third order stencil reconstruction: CWENO approach	12
2.1.1 Stencil of non overlapping cells	12
2.1.2 Stencil of overlapping cells	14
2.1.3 Numerical results	15
2.2 The CWENO-ADER approach for advective equations	17
2.2.1 Local space-time Galerkin predictor	23
2.2.2 The mesh motion	25
2.2.3 Finite volume scheme over the space-time cell	26
2.2.4 Cell management during the chimera meshes motion	28
2.2.5 Numerical results	29
2.3 Approximation of the first derivative over an overlapping stencil	30
2.4 The Poisson equation	35
2.4.1 Numerical results	35
3 The Advection-Diffusion problem	39
3.1 The overset grid	40
3.1.1 The automatic definition of the stencil at the transmission condition	40
3.2 The numerical method	41
3.2.1 Local polynomial reconstruction	41
3.2.2 Local space-time Galerkin predictor	44
3.2.3 Recovery of the map and foreground mesh motion	47
3.2.4 Correction stage: the finite volume scheme over the space-time cell	49
3.2.5 Dynamics of the overlapping zone	50
3.3 The stabilization of the scheme	51
3.3.1 The local advective-diffusive stabilization term	51

3.3.2	The choice of the relaxation time	52
3.3.3	The local advective stabilization term	55
3.4	Numerical results	56
3.4.1	Order of convergence	57
3.4.2	Empirical analysis of stability condition	60
3.4.3	Relationship between the convective field and the foreground mesh velocity	63
3.4.4	Further topics	66
Nonlinear system	66	
Multimesh setting	67	
Complex domains	68	
3.5	Conclusions of the chapter	68
4	The incompressible Navier-Stokes equations	75
4.1	The governing equations	75
4.2	The numerical method	76
4.2.1	The predictor solution	78
Local space-time Galerkin predictor	78	
The space-time finite volume scheme	79	
4.3	The pressure equation	80
4.3.1	The geometric reconstruction	81
4.3.2	Truncation error and stencil at fringe cells	83
4.4	The face-center discrete operators on overset grids	86
4.5	Numerical results	87
4.5.1	Poisson equation	87
4.5.2	Order of convergence	87
4.5.3	The lid driven cavity	90
4.5.4	The cylinders	92
Steady cylinder	93	
Impulsively started cylinders	94	
Impulsively started then stopped cylinders	95	
4.6	Sedimentation of a cylinder	95
4.7	Conclusions of the chapter	102
5	Reduced and Hyper-reduced ADER method	103
5.1	Reduced-order model based on ADER approach	104
5.1.1	The prediction stage	104
5.1.2	The correction step	106
5.1.3	Domain decomposition approach	107
5.2	Proper Orthogonal Decomposition	108
5.3	Hyper-reduction	109
5.4	Numerical results	112
5.4.1	Linear test case	113
5.4.2	Nonlinear test case	118
5.5	Conclusions and future perspectives of the chapter	119
	Conclusions	125
A	The CWENO polynomial	131
A.1	The non overlapping stencil	131
A.2	The overlapping stencil	132

B	ADER approach for the 1D advection equation	133
B.1	The research of the Galerkin predictor solution	133
B.2	Constants in Rusanov flux	133
C	The ADER approach for the advection-diffusion problem	135
C.1	The Galerkin predictor	135
C.2	Time step Δt in the limit of large diffusion	136
D	Chorin-Temam method	137
D.1	Poisson equation with fully homogeneous Neumann conditions	138
	Bibliography	141

List of Figures

1.1	An exemple of Immersed Boundary discretization	3
1.2	Sketch of the Chimera mesh	5
1.3	Sketch of Chimera mesh for explaining the interpolation on the overlapping region	5
1.4	Sketch of grid connectivity in 1D	5
1.5	Comparison between Chimera and Dragon grids	6
2.1	An overlapping configuration in 1D	15
2.2	Comparison of solution for <i>CASE2</i> with different steady mesh configurations.	18
2.3	Comparisons of the L^1 -errors for $\epsilon = h$ and $\epsilon = 10^{-6}$ for one overlapping zone ($IO = 50\%$)	21
2.4	Comparisons of the L^1 -errors for $\epsilon = h$ and $\epsilon = 10^{-6}$ for two overlapping zones ($IO = 50\%$).	22
2.5	Overlapping space-time cell in 1D	26
2.6	Comparison between non overlapping and overlapping cells in 1D	28
2.7	The three possible configurations of overlapping cells during the meshes motion in 1D	29
2.8	Three time instances for <i>CASE1</i> with a rigid translation movement of the inside mesh.	31
2.9	Three time instances for <i>CASE3</i> with translation and deformation movement of the inside mesh.	32
2.10	An overlapping stencil in 1D	33
2.11	Solution of <i>CASE4</i> (Poisson)	36
2.12	Solution of <i>CASE5</i> (Poisson)	37
3.1	Example of Chimera grid configuration	40
3.2	Two possible stencils: all cells in the same partition and cells in different partitions	42
3.3	Visualization of Algorithm 3.1.	42
3.4	Representation of the map \mathcal{M}_i from the reference space-time cell $\hat{\mathcal{C}}$ to the physical space-time cell \mathcal{C}_i^n	45
3.5	Three time instants for the 1D test case <i>test2</i>	59
3.6	Three time instants for test cases <i>TEST1</i> and <i>TEST2</i> for AD problem	62
3.7	Numerical solutions and point-wise error for <i>TEST3</i> (AD problem) with respect to the three possible foreground mesh speed $P1$, $P2$ and $P3$	65
3.8	Comparison between the numerical and exact solution of <i>TEST3</i> (AD problem) at time $t = 0.84$ for a moving foreground mesh travelling with a speed generating a loss of information.	66
3.9	Components of the solution of nonlinear test at time $t = T = 0.5$ (AD problem)	67
3.10	Multi-block meshing for <i>TEST2</i> (AD problem)	69
3.11	Numerical solution and mesh configuration of <i>TEST4</i> (AD problem)	71

3.12	Numerical solution and mesh configuration of <i>TEST5</i> (AD problem)	72
4.1	Sketch of the mesh configuration in fluid-structure interaction setting	77
4.2	Sketch of two internal cells Ω_1 and Ω_2 sharing the edge γ .	81
4.3	Zoom of unit directions \mathbf{d}_c , \mathbf{d}_t and \mathbf{n} over the face-center P .	82
4.4	Sketch of overlapping configurations	85
4.5	Three different chimera-meshes for the Poisson problem.	88
4.6	Solution of the Poisson problem for the different configurations	89
4.7	Pointwise errors of the divergence of the Poisson problem for the different configurations.	90
4.8	Steady streamlines for the lid driven cavity test	92
4.9	Drag coefficient for steady cylinder at $\text{Re} = 550$	93
4.10	Chimera configuration of <i>Grid3</i> .	94
4.11	Drag and lift coefficients for the steady cylinder at $\text{Re} = 200$.	95
4.12	Comparison of drag coefficient between the steady and impulsively started cylinder at $\text{Re} = 550$	96
4.13	Pressure at $t = 5$ for steady and impulsively moving cylinders at $\text{Re} = 550$.	96
4.14	Drag coefficient for the impulsively started cylinder at $\text{Re} = 200$	97
4.15	Drag coefficient for the impulsively started and then stopped cylinder at $\text{Re} = 40$	97
4.16	Drag coefficient for the impulsively started and then stopped cylinder at $\text{Re} = 550$	98
4.17	Chimera configuration for the sedimentation cylinder.	99
4.18	Vertical velocity on a horizontal cut through the center of the cylinder at time $t = 0.1$ for the sedimentation test case	100
4.19	Vertical position of the center of the cylinder for the sedimentation test case	100
5.1	High-fidelity solution at time $t = 1.5$ for the linear test case for some instances of cylinder velocity z .	114
5.2	ROM solutions at time $t = 1.5$ for the linear test case.	115
5.3	Evolution of the first five reduction coefficients for the in-sample, out-of-sample and variable velocity reconstruction. These coefficients do not refer to the specific time instance t^n but to all times in $[t^n, t^{n+1})$.	116
5.4	Error analysis for linear test case	117
5.5	Percentage analysis of $N_{hr}/(N_E N_{int})$ as function of the number of modes for the linear test case	118
5.6	High-fidelity solution at time $t = 1.5$ for the nonlinear test case for some instances of cylinder velocity z .	120
5.7	ROM solutions at time $t = 1.5$ for the nonlinear test case.	121
5.8	Evolution of the first five reduction coefficients for the in-sample and variable velocity reconstructions. These coefficients do not refer to the specific time instance t^n but to all times in $[t^n, t^{n+1})$.	122
5.9	Error analysis for nonlinear test case	123
5.10	Percentage analysis of $N_{hr}/(N_E N_{int})$ as function of the number of modes for the nonlinear test case	124

List of Tables

2.1	L^1 -norm error and converge rate with one uniform mesh as function of the total number of nodes N .	17
2.2	L^1 -norm error and converge rate with two overlapping meshes as function of the total number of nodes N ($IO = 10\%$)	19
2.3	L^1 -norm error and converge rate with two overlapping meshes as function of the total number of nodes N ($IO = 50\%$)	19
2.4	L^1 -norm error and converge rate with two overlapping meshes as function of the total number of nodes N ($IO = 80\%$)	19
2.5	L^1 -norm error and converge rate with three overlapping meshes as function of the total number of nodes N ($IO = 10\%$)	20
2.6	L^1 -norm error and converge rate with three overlapping meshes as function of the total number of nodes N ($IO = 50\%$)	20
2.7	L^1 -norm error and converge rate with three overlapping meshes as function of the total number of nodes N ($IO = 80\%$)	20
2.8	L^1 -norm error and convergence rate in the <i>translation</i> and <i>translation and deformation</i> configurations as function of the total number N of nodes.	30
2.9	L^2 -errors and order of convergence for <i>CASE4</i> and <i>CASE5</i> as function of the total number N of cells.	36
3.1	Summary of 1D test cases <i>test1</i> and <i>test2</i> and 2D test cases <i>TEST1</i> and <i>TEST2</i> for AD problem	58
3.2	Convergence analysis for 1D test cases <i>test1</i> and <i>test2</i> for AD problem	60
3.3	Convergence analysis for 2D test cases <i>TEST1</i> and <i>TEST2</i>	60
3.4	Convergence analysis for 2D test cases <i>TEST1</i> and <i>TEST2</i> in H^1 -seminorm.	61
3.5	Experimental stability analysis	61
3.6	Features of <i>TEST3</i> for AD problem	64
3.7	Errors for <i>TEST3</i> for AD problem	64
3.8	Convergence analysis of the nonlinear test case (AD problem)	67
3.9	Convergence analysis of the nonlinear test case in H^1 -seminorm.	67
3.10	Summary scheme of <i>TEST4</i> and <i>TEST5</i> (AD problem)	70
4.1	Errors and convergence rate in L^2 -norm for the Poisson equation	89
4.2	Convergence analysis for Taylor-Green Vortices	90
4.3	Maximum stream-function Ψ_{\max} , vorticity ω and location of the topological point for the lid driven cavity	91
4.4	Features of the five considered Chimera meshes for the convergence grid study	93
4.5	Drag coefficient C_D and the Strouhal number S_t for the steady cylinder at $Re = 200$	94
5.1	Characteristics of the generator functional \mathcal{H}_E^z for the hyper-reduction	110

5.2 Total number $N_E N_{int}$ of quadrature points with respect to the domain
integration E 114

List of Abbreviations

A	Advection
AD	Advection Diffusion
ADER	Arbitrary high-order Derivates
ALE	Arbitrary Lagrangian Eulerian
AMR	Adaptive Mesh Refinement
BC	Boundary Conditions
bg	back ground
cc	cell center
CFL	Courant Friedrichs Lewy
CWENO	Central Weighted Essentially Non-Oscillatory
DD	Domain Decomposition
DG	Discontinuous Galerkin
DOF	Degree Of Freedom
fc	face center
FE(M)	Finite Element (Method)
fg	foreground
FV(M)	Finite Volume (Method)
GBM	Ghost Boundary Method
HF(M)	High-Fidelity (Method)
HR	Hyper-Reduction
IC	Initial Ccondition
IBM	Immersed Boundary Method
IO	Index of Overlapping
LLF	Local Lax-Friedrichs
NS	Navier Stokes
ODE	Ordinary Differential Equation
PDE	Partial Differential Equation
PM	Penalization Method
POD	Proper Orthogonal Decomposition
ROM	Reduced Order Method
SVD	Singular Value Decomposition
TVD	Total Variation Diminishing
WENO	Weighted Essentially Non-Oscillatory

To Iphigenia

Chapter 1

Introduction and state of the art

Background

One of the main difficulties for the simulation of a phenomenon modeled by a Partial Differential Equation (PDE) is the geometrical modeling of the computational domain with a single mesh block. This problem is especially relevant when the domain is complex or its shape and its topology evolve during the simulation. Classical approaches to tackle this problem include the Arbitrary Lagrangian-Eulerian (ALE) method, fictitious domain approaches and Chimera grids.

ALE methods [61] allow a certain degree of mesh deformation and adaptation thanks to an appropriate reformulation of the governing equations and to sophisticated and efficient grid displacement algorithms. In 1969, Harlow listed the main schemes for solving problems in fluid dynamics accordingly to their formulation in Lagrangian or Eulerian coordinates [54]. When the method uses meshes whose nodes move accordingly to the movement of the fluid, it is said to be Lagrangian. On the contrary, if the mesh is always fixed (namely it does not change with respect to the movement of the fluid), the method is Eulerian. The first attempt of a formulation of a method using a mesh whose movement is independent of the dynamics of the fluid was proposed by Trulio in 1966 for compressible flows [113]. The proposed method is explicit, thus the movement of the mesh is related to the movement of the fluid through a stability condition. Successively, in papers by Hirt in 1970 [60] and Hirt *et al.* in 1974 [61], a finite differences ALE method was defined. In those works, because of an implicit formulation, the velocity of the mesh is decoupled by the velocity of the fluid. However, when the grid deformation leads to excessively stretched cells, a delicate (and computationally expensive) global re-meshing step may be necessary. In turn, this operation can introduce approximation irregularities that are caused by the interpolation of the solution from the old grid to the new one.

In fictitious domain approaches, including ghost boundary methods [47], immersed boundary [78] or penalization methods [4], the original problem is discretised on a simple mesh, usually structured and Cartesian, constant in time [48, 88, 4].

Fedkiw *et al.* in [45] proposed for the first time a Ghost Boundary Method (GBM). With the objective of simulating gas dynamics problems, GBM combines the robustness of Eulerian schemes with a multimaterial interface method characteristic of a Lagrangian scheme. By tracking the interface with a level set function [82, 106], at the interface location an approximate Riemann problem is solved. Consequently, this technique results useful when a shock wave or a discontinuity moves in the computational domain.

In his PhD thesis of 1972, Peskin proposed the Immersed Boundary method (IBM)

in order to simulate cardiac mechanics associated to the blood flow [89]. In this former work, the author proposes the usage of a single Cartesian block nonconforming with the real shape of the heart (i.e. the domain); thus an immersed boundary is built into the Cartesian block for simulating the effects of the blood flow. Today IBM is related to a *Cartesian grid method* originally developed for simulating inviscid flows with complex embedded boundaries on Cartesian grids [15, 34, 37]. Successively, these methods were extended to unsteady viscous flows [114, 119]. Today IBMs are addressed not only to fluid-structure interactions but also to liquid-liquid and liquid-gas interactions [2, 97]. In Figure 1.1 there is a sketch of IBM spatial discretization from [78].

For the study of incompressible flows, another approach is provided by the Penalization Methods (PM). Also this method aims in avoiding building body-fitted unstructured meshes in order to use fast and efficient numerical schemes (e.g. spectral, finite differences or finite volume methods) on Cartesian meshes. To do this, a penalization velocity term in the momentum equation for the incompressible Navier-Stokes equations is added. In the former works [86, 87] by Peskin on the blood flow in the heart and in some other reviewed formulations (such as in [51]), both a time integral of the velocity and a velocity penalization term are added only at the surface defining the obstacle. Successively, Saiki and Biringen [96] extended the penalization to the whole domain in order to take into account large Reynolds numbers. The firsts to extend the penalization to a volume of a porous medium were Arquis and Caltagirone [6]. Finally, Angot and Caltagirone [5, 3] extended the penalization in order to deal with fluid-porous solid systems. In particular, let $\Omega \subset \mathbb{R}^d$, with $d = 2, 3$, be the computational domain and let it contain a certain number of irregular solid obstacles whose union is defined by Ω_s whose possible velocity is \mathbf{u}_s . Consequently The remaining subdomain $\Omega_f = \Omega/\Omega_s$ is occupied by the fluid. The incompressible Navier-Stokes equations for this problem read: *find the velocity $\mathbf{u} : \Omega_f \times \mathbb{R}_+ \rightarrow \mathbb{R}^d$ and the pressure $p : \Omega_f \times \mathbb{R}_+ \rightarrow \mathbb{R}$ of the fluid such that*

$$\begin{aligned} \partial_t \mathbf{u} + \mathbf{u} \cdot \nabla \mathbf{u} &= \nabla p + \frac{1}{\text{Re}} \Delta \mathbf{u} & \text{in } \Omega_f \times \mathbb{R}_+ \\ \nabla \cdot \mathbf{u} &= 0 & \text{in } \Omega_f \times \mathbb{R}_+ \\ \mathbf{u} &= \mathbf{u}_s & \text{in } \partial\Omega_s \times \mathbb{R}_+ \end{aligned} \quad (1.1)$$

properly closed with initial and boundary conditions over the remaining part of the boundary $\partial\Omega$ of the domain. The PM solves the incompressible Navier-Stokes equations by substituting the first line of problem (1.1) with

$$\partial_t \mathbf{u} + \mathbf{u} \cdot \nabla \mathbf{u} = \nabla p + \frac{1}{\text{Re}} \Delta \mathbf{u} + \frac{\chi_s}{K} (\mathbf{u}_s - \mathbf{u}) \quad \text{in } \Omega_f \times \mathbb{R}_+, \quad (1.2)$$

where χ_s is the indicator function¹ over Ω_s and K is the penalization constant. For the theoretical results of converge in the limit of vanishing K of solution for (1.2) to the solution for (1.1), the reader is addressed to [4].

For these briefly introduced fictitious domain approaches, the grid does not necessarily fit the physical boundaries and special care must be taken to attain a sufficient degree of accuracy at the boundaries. Moreover, the presence of thin boundary layers can significantly reduce the computational advantages deriving from a simple

1.

$$\chi_s(\mathbf{x}) = \begin{cases} 1, & \mathbf{x} \in \Omega_s \\ 0, & \text{otherwise} \end{cases}.$$

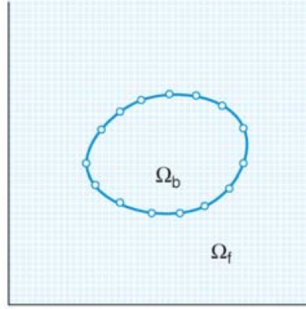


FIGURE 1.1 – An example of Immersed Boundary discretization. The solid boundary Ω_b is defined by a closed line into a Cartesian grid. Over the fluid domain Ω_f and the solid domain Ω_b the system of PDEs describes the fluid and solid dynamics, respectively. This figure is from [78].

meshing algorithm, because of the uniform aspect ratio of the mesh. Hybrid techniques employing immersed boundary methods with anisotropic mesh adaptations can be employed for circumventing this problem [1].

Overset grids

We focus our investigations on Chimera grids [116, 14, 75, 90]. Chimera grids consist of multiple overlapping mesh blocks that together define an overset grid used for spatially discretize a PDE [104, 105, 103] (see Figure 1.2). Usually, one has a background mesh that includes one or more foreground mesh patches that are fitted to the physical domain boundaries. This mesh generation approach considerably simplifies the task of mesh adaptation in the case of boundary layers, changing geometry for an unsteady problem (e.g. fluid-structure interaction problems in fluid-dynamics) and for unsteady multiply connected domains [10, 8, 98, 9, 30]. Once the multiple mesh patches are generated, they are collated in order to obtain an appropriate overlapping zone between the neighboring blocks [75].

The usage of Chimera meshes is essentially based on grid embedding techniques for discretizing the possible evolving computational domain. A major grid (*background block*) is first built. It is non-conformal with respect to the complex shape of the domain. Successively minor grids (*foreground blocks*) are constructed in order to precisely describe the particular shapes of those regions where the obstacles are located. Since the minor blocks overlap the major block, an overlapping region is defined among all blocks. Along the overlapping regions the information of the solution needs to be mutually exchanged from one block to another. In this thesis, a compact transmission condition is sought in order to limit communications between the grids. Namely, a compact stencil only composed of the first layer of cells is defined around any cell.

The choice of the interpolation scheme at the interface falls between two possibilities: nonconservative and conservative approaches. The nonconservative schemes (the most used) are defined on the local study of the particular overlapping configuration of cells used for defining the interpolation itself. References on the order of accuracy affecting the global numerical scheme can be found in [30]. The conservative interpolations involve patched interfaces [16, 94] or arbitrarily overlapped regions [81, 118]. In general these schemes are not attractive because if they are relatively easy to implement in two dimension, they become cumbersome or impossible

to be applied in three dimensions. Moreover, even though a global conservation of fluxes is ensured among the overlapping boundaries or on the boundary of the holes, local flux conservation could not be preserved. Figure 1.3 from [65] sums up a classical chimera configuration.

In the thesis, we propose a space-time Finite Element Finite Volume scheme on Chimera grids. Our objective is to combine some aspects of an ALE approach, notably its flexibility with respect to grid displacement and deformation, to the multi-block discretization strategy of overset grids. In particular, we devote special care to grid overlapping zones in order to devise a compact and accurate discretization stencil to exchange information between different mesh patches, in the spirit of previous works on Cartesian hierarchical grids [93]. We then apply this approach to integrate linear and nonlinear Advection-Diffusion partial differential equations and show how the method can exploit the versatility of the Chimera meshes to reach second order accuracy in unsteady multiply connected domains.

The numerical solution on Chimera grids is obtained by exchanging data through the fringe cells at the overlapping zone. For example, in [32, 53, 117, 74], fringe (namely *donor*) cells of a block in proximity of the overlapping zone provide the information to the fringe (i.e., *receptor*) cells of another block by polynomial interpolation. In [58] a coarse grid is automatically generated and a connection of interpolation information at the overlapping zone is presented through a multigrid approach (as sketched in Figure 1.4 for a one dimensional overset grid).

Another way of making the different blocks communicate is to use proper Domain Decomposition (DD) methods (e.g., Schwartz, Dirichlet/Neumann or Dirichlet/Robin methods). In particular, each mesh block is considered as a decomposition of the domain and the overlapping zones are the interfaces for coupling the different blocks. Accordingly to these approaches, typically iterative discrete methods are employed. For this two-way communication, the reader is referred to [62] for further details.

In the same framework, other approaches connect the background and the foreground meshes, such as the DRAGON grids [65] for which the overlapping zone is replaced by a unstructured grid during a further stage by preserving the body-fitting advantages of the Chimera meshes. Figure 1.5 compares a Chimera mesh with a Dragon grid. Finally, a Dragon grid consists in creating a unique block mesh from a Chimera configuration. However, the computational costs for achieving a Dragon grid for evolving domain largely increase because possibly at any time instance a new DRAGON mesh needs to be created.

In contrast, here we derive a second order compact transmission condition by properly defining a set of cells, i.e. the *stencil*, that belong to *both* the back- and foreground meshes, over which the solution is interpolated in space and time by an appropriate polynomial. This hybrid stencil allows a smooth discretization transition from one block to another. In particular, first a mesh-free discontinuous FEM-solution is recovered and then a FVM-correction is performed in any cell by using information provided by neighboring cells. Thus, for fringe cells, the solution is obtained by combining values from different grids.

ADER scheme

The Arbitrary high order DERivatives (ADER) method provides an ideal setting for pursuing our purpose. In [41, 109, 108, 29], the authors presented a method to recover an accurate solution for hyperbolic PDEs with an arbitrary order of accuracy

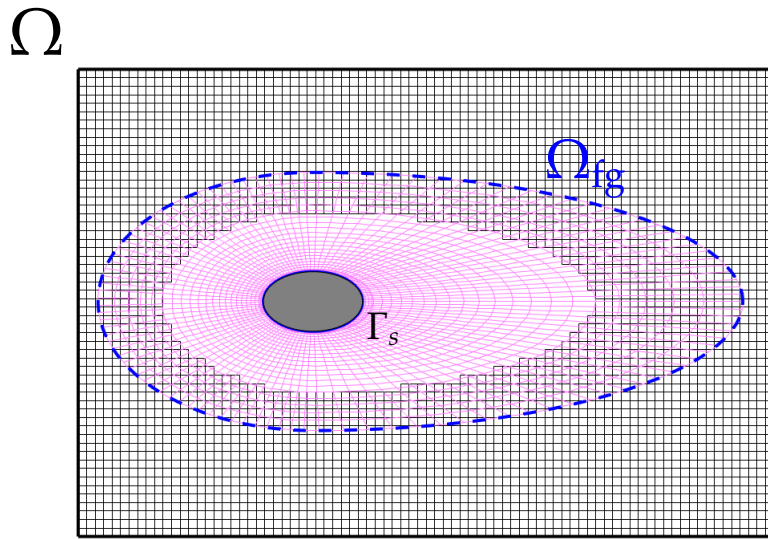


FIGURE 1.2 – Sketch of the mesh configuration. The computational (i.e. fluid) domain contains the solid body whose boundary is Γ_s . The foreground mesh (in blue) defines the foreground subdomain Ω_{fg} whose boundary is the union of an external (dashed line) and internal (continuous line) boundary. Consequently, the internal foreground boundary coincides with the solid body boundary.

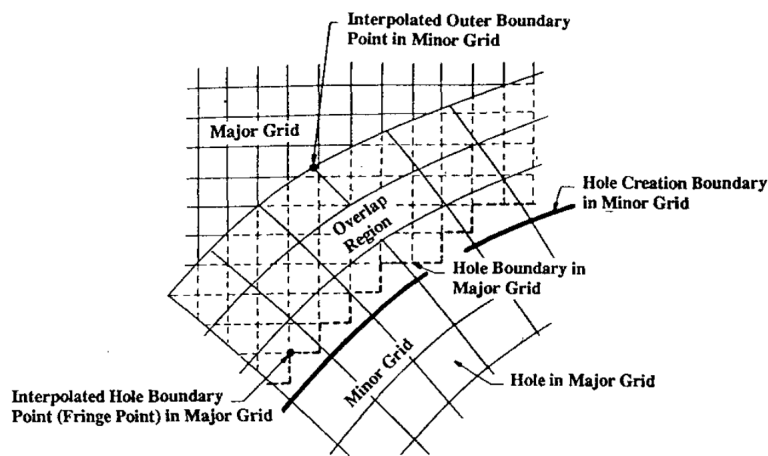


FIGURE 1.3 – Sketch of Chimera mesh for explaining the interpolation on the overlapping region. The figure is from [65].

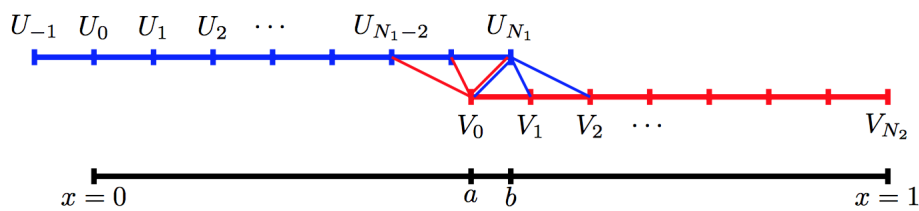


FIGURE 1.4 – Sketch of grid connectivity in 1D. Values of interpolation points, U_{N_1} and V_0 , are obtained by interpolation. The figure is from [58].

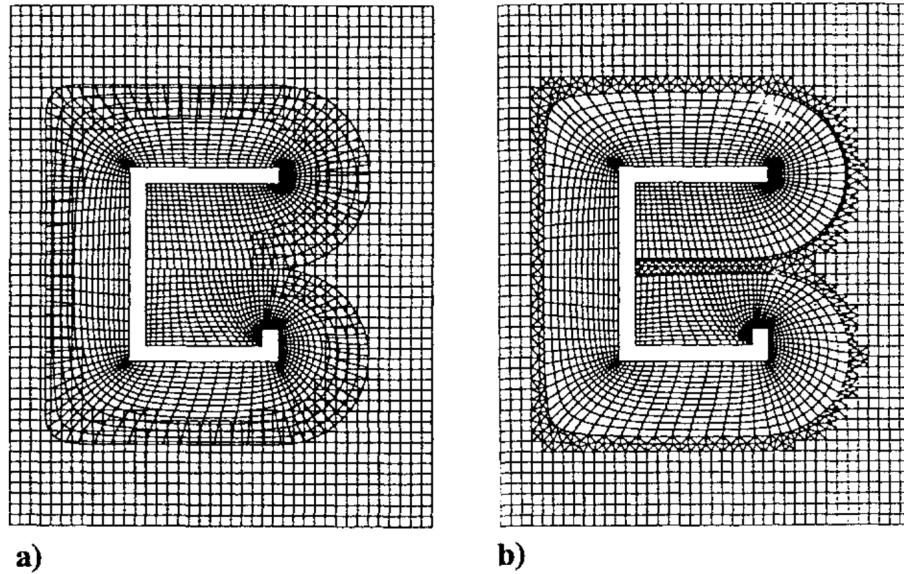


FIGURE 1.5 – Comparison between Chimera (a) and Dragon (b) grids for a C-shape structure. In particular, the dragon grid replaces the overlapping zone between the two blocks of the chimera configuration through a unstructured grid. The figure is from [65].

on a single mesh block. More recently, in [28] the authors presented an ADER Discontinuous Galerkin scheme with *a posteriori* subcell finite volume limiter on fixed and moving grids such as space-time adaptive Cartesian AMR meshes. The numerical scheme treats the temporal variable indistinctly with respect to the spatial variables by defining the solution on a space-time slab. This discretization approach, therefore, allows us to re-consider the problem of Chimera grids transmission conditions: instead of time-dependent spatial transmission conditions between relatively moving grid blocks, we define interpolation polynomials on arbitrarily intersecting space-time cells at the block boundaries.

In the ADER scheme a local space-time weak solution of the problem from the generic time t to $t + \Delta t$ is computed in every single space-time cell. This solution is defined as the *predictor*. The prediction step is local and hence embarrassingly parallel, because the solution is calculated independently of the information of the neighboring cells. Then, in the subsequent stage of *correction*, the computation of a space-time numerical flux between neighboring cells provides the appropriate stabilization of the integration scheme. We extend this prediction-correction method to Advection-Diffusion PDEs on overset grids and propose a space-time flux among the space-time cells that provides improved stabilization and precision as it takes into account both the advective and diffusive nature of the local (eventually nonlinear) operator.

ADER scheme, in its former formulation, can be seen as an evolution of a classical Godunov-type scheme for hyperbolic conservation laws [49, 50]. This type of methods uses the self-similarity of the solution for the local Riemann problem with a piece-wise constant initial data to compute the upwind numerical flux. Successively, the method was extended by employing non-oscillatory piece-wise linear reconstruction for the local generalized Riemann problem at the interface of cells with which space is discretized [68, 115]. The numerical resolution of generalized Riemann problem is usually cumbersome and it may be impossible to obtain for complicated Euler equations (e.g. Magneto-Hydro Dynamics problems). The ADER

method is an attempt in order to overcome this difficulty. It is a high-order accuracy method in space and time. In order to evaluate the numerical flux, for ADER method the generalized Riemann problem is solved with initial condition defined by smooth functions using a semi-analytic method [110]. The approximate solution is given by a local (i.e. at the interface or between cells) Taylor expansion in time up to any order of accuracy.

Overset grids for incompressible flows and fluid-structure interaction problems

One of the goals of this thesis is to develop a scheme for solving the incompressible Navier-Stokes equations (1.1) where the possibly deforming domain $\Omega(t)$ is discretized through overset grids. In particular, the domain $\Omega(t)$ can be considered as the geometric space in which the fluid performs its dynamics. Consequently, the Chimera mesh deforms accordingly to a deformation of the solid space represented and discretized by an internal surface of the foreground meshes, as sketched in Figure 1.2. Historically, the first to propose overset grids was Volkov in '70s [116]; the first implementations of scientific relevance are by Starius for hyperbolic equations [105]. Successively, among all, we mention Atta [7] for studying adaptive grid interfacing, Kreiss [70] for the introduction of curvilinear grids overlapping each other, Benek *et al.* [13, 14] and Rai [94], for the Euler equation, and Chesshire and Henshaw [30], for a generalization of chimera meshes for a wide range of PDEs.

All the cited works use several methods for numerically solving the different differential problems. It is possible to group them into two main categories: Fractional Step methods (FSM) and Domain Decomposition (DD) approaches. In the context of incompressible flows and fluid-structure interaction, among the works using a FSM, we cite a recent paper² by Meng *et al.* [76]. In this work the authors achieve a fourth order accuracy. Concerning the DD approaches, one of the last work is by Mittal, Dutta and Fischer [77], in which a Schwarz-spectral approach is used by decomposing the domain with respect to the different blocks of the overset grid. Despite of the different methods, all the works have in common the fact that fringe cells, namely the cells at the boundary of the overlapping regions, exchange the information by a proper interpolation. In general, special effort is devoted to the definition of a quick and efficient interpolation ensuring the required order of accuracy for the final solution. For example, in [76] a BWENO polynomial interpolation is employed, instead an efficient parallelization for the interpolation process at the overlapping regions is proposed in [77]. One of the most recent works by Sharma *et al.* [100] defines the following differentiation of the nodes of an overset grid:

- **Field points:** mesh nodes at which the governing equations are solved;
- **Fringe points:** mesh nodes at which the information is transferred between overlapping meshes;
- **Hole points:** mesh nodes at which the solution does not exist.

This classical nodes clustering gives us the opportunity to outline the differences of the method proposed in this thesis with respect to the actual state of the art. Since we employ an ADER approach and spend part of the global computational costs

2. This paper is listed in the **Overture** website <https://www.overtureframework.org/publications.html>. We refer the reader to this website for an exhaustive bibliography related to the overset grids.

for finding a compact stencil at the overlapping interfaces, we never need to exchange information by interpolation. In particular, as it will be clear along the thesis, the prediction step of ADER defines a free-mesh approach for which all nodes are undistinguished with respect to the classical clustering; thus, their belonging to a specific block is no longer important; successively, in the subsequent correction step, due to the definition of a hybrid stencil composed of nodes belonging to different meshes, the finite volume approach allows to automatically exchange the information of the previous step. The method does not consider the nodes as part of a block but rather their Euclidean distances in the definition of the stencil. In other words, the problem-specific overlapping configuration is effortlessly managed. The performed interpolation is mandatory only when a hole cell turns into an active cell due to the movement of the foreground mesh.

Since the proposed method for the incompressible Navier-Stokes equations is fractional, the pressure is solved via a Poisson problem. Also in this case, fringe cells are no longer exploited as donors or receptors of information. As a matter of fact, a proper discretization of the gradient operator is proposed at the interfaces using all the information of the compact hybrid stencil. Consequently, the relations described by the stiffness matrix resulting from the discretization of the Laplace operator automatically manages the exchange of information without going through a subsequent interpolation step.

The current state of the art considers chimera grids as discretization of the space. Due to the ADER method, the proposed overset grids in the thesis discretize the space-time continuum and, consequently, define space-time chimera meshes. This is an advantage that allows to evolve the domain as well as the overset grid (with a possible dependency on the solution itself) and, at the same time, to compute the solution over this evolving computational structure.

Reduction and hyper-reduction of ADER approach

In the last part of the thesis, a reduced and hyper-reduced version of the ADER approach is introduced. Model Order Reduction (MOR) methods are formulated in order to significantly reduce the computational costs for achieving a numerical approximation of the solution for a PDE. In particular, when one wants a solution that is parametric with respect to a given set of variable parameters (such as geometrical parameters or diffusion variables, etc.), MOR methods give the possibility to easily evaluate this solution along the specific instance of parameters. This type of methods typically consists of an offline stage of training (eventually expansive in terms of computational costs) and an online stage which allows to reconstruct the new required solution with a large advantage in terms of computational costs and times.

The proposed reduced method for obtaining the approximated solution is the Proper Orthogonal Decomposition (POD) [102, 22]. The collected high-fidelity solutions via ADER for some instances of the parameters are hierarchically rearranged in order to define a basis spanning the subspace V_M , of dimension M , of a proper functional space V over which the reduced solution is projected in the online step. We are interested in looking for solutions depending on parameter(s) leading the deformation of the domain. For this reason, a DD approach is applied to the reduction. This means that in some particular regions particularly affected by the evolution of the domain the solution is reduced and in the remaining sub-regions the solution is still high-fidelity. In particular, the decomposition is defined by the overset grid itself. The

reduction approach gives the opportunity to re-define the ADER scheme by considering a macro-cell identified by the foreground mesh.

Since the new reformulation of ADER over a macro-cell needs a slight modification with respect to its classical (i.e., high-fidelity) formulation, the arising matrices in the algebraic counterpart of the scheme need to be computed at each time instance. As a matter of fact, the projecting space V is composed of functions which are assured only a local (and not a global) continuity along the spatial coordinates. For this reason, a hyper-reduction approach is proposed in order to easily integrate and compute the matrices by employing a largely small quadrature nodes than are needed to obtain an integral approximation at the fixed order of accuracy.

Structure of the thesis

The thesis is organized as follows. In Chapter 2, the preliminary results in 1D problems are presented. In particular, some former analysis on both the nature of the superposition and the definition of a polynomial interpolation over the overlapping are studied over linear hyperbolic equations. In addition, a FV approach is proposed for the discretization of the second order Laplace operator in the presence of the overlapping cells.

These studies were therefore preparatory to the results of Chapter 3. In this chapter a second order ADER scheme for linear and nonlinear advection-diffusion problems on moving overset grids with a compact transmission condition is introduced. The numerical method is explained in order to be adapted to the chimera mesh and especially to the dynamics of the overlapping zone. A new local advective-diffusive stabilization term allowing to increase the CFL condition with respect to the local advective stabilization term from the literature is proposed.

Consequently, the scheme for the advection-diffusion problem is used in Chapter 4 together with the scheme for the Poisson equation for achieving a numerical solution for the incompressible Navier-Stokes equations. Special care is devoted to the discretization of the gradient operator in order to easily manage the information exchange at the overlapping zone without going through an interpolation step.

Finally, in Chapter 5 the reduction and hyper-reduction models for ADER scheme for linear and nonlinear advection-diffusion problems are presented. The reduced space onto which the reduced solution is projected is properly defined. In particular, the POD is explained for the construction of the basis spanning this space. In addition, the hyper-reduction technique is introduced in order to integrate over the domain regardless of the evolution to which it is constrained. This allows to compute the involved matrices by employing a largely small set of quadrature points for any admissible movement of the mesh.

Throughout the thesis, a number of test cases are shown in order to numerically verify what is asserted in the first parts of any chapter.

In the last part of the thesis, the Conclusions are discussed.

Chapter 2

The one dimensional case

In this chapter the overset grid in one dimension is introduced. It is used for discretizing a real domain for the resolution of two types of PDEs, namely the scalar linear advective equation and the Poisson problem. These two classes of equations result to be useful for the partial differential problems which are faced in the next chapters. As a matter of fact, the majority of the topics in the future chapters address as proper extensions of what is presented in this chapter.

Here, the presented schemes are a proper extension of methods originally introduced for one-block grid. The nature of the superposition between cells covering a real segment is analyzed. In particular, the superposition condition is studied also in the two extreme limits of zero superposition as well as a total superposition of one cell over another one. The former limit condition describes the classical one-block mesh. In this case the intersection between two consecutive cells is represented by the shared vertex (thus, it has zero-measure). On the contrary, the latter condition produces a doubling in the degrees of freedom because at least two whole cells cover the same subset of the domain. We expect that, when the measure of the superposition vanishes, the presented schemes fall onto the original schemes. On the other side, when an ill-posed doubling of information is reproduced, we are interested in understanding where the arising algebraic systems become undetermined.

The evolving space-time computational domain formally is $\cup_{t \in (0, T)} \Omega(t) \times \{t\}$; however, by abuse of language and along the whole thesis, this set is written as $\Omega(t) \times (0, T)$ even though it is not possible to define it through a Cartesian product representation because the domain $\Omega(t)$ varies in time and it cannot be factored out. The 1D linear advective equation over a domain Ω is: *find* $u : \Omega(t) \times (0, T) \rightarrow \mathbb{R}$ such that

$$\partial_t u + a \partial_x u = 0 \quad \text{in } \Omega(t) \times (0, T) \quad (2.1)$$

completed by suitable boundary conditions. Let $\mathcal{T} = \{\Omega_j\}_{j=1}^N$ a suitable partition of the domain Ω . Velocity $a \neq 0$ is the advective velocity. Originally, any intersection between two successive cells Ω_j and Ω_{j+1} is supposed. Successively, the intersection is considered and the schemes extended. Along the chapter, the average of the solution u over the cell Ω_j at time t is indicated as

$$U_j = \frac{1}{h_j} \int_{\Omega_j} u(t, x) dx.$$

with $h_j = |\Omega_j|$.

For problem (2.1), if the initial condition writes: $u(x, 0) = u_0(x)$ for any x in the domain Ω , thus the exact solution reads $u(x, t) = u_0(x - at)$ for any x in Ω and any time t in $[0, T]$.

In the last part of the chapter, an approximation of the first derivative exact up to the

second order is provided.

2.1 The third order stencil reconstruction: CWENO approach

In this section the compact version of the WENO polynomial reconstruction [63, 73] is presented. This method, known in literature with the name CWENO [99], consists in constructing a second order polynomial over a stencil \mathcal{S}_j . For both overlapping and non overlapping stencils, an optimal polynomial P_{opt} of degree 2 is looked for. In order to control the total variation, we describe the optimal polynomial as a convex combination of polynomials. The weights of the linear combination take into account the possibility of a discontinuity or of a quick variation of the interpolating function:

$$P_{\text{opt}} = \alpha_0 P_0 + \sum_{\gamma=1}^2 \alpha_\gamma P_\gamma,$$

where P_0 is a polynomial of degree 2 and P_γ , $\gamma = 1, 2$, are polynomials of degree 1. The weights α_γ , $\gamma = 1, 2, 3$, define a convex combination, i.e. they are positive and their sum is 1. Concerning the reconstruction, the optimal polynomial P_{opt} and the linear polynomials P_1 and P_2 are computed. Therefore P_0 is computed as

$$P_0 = \tilde{\alpha}_0 P_0 + \sum_{\gamma=1}^2 \tilde{\alpha}_\gamma P_\gamma,$$

where the coefficients $\tilde{\alpha}_\gamma$ are a linear combination of the convex weights α_γ with suitable smoothness indicators. For the presented numerical results, the convex set of weights are $\{0.5, 0.25, 0.25\}$.

2.1.1 Stencil of non overlapping cells

In this subsection, the stencil $\mathcal{S}_j = \cup_{i=-1}^1 \Omega_{j+i}$, $j = 1, \dots, N$, is such that the intersection between two consecutive cells has zero-measure. Under the hypothesis that u solving (2.1) is smooth over \mathcal{S}_j , we look for an optimal polynomial satisfying the WENO property of any cell composing the stencil:

$$\frac{1}{h_{j+i}} \int_{\Omega_{j+i}} P_{\text{opt}}(x) dx = U_{j+i}, \quad i = -1, 0, 1. \quad (2.2)$$

By choosing a basis of zero mean polynomials over Ω_j for $\mathcal{P}_2(\mathcal{S}_j)$, hence the set of all polynomials of degree equal or less than 2 over the stencil \mathcal{S}_j , (see the appendix in subsection A.1) the optimal polynomial formally reads:

$$P_{\text{opt}}(x) = U_j + p_x(x - x_j) + \frac{1}{2} p_{xx} \left[(x - x_j)^2 - \frac{h_j^2}{12} \right], \quad (2.3)$$

where x_j is the mean point of interval Ω_j and the coefficients are defined as:

$$\begin{aligned} p_x &= \frac{(h_j + 2h_{j+1})U[j-1, j] + (h_j + 2h_{j-1})U[j, j+1]}{2(h_{j-1} + h_j + h_{j+1})}, \\ p_{xx} &= \frac{3(2h_j + h_{j-1} + h_{j+1})U[j-1, j+1]}{2(h_{j-1} + h_j + h_{j+1})}, \end{aligned} \quad (2.4)$$

with

$$U[j-1, j] = \frac{U_j - U_{j-1}}{x_j - x_{j-1}}, \quad U[j, j+1] = \frac{U_{j+1} - U_j}{x_{j+1} - x_j},$$

$$U[j-1, j+1] = \frac{U[j, j+1] - U[j, j-1]}{x_{j+1} - x_{j-1}}.$$

Since the hypothesis of smoothness of u cannot be always validated, a reconstruction only defined by the optimal polynomial could present a Gibbs phenomenon, hence the optimal polynomial could present numerical oscillations. For this reason, by considering a basis of zero mean polynomials in $\mathcal{P}_1(\mathcal{S}_j)$, the set of all polynomials of degree equal or less than 1 over the stencil \mathcal{S}_j , we construct two linear polynomials P_γ , $\gamma = 1, 2$, matching the cell averages U_j and $U_{j+2\gamma-3}$:

$$P_\gamma(x) = U_j + U[j-2+\gamma, j-1+\gamma](x-x_j), \quad \gamma = 1, 2.$$

At this stage, we can compute the central polynomial P_0 by solving the linear equation:

$$P_{\text{opt}} = \sum_{\gamma=0}^2 \alpha_\gamma P_\gamma,$$

with convex coefficients α_γ .

Finally, the central polynomial built over the stencil reads:

$$P = \sum_{\gamma=0}^2 \tilde{\alpha}_\gamma P_\gamma, \quad (2.5)$$

where the new weights $\tilde{\alpha}_\gamma$ are a linear combination of the convex weights α_γ and the smoothness indicators β_γ :

$$\tilde{\alpha}_\gamma = \frac{\omega_\gamma}{\sum_{\delta=0}^2 \omega_\delta}, \quad \text{with } \omega_\gamma = \frac{\alpha_\gamma}{(\epsilon + \beta_\gamma)^2}, \quad \gamma = 0, 1, 2. \quad (2.6)$$

The smoothness indicators β_γ detect large gradients or eventual discontinuities. Thus, when the solution is not smooth, they avoid the presence of big oscillations in the polynomial reconstruction and the central polynomial P is largely defined by the linear polynomials P_1 and P_2 . On the contrary, if the solution is smooth and does not present a large variation over the stencil, the smoothness indicators are such that the new weights $\tilde{\alpha}_\gamma$ coincide with the previous ones α_γ (i.e. $P \approx P_{\text{opt}}$). In the literature, several definition of the smoothness indicators are present. Following [101, 73], we define the indicators as

$$\beta_\gamma = \sum_{l=1}^2 \int_{\Omega_j} h_j^{2l-1} (P_\gamma^{(l)}(x))^2 dx, \quad \gamma = 0, 1, 2. \quad (2.7)$$

By rewriting the central polynomial as

$$P_0 = U_j + p_x^0(x-x_j) + \frac{1}{2} p_{xx}^0 \left[(x-x_j)^2 - \frac{h_j^2}{12} \right],$$

we can explicitly define the smoothness indicators in (2.7):

$$\beta_0 = \frac{13}{12} h_j^4 (p_{xx}^0)^2 + h_j^2 (p_x^0)^2,$$

$$\beta_1 = U[j-1, j]^2 h_j^2, \quad \beta_2 = U[j, j+1]^2 h_j^2.$$

At the denominator of the definition of the new weights there is the term ϵ . In origin, it was introduced in the formulas to give a numerical meaning to the weights in case of a vanishing smoothness indicator. Anyway the role of ϵ goes beyond the simply avoidance of a zero denominator for the non linear weights ω_γ . In the literature, in the work by Kolb [67], it was numerically proven that the choice of ϵ influences the convergence of the numerical scheme. In particular it can be noticed that a high value (say $\epsilon \sim h$) may allow numerical oscillation while very small values (say $\epsilon \leq 10^{-6}$) allow to achieve the theoretical order of convergence only for very fine grids. In this thesis, an analysis at varying of ϵ is conducted in the case of a non-moving foreground mesh.

2.1.2 Stencil of overlapping cells

In this subsection the hypothesis of non overlapping cells for the stencil \mathcal{S}_j is relaxed. For sake of simplicity but with no loss of generality, we suppose that $|\Omega_j \cap \Omega_{j+1}| \neq 0$ (the overlapping could involve also cells of indexes $j-1$ and j). This means that the problem consists in constructing a polynomial over this new defined stencil. Due to the chimera configuration, there exist two (partial) partitions $\mathcal{T}_1 = \{\Omega_i^1\}_{i=1}^{N_1}$ and $\mathcal{T}_2 = \{\Omega_k^2\}_{k=1}^{N_2}$ of the physical domain Ω such that $\bigcup_{i=1}^{N_1} \Omega_i^1 \cup \bigcup_{k=1}^{N_2} \Omega_k^2 = \Omega$. With respect to the stencil \mathcal{S}_j , let $\Omega_j \subset \mathcal{T}_1$ and $\Omega_{j+1} \subset \mathcal{T}_2$ (see Figure 2.1)¹. For a non overlapping configuration, the distance between the two consecutive middle points x_j and x_{j+1} is $(h_j + h_{j+1})/2$. In the overlapping configuration, a corrector term σ is defined. It measures the intersection of the two overlapping cells, i.e. $\sigma = |\Omega_j \cap \Omega_{j+1}| = x_j + h_j/2 - x_{j+1} + h_{j+1}/2$. The objective consists in looking for a polynomial with the same *modus operandi* of the previous subsection with the correction defined by σ .

By choosing the same previously introduced polynomial basis for $\mathcal{P}_2(\mathcal{S}_j)$, and by satisfying the WENO properties (2.2), the optimal polynomial writes as (2.5) but the polynomial coefficients are corrected as follows:

$$\begin{aligned} p_x &= \frac{(h_j + 2h_{j+1} + 6\tilde{\sigma}_{j,j+1})U[j-1, j] + (h_j + 2h_{j-1})U[j, j+1]}{2(h_{j-1} + h_j + h_{j+1} + 3\tilde{\sigma}_{j,j+1})}, \\ p_{xx} &= \frac{3(2h_j + h_{j-1} + h_{j+1} - 2\sigma)U[j-1, j+1]}{2(h_{j-1} + h_j + h_{j+1} + 3\tilde{\sigma}_{j,j+1})}, \end{aligned} \quad (2.8)$$

with the lumped corrector term

$$\tilde{\sigma}_{j,j+1} = \frac{\sigma[3\sigma - (h_{j+1} + 2h_j)]}{3(h_{j+1} + h_j - 2\sigma)}.$$

Proposition 2.1.1. *In the limit of $\sigma \rightarrow 0$, i.e. in the limit of the non overlapping stencil, the above polynomial coefficients (2.8) tend to the ones of the non overlapping case in (2.4).*

Remark 2.1.1. *Since the optimal polynomial is looked for by the conditions in (2.2), it holds that*

$$|\Omega_j \cap \Omega_{j+1}| < \min_{k=j,j+1} |\Omega_k|.$$

1. By abuse of notation, the superscript on the cell defining its belonging to the specific partition is omitted.

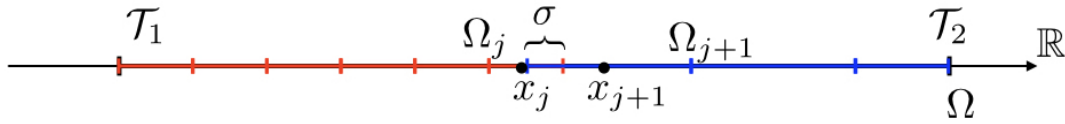


FIGURE 2.1 – An overlapping configuration in 1D. The cells belonging to the partitions \mathcal{T}_1 and \mathcal{T}_2 are in red and in blue, respectively.

Thus, it is not possible to determine a unique polynomial if $\Omega_j \cap \Omega_{j+1} = \Omega_k$, with $k = j, j + 1$, i.e. when a total overlapping occurs. In this case, the algebraic system deriving from (2.2) is undetermined.

The correction term only insists on the definition of the optimal polynomial. The linear polynomials P_1 and P_2 are the same ones previously found. Consequently, the central polynomial P_0 is found with the same relation previously stated. Finally, the non linear weights ω_γ depend on the smoothness indicator whose definitions do not change. Therefore they will be function of the central polynomial coefficients p_x^0 and p_{xx}^0 corrected with the new coefficients p_x and p_{xx} . In Section A.2 of the appendix there are all the formal computations of this subsection.

2.1.3 Numerical results

In this subsection some preliminary results on the CWENO polynomial reconstruction are presented, by analyzing the rates of convergence of four test cases at varying of both the type of overlapping and the value of ϵ in the definition of the non linear weights (2.6). In particular, the performances of the CWENO reconstruction are evaluated in one case by recovering the local CWENO polynomials, in other cases by solving (2.1) through a finite volume method over unsteady overset grids. Due to the boundary conditions, two ghost cells are created at the beginning and at the end of the physical domain Ω , respectively. The size of these cells matches the size of the adjacent cells in the domain. The value of the solution into the ghost cells is led by the type of the boundary conditions with which the hyperbolic equation is completed (e.g. periodic conditions, Dirichlet conditions, etc.). By denoting with U_j^n the cell average of the solution over the cell Ω_j at the discrete time t^n , the fully discrete scheme of (2.1) for solving the numerical tests reads:

$$U_j^{n+1} = U_j^n - \frac{\Delta t}{h_j} \mathcal{Q}(\partial\Omega_j; u),$$

where Δt is the time step and $\mathcal{Q}(\partial\Omega_j; u)$ represents the numerical approximation of the fluxes $H_{j\pm 1/2}$ at the boundary $\partial\Omega_j$ of the cell. In all shown simulations of the subsection, the flux is numerically approximated through a Lax-Friedrichs scheme. In particular, by considering the flux across the cells Ω_j and Ω_{j+1} , we distinguish two cases:

- $\Omega_j \cap \Omega_{j+1} = \{x_{j+1/2}\}$, with $x_{j+1/2} = x_j + h_j/2 \equiv x_{j+1} - h_{j+1}/2$ the common vertex to both cells. In this case the numerical flux $H_{j+1/2}$ over the vertex is:

$$H_{j+1/2} = \frac{1}{2} \left[a(u_{j+1/2}^+ + u_{j+1/2}^-) - \frac{h_j}{\Delta t} (u_{j+1/2}^+ - u_{j+1/2}^-) \right],$$

where $u_{j+1/2}^+ = P_{j+1}(x_{j+1/2})$ and $u_{j+1/2}^- = P_j(x_{j+1/2})$, being P_j and P_{j+1} the CWENO polynomial reconstructions over the stencils \mathcal{S}_j and \mathcal{S}_{j+1} , respectively.

- $|\Omega_j \cap \Omega_{j+1}| = [p, q]$, such that the vertex $p = x_{j+1} - h_{j+1}/2 < x_j + h_j/2 = q$. In this case the numerical flux $H_{j+1/2}$ across the vertex q reads:

$$H_{j+1/2} = \frac{1}{2} \left[a(P_{j+1}(q) + P_j(q)) - \frac{h_j}{\Delta t} (P_{j+1}(q) - P_j(q)) \right].$$

Finally, a third-order TVD Runge-Kutta scheme is adopted:

$$\begin{aligned} U_j^{(1)} &= U_j^n + \frac{\Delta t}{h_j} \mathcal{Q}(\partial\Omega_j; u^n) \\ U_j^{(2)} &= \frac{3}{4} U_j^n + \frac{1}{4} U_j^{(1)} + \frac{1}{4} \frac{\Delta t}{h_j} \mathcal{Q}(\partial\Omega_j; u^{(1)}) \\ U_j^{n+1} &= \frac{1}{3} U_j^n + \frac{2}{3} U_j^{(2)} + \frac{2}{3} \frac{\Delta t}{h_j} \mathcal{Q}(\partial\Omega_j; u^{(2)}). \end{aligned}$$

The considered test cases are:

- CASE0: CWENO reconstruction of $u(x) = e^{-x^2} + 0.1\chi_{\mathbb{R}_+}(x)$;
- CASE1: Periodic B.C. with $u_0(x) = \sin(\pi x)$;
- CASE2: Periodic B.C. with $u_0(x) = \sin(2\pi x) - \sin(2\pi x)/\pi$;
- CASE3: Periodic B.C. with $u_0(x) = \sin(\pi x) + 0.25 \sin(15\pi x)e^{-20x^2}$.

For all cases the domain Ω is the real interval $(-1, 1)$.

Remark 2.1.2. For CASE0, just a CWENO polynomial reconstruction is performed. For the remaining cases, problem (2.1) is integrated up to the final time $T = 3$ with an advective speed $a = 1$.

Remark 2.1.3. Function of CASE0 presents a discontinuity in $x = 0$.

Remark 2.1.4. The solution of CASE3 has a large space derivative.

For all the cases, the analysis is computed by computing the L^1 -norm error of the mismatch between the CWENO polynomial reconstruction and the cell average of the exact solution by doubling the number of cells at any simulation. For TEST1, TEST2 and TEST3, the error is evaluated at final time T . In particular, first the reconstruction is validated over a unique uniform mesh (see Table 2.1). Successively, two uniform meshes overlapping around $x = 1/320$ are considered. Finally, the same computations are performed over three overlapping meshes around points $x = \pm 0.4$. In Figure 2.2, three configurations for CASE2 are showed.

The algebraic system deriving from (2.2) tends to be undetermined at the increasing of the overlapping area (i.e. the rows of the deriving matrix tend to be more and more strictly correlated, see Remark 2.1.1). Thus, the following *overlapping index* $IO_{j,j+1}$ is defined. It measures the overlapping area over the measure of the union set for two overlapping cells Ω_j and Ω_{j+1} as follows:

$$IO_{j,j+1} = \frac{|\Omega_j \cap \Omega_{j+1}|}{|\Omega_j \cup \Omega_{j+1}|} = \frac{h_j + h_{j+1} + 2(x_j - x_{j+1})}{h_j + h_{j+1} + 2(x_{j+1} - x_j)}. \quad (2.9)$$

Thus, for the same configuration of overlapping meshes, a gradually larger overlapping index is considered. Tables 2.2, 2.3 and 2.4 refer to the overlapping indexes (in

TABLE 2.1 – L^1 -norm error and converge rate with one uniform mesh as function of the total number of nodes N .

N	CASE0		CASE1		CASE2		CASE3	
	L^1 -err	L^1 -rate						
20	2.10e-03	-	5.38e-02	-	3.94e-01	-	5.24e-02	-
40	8.98e-04	1.25	5.10e-03	3.40	9.27e-02	2.09	5.30e-02	-0.02
80	3.16e-04	1.51	5.20e-04	3.29	1.04e-02	3.16	6.02e-02	-0.19
160	8.62e-05	1.87	6.43e-05	3.01	1.00e-03	3.33	5.36e-02	0.17
320	1.78e-05	2.27	8.04e-06	3.00	1.15e-04	3.16	1.62e-02	1.73
640	2.96e-06	2.59	1.01e-06	3.00	1.40e-05	3.04	2.10e-03	2.95
1280	4.30e-07	2.79	1.26e-07	3.00	1.72e-06	3.02	2.45e-04	3.09
2560	5.79e-08	2.89	1.57e-08	3.00	2.13e-07	3.01	3.02e-05	3.02

percentage) of 10%, 50% and 80%, respectively. Tables 2.6, 2.5 and 2.7 refer to the overlapping indexes of 10%, 50% and 80%, respectively, for both the present overlapping zones.

Remark 2.1.5. For three overlapping meshes, the two overlapping indexes are always equal, i.e. the first and the second meshes are overlapping the same way the second and the third meshes do.

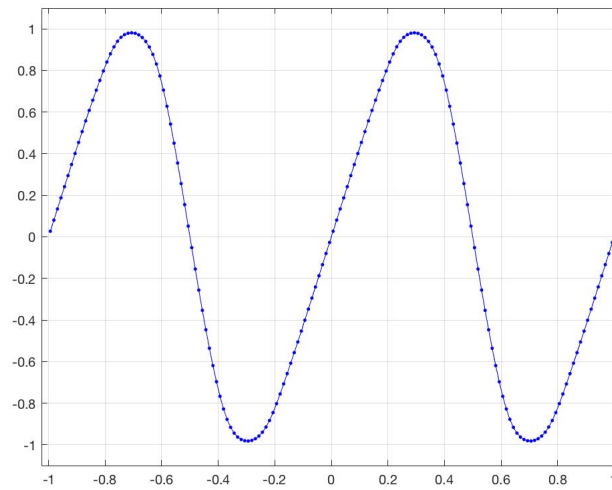
For CASE1 and CASE2, the expected rate of convergence is 3. For the remaining cases we expect a lower (or equal) rate of convergence due to the discontinuity (for CASE0) and the large space-derivative (for CASE3) of the exact solutions. All errors shown in Tables 2.1 - 2.7 point to CWENO reconstructions with parameter $\epsilon = h$ in weights (2.6).

For the same type of overlapping configuration, when the solution is quite smooth with a slow variation in space, increasing the overlapping index does not largely effect the performance. On the contrary, when the exact solution presents large space-derivative, a large overlapping reduces the precision (i.e., a large error). By moving from one overlapping to two overlapping zones, the smoothness of the solution seems again to have a key role in the performances. As expected, when a second overlapping zone is introduced, the precision reduces at least of one order of magnitude. Finally, we can notice that, with a controlled overlapping, the results obtained over one mesh and the ones obtained over a chimera grid are similar. This is due to the fact that the CWENO reconstruction takes into account both the right distances between the cell centers and the overlapping configuration of the meshes over which the solution is computed.

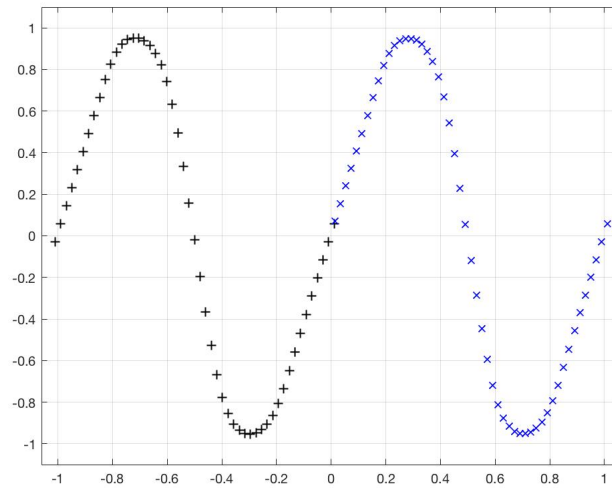
Finally, in Figures 2.3 and 2.4 it is reported the comparison of the L^1 -error with respect to $\epsilon = h$ and $\epsilon = 10^{-6}$. The percentage of the overlapping index is always kept constant at 50%. It is evident that, with a smaller value of ϵ , the convergence is always reached or sometimes overcome. On the other hand, the error corresponding to $\epsilon = h$ is always lower (except for CASE0 with two overlapping zones), therefore the numerical solution is closer to the exact solution in the sense of the L^1 -norm.

2.2 The CWENO-ADER approach for advective equations

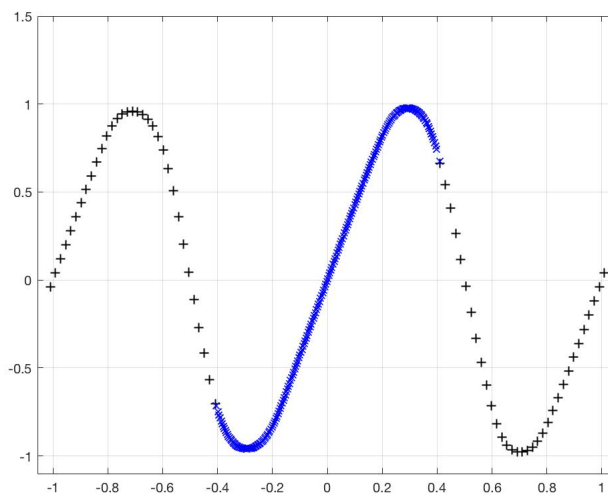
In this section it is presented a finite volume scheme for the resolution of equation (2.1) in the case of a moving chimera grids. In particular, it is explained how to



(A) One mesh



(B) One overlapping section



(C) Two overlapping sections

FIGURE 2.2 – Comparison of solution for *CASE2* with different steady mesh configurations. For (B) and (C), the overlapping indices are $IO = 80\%$.

TABLE 2.2 – L^1 -norm error and converge rate with two overlapping meshes as function of the total number of nodes N ($IO = 10\%$)

N	CASE0		CASE1		CASE2		CASE3	
	L^1 -err	L^1 -rate						
20	3.78e-05	-	5.68e-02	-	3.99e-01	-	5.24e-02	-
40	5.37e-06	3.04	5.20e-03	3.70	9.31e-02	2.25	5.67e-02	-0.25
80	7.59e-07	2.93	5.21e-04	3.45	1.04e-02	3.28	6.67e-02	-0.13
160	9.71e-08	3.06	6.44e-04	3.07	1.00e-03	3.40	7.29e-02	0.44
320	1.25e-08	3.00	8.05e-06	3.03	1.15e-04	3.18	5.39e-02	1.74
640	1.57e-09	3.01	1.01e-06	3.01	1.40e-05	3.06	1.63e-03	2.95
1280	1.98e-10	3.00	1.26e-07	3.01	1.72e-06	3.03	2.98e-04	2.85
2560	2.48e-11	3.00	1.57e-08	3.00	2.13e-07	3.01	1.14e-04	1.39

TABLE 2.3 – L^1 -norm error and converge rate with two overlapping meshes as function of the total number of nodes N ($IO = 50\%$)

N	CASE0		CASE1		CASE2		CASE3	
	L^1 -err	L^1 -rate						
20	3.85e-05	-	6.52e-02	-	4.43e-01	-	5.24e-02	-
40	5.38e-06	3.07	5.60e-03	3.79	9.64e-02	2.30	5.73e-02	-0.37
80	7.60e-07	2.94	5.44e-04	3.48	1.07e-02	3.29	7.28e-02	-0.03
160	9.72e-08	3.06	6.52e-05	3.12	1.00e-03	3.42	7.43e-02	0.45
320	1.25e-08	3.00	8.09e-06	3.04	1.16e-04	3.20	5.46e-02	1.75
640	1.57e-09	3.01	1.01e-06	3.02	1.40e-05	3.06	2.10e-03	2.95
1280	1.98e-10	3.00	1.26e-07	3.01	1.72e-06	3.03	2.98e-04	2.85
2560	2.48e-11	3.00	1.57e-08	3.00	2.13e-07	3.01	1.14e-04	1.39

TABLE 2.4 – L^1 -norm error and converge rate with two overlapping meshes as function of the total number of nodes N ($IO = 80\%$)

N	CASE0		CASE1		CASE2		CASE3	
	L^1 -err	L^1 -rate						
20	3.93e-05	-	7.57e-02	-	4.45e-01	-	6.30e-02	-
40	5.40e-06	3.19	6.30e-03	3.85	1.00e-02	2.31	7.53e-02	-0.28
80	7.60e-07	2.95	5.94e-04	3.52	1.10e-03	3.30	7.70e-02	-0.03
160	9.72e-08	3.10	6.78e-05	3.19	1.00e-03	3.43	5.49e-02	0.50
320	1.25e-08	3.00	8.27e-06	3.06	1.15e-04	3.21	1.65e-02	1.75
640	1.57e-09	3.02	1.02e-06	3.03	1.40e-05	3.07	2.10e-03	2.95
1280	1.98e-10	3.01	1.28e-07	3.01	1.72e-06	3.03	2.98e-04	2.85
2560	2.48e-11	3.00	1.59e-08	3.01	2.14e-07	3.02	1.14e-04	1.39

TABLE 2.5 – L^1 -norm error and converge rate with three overlapping meshes as function of the total number of nodes N ($IO = 10\%$)

N	CASE0		CASE1		CASE2		CASE3	
	L^1 -err	L^1 -rate						
17	2.40e-03	-	2.24e-01	-	7.29e-01	-	1.52e-01	-
32	1.00e-03	1.31	1.81e-02	3.98	2.12e-01	1.95	7.31e-02	1.16
61	3.73e-04	1.58	1.60e-03	3.77	3.07e-02	2.99	6.10e-02	0.28
120	1.05e-04	1.88	6.78e-04	3.30	3.10e-03	3.40	6.14e-02	-0.01
237	2.28e-05	2.22	2.08e-05	3.09	3.11e-04	3.39	3.47e-02	0.84
472	3.99e-06	2.53	2.59e-06	3.02	3.64e-05	3.12	6.30e-03	2.47
941	5.99e-07	2.74	3.23e-07	3.01	4.44e-06	3.05	1.30e-03	2.25
1880	8.24e-08	2.87	4.03e-08	3.01	5.48e-07	3.02	1.38e-04	3.29

TABLE 2.6 – L^1 -norm error and converge rate with three overlapping meshes as function of the total number of nodes N ($IO = 50\%$)

N	CASE0		CASE1		CASE2		CASE3	
	L^1 -err	L^1 -rate						
17	2.40e-03	-	2.56e-01	-	7.77e-01	-	1.77e-01	-
32	1.10e-03	1.29	1.98e-02	4.05	2.19e-01	1.98	7.59e-02	1.39
61	3.75e-04	1.59	1.70e-03	3.77	3.17e-02	3.00	5.49e-02	0.50
120	1.04e-04	1.88	1.80e-04	3.36	3.10e-03	3.42	6.42e-02	-0.23
237	2.28e-05	2.22	2.20e-05	3.09	3.25e-04	3.34	4.24e-02	0.61
472	3.99e-06	2.53	2.67e-06	3.06	3.72e-05	3.14	9.70e-03	2.14
941	5.99e-07	2.74	3.39e-07	2.99	4.62e-06	3.03	6.70e-04	3.87
1880	8.23e-08	2.87	4.16e-08	3.03	5.61e-07	3.05	6.43e-04	0.05

TABLE 2.7 – L^1 -norm error and converge rate with three overlapping meshes as function of the total number of nodes N ($IO = 80\%$)

N	CASE0		CASE1		CASE2		CASE3	
	L^1 -err	L^1 -rate						
17	1.70e-03	-	2.30e-01	-	7.76e-01	-	2.32e-01	-
32	1.10e-03	0.75	2.14e-02	4.16	2.23e-01	1.90	7.63e-02	1.77
61	2.25e-04	2.38	1.70e-03	3.92	3.23e-02	3.04	5.50e-02	0.51
120	1.05e-04	1.13	1.88e-04	3.26	3.20e-03	3.42	7.02e-02	-0.36
237	2.28e-05	2.22	2.17e-05	3.18	3.24e-04	3.37	3.39e-02	1.07
472	4.00e-06	2.53	2.74e-06	3.00	3.79e-05	3.11	9.50e-03	1.85
941	5.99e-07	2.74	3.35e-07	3.05	4.62e-06	3.05	6.70e-04	3.84
1880	8.24e-08	2.87	4.26e-08	2.98	5.69e-07	3.02	2.78e-04	1.27

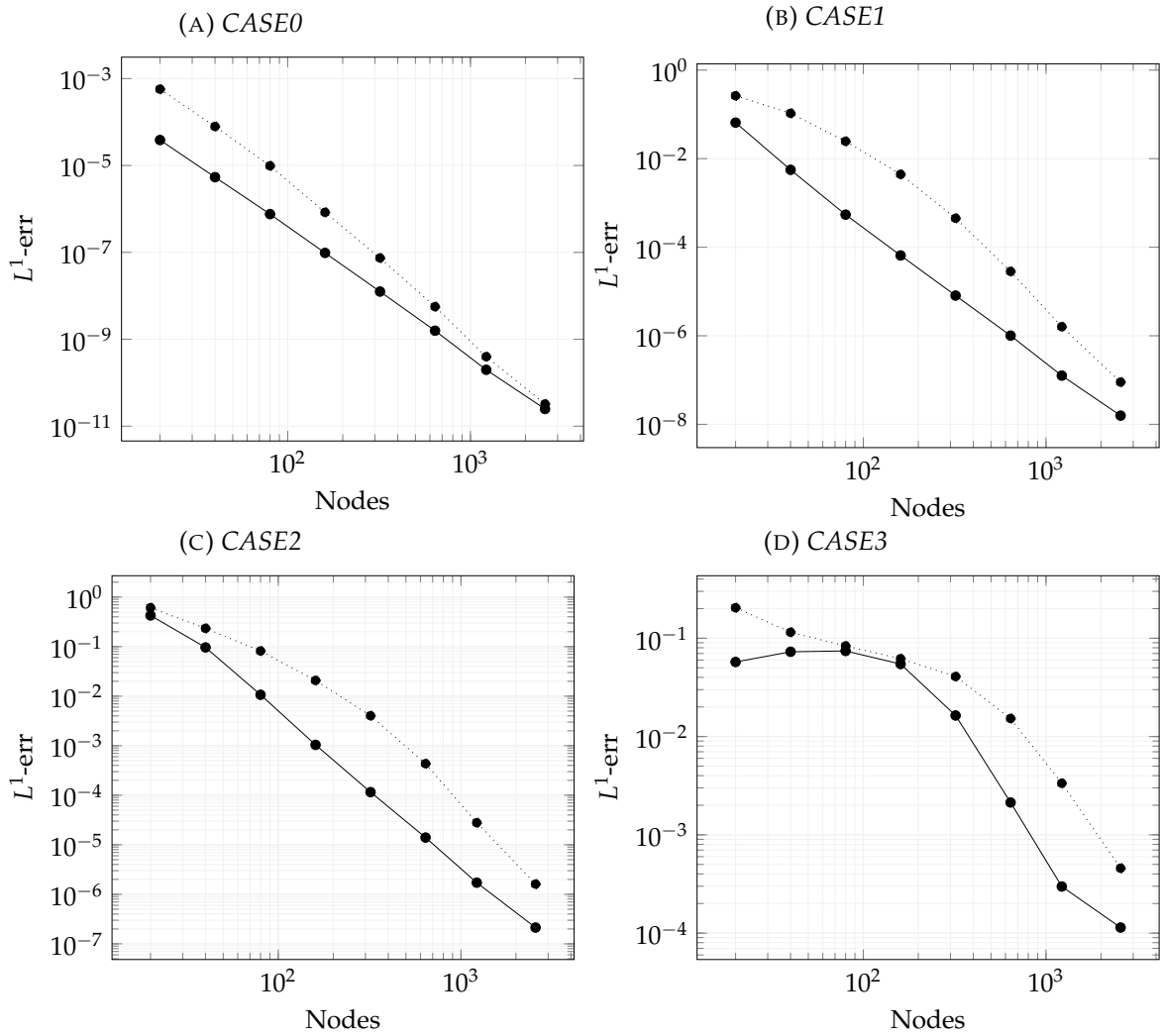


FIGURE 2.3 – Comparisons of the L^1 -errors for $\epsilon = h$ (continuous lines) and $\epsilon = 10^{-6}$ (dotted lines) for one overlapping zone ($IO = 50\%$).

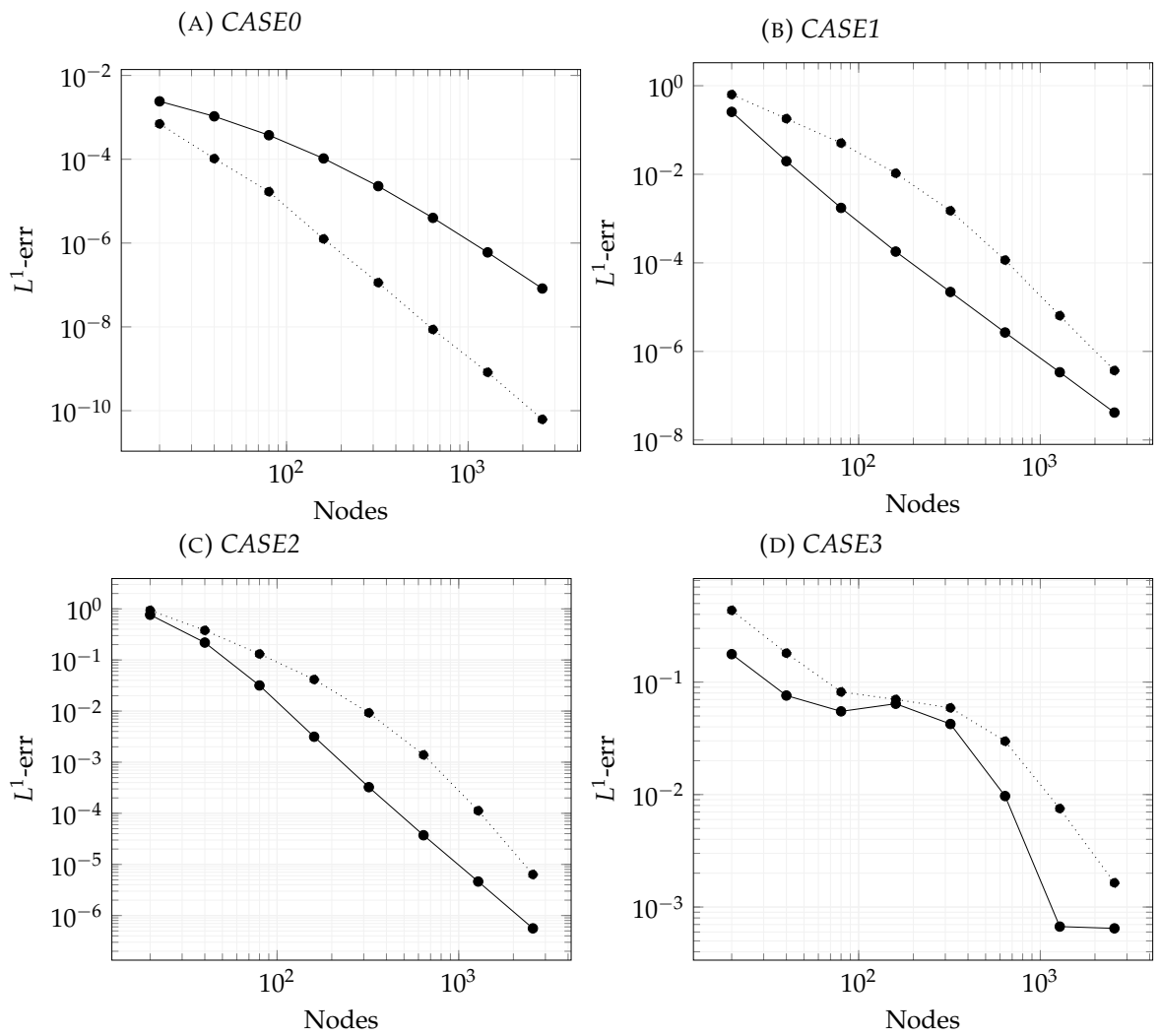


FIGURE 2.4 – Comparisons of the L^1 -errors for $\epsilon = h$ (continuous lines) and $\epsilon = 10^{-6}$ (dotted lines) for two overlapping zones ($IO = 50\%$).

reach a solution with a patch of several grids which can move, deform and overlap. The presented algorithm is a reformulation in the case of moving chimera meshes of the ADER finite volume scheme [108, 109, 40] originally presented by Dumbser *et al.* [41]. The numerical scheme, defined as a *predictor-corrector* method, is composed of two steps for the recovery of the numerical solution at time t^{n+1} from the previous numerical solution at time t^n .

At the base of any stage, there is a polynomial reconstruction matching the cell average of the solution. In this section a third-order CWENO polynomial is built as explained in the previous section. Nevertheless, *a priori*, the order of the reconstruction can be general. Since the mesh evolves in time, if \mathcal{T} is a (either global or local) partition of the physical domain, any cell $\Omega_j(t) \in \mathcal{T}$ evolve as well in time with the possibility to move (*translation*) and to change its length (*deformation*).

2.2.1 Local space-time Galerkin predictor

At this stage, the polynomial reconstruction of the solution at the discrete time t^n is known and it is denoted as $w(x)$. Since the method needs a predictor solution for computing the space-time fluxes, a local solution of (2.1) is solved in the space-time cell $\Omega_j(t) \times [t^n, t^{n+1}]$ under the form of a space-time polynomial of degree 3². This method is based on the discrete counterpart of the Cauchy-Kovalevskaya procedure [110, 112, 12, 25, 55]. In particular, it consists in solving the hyperbolic equation via a non linear finite volume element method over a specific set of nodes over the space-time cell. This local solution represents the local evolution of the polynomial reconstruction $w(x)$. No neighbor information is required at this stage. The local information referring to any space-time cell is managed in the last stage of the method.

First, the governing equation (2.1) is written in a space-time reference system defined by the coordinates $\xi = (\xi, \tau)$. It is denoted with $x = (x, t)$ the coordinates in the space-time cell. Let a Lagrangian basis $\{\theta_l(\xi)\}_{l=1}^6$ be defined by a Lagrangian interpolation through a set of space-time nodes $(\xi_l)_{l=1}^6$ in the reference space-time domain. For our purposes, and according to [40], the nodes are

$$(0, 0); \quad (1/2, 0); \quad (1, 0); \quad (0, 1/2); \quad (1, 1/2); \quad (1/2, 1).$$

The reader is referred to the appendix section B.1 for the formal definition of the used Lagrangian basis. The basis has the property to reproduce the Kronecker symbol if any of its components is evaluated over a node as: $\theta_l(\xi_m) = \delta_{lm}$. Let q_h be the local predictor solution, it is defined

$$q_l = q_l(\xi, \tau) = \theta_l(\xi, \tau) \hat{q}_l, \quad (2.10)$$

with $\hat{q}_l = q(\xi_l)$. In the above expression the Einstein notation for sum on repeated indexes is used.

The map from the physical space-time coordinates x and the reference space-time coordinates ξ is achieved through an *isoparametric approach*. Hence, the physical coordinates are a function of the reference coordinates via the Lagrangian basis:

$$x = x(\xi, \tau) = \theta_l(\xi, \tau) \hat{x}_l. \quad (2.11)$$

2. *A priori*, the reconstruction can be computed with a generic order M . In that case, the CWENO reconstruction of the solution at time t^n is a polynomial of order M .

As usual, $\hat{x}_l = x(\xi_l)$. For the time variable t , the reference map is written as the linear dilatation

$$t = t(\tau) = t^n + \Delta t \tau, \quad (2.12)$$

where Δt is the time step equal to $t^{n+1} - t^n$. Through (2.10) and (2.12), the Jacobian matrix of the map is determined:

$$J = \frac{\partial x}{\partial \xi} = \begin{bmatrix} x_\xi & x_\tau \\ 0 & \Delta t \end{bmatrix}, \quad (2.13)$$

whose inverse reads:

$$J^{-1} = \frac{\partial \xi}{\partial x} = \begin{bmatrix} \xi_x & \xi_t \\ 0 & 1/\Delta t \end{bmatrix}. \quad (2.14)$$

The PDE equation (2.1) rewritten with respect to the reference coordinates is:

$$\partial_\tau q \tau_t + \partial_{\xi} q \xi_t + \partial_{\xi} q \xi_x = 0, \quad (2.15)$$

which is equivalent to

$$\partial_\tau q = -\Delta t H(q), \quad (2.16)$$

with $H(q) = (\xi_t + \xi_x) \partial_\xi q$.

By considering any element of the Lagrangian basis, the weak formulation of (2.16) expressed through (2.10) reads

$$\langle \theta_k, \partial_\tau \theta_l \rangle \hat{q}_l = -\Delta t \langle \theta_k, \theta_l \rangle \hat{H}_l, \quad \forall k = 1, \dots, 6, \quad (2.17)$$

with $\hat{H}_l = H(\hat{q}_l)$ and $\langle \cdot, \cdot \rangle$ the L^2 -scalar product over the reference domain:³

$$\langle f, g \rangle = \int_0^1 \int_0^1 f(\xi, \tau) g(\xi, \tau) d\xi d\tau, \quad \forall f, g \text{ Lebesgue measurable over } (0, 1)^2.$$

The algebraic counterpart of the weak form (2.17) is:

$$K \hat{q} = -\Delta t M \hat{H}, \quad (2.18)$$

such that:

$$K_{lm} = \langle \theta_l, \partial_\tau \theta_m \rangle; \quad M_{lm} = \langle \theta_l, \theta_m \rangle; \quad [\hat{q}]_m = \hat{q}_m; \quad [\hat{H}]_m = \hat{H}_m. \quad (2.19)$$

The algebraic system (2.18) has vector \hat{H} on the right hand side implicitly defined by the unknown vector \hat{q} . For this reason, let \hat{q}^0 denote the degrees of freedom that are known from the initial condition $w(x)$ (for $\tau = 0$, i.e., $t = t^n$). Thus, \hat{q}^1 refers to those degrees of freedom defined for $\tau > 0$. With these definitions, we can split the algebraic system (2.18) as

$$\begin{bmatrix} K^{00} & K^{01} \\ K^{10} & K^{11} \end{bmatrix} \begin{bmatrix} \hat{q}^0 \\ \hat{q}^1 \end{bmatrix} = -\Delta t \begin{bmatrix} M^{00} & M^{01} \\ M^{10} & M^{11} \end{bmatrix} \begin{bmatrix} \hat{H}^0 \\ \hat{H}^1 \end{bmatrix}. \quad (2.20)$$

In the above algebraic system, only the second multi-row is of our interest, but the deriving linear system is still nonlinear. It is linearized through a fixed point iteration indexed though r as follows:

$$K^{11} \hat{q}_{r+1}^1 = K^{10} \hat{q}^0 - \Delta t M^{10} \hat{H}^0 - \Delta t M^{11} \hat{H}_r^1. \quad (2.21)$$

3. In the next chapter a proper functional environment will be introduced for all the weak forms.

For an adequate initial guess \hat{q}_0^1 for problem (2.21), we refer to [59].

Since part of the chimera grid is moving, we have to take it into account. The motion of the computational space fulfills the following ODE:

$$\frac{dx}{dt} = V(x, t), \quad (2.22)$$

with $V(x, t)$ the local mesh velocity. When the mesh is moving independently of the advective velocity a , the method is an ALE (Arbitrary Lagrangian-Eulerian) scheme. According with the isoparametric approach defined by (2.11), the local velocity in the physical space-time cell reads:

$$V_h = V_h(\xi, \tau) = \theta_l(\xi, \tau) \hat{V}_l, \quad (2.23)$$

with $\hat{V}_l = V(\xi_l)$.

Through (2.23), it is possible to express the motion equation (2.22) in an algebraic system after a weak formulation (as done for the hyperbolic equation). Consequently, since the velocity $V(x, t)$ also depends on the unknown positions of the space x , we solve the linearized system through a fixed point iteration:

$$K^{11} \hat{x}_{r+1}^1 = K^{10} \hat{x}^0 + \Delta t M^{00} \hat{V}^0 + \Delta t M^{10} \hat{V}_r^1. \quad (2.24)$$

Equations (2.24) and (2.21) have to be solved together.

Here the first stage of the method finishes. In the sequel the most salient steps are listed:

- Through (2.24), solve the mesh motion (2.22);
- Compute the Jacobian matrix (2.13) and its inverse (2.14);
- Update the terms in the definition of $H(\cdot)$;
- Finally, evolve the local solution through (2.21).

2.2.2 The mesh motion

Since the mesh motion equation (2.22) is solved through a fully local method, a shared vertex x_j by the cells Ω_j and Ω_{j+1} , both belonging to the same partition \mathcal{T} , could have different (namely discontinuous) velocity even though it is not physically true. For this reason a weighted average is considered in order to tackle this problem. As suggested in [24], the unique mesh velocity \bar{V}_j^n of point x_k at time t^n is written as:

$$\bar{V}_k^n = \frac{1}{N_k} \sum_{\Omega_j^n \in \mathcal{T}} \bar{V}_{k,j}^n, \quad \text{with } \bar{V}_{k,j}^n = \int_0^1 \theta_l(\xi^*, \tau) d\tau \hat{V}_{l,j}, \quad (2.25)$$

where N_k is the number cells, in the partition \mathcal{T} , sharing the vertex x_k , $\Omega_j^n = \Omega_j(t^n)$ and ξ^* is that specific reference spatial coordinate such that $x(\xi^*, \tau^*) = x_k^v$, with $v = n$ if $\tau^* = 0$ and $v = n + 1$ if $\tau^* = 1$. For a more sophisticated definition of the unique velocity \bar{V}_k^n in (2.25) we refer to [41].

In general, the partition \mathcal{T} of the domain is considered globally covering the domain, even though the cells are allowed to move during the simulation. This means that a continuous displacement field is ensured for the cells' movement. When a chimera grid is used, this could be no longer valid. As a matter of fact, there exists a set of

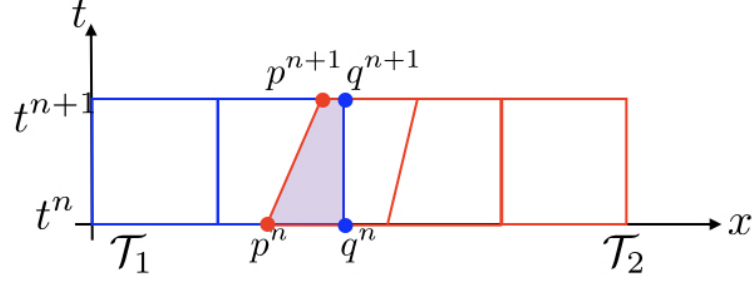


FIGURE 2.5 – Overlapping space-time cell (remarked in light violet). The last cell of \mathcal{T}_1 (in blue) overlaps the first cell in \mathcal{T}_2 (in red). The velocity of the two meshes can be different due to the chimeric behavior of the grid composition.

(partial) partitions \mathcal{T}_i such that $\cup_i \mathcal{T}_i = \Omega$ and a discontinuous velocity for the cells is possible. For instance, by thinking to the simplest possible configuration of two partitions \mathcal{T}_1 and \mathcal{T}_2 overlapping around a certain point \bar{x} , there will exist two cells $\Omega_1 \in \mathcal{T}_1$ and $\Omega_2 \in \mathcal{T}_2$ such that $\Omega_1 \cap \Omega_2 = [p, q]$ (thus $\bar{x} \in [p, q]$). The spatial position occupied by p could have a velocity and a movement which are discontinuous due to the chimera behavior of the grids even though that point is shared by two different cells. In particular, $N_p = 1$ in both \mathcal{T}_1 and \mathcal{T}_2 and consequently the velocity of the point depends on the partition velocity. In Figure 2.5 this configuration is sketched.

2.2.3 Finite volume scheme over the space-time cell

The proposed numerical scheme is an ALE finite volume scheme. Let $\mathcal{C}_j^n = \Omega_j(t) \times [t^n, t^{n+1}]$ be the space-time control volume, describing the evolution of the cell Ω_j from times t^n to t^{n+1} . Geometrically, we identify the space-time control volume as a quadrilateral with two parallel basis Ω_j^n and Ω_j^{n+1} whose end points, namely the left vertices $X_{1,j}^n$ and $X_{1,j}^{n+1}$ and the right vertexes $X_{2,j}^n$ and $X_{2,j}^{n+1}$, are connected by straight lines (see Figure 2.5). Formally, the boundary $\partial\mathcal{C}_j^n$ of the control space-time cell is defined as:

$$\partial\mathcal{C}_j^n = \Omega_j^n \cup \Omega_j^{n+1} \cup \bigcup_{\Omega_i \in \mathcal{N}_j^n} \partial\mathcal{C}_{ji}^n, \quad (2.26)$$

with \mathcal{N}_j^n the set of the neighboring cells to Ω_j^n . Since equation (2.1) has to be integrated over the control volume \mathcal{C}_j^n , in order to simplify the computation of the integrals, a map from $\tau \in [0, 1]$ is defined for the straight lines connecting the vertexes of the cell from time t^n to t^{n+1} . In particular, through the basis functions

$$\beta_1(\tau) = 1 - \tau; \quad \beta_2(\tau) = \tau, \quad (2.27)$$

any point \tilde{x}_{ji} on the straight line $\partial\mathcal{C}_{ji}^n$ can be described as the convex expansion:

$$\tilde{x}_{ji}(\tau) = \beta_1(\tau)X_{ji}^n + \beta_2(\tau)X_{ji}^{n+1}. \quad (2.28)$$

Via (2.28), it is possible to compute the length $|\partial C_{ji}^n|$ of the lateral side ∂C_{ji}^n and its one-unit outward normal vector \mathbf{n}_{ji} :

$$|\partial C_{ji}^n| = \sqrt{(\Delta t)^2 + (\Delta X_{ji}^n)^2}; \quad \mathbf{n}_{ji} = [\pm \Delta t, \mp \Delta X_{ji}^n]^T, \quad (2.29)$$

with $\Delta X_{ji}^n = X_{ji}^{n+1} - X_{ji}^n$. The signs into the formal definition of the outward normal \mathbf{n}_{ji} depend on the position (namely right or left) of the side ∂C_{ji}^n .

Equation (2.1) can now be integrated over the control volume. First, the equation is expressed in divergence form:

$$\tilde{\nabla} \cdot \tilde{\mathbf{u}} = 0, \quad (2.30)$$

with $\tilde{\nabla} = [\partial_x, \partial_t]^T$ and $\tilde{\mathbf{u}} = [a u, u]^T$. The integration of the equation (2.30) over the control volume

$$\int_{C^n} \tilde{\nabla} \cdot \tilde{\mathbf{u}} \, dx \, dt = 0 \quad (2.31)$$

can be rewritten as

$$\oint_{\partial C^n} \tilde{\mathbf{u}} \cdot \tilde{\mathbf{n}} \, d\gamma = 0, \quad (2.32)$$

due to the Gauss divergence theorem. Using the boundary decomposition (2.26) and since the unit normal vectors at the faces Ω_j^n and Ω_j^{n+1} are $[0, -1]$ and $[0, 1]$, respectively, equation (2.32) defines the following scheme:

$$h_j^{n+1} U_j^{n+1} = h_j^n U_j^n - \sum_{\Omega_i \in \mathcal{N}_j^n} \int_0^1 |\partial C_{ji}^n| \tilde{\mathbf{u}}_{ji} \cdot \mathbf{n}_{ji} \, d\tau. \quad (2.33)$$

The term $\tilde{\mathbf{u}}_{ji} \cdot \mathbf{n}_{ji}$, evaluated on the particular ξ^* such that $x(\xi^*, \tau) = \tilde{x}_{ji} \in \partial C_{ji}$ for any $\tau \in [0, 1]$, represents the numerical flux. Let q^- and q^+ denote the predictor solutions computed in the cells Ω_j and Ω_i , respectively. The numerical flux is approximated using a Rusanov-type scheme:

$$\tilde{\mathbf{u}}_{ji} \cdot \mathbf{n}_{ji} = \frac{1}{2}(\mathbf{u}^+ + \mathbf{u}^-) \cdot \mathbf{n}_{ji} - \frac{1}{2}s(q^+ - q^-), \quad (2.34)$$

where $\mathbf{u}^\pm = [aq^\pm, q^\pm]^T$ and s , deriving from the maximum eigenvalue of the ALE Jacobian matrix reads:

$$s = \pm \Delta t \left(1 - \frac{\Delta t}{\Delta X_{ji}^n} \right). \quad (2.35)$$

Remark 2.2.1. In this case the parameter s coincides with the flatten ALE Jacobian matrix, we refer to all the paper in the bibliography devoted to the ADER method for its specific definition in the multidimensional case.

As for the definition of the normal vector to the side ∂C_{ji}^n in (2.29), also for the parameter s the sign is defined by the orientation of the line ∂C_{ji}^n . In Section B.2 of the appendix there are all the computations for deriving the constants involved in the integration of the flux approximated via a Rusanov scheme. In [41] a more sophisticated numerical approximation based on the Osher-Solomon scheme [84] is provided.

An important issue is the integration of the numerical flux. As a matter of fact, for a unique partition of the physical domain, the integration of (2.34) is computed over the line ∂C_{ji}^n which is shared at the boundaries of both $\Omega_j(t)$ and $\Omega_i(t)$ for any

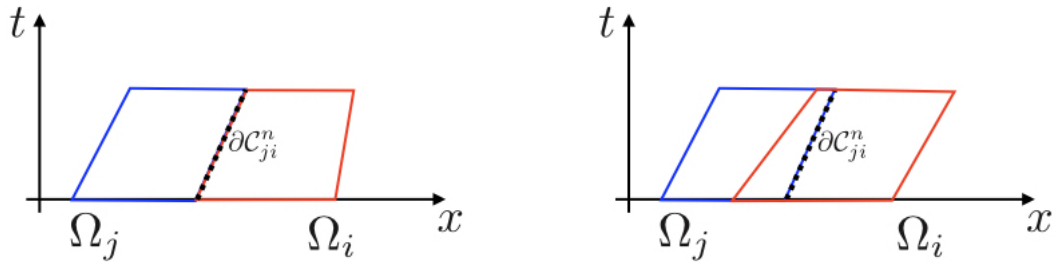


FIGURE 2.6 – Comparison between non overlapping and overlapping cells. The boundary ∂C_{ji}^n (dashed line), over which the Rusanov flux is integrated, is at the boundaries of both space-time cell when there is no overlapping (left picture) while it completely falls inside the neighboring cell when the two cells overlap (right picture).

t between t^n and t^{n+1} . With a chimera grid, in case that the two cells $\Omega_j(t)$ and $\Omega_i(t)$ overlap, the line ∂C_{ji}^n falls inside the cell $\Omega_i(t)$ (see Figure 2.6). Consequently, if the integral for the numerical flux can be preformed exactly once the Lagrangian basis for describing the predictor solution is defined, the same integral in the case of overlapping cells cannot be exactly performed. In this thesis a Gauss-quadrature scheme is employed for this type of integration.

2.2.4 Cell management during the chimera meshes motion

The last part of the presentation of the CWENO-ADER method with a chimera grid is devoted on the possibility, during the motion of some partitions, of either creation or suppression of some cells. As already noticed in Remark 2.1.1, the overlapping area is confined only to one layer of any partition covering the physical spatial domain. Consequently, when a mesh is moving, in order to fulfill this condition and for not having degenerative cases (such as a cell globally bounded in another one), during the motion some cells could appear (in order to not have void between two different meshes) and some others could disappear. In Figure 2.7, all possible configuration of overlapping cells are sketched.

Since the computation of the predictor solutions over any space-time cell only refers to the specific cell (without involving the neighbor cells), this process does not affect that part of the algorithm. On the other hand, when it is needed to compute the integral of the Rusanov flux, it has to be understood which cells are involved in the predictor solutions.

In case of suppression, the computation of the integral is the same one described in the previous subsection. In particular, when the cell is suppressed, another cell moved and completely covers it. Therefore, for the computation of the integral, the predictor solution defined over the suppressing cell is used for solving the numerical solution in its neighbor space-time cells. Since its cell average value is not necessary at time t^{n+1} , equation (2.33) is not solved in that cell.

On the contrary, when the meshes move by creating a void in the physical domain, a new cell Ω_b is created. The values of the predictor solution q_b on the nodes at time t^n are computed evaluating the CWENO polynomial reconstruction of the closest cell at those specific points. Successively, the CWENO-ADER approach is applied. The finite volume stage is performed over born cell by treating it as an overlapping cell. In the case of small overlapping that does not imply neither a suppression nor the creation of a cell, the integral of flux (2.34) over the space-time edge C_{ji}^n is performed

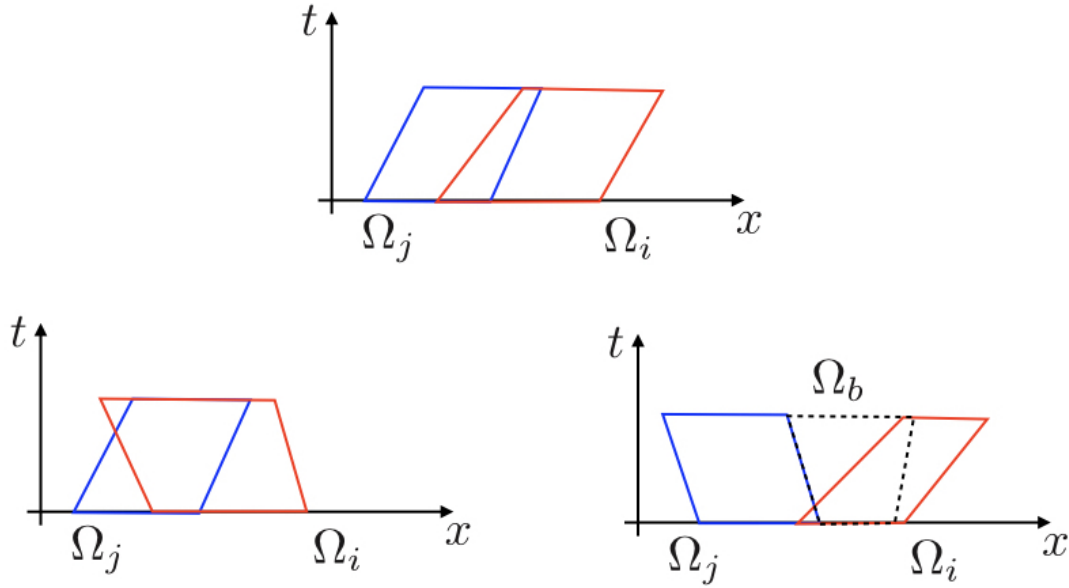


FIGURE 2.7 – The three possible configurations of overlapping cells during the meshes motion. On the top there is a simple overlapping. On the bottom left Ω_i completely covers Ω_j during the motion, consequently Ω_j will disappear at time t^{n+1} . Finally, on the bottom right, due to the void created by the motions of Ω_i and Ω_j , a new cell Ω_b (dashed line) is created.

over specific quadrature points $\bar{x} \in \partial\mathcal{C}_{ji}^n$. A generic point over the space-time edge is parametrized in the (ζ, τ) reference system through the unique couple $(\zeta^*, \bar{\tau})$ to be found. Since any point in the space-time cell $\bar{\mathcal{C}}_{ji}^n$ is represented as projection over a Lagrangian basis (i.e. $x(\zeta, \tau) = \sum_{l=1}^6 \theta_l(\zeta, \tau) \hat{x}_l$), the specific $\zeta^* \in (0, 1)$ mapping $\bar{x} \in \mathcal{C}_{ji}^n$ is found by inverting $\bar{x}(\zeta^*, \bar{\tau}) = \sum_{l=1}^6 \theta_l(\zeta^*, \bar{\tau}) \hat{x}_l$.

2.2.5 Numerical results

In this subsection the presented method is numerically validated. Two test cases are considered: *CASE1* and *CASE3* described in Section 2.1.3. Two overlapping mesh \mathcal{T}_{out} and \mathcal{T}_{in} covers the domain. Let h be the length of a cell in \mathcal{T}_{in} , thus the length of a cell in \mathcal{T}_{out} is set equal to $4h$. In particular, the outside mesh \mathcal{T}_{out} covers the entire domain $\Omega = [-1, 1]$ while the inside mesh \mathcal{T}_{in} covers the sub-interval $[-0.875, -0.75]$. The outside mesh is steady, hence it does not move or deform during the simulation, while the inside mesh can either translate or deform. This means that there is a hole in the outside which is covered by the inside mesh. Consequently, during the entire simulation, there are two zones of superposition moving accordingly to the movement of the inside mesh. For both test cases, the final time is $T = 2$. Two configurations are simulated:

- *Rigid translation*. The inside mesh moves with respect to the velocity $V(x, t) = \chi_{\{t \leq 1\}}(t) - 0.3\chi_{\{t > 1.1\}}(t)$;
- *Translation and deformation*. The inside mesh moves according to the velocity law given by $V(x, t) = e^x \chi_{\{t \leq 1\}}(t) - 0.2\chi_{\{t > 1.5\}}(t)$.

Figure 2.8 depicts three time instances for *CASE1* with a rigid translation configuration. Similarly, in Figure 2.9, the plot for three time instances are reported for a translation and deformation movement of the inside mesh. Table 2.8 resumes the

TABLE 2.8 – L^1 -norm error and convergence rate in the *translation* and *translation and deformation* configurations as function of the total number N of nodes.

<i>Rigid translation</i>					<i>Translation and deformation</i>				
N	CASE1		CASE3		N	CASE1		CASE3	
	L^1 -err	L^1 -rate	L^1 -err	L^1 -rate		L^1 -err	L^1 -rate	L^1 -err	L^1 -rate
71	1.96e-04	-	1.00e-1	-	62	2.11e-04	-	9.68e-2	-
142	2.38e-05	3.04	1.59e-1	-0.68	125	2.52e-05	3.03	1.57e-1	-0.69
278	3.23e-06	2.97	1.71e-2	3.32	247	3.87e-06	2.75	1.62e-2	3.33
553	4.61e-07	2.83	1.10e-3	3.95	493	6.29e-07	2.63	1.10e-3	3.91
1103	9.00e-08	2.37	8.17e-5	3.81	983	1.42e-07	2.16	7.88e-5	3.80
2203	2.37e-8	1.93	7.01e-6	3.55	1966	3.95e-08	1.84	6.80e-6	3.53

L^1 -norm errors between the numerical solution and the exact solution at final time T and rate of convergence for the two listed configurations. We notice that, after a certain threshold of error, around $1e-8$, the rate of convergence decreases. This is likely due to the presence of the two overlapping zones. The method seems to perform well also in the case of a large space derivative.

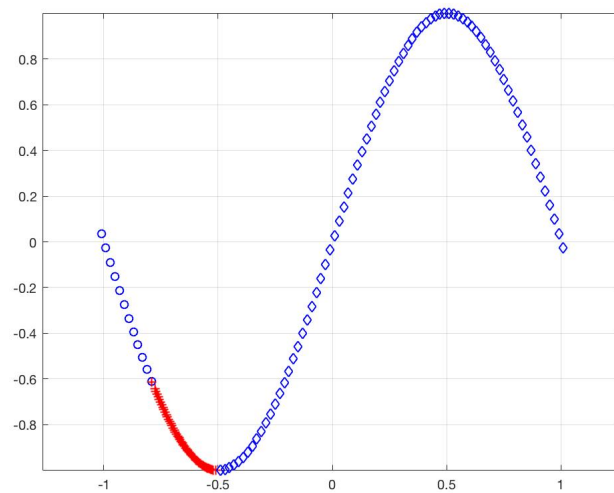
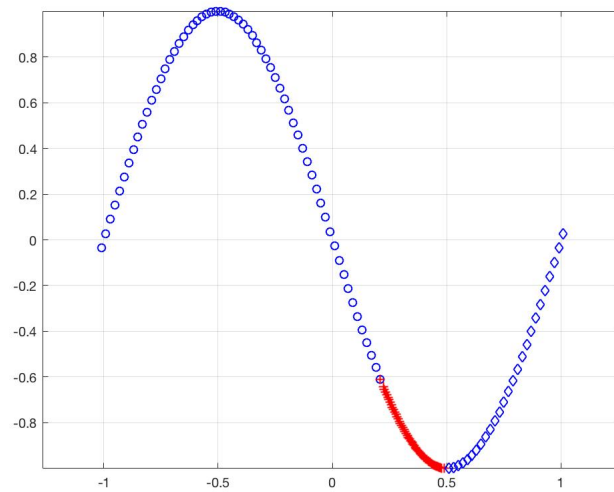
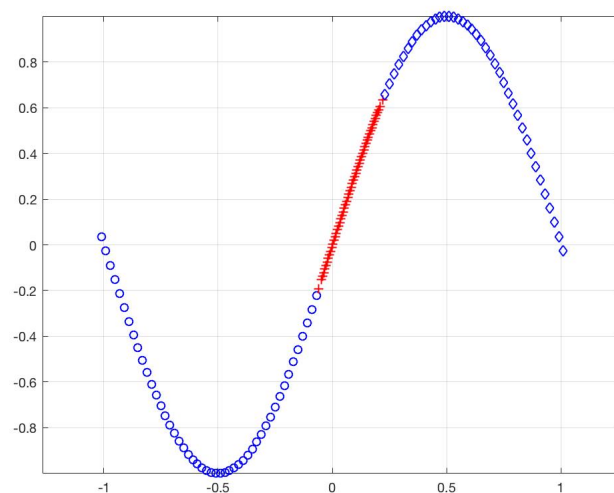
2.3 Approximation of the first derivative over an overlapping stencil

Let $\mathcal{S}_j = \bigcup_{i=j-1}^{j+1} \Omega_i$ be a stencil of three cells $\Omega_i = [x_{i-1/2}, x_{i+1/2}]$, with center x_i ($i = j-1, j, j+1$), covering a part of a domain in \mathbb{R} . The stencil is overlapping if the right extreme point $x_{i+1/2}$ of any cell does not coincide with the left extreme point $x_{(i+1)+1/2}$, as shown in Figure 2.10. The measure of a single cell is $|\Omega_j| = h_j = x_{j+1/2} - x_{j-1/2}$. Moreover let $\delta_{j+1/2} = x_{j+1} - x_j$ and $\delta_{j-1/2} = x_j - x_{j-1/2}$ be the distances between two consecutive centers. When $\delta_{j+1/2} = h_{j+1}/2$ and $\delta_{j-1/2} = h_{j-1}/2$ the stencil is composed of contiguous cells and it is no longer overlapping.

The objective is to approximate the first derivative of a function $u : \mathcal{S}_j \rightarrow \mathbb{R}$ at points $x = x_{j\pm 1/2}$ with second-order accuracy through a linear expansion of the values of u at the nodes. Let u_j be the function $u(x_j)$ evaluated at the center x_j . The minimal required regularity on the function is $u \in C^3(\mathcal{S}_j)$. By Taylor's expansion with remainder in Lagrange form, it holds

$$\begin{aligned} u_{j+1} &= u(x_{j+1/2} + \delta_{j+1/2}) \\ &= u(x_{j+1/2}) + \delta_{j+1/2} u'(x_{j+1/2}) + \frac{1}{2} \delta_{j+1/2}^2 u''(x_{j+1/2}) + \frac{1}{6} \delta_{j+1/2}^3 u'''(\xi_{j+1/2}^r); \end{aligned} \quad (2.36)$$

$$\begin{aligned} u_j &= u\left(x_{j+1/2} - \frac{h_j}{2}\right) \\ &= u(x_{j+1/2}) - \frac{1}{2} h_j u'(x_{j+1/2}) + \frac{1}{8} h_j^2 u''(x_{j+1/2}) - \frac{1}{48} h_j^3 u'''(\xi_{j+1/2}^l); \end{aligned} \quad (2.37)$$

(A) $t = 0$ (B) $t = 1$ (C) $t = T = 2$ FIGURE 2.8 – Three time instances for *CASE1* with a rigid translation movement of the inside mesh.

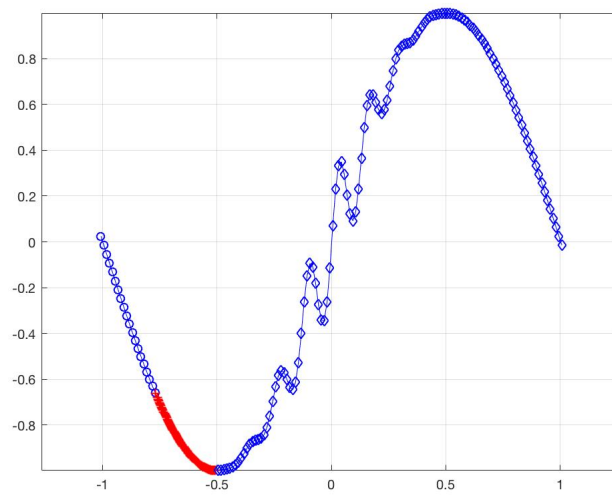
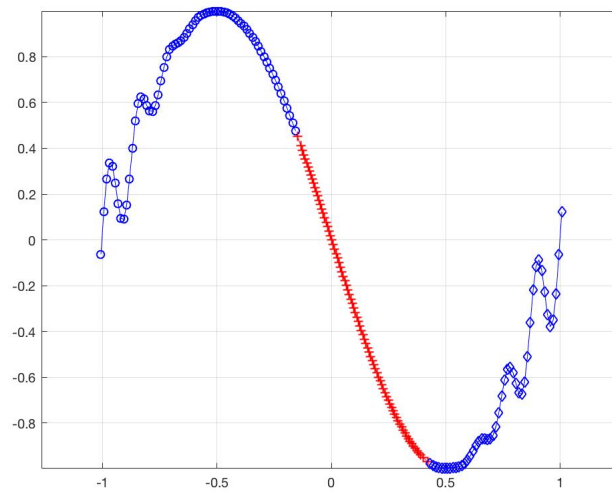
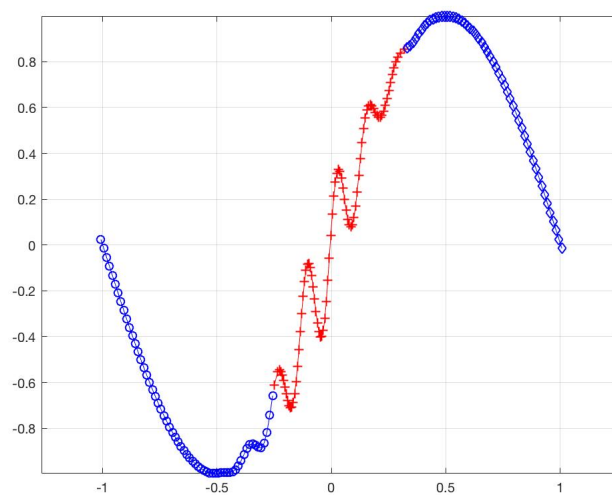
(A) $t = 0$ (B) $t = 1$ (C) $t = T = 2$

FIGURE 2.9 – Three time instances for CASE3 with translation and deformation movement of the inside mesh.

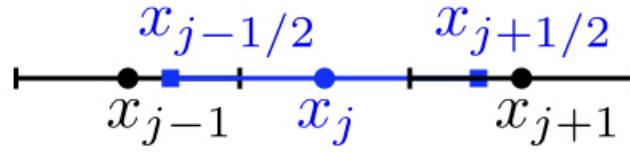


FIGURE 2.10 – An overlapping stencil. The blue squared points represent the extremes cell Ω_j , the circular points are the nodes.

$$\begin{aligned}
 u_{j-1} &= u(x_{j+1/2} - (h_j + \delta_{j-1/2})) \\
 &= u(x_{j+1/2}) - (h_j + \delta_{j-1/2})u'(x_{j+1/2}) + \frac{1}{2}(h_j + \delta_{j-1/2})^2u''(x_{j+1/2}) \\
 &\quad + \frac{1}{6}(h_j + \delta_{j-1/2})^3u'''(\xi_{j+1/2}^{ll});
 \end{aligned} \tag{2.38}$$

with $\xi_{j+1/2}^r \in [x_{j+1/2}, x_{j+1}]$, $\xi_{j+1/2}^l \in [x_j, x_{j+1/2}]$ and $\xi_{j+1/2}^{ll} \in [x_{j-1}, x_{j+1/2}]$. Let $\{\alpha_{i,j+1/2}\}_{i=1}^3$ be the set of the unknown expansion coefficients. The linear combination of equations (2.36), (2.37) and (2.38) for approximating $u'(x_{j+1/2})$ reads

$$\begin{aligned}
 \alpha_{1,j+1/2}u_{j+1} + \alpha_{2,j+1/2}u_j + \alpha_{3,j+1/2}u_{j-1} &= (\alpha_{1,j+1/2} + \alpha_{2,j+1/2} + \alpha_{3,j+1/2})u(x_{j+1/2}) \\
 &\quad + \left[\alpha_{1,j+1/2}\delta_{j+1/2} - \frac{1}{2}\alpha_{2,j+1/2}h_j - \alpha_{3,j+1/2}(h_j + \delta_{j-1/2}) \right] u'(x_{j+1/2}) \\
 &\quad + \frac{1}{2} \left[\alpha_{1,j+1/2}\delta_{j+1/2}^2 + \frac{1}{4}\alpha_{2,j+1/2}h_j^2 + \alpha_{3,j+1/2}(h_j + \delta_{j-1/2})^2 \right] u''(x_{j+1/2}) \\
 &\quad + \frac{1}{6}\alpha_{1,j+1/2}\delta_{j+1/2}^3u'''(\xi_{j+1/2}^r) - \frac{1}{48}\alpha_{2,j+1/2}h_j^3u'''(\xi_{j+1/2}^l) \\
 &\quad - \frac{1}{6}\alpha_{3,j+1/2}(h_j + \delta_{j-1/2})^3u'''(\xi_{j+1/2}^{ll}).
 \end{aligned} \tag{2.39}$$

Consequently, the following constraints are imposed:

$$\begin{cases} \alpha_{1,j+1/2} + \alpha_{2,j+1/2} + \alpha_{3,j+1/2} &= 0 \\ \alpha_{1,j+1/2}\delta_{j+1/2} - \frac{1}{2}\alpha_{2,j+1/2}h_j - \alpha_{3,j+1/2}(h_j + \delta_{j-1/2}) &= 1, \\ \alpha_{1,j+1/2}\delta_{j+1/2}^2 + \frac{1}{4}\alpha_{2,j+1/2}h_j^2 + \alpha_{3,j+1/2}(h_j + \delta_{j-1/2})^2 &= 0 \end{cases} \tag{2.40}$$

whose solution is

$$\begin{cases} \alpha_{1,j+1/2} = \frac{\delta_{j-1/2} + 1.5h_j/2}{\delta_{j+1/2}^2 + \delta_{j+1/2}\delta_{j-1/2} + 1.5\delta_{j+1/2}h_j + 0.5\delta_{j-1/2}h_j + 0.5h_j^2} \\ \alpha_{2,j+1/2} = \frac{\delta_{j+1/2} - \delta_{j-1/2} - h_j}{\delta_{j+1/2}\delta_{j-1/2} + 0.5\delta_{j+1/2}h_j + 0.5\delta_{j-1/2}h_j + 0.25h_j^2} \\ \alpha_{3,j+1/2} = \frac{-\delta_{j+1/2} + 0.5h_j}{\delta_{j+1/2}\delta_{j-1/2} + 0.5\delta_{j+1/2}h_j + \delta_{j-1/2}^2 + 1.5\delta_{j-1/2}h_j + 0.5h_j^2} \end{cases} \tag{2.41}$$

This allows to write that

$$u'(x_{j+1/2}) = \alpha_{1,j+1/2}u_{j+1} + \alpha_{2,j+1/2}u_j + \alpha_{3,j+1/2}u_{j-1} + \mathcal{O}(h_j^2). \tag{2.42}$$

Similarly, it is possible to approximate the derivative $u'(x_{j-1/2})$. At the left extreme of Ω_j , by Taylor expansion with Lagrange remainder, it holds

$$\begin{aligned} u_{j+1} &= u(x_{j-1/2} + (h_j + \delta_{j+1/2})) \\ &= u(x_{j-1/2}) + (h_j + \delta_{j+1/2})u'(x_{j-1/2}) + \frac{1}{2}(h_j + \delta_{j+1/2})^2 u''(x_{j-1/2}) \\ &\quad + \frac{1}{6}(h_j + \delta_{j+1/2})^3 u'''(\xi_{j-1/2}^{rr}); \end{aligned} \quad (2.43)$$

$$\begin{aligned} u_j &= u\left(x_{j-1/2} + \frac{h_j}{2}\right) \\ &= u(x_{j-1/2}) + \frac{1}{2}h_j u'(x_{j-1/2}) + \frac{1}{8}h_j^2 u''(x_{j-1/2}) - \frac{1}{48}h_j^3 u'''(\xi_{j-1/2}^r); \end{aligned} \quad (2.44)$$

$$\begin{aligned} u_{j-1} &= u(x_{j+1/2} - \delta_{j-1/2}) \\ &= u(x_{j-1/2}) - \delta_{j-1/2} u'(x_{j-1/2}) + \frac{1}{2}\delta_{j-1/2}^2 u''(x_{j-1/2}) + \frac{1}{6}\delta_{j-1/2}^3 u'''(\xi_{j-1/2}^l); \end{aligned} \quad (2.45)$$

with $\xi_{j-1/2}^{rr} \in [x_{j-1/2}, x_{j+1}]$, $\xi_{j-1/2}^r \in [x_{j-1/2}, x_j]$ and $\xi_{j-1/2}^l \in [x_{j-1}, x_{j-1/2}]$. A linear combination of terms in (2.43), (2.44) and (2.45) for approximating $u'(x_{j-1/2})$ reads:

$$\begin{aligned} \alpha_{1,j-1/2}u_{j+1} + \alpha_{2,j-1/2}u_j + \alpha_{3,j-1/2}u_{j-1} &= (\alpha_{1,j-1/2} + \alpha_{2,j-1/2} + \alpha_{3,j-1/2})u(x_{j-1/2}) \\ &\quad + \left[\alpha_{1,j-1/2}(h_j + \delta_{j+1/2}) + \frac{1}{2}\alpha_{2,j-1/2}h_j - \alpha_{3,j-1/2}\delta_{j-1/2} \right] u'(x_{j-1/2}) \\ &\quad + \frac{1}{2} \left[\alpha_{1,j-1/2}(h_j + \delta_{j+1/2})^2 + \frac{1}{4}\alpha_{2,j-1/2}h_j^2 + \alpha_{3,j-1/2}\delta_{j-1/2}^2 \right] u''(x_{j-1/2}) \\ &\quad + \frac{1}{6}\alpha_{1,j-1/2}(h_j + \delta_{j+1/2})^3 u'''(\xi_{j-1/2}^{rr}) + \frac{1}{48}\alpha_{2,j-1/2}h_j^3 u'''(\xi_{j-1/2}^r) \\ &\quad - \frac{1}{6}\alpha_{3,j-1/2}\delta_{j-1/2}^3 u'''(\xi_{j+1/2}^l), \end{aligned} \quad (2.46)$$

with $\{\alpha_{i,j-1/2}\}_{i=1}^3$ real coefficients to be found. The following system of constraints arises

$$\begin{cases} \alpha_{1,j-1/2} + \alpha_{2,j-1/2} + \alpha_{3,j-1/2} &= 0 \\ \alpha_{1,j-1/2}(h_j + \delta_{j+1/2}) + \frac{1}{2}\alpha_{2,j-1/2}h_j - \alpha_{3,j-1/2}\delta_{j-1/2} &= 1, \\ \alpha_{1,j-1/2}(h_j + \delta_{j+1/2})^2 + \frac{1}{4}\alpha_{2,j-1/2}h_j^2 + \alpha_{3,j-1/2}\delta_{j-1/2}^2 &= 0 \end{cases} \quad (2.47)$$

whose solution is:

$$\begin{cases} \alpha_{1,j-1/2} = \frac{\delta_{j-1/2} - 0.5h_j/2}{\delta_{j+1/2}^2 + \delta_{j+1/2}\delta_{j-1/2} + 1.5\delta_{j+1/2}h_j + 0.5\delta_{j-1/2}h_j + 0.5h_j^2} \\ \alpha_{2,j-1/2} = \frac{\delta_{j+1/2} - \delta_{j-1/2} + h_j}{\delta_{j+1/2}\delta_{j-1/2} + 0.5\delta_{j+1/2}h_j + 0.5\delta_{j-1/2}h_j + 0.25h_j^2} \\ \alpha_{3,j-1/2} = -\frac{\delta_{j+1/2} + 1.5h_j}{\delta_{j+1/2}\delta_{j-1/2} + 0.5\delta_{j+1/2}h_j + \delta_{j-1/2}^2 + 1.5\delta_{j-1/2}h_j + 0.5h_j^2} \end{cases} \quad (2.48)$$

Finally, it holds

$$u'(x_{j-1/2}) = \alpha_{1,j-1/2}u_{j+1} + \alpha_{2,j-1/2}u_j + \alpha_{3,j-1/2}u_{j-1} + \mathcal{O}(h_j^2). \quad (2.49)$$

2.4 The Poisson equation

Let $\Omega \subset \mathbb{R}$ be the computational domain of the Poisson equation:

$$\partial_x(-v\partial_x u) = f \quad \text{in } \Omega, \quad (2.50)$$

completed with some compatible boundary conditions and with $v > 0$ the diffusion parameter. Problem (2.50) is solved via finite volumes on a chimera grid. The computational domain is discretized through a patch of n partitions \mathcal{T}_i , with $i = 1, \dots, n$. By integrating equation (2.50) over a cell Ω_j and by divergence theorem, it follows

$$-v\partial_x u(x_{j-1/2}) + v\partial_x u(x_{j+1/2}) = \int_{\Omega_j} f(x) \, dx. \quad (2.51)$$

Since the scheme is *cell-centered*, it is needed to approximate the derivatives at the extremes of the cell in (2.51). By using approximations in (2.42) and (2.49), equation (2.51) reads

$$\begin{aligned} -v(\alpha_{1,j+1/2} - \alpha_{1,j-1/2})u_{j+1} - v(\alpha_{2,j+1/2} - \alpha_{2,j-1/2})u_j \\ - v(\alpha_{3,j+1/2} - \alpha_{3,j-1/2})u_{j-1} = \int_{\Omega_j} f(x) \, dx. \end{aligned} \quad (2.52)$$

This yields to the linear system whose j -th equation looks for the j -th unknown u_j , for any $j = 1, \dots, N$.

2.4.1 Numerical results

Let us consider the domain $\Omega = [-1, 1]$ for the two test cases *CASE4* and *CASE5* of problem (2.50) whose exact solutions are

$$u_{ex}(x) = \sin(\pi x) \quad \text{and} \quad u_{ex}(x) = \sin^2(\pi x) \tanh(x - 0.3),$$

respectively. Both test cases are completed with homogeneous Dirichlet boundary conditions with diffusive term $v = 1$. The computational domain is covered with three uniform overlapping meshes. They superpose around points $\bar{x}_1 = -0.4$ and $\bar{x}_2 = 0.4$. Let h be the space step of the first and the third grid (covering the beginning and the end of the domain), thus $h/3$ is the space step of the second mesh in the middle. The overlapping indexes are 0.6 and 0.5, respectively.

The order of convergence of the L^2 -error between the numerical and exact solutions is analyzed and reported in Table 2.9. A second-order accuracy is achieved. In Figures 2.11 and 2.12 there are the plots of the numerical solutions of *CASE4* and *CASE5*, respectively. The different markers define the different overlapping meshes.

TABLE 2.9 – L^2 -errors and order of convergence for CASE4 and CASE5 as function of the total number N of cells.

N	CASE4		CASE5	
	L^2 -err	L^2 -rate	L^2 -err	L^2 -rate
61	4.71e-4	-	5.98e-4	-
120	1.03e-4	2.25	1.43e-4	2.12
237	2.42e-5	2.13	3.64e-5	2.01
472	5.83e-6	2.07	9.32e-6	1.98
883	1.63e-6	2.03	2.69e-6	1.98
1763	4.05e-7	2.01	6.78e-7	1.99

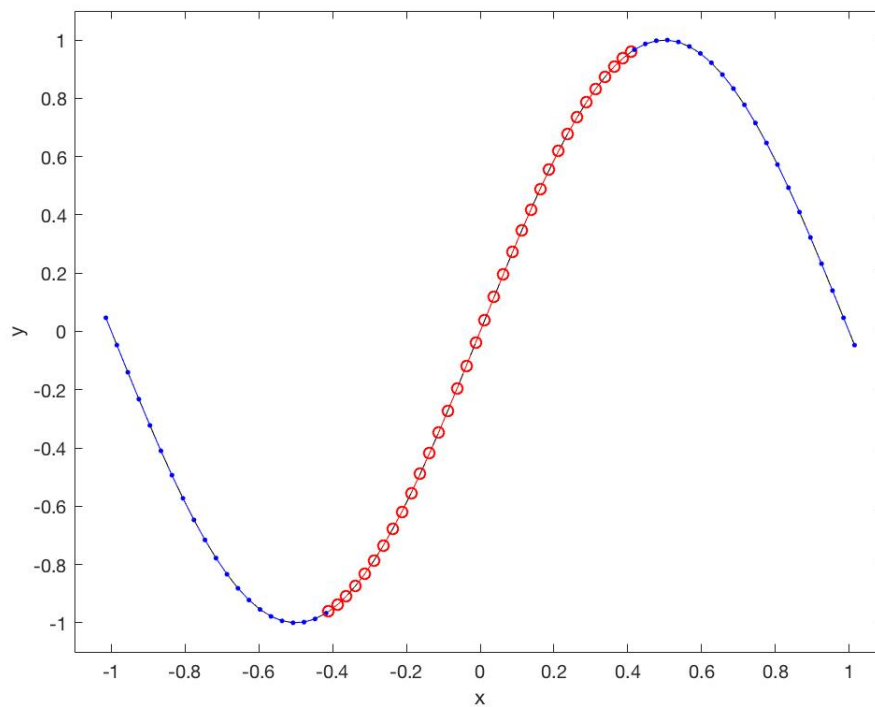


FIGURE 2.11 – Numerical solution of CASE4. The different markers define the different meshes.

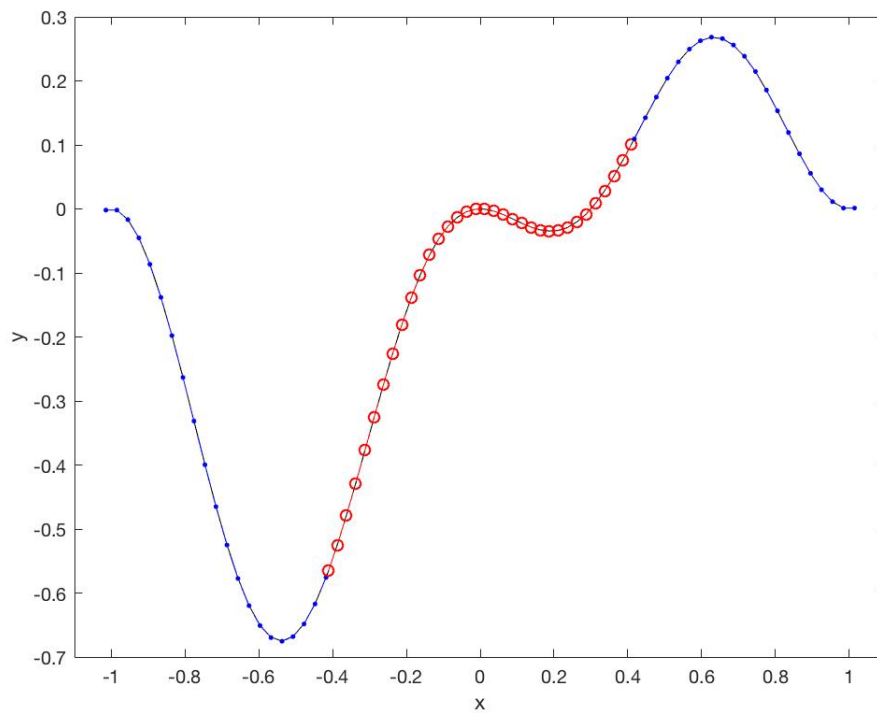


FIGURE 2.12 – Numerical solution of CASE5. The different markers define the different meshes.

Chapter 3

The Advection-Diffusion problem

As already noted in the previous chapter, the Arbitrary high order DERivatives (ADER) method provides an ideal setting for pursuing the purpose of solving a PDE over a moving and deforming overset grid. In [41, 109, 108, 29], the authors present a method to recover an accurate solution for hyperbolic PDEs with an arbitrary order of accuracy on a single mesh block. More recently, in [28] the authors present an ADER Discontinuous Galerkin scheme with *a posteriori* subcell finite volume limiter on fixed and moving grids such as space-time adaptive Cartesian AMR meshes. The numerical scheme treats the temporal variable indistinctly with respect to the spatial variables by defining the solution on a space-time slab. This discretization approach, therefore, allows to re-consider the problem of Chimera grids transmission conditions: instead of time-dependent spatial transmission conditions between relatively moving grid blocks, we define interpolation polynomials on arbitrarily intersecting space-time cells at the block boundaries.

In the ADER scheme a local space-time weak solution of the problem from the generic time t to $t + \Delta t$ is computed in every single space-time cell. This solution is defined as the *predictor*. The prediction step is local and hence embarrassingly parallel, because the solution is calculated independently of the information of the neighboring cells. Then, in the subsequent stage of *correction*, the computation of a space-time numerical flux between neighboring cells provides the appropriate stabilization of the integration scheme. We extend this prediction-correction method to Advection-Diffusion PDEs on overset grids and propose a space-time flux among the space-time cells that provides improved stabilization and precision as it takes into account both the advective and diffusive nature of the equation.

Part of this chapter is in [18].

Let $\Omega(t) \subset \mathbb{R}^d$ be the time-dependent computational domain and let T be a positive real. In the following we consider the parabolic problem: *find* $u : \Omega(t) \times [0, T] \rightarrow \mathbb{R}^\delta$ such that

$$\partial_t \mathbf{u} + \nabla \cdot \mathbf{F}(\mathbf{u}, \nabla \mathbf{u}) = \mathbf{f}, \quad \mathbf{x} \in \Omega(t), \quad t \in [0, T], \quad (3.1)$$

closed with appropriate initial and boundary conditions. Problem (3.1) is a rather general representation of an advection-diffusion model. In (3.1) the diffusive-convective vector $\mathbf{F}(\mathbf{u}, \nabla \mathbf{u})$, eventually nonlinear, and the force term $\mathbf{f}(\mathbf{x}, t)$ are defined. In particular, the problem is linear when the diffusive-convective term is written as $\mathbf{F}(\mathbf{u}, \nabla \mathbf{u}) = \mathbf{A}\mathbf{u} - \nu \nabla \mathbf{u}$, where $\mathbf{A} : \Omega \times [0, T] \rightarrow \mathbb{R}^{\delta \times \delta}$ is the advective field and $\nu : \Omega \times [0, T] \rightarrow \mathbb{R}_+$ is the diffusion parameter.

With respect to the pure advective PDEs of Chapter 2, in this chapter a non-vanishing diffusion parameter is considered. For this reason, the solution of problem (3.1) is continuous and enough regular to be \mathcal{P}_2 -interpolated. In particular, due to the Laplacian operator, the solution never presents shock waves or discontinuities.

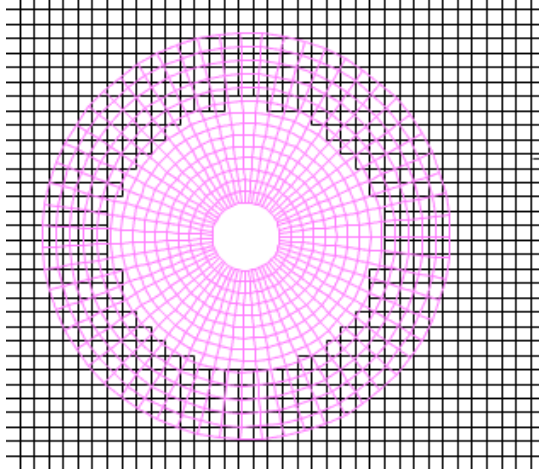


FIGURE 3.1 – Example of Chimera grid configuration. In black there is the *background* mesh and in pink the *foreground* mesh.

3.1 The overset grid

An overset grid or Chimera mesh is a set of mesh blocks covering the computational domain. Each block may overlap other block(s) in some particular sub-region(s) said *overlapping zone(s)*. Once the multiple mesh patches are generated, they are collated in order to generate an appropriate topology [75]. Consequently, an overlapping zone between two neighboring blocks is defined. For the sake of simplicity with no loss of generality, the whole method is explained by considering a two blocks overset grid (i.e., the background and the foreground meshes). For multiple-block meshes (e.g. $\mathcal{T}_1, \dots, \mathcal{T}_N$), a hierarchy of meshes from the background to the foreground is defined (e.g. $\mathcal{T}_1 < \dots < \mathcal{T}_N$)¹. Successively the presented algorithm for setting the overset grid is performed from one mesh to the union of all other meshes towards the background (e.g. \mathcal{T}_i for $\bigcup_{j=1}^{i-1} \mathcal{T}_j$ for any $i = 2, \dots, N$). Figure 3.1 shows an overset grid; in black there is the *background* mesh and in pink the *foreground* mesh. In particular, the foreground mesh can move and deform. The overlapping zone is necessary for the communication and data transfer from one mesh to the other.

In this thesis, the cell of any block mesh is considered quadrilateral. In particular, when all the cells are squared, the mesh is uniform. When the cells are either squared or rectangular and the edges are oriented as the Cartesian axes, the mesh is said to be Cartesian.

3.1.1 The automatic definition of the stencil at the transmission condition

Let $\mathcal{T}_k = \{\Omega_i^k\}_{i=1}^{N_k}$ be the partition composed of N_k cells referring to the k -th block mesh², moreover, let \mathcal{S}_i be the stencil centered over the cell Ω_i . Thus, stencil \mathcal{S}_i is the set collecting the indexes of neighboring cells to Ω_i . By abuse of language, sometimes we will refer to the physical set $\Omega_i \cup \bigcup_{j \in \mathcal{S}_i} \Omega_j$ as the stencil.

It is possible to distinguish two classes of cells with respect to their proximity to the overlapping interface. The definition of the stencil depends on the class.

If cell Ω_i is not at the boundary of the overlapping zone (Figure 3.2a), the stencil \mathcal{S}_i is composed of all the cells Ω_j sharing at least one vertex with Ω_i . Thus, if Ω_i belongs

1. In this case, symbol $>$ defines the position in the hierarchy among meshes.

2. In order to simplify the notation, we will omit the superscript k to the cell Ω_i^k by writing Ω_i

to the partition \mathcal{T}_1 , all cells Ω_j , with $j \in \mathcal{S}_i$, also belong to \mathcal{T}_1 .

If the cell Ω_i of partition \mathcal{T}_k is at the boundary of the interface, it is no longer possible to use the criterion of the cells sharing at least a vertex. In fact, there will be at least one edge e_{il} not shared by any other cell of the same partition (see right edge of cell Ω_{16} in Figure 3.2b). For these cells, we aim in automatically finding the other cells of partition \mathcal{T}_j ($j \neq k$) belonging to the stencil. Let the extremes of the edge be indicated as v_1 and v_2 and its middle point with v_3 , respectively. Point c_* is the center of mass of generic cell Ω_* . For our numerical tests, Algorithm 3.1 is adopted through the two steps:

1. look for the nodes of cells of the other partition \mathcal{T}_j minimizing the Euclidean distance with respect to points v_μ , $\mu = 1, 2, 3$, (line 5, see Figure 3.3a);
2. compute the symmetric points \tilde{v}_μ of center c_i^k with respect to points v_μ for $\mu = 1, 2, 3$ (line 6), then look for the cells of partition \mathcal{T}_j whose centers minimize the Euclidean distance with the three symmetric points (line 7, see Figure 3.3b).

For the edges shared by other cells in the same partition, the cells of the stencil will be those ones sharing at least one vertex (as cells of indexes 13, 14, 17, 19 and 20 in Figure 3.2b).

The routine presented in this section will be run whenever the foreground mesh configuration as well as the hole change.

Algorithm 3.1 could not define a compact stencil in the case of widely different mesh spacing. In this case, more than three points v_μ can be considered for lines 5 and 6. Moreover a weighted symmetry (possibly led by the different spacing) can be performed at line 6.

Algorithm 3.1 Compute stencil for cells at the boundary of the overlapping zone.

Input: $\Omega_i^k, e_{il}^k, \mathcal{T}_j, \mathcal{S}_i^k$; $\triangleright j \neq k$, i.e. \mathcal{T}_j is the other partition with respect to \mathcal{T}_k

- 1: Initialize v_1 and v_2 as the two vertexes of edge e_{il}^k ;
- 2: $v_3 \leftarrow (v_1 + v_2)/2$; \triangleright Middle point of edge e_{il}^k
- 3: $\mathcal{Z}_j \leftarrow \emptyset$; \triangleright Temporary set of indexes of partition \mathcal{T}_j
- 4: **for** $\mu = 1, 2, 3$ **do**
- 5: $\mathcal{Z}_j \leftarrow \mathcal{Z}_j \cup \{n = 1, \dots, N_j : \|v_\mu - c_n^j\| \leq \|v_\mu - c_m^j\| \quad \forall m = 1, \dots, N_j\}$;
- 6: $\tilde{v} \leftarrow 2v_\mu - c_i^k$; \triangleright Symmetric point of cellcenter c_i^k of Ω_i^k with respect to v_μ
- 7: $\mathcal{Z}_j \leftarrow \mathcal{Z}_j \cup \{n = 1, \dots, N_j : \|\tilde{v} - c_n^j\| \leq \|\tilde{v} - c_m^j\| \quad \forall m = 1, \dots, N_j\}$;
- 8: $\mathcal{S}_i^k \leftarrow \mathcal{S}_i \cup \mathcal{Z}_j$;
- 9: **return** \mathcal{S}_i^k

3.2 The numerical method

Once the stencil has been defined, the numerical method can both numerically solve problem (3.1) and eventually evolve the overset grid. In this section the scheme is presented. The method consists in a FEM-predictor FVM-corrector scheme stabilised with a Local Lax-Friedrichs approach whose stabilization coefficient is explained in the following section.

3.2.1 Local polynomial reconstruction

The first step of the numerical method is to recover a reconstruction of the solution over any point of the actual cell Ω_i . Since the scheme is cell-centered, at time t^n ,

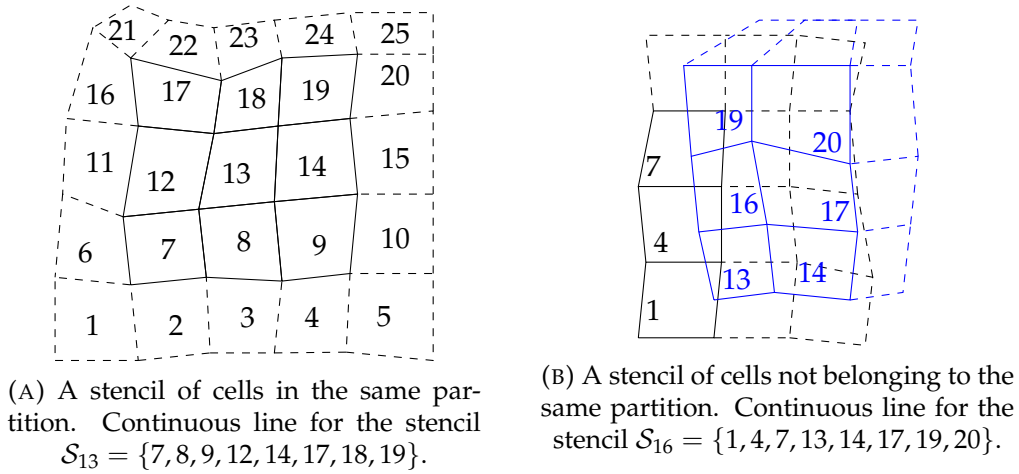


FIGURE 3.2 – Two possible stencils: on the left the stencil is in the same partition; on the right the stencil is composed of cells not belonging to the same partition.

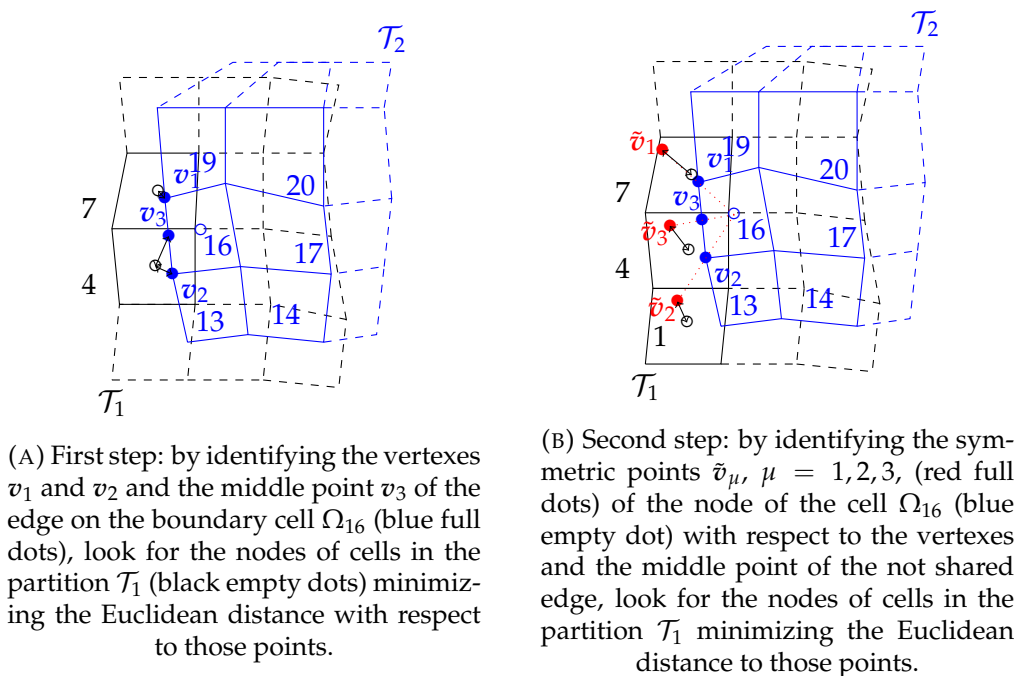


FIGURE 3.3 – The two steps for the research of cells in the partition \mathcal{T}_1 for the cell $\Omega_{16} \in \mathcal{T}_2$.

we would like to extend (at least locally) the solution to the whole cell by exploiting the information in the cells of the stencil referring to Ω_i^n . In order to explain the reconstruction, let us consider a generic regular³ function $\phi : E \rightarrow \mathbb{R}$ by identifying the stencil $E = \Omega_i^n \cup \bigcup_{j \in \mathcal{S}_i} \Omega_j^n$. We remark that, due to the overlapping zone, the cell composing the subdomain E does not necessary fulfill the non-overlapping condition, i.e., it could be verified that there is a couple of indexes $k, l \in \{i\} \cup \mathcal{S}_i$ such that $\Omega_k^n \cap \Omega_l^n \neq \emptyset$. Let us suppose to know the value of function ϕ over the center of mass $(x_k, y_k) = \mathbf{x}_k$, with $k \in \{i\} \cup \mathcal{S}_i$, of any Ω_k composing E . We would like to have a polynomial function $\Pi_i \phi(x, y)$ for any $(x, y) \in E$ by using the knowledge of the function ϕ only on the centers of mass. Let us define $\phi_k = \phi(x_k, y_k)$. For any $(x, y) \in E$ it is always possible to write the Taylor's polynomial truncated to the quadratic terms with respect to ϕ_i :

$$\begin{aligned} \phi(x, y) &= \phi_i + (\partial_x \phi)_i (x - x_i) + (\partial_y \phi)_i (y - y_i) + (\partial_{xy}^2 \phi)_i (x - x_i)(y - y_i) \\ &\quad + \frac{1}{2} (\partial_{xx}^2 \phi)_i (x - x_i)^2 + \frac{1}{2} (\partial_{yy}^2 \phi)_i (y - y_i)^2 + \mathcal{O}(H^3), \end{aligned} \quad (3.2)$$

with $H = \max\{|x - x_i|, |y - y_i|\}$. In the expansion (3.2) all the derivatives of ϕ_i are unknown. Moreover, by renaming those derivatives as

$$p_1 = (\partial_x \phi)_i \quad p_2 = (\partial_y \phi)_i \quad p_3 = (\partial_{xy}^2 \phi)_i \quad p_4 = (\partial_{xx}^2 \phi)_i \quad p_5 = (\partial_{yy}^2 \phi)_i, \quad (3.3)$$

the Taylor's expansion (3.2) can be seen as a linear combination of the components of the basis $\{1, x - x_i, y - y_i, (x - x_i)(y - y_i), \frac{1}{2}(x - x_i)^2, \frac{1}{2}(y - y_i)^2\}$ which defines the polynomial space function \mathcal{P}_2 of quadratic polynomials centered in \mathbf{x}_i ; thus the polynomial interpolation function $\Pi_i \phi$ reads:

$$\begin{aligned} \Pi_i \phi(x, y) &= \phi_i + p_1(x - x_i) + p_2(y - y_i) + p_3(x - x_i)(y - y_i) \\ &\quad + \frac{1}{2} p_4(x - x_i)^2 + \frac{1}{2} p_5(y - y_i)^2, \end{aligned} \quad (3.4)$$

with the polynomial coefficients $p_l, l = 1, \dots, 5$, to be sought. By imposing as constraint that the polynomial $\Pi_i \phi(x, y)$ exactly coincides with the function ϕ on the nodes, i.e. $\Pi_i \phi(x_j, y_j) = \phi_j$ for any $j \in \mathcal{S}_i$, the system in the unknown polynomial coefficients arises:

$$\begin{bmatrix} h_{ik}^x & h_{ik}^y & h_{ik}^x h_{ik}^y & \frac{1}{2}(h_{ik}^x)^2 & \frac{1}{2}(h_{ik}^y)^2 \\ \vdots & \vdots & \vdots & \vdots & \vdots \\ h_{ij}^x & h_{ij}^y & h_{ij}^x h_{ij}^y & \frac{1}{2}(h_{ij}^x)^2 & \frac{1}{2}(h_{ij}^y)^2 \end{bmatrix} \begin{bmatrix} p_1 \\ \vdots \\ p_5 \end{bmatrix} = \begin{bmatrix} \delta \phi_{ik} \\ \vdots \\ \delta \phi_{ij} \end{bmatrix}, \quad (3.5)$$

with $h_{ij}^x = x_j - x_i$, $h_{ij}^y = y_j - y_i$ and $\delta \phi_{ij} = \phi_j - \phi_i$, for $j \in \mathcal{S}_i$. The algebraic system (3.5) has to be solved in least-square sense if $|\mathcal{S}_i| > 5$. Moreover, if the chosen polynomial basis is not reduced, namely if the Taylor's expansion (3.2) is arrested to the bi-linear or linear terms, the stencil has to contain at least 5 cells in order to ensure a solution for (3.5). The proposed \mathcal{P}_2 -interpolation, with the second-order accurate scheme, fulfills the condition for the accuracy in the interpolation for overlapping zones whose depth d_o degrades as the characteristic length h of the chimera mesh (i.e., $d_o = \mathcal{O}(h)$) [30].

This method allows to locally reconstruct all over the stencil a given function. If the function is defined over the computational domain $\Omega \subset \mathbb{R}^2$ and it is (at least locally)

3. We require at least $\phi \in C^2(E)$.

C^2 , then the reconstruction is locally computed over any stencil and the ensured order of convergence is 3. On the contrary, if the solution presents propagating shock waves or discontinuities, this interpolation is no longer adequate because of well-known Gibbs' phenomenon, for which spurious oscillation are produced near the discontinuity. For those cases, other interpolation could be adopted, such as the central weighted ENO for hyperbolic equations for moving meshes in [41] or in Chapter 2.

In the sequel, the local polynomial reconstruction $\Pi_i \mathbf{u}^n$ will be referred as w_i^n .

3.2.2 Local space-time Galerkin predictor

Let be the time interval $[0, T]$ subdivided in N subintervals $[t^n, t^{n+1}]$, with $n = 0, \dots, N-1$; thus for a generic time-dependent variable $\mathbf{g}(t)$, we define \mathbf{g}^n for $\mathbf{g}^n = \mathbf{g}(t^n)$. In particular, the domain Ω^n and the solution \mathbf{u}^n at time t^n are considered the actual spatial configuration and the actual time, respectively. Let $C_i^n = \Omega_i(t) \times [t^n, t^{n+1}]$ be the physical space-time cell whose lower and upper bases represent the evolution of cell $\Omega_i(t)$ from t^n to t^{n+1} . First, the governing equation (3.1) is rewritten with respect to a space-time reference system identified by the independent variables $\boldsymbol{\xi} \equiv (\zeta, \eta, \tau)$ in the unit cube $\hat{C} = [0, 1]^3$. Let $\Xi = (\zeta, \eta)$ be the reference spatial vector. Inspired by [59], the governing equation is discretized using an efficient nodal formulation of space-time nodes given by a tensor product of Gauss-Legendre quadrature points along space and time directions. This choice defines an L^2 -orthogonal Lagrange basis used for the definition of the Galerkin solution. For our purposes, the single direction nodes over the unit interval $[0, 1]$ are $\{(5 - \sqrt{15})/10; 1/2; (5 + \sqrt{15})/10\}$. Consequently, over a space-time cell there will be 27 Gauss-Legendre nodes $\hat{\boldsymbol{\xi}}_m$ and 27 Lagrange polynomial $\theta_l : \hat{C} \rightarrow \mathbb{R}$ such that $\theta_l(\hat{\boldsymbol{\xi}}_m) = \delta_{lm}$ and $\int_{\hat{C}} \theta_l \theta_m d\boldsymbol{\xi} = \delta_{lm} \|\theta_l\|_{L^2(\hat{C})}^2$, with δ_{lm} the Kronecker symbol. Let $\mathbf{m} : \{1, 2, 3\}^3 \rightarrow \{1, \dots, 27\}$ be a discrete map from a single direction index to the global three dimensional index defined as

$$\mathbf{m}(i, j, k) = i + 3(j - 1) + 9(k - 1), \quad (3.6)$$

where indexes $i, j, k \in \{1, 2, 3\}$ lead the discretization along ζ, η, τ , respectively. By denoting the Gauss-Legendre nodes with $\hat{\zeta}_i, \hat{\eta}_j$ and $\hat{\tau}_k$ along ζ, η and τ , respectively, and with $\theta_i^\zeta(\zeta), \theta_j^\eta(\eta)$ and $\theta_k^\tau(\tau)$ the Lagrange polynomial for ζ -, η - and τ -directions, respectively, the three dimensional Gauss-Legendre node $\hat{\boldsymbol{\xi}}_l$ and its associated Lagrange polynomial $\theta_l(\boldsymbol{\xi})$ read

$$\hat{\boldsymbol{\xi}}_l = (\hat{\zeta}_i, \hat{\eta}_j, \hat{\tau}_k); \quad \theta_l(\zeta, \eta, \tau) = \theta_i^\zeta(\zeta) \theta_j^\eta(\eta) \theta_k^\tau(\tau), \quad (3.7)$$

with index $l = \mathbf{m}(i, j, k)$.

We want to solve the following problem: find $\mathbf{q} : C_i^n \rightarrow \mathbb{R}^\delta$ such that

$$\begin{cases} \partial_t \mathbf{q} + \nabla \cdot \mathbf{F}(\mathbf{q}, \nabla \mathbf{q}) = \mathbf{f} & \text{in } C_i^n \\ \mathbf{q}|_{t=t^n} = \mathbf{w}_i^n & \text{on } \Omega_i^n \end{cases} \quad (3.8)$$

which is problem (3.1) restricted to the space-time cell C_i^n and redefined as a boundary value problem. We denote with \mathbf{q}_h as the discretized solution of (3.8). In order

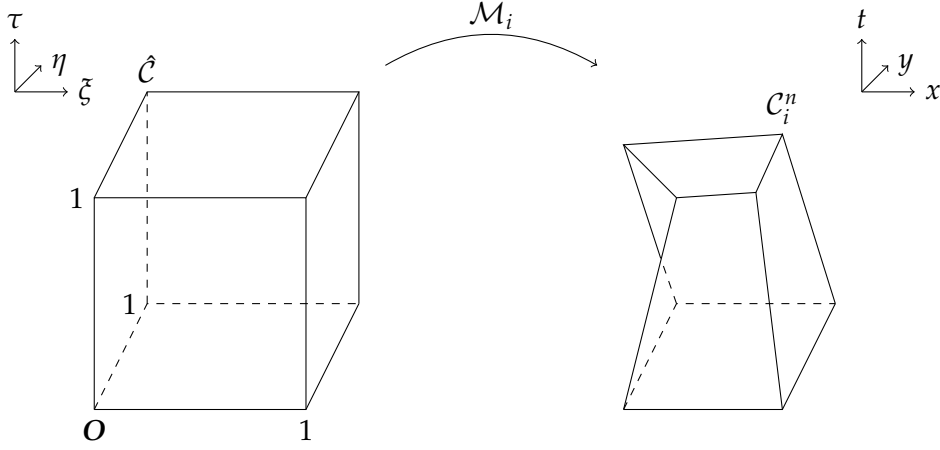


FIGURE 3.4 – Representation of the map \mathcal{M}_i from the reference space-time cell $\hat{\mathcal{C}}$ to the physical space-time cell \mathcal{C}_i^n .

to refer problem (3.8) to the reference domain $\hat{\mathcal{C}}$, we use a map $\mathcal{M}_i : \hat{\mathcal{C}} \rightarrow \mathcal{C}_i^n$

$$\mathcal{M}_i : \begin{cases} x = x(\xi, \eta, \tau) \\ y = y(\xi, \eta, \tau) \\ t = t^n + \Delta t \tau \end{cases}, \quad (3.9)$$

such that any space-time point $x \equiv (x, y, t)$ in the physical space-time cell \mathcal{C}_i^n is a function $x = x(\xi)$, with $\xi \in \hat{\mathcal{C}}$ (see Figure 3.4). Time t is considered as a linear function of τ . From map (3.9), we define the Jacobian matrix J as

$$J = \frac{dx}{d\xi} = \begin{bmatrix} x_\xi & x_\eta & x_\tau \\ y_\xi & y_\eta & y_\tau \\ 0 & 0 & \Delta t \end{bmatrix}, \quad (3.10)$$

whose inverse is

$$J^{-1} = \frac{d\xi}{dx} = \begin{bmatrix} \xi_x & \xi_y & \xi_t \\ \eta_x & \eta_y & \eta_t \\ 0 & 0 & 1/\Delta t \end{bmatrix} = \begin{bmatrix} J_s^{-1} & \Xi_t \\ \mathbf{0} & 1/\Delta t \end{bmatrix}. \quad (3.11)$$

In the above notation, we call J_s^{-1} the restriction to the spatial coordinates of the inverse of the Jacobian matrix

$$J_s^{-1} = \begin{bmatrix} \xi_x & \xi_y \\ \eta_x & \eta_y \end{bmatrix}. \quad (3.12)$$

and $\Xi_t = [\xi_t, \eta_t]^T$ the derivative of the spatial reference vector with respect to time. Through (3.12), the problem in the reference domain reads

$$\partial_\tau q + \Delta t \mathcal{F}^*(\hat{\nabla} q) + \Delta t J_s^{-T} \hat{\nabla} \cdot \mathcal{F}^{**}(q, \hat{\nabla} q) = \Delta t f, \quad (3.13)$$

where

$$\begin{aligned} \partial_t q &= \frac{\partial_\tau q}{\Delta t} + \mathcal{F}^*(\hat{\nabla} q); & \mathcal{F}^*(\hat{\nabla} q) &= \hat{\nabla} q \Xi_t; \\ \mathcal{F}^{**}(q, \hat{\nabla} q) &= F(q, J_s^{-T} \hat{\nabla} q) = (\mathcal{F}_\xi^{**}, \mathcal{F}_\eta^{**}); & \hat{\nabla} &= \begin{bmatrix} \partial_\xi \\ \partial_\eta \end{bmatrix}. \end{aligned}$$

The hat differential operators refer to reference space variables ξ and η in the reference space-time cell $\hat{\mathcal{C}}$. By abuse of notation and for sake of simplicity, we call all functions involved in both equations (3.8) and (3.13) with the same symbol (e.g., q and f) even though they take inputs in the physical space-time cell \mathcal{C}_i^n and in the reference space-time cell $\hat{\mathcal{C}}$, respectively. In order to weaken equation (3.13), the following functional space is defined:

$$\Theta = \left\{ v \in L^2(\hat{\mathcal{C}}) : (0,1)^2 \ni (\xi, \eta) \mapsto v(\xi, \eta, \tau) \in H^1((0,1)) \right\}$$

being the subspace of finite energy function space $L^2(\hat{\mathcal{C}})$ of functions in Sobolev space $H^1((0,1))$ at any fixed reference space couple (ξ, τ) . Moreover, the following notation is introduced:

$$\langle f, g \rangle = \int_{\hat{\mathcal{C}}} f g \, d\xi; \quad [f, g]_\tau = \int_0^1 \int_0^1 f(\xi, \eta, \tau) g(\xi, \eta, \tau) \, d\xi. \quad \forall f \in \Theta, \quad \forall g \in \Theta^D.$$

with $D = 1, \dots, \delta$. For our purposes, functional space Θ is identified as a test space and the following trial functional spaces is defined:

$$Q = \left\{ v \in H^1(\hat{\mathcal{C}}) : v(\xi, \eta, 0) = w_k^n \wedge J^{-1} \left[\hat{\nabla} v \right] \in L^2(\hat{\mathcal{C}}; \mathbb{R}^3) \right\},$$

where w_k is the k -th component of the interpolated polynomial w^n . By multiplying left and right side of (3.13) by a generic test function $\theta \in \Theta$ and by integrating over the reference space-time cell $\hat{\mathcal{C}}$, the problem reads: *find $q \in Q^\delta$ such that*

$$[\theta, q]_1 - \langle \partial_\tau \theta, q \rangle + \Delta t \langle \theta, \mathcal{F}^*(\hat{\nabla} q) \rangle + \Delta t \langle \theta, J_s^{-T} \hat{\nabla} \cdot \mathcal{F}^{**}(q, \hat{\nabla} q) \rangle = \Delta t \langle \theta, f \rangle + [\theta, w^n]_0 \quad (3.14)$$

$\forall \theta \in \Theta$, with $[\theta, w^n]_0 = \int_0^1 \int_0^1 \theta(\xi, \eta, 0) w^n(\xi, \eta) \, d\xi$. For the Galerkin solution q_h and the convective-diffusive terms \mathcal{F}^* and \mathcal{F}^{**} in the reference domain, a Lagrangian polynomial expansion is performed, i.e., by adopting the Einstein's notation, $q_h = \theta_l \hat{q}_l$ and $\mathcal{F}_h^* = \theta_l \hat{\mathcal{F}}_l^*$, with $\star = *, **$, where $\hat{q}_l = q(\hat{\xi}_l)$ and $\hat{\mathcal{F}}_l^* = \mathcal{F}^*|_{\hat{\xi}_l}$. Considering as the test function the k -th Lagrangian polynomial θ_k and by using the Lagrange expansion, we rewrite equation (3.14) as:

$$\begin{aligned} & ([\theta_k, \theta_l]_1 - \langle \partial_\tau \theta_k, \theta_l \rangle) \hat{q}_l + \Delta t \langle \theta_k, \theta_l \rangle \hat{\mathcal{F}}_l^* + \Delta t \langle \theta_k, (\xi_x \partial_\xi + \eta_x \partial_\eta) \theta_l \rangle \hat{\mathcal{F}}_{\xi,l}^{**} \\ & + \Delta t \langle \theta_k, (\xi_y \partial_\xi + \eta_y \partial_\eta) \theta_l \rangle \hat{\mathcal{F}}_{\eta,l}^{**} = \Delta t \langle \theta_k, f \rangle + [\theta_k, w^n]_0, \end{aligned} \quad (3.15)$$

for any $k = 1, \dots, 27$.

In the left hand side of (3.15), we remark that the arising matrices have a sparse pattern due to the L^2 -orthogonality of the Lagrangian basis (e.g. the mass matrix by $\langle \theta_k, \theta_l \rangle$ is diagonal). Matrices involving the derivatives of the map \mathcal{M}_i , i.e. $\langle \theta_k, (\xi_x \partial_\xi + \eta_x \partial_\eta) \theta_l \rangle$ and $\langle \theta_k, (\xi_y \partial_\xi + \eta_y \partial_\eta) \theta_l \rangle$, cannot be explicitly computed before finding the map itself. On the contrary, the components which do not involve the map, namely $([\theta_k, \theta_l]_1 - \langle \partial_\tau \theta_k, \theta_l \rangle)$ and $\langle \theta_k, \theta_l \rangle$, can be pre-computed once for all before solving problem (3.15). In appendix Section C.1 it is described how to compute the matrices of (3.15).

In equation (3.15) the convective-diffusive terms \mathcal{F}^* and \mathcal{F}^{**} are implicitly defined by the solution q_h . For this reason a fixed point problem is solved: let r be the index

of the fixed point iteration, therefore we solve q_h^{r+1}

$$\begin{aligned} &([\theta_k, \theta_l]_1 - \langle \partial_\tau \theta_k, \theta_l \rangle) \hat{q}_l^{r+1} + \Delta t \langle \theta_k, \theta_l \rangle \hat{\mathcal{F}}_l^{*,r} + \Delta t \langle \theta_k, (\xi_x \partial_\xi + \eta_x \partial_\eta) \theta_l \rangle \hat{\mathcal{F}}_{\xi,l}^{*,r} \\ &+ \Delta t \langle \theta_k, (\xi_y \partial_\xi + \eta_y \partial_\eta) \theta_l \rangle \hat{\mathcal{F}}_{\eta,l}^{*,r} = \Delta t \langle \theta_k, f \rangle + [\theta_k, w^n]_0, \end{aligned} \quad (3.16)$$

where terms of fixed point index r are computed by using the previous solution q_h^r . In our numerical tests, the fixed point iteration stops when the $L^2(\hat{\mathcal{C}})$ -norm of residual of equation (3.16) is less than a fixed tolerance.

3.2.3 Recovery of the map and foreground mesh motion

In the previous subsection, the local map $\mathcal{M}_i : \hat{\mathcal{C}} \rightarrow \mathcal{C}_i^n$ has been involved for the computation of the local weak predictor solution. Moreover, the foreground mesh of coordinates \mathbf{X} is moving accordingly to the following motion equation:

$$\frac{d\mathbf{X}}{dt} = \mathbf{V}, \quad (3.17)$$

where $\mathbf{V} = \mathbf{V}(x, t; u)$ is the mesh velocity, eventually dependent on the solution. Equation (3.17) is closed with a Cauchy condition $\mathbf{X}(0) = \mathbf{X}_0$, which is the initial spatial configuration. Through equation (3.17), we recover the map \mathcal{M}_i for any cell at least on the foreground mesh. The motion equation (3.17) is solved through an *isoparametric* or *Lagrangian* approach by locally referring it to the same reference system as done for the local equation (3.8). This means that the spatial coordinates \mathbf{X} are considered as function of the reference coordinates, i.e. $\mathbf{X}(\xi)$, with $\xi \in \hat{\mathcal{C}}$. Finally, the solution of the referred motion equation is approximated via a Lagrangian expansion by employing the same Lagrangian basis $\{\theta_k\}_{k=1}^{27}$ built on the tensor combination of three Gauss-Legendre nodes in $(0, 1)$ along any direction as previously introduced: $\mathbf{X}_h = \theta_l \hat{\mathbf{X}}_l$, with $\hat{\mathbf{X}}_l = \mathbf{X}(\hat{\xi}_l)$. Thus, from time t^n to t^{n+1} , the motion equation (3.17) is locally re-written as

$$\frac{d\mathbf{X}}{dt} = \mathbf{V} \text{ in } \mathcal{C}_i^n, \quad (3.18)$$

and closed by strongly imposing that the solution \mathbf{X}^n at current time is equal to $\mathbf{X}(t^n)$ found at the previous physical space-time cell \mathcal{C}_i^{n-1} . The local motion equation (3.18) is weakened in a similar way to the local equation (3.8) and in algebraic form it reads

$$([\theta_k, \theta_l]_1 - \langle \partial_\tau \theta_k, \theta_l \rangle) \hat{\mathbf{X}}_l = \Delta t \langle \theta_k, \theta_l \rangle \hat{\mathbf{V}}_l + [\theta_k, \theta_l]_0 \hat{\mathbf{X}}_l^n, \quad (3.19)$$

with $\hat{\mathbf{V}}_l = \mathbf{V}|_{\hat{\xi}_l}$. The last term $[\theta_k, \theta_l]_0 \hat{\mathbf{X}}_l^n$ takes into account the initial given configuration of the space at time t^n .

When the mesh is neither moving nor deforming, as for cells in the background, the mesh velocity is thus coincident with zero, i.e. $\mathbf{V} \equiv \mathbf{0}$. In that case, the map is known *a priori* and it consists in the re-scaling of the reference space-time cell $\hat{\mathcal{C}}$ to the physical space-time cell \mathcal{C}_i^n :

$$\begin{cases} x = x(\xi) = x_{i-1/2} + h_i^x \xi \\ y = y(\eta) = y_{i-1/2} + h_i^y \eta \end{cases}, \quad (3.20)$$

where coordinates $x_{i-1/2}$ and $y_{i-1/2}$ and $x_{i+1/2}$ and $y_{i+1/2}$ define the extremes along x - and y -direction of the physical space-time cell

$$\mathcal{C}_i^n \equiv [x_{i-1/2}, x_{i+1/2}] \times [y_{i-1/2}, y_{i+1/2}] \times [t^n, t^{n+1}];$$

and h_i^x and h_i^y are the length along x and y of the cell, respectively, i.e. $h_i^x = x_{i+1/2} - x_{i-1/2}$ and $h_i^y = y_{i+1/2} - y_{i-1/2}$.

Since the mesh motion equation (3.17) is essentially solved via a sort of Discontinuous Galerkin (DG) approach, possible numerical (and non physical) discontinuities could arise. As a matter of fact, for a given vertex $\bar{\mathbf{X}}_k^{n+1}$ shared by a set of spatial cells $\{\Omega_i^{n+1}\}_{i \in \mathcal{Z}_k^{n+1}}$ at time t^{n+1} , there could be as many different values of the vertex, namely $\{\bar{\mathbf{X}}_{k,i}^{n+1}\}_{i \in \mathcal{Z}_k^{n+1}}$, for any map \mathcal{M}_i referring to the cell \mathcal{C}_i^n to which Ω_i^{n+1} belongs. The set \mathcal{Z}_k^{n+1} collects the index(es) of the cells sharing the vertex $\bar{\mathbf{X}}_k^{n+1}$. The cardinality N_k of set $\{\Omega_i^{n+1}\}_{i \in \mathcal{Z}_k^{n+1}}$, coinciding with the cardinality of the indexes set \mathcal{Z}_k^{n+1} , depends on the position of the vertex $\bar{\mathbf{X}}_k^{n+1}$ on the foreground mesh: it is either 1 or 2 if the vertex is on the boundary of the mesh, otherwise it is 4. For this reason we consider a weighted average value for the shared vertex in order to tackle the possible arising discontinuities. As suggested in [24], we first consider a weighted velocity $\bar{\mathbf{V}}_k^{n+1}$ corresponding to the vertex $\bar{\mathbf{X}}_k^{n+1}$

$$\bar{\mathbf{V}}_k^{n+1} = \frac{1}{N_k} \sum_{i \in \mathcal{Z}_k^{n+1}} \bar{\mathbf{v}}_{k,i}^{n+1}, \text{ with } \bar{\mathbf{v}}_{k,i}^{n+1} = \int_0^1 \theta_l(\zeta^*, \eta^*, \tau) \, d\tau \hat{\mathbf{V}}_{l,i}, \quad (3.21)$$

where coordinates (ζ^*, η^*) depend on the position of the coordinate $\bar{\mathbf{X}}_k^{n+1}$ in the cell Ω_i^{n+1} ; it can assume four values: $(0,0)$, $(1,0)$, $(1,1)$ and $(0,1)$. Once equation (3.19) is solved, the just found coordinates $\{\hat{\mathbf{X}}_l\}_{l=1}^{27}$ are used for computing the velocity components $\hat{\mathbf{V}}_{l,i}$ and, thus, the weighted velocities $\bar{\mathbf{v}}_{k,i}^{n+1}$ in (3.21). Finally, the coordinates $\bar{\mathbf{X}}_k^{n+1}$ at time t^{n+1} is

$$\bar{\mathbf{X}}_k^{n+1} = \bar{\mathbf{X}}_k^n + \Delta t \bar{\mathbf{V}}_k^{n+1}. \quad (3.22)$$

We refer the reader to [41] for another definition of the weighted vertex velocities $\bar{\mathbf{V}}_k^{n+1}$ in (3.21) where the Voronoi neighborhood parameters of any vertex are exploited.

In Algorithm 3.2 we resume the salient stages of the prediction step.

Algorithm 3.2 Prediction step

- 1: Compute the foreground mesh motion (3.22) from the motion equation (3.17) and through the weighted velocity (3.21);
 - 2: **for** $i = 1, \dots, N$ **do**
 - 3: Find the map \mathcal{M}_i for the space-time cell \mathcal{C}_i^n ;
 - 4: Compute the Jacobian matrix J associated to \mathcal{M}_i ;
 - 5: Compute J^{-1} and take the submatrix J_s^{-1} to the spatial coordinates defined in (3.12);
 - 6: Update the convective-diffusive terms \mathcal{F}^* and \mathcal{F}^{**} in the reference domain;
 - 7: Evolve the local predictor solution through (3.15);
-

3.2.4 Correction stage: the finite volume scheme over the space-time cell

Once the local predictor solution \mathbf{q}_h is computed in each space-time cells \mathcal{C}_i^n , we can perform the correction stage. First, we rewrite the convective-diffusive equation (3.1) in divergence form. Let $\nabla_{x,t} = [\nabla, \partial_t]^T$ be the space-time differential operator and let $\mathbf{U} = [F(\mathbf{u}, \nabla \mathbf{u}), \mathbf{u}]^T$ be the space-time solution, thus problem (3.1) can be rewritten as

$$\nabla_{x,t} \cdot \mathbf{U} = \mathbf{f} \quad \text{in } \Omega(t) \times [0, T]. \quad (3.23)$$

We want to find a finite volume solution for the above equation, where the finite volume is the space-time cell \mathcal{C}_i^n , whose boundary reads

$$\partial \mathcal{C}_i^n = \Omega_i^n \cup \Omega_i^{n+1} \cup \bigcup_{j=1}^4 \Gamma_{ij}^n, \quad (3.24)$$

where the boundaries Γ_{ij}^n , $j = 1, \dots, 4$, are the space-time boundaries of \mathcal{C}_i^n linking any edge of Ω_i^n at time t^n to any edge of Ω_i^{n+1} at time t^{n+1} . By integrating equation (3.23) over \mathcal{C}_i^n and by applying the divergence theorem to the left side, we obtain

$$\int_{\partial \mathcal{C}_i^n} \mathbf{U} \cdot \mathbf{n}_{x,t} \, d\Gamma = \int_{\mathcal{C}_i^n} \mathbf{f} \, d\mathcal{C}, \quad (3.25)$$

with $\mathbf{n}_{x,t}$ being the normal unit vector to the boundary $\partial \mathcal{C}_i^n$ of the cell. Let \mathbf{U}_i^n be the spatial average of the solution u of (3.1) over the spatial cell Ω_i^n and located on its center, i.e.,

$$\mathbf{U}_i^n = \frac{1}{|\Omega_i^n|} \int_{\Omega_i^n} \mathbf{u}(x, y, t^n) \, dx \, dy, \quad (3.26)$$

where $|\Omega_i^n|$ is the measure of the spatial cell Ω_i^n . Though (3.24) and (3.26), equation (3.25) explicitly is

$$-|\Omega_i^n| \mathbf{U}_i^n + |\Omega_i^{n+1}| \mathbf{U}_i^{n+1} + \sum_{j=1}^4 \int_{\Gamma_{ij}^n} \mathbf{U} \cdot \mathbf{n}_{x,t} \, d\Gamma = \int_{\mathcal{C}_i^n} \mathbf{f} \, d\mathcal{C}, \quad (3.27)$$

where the unknown is the average solution \mathbf{U}_i^{n+1} at time t^{n+1} , while the last term of the left hand side is the space-time flux along the space-time sides $\bigcup_{j=1}^4 \Gamma_{ij}^n$. Scheme (3.27) is the Finite Volume scheme; we remark that it is still exact. In order to solve (3.27), we need to approximate the integral function of the space-time flux. Among the several methods proposed in the literature (such as in [41, 38, 39, 109, 59]), we here present a Local Lax-Friedrichs (LLF) approach:

$$[\mathbf{U} \cdot \mathbf{n}_{x,t}]_{\Gamma_{ij}^n} \approx \Phi(\mathbf{q}_j^+, \mathbf{q}_j^-) = \frac{1}{2} (\mathbf{U}_j^+ + \mathbf{U}_j^-) \cdot \mathbf{n}_{x,t} - \frac{s}{2} (\mathbf{q}_j^+ - \mathbf{q}_j^-), \quad (3.28)$$

where $\mathbf{U}_j^+ = \mathbf{U}(\mathbf{q}_j^+)$ and $\mathbf{U}_j^- = \mathbf{U}(\mathbf{q}_j^-)$ are the space-time solution of (3.23) computed by solutions \mathbf{q}_j^+ and \mathbf{q}_j^- , which represent the local predictor solutions outside and inside the cell, respectively, with respect to the space-time side Γ_{ij}^n . The term s is the stabilization coefficient. Equation (3.27) with the flux approximation (3.28) closes the correction stage of the ADER method. At the end of this stage, a solution u_i^{n+1} is found over any cell Ω_i^{n+1} . Since the predictor solution over space-time cells \mathcal{C}_i^{n+1} needs to be evaluated over the Gauss nodes, a second order local polynomial interpolation is performed as explained in Section 3.2.1.

For the computation of the integrals along the space-time manifolds Γ_{ij}^n , we still use the previously computed map \mathcal{M}_i . As a matter of fact, for a generic function $g : \mathcal{C}_i^n \rightarrow \mathbb{R}$ it holds:

$$\int_{\Gamma_{ij}^n} g(\mathbf{x}) \, d\Gamma = \int_{\hat{\Gamma}_j} g(\mathbf{x}(\boldsymbol{\xi})) |\text{Cof}(J) \hat{\mathbf{n}}_j| \, d\hat{\Gamma},$$

where $\hat{\Gamma}_j$ is the j -th lateral side of the reference cubic domain $\hat{\mathcal{C}}$ of unit outer normal $\hat{\mathbf{n}}_j$, $\Gamma_{ij}^n = \mathcal{M}_i(\hat{\Gamma}_j)$ and $\text{Cof}(J)$ is the cofactor matrix of the Jacobian tensor J of the map (see Section C.1 for the formal definition of the cofactor matrix of the Jacobian).

Concerning the time step Δt , due to the combination of the weak predictor solution by problem (3.14) and the consequent plug of this solution in the finite volume scheme (3.27) through the LLF flux (3.28), a classical stability analysis is not evident. We assumed the time step to be

$$\Delta t = \text{CFL} \frac{h}{\max\{\sup_{\Omega \times [0, T]} |a_x|, \sup_{\Omega \times [0, T]} |a_y|\}}, \quad (3.29)$$

where h is the smallest characteristic length among all cells (both of background and foreground meshes) along the whole temporal window $[0, T]$, i.e., $h = \min_{i, n} h_i^n$, with h_i^n the characteristic length of spatial cell Ω_i^n at discrete time t^n . Coefficient CFL in (3.29) is the Courant-Friedrichs-Lewy number. In this thesis, the CFL coefficient is experimentally sought by conducting an empirical analysis in Section 3.4.2.

3.2.5 Dynamics of the overlapping zone

During the simulation, the foreground mesh moves and, consequently, the background mesh changes its configuration in the zone of the overlapping as well as in the hole. Let $\Omega_i(t)$ be a background cell in a neighborhood of the overlapping. From times t^n to t^{n+1} , there are three possibilities:

1. Cell $\Omega_i(t)$ is present at time t^n and it disappears at time t^{n+1} because the hole completely covers it;
2. Cell $\Omega_i(t)$ is not present at time t^n but it appears at time t^{n+1} because the hole gets away;
3. The overlapping zone does not drastically change its configuration with respect to cell $\Omega_i(t)$, thus the cell is present at time t^n and it still continues to be present at time t^{n+1} .

The third case is trivial. For the first case, the predictor solution is executed in order to compute the fluxes of the neighboring cells even though the correction stage is not performed. For the second case, information u_i^n is missing and it is necessary for computing u_i^{n+1} . For this reason, let N_1 the total number of background cells (those ones in the hole included). Consequently $i \leq N_1$. By recalling that the order of foreground cells starts from $N_1 + 1$, we look for an index $j > N_1$ such that

$$\mathbf{x}_j = \arg \min_{k > N_1} \|\mathbf{x}_i - \mathbf{x}_k\|, \quad (3.30)$$

where \mathbf{x}_μ is the center of mass of cell Ω_μ^n , for $\mu = i, j, k$. Then, a local polynomial interpolation w_j^n on the stencil \mathcal{S}_j centered on cell Ω_j^n of the foreground mesh is computed as previously explained in Section 3.2.1. In particular, since Ω_j^n is chosen

to be as the closest foreground cell to background cell Ω_i^n through (3.30), a third order polynomial approximation of solution u^n on x_i is ensured by imposing $u_i^n = w_j^n(x_i)$. Finally the ADER prediction-correction is performed as usual.

3.3 The stabilization of the scheme

For the definition of the coefficient s in (3.28), there are different approaches leading to different definitions. Here we analyse two stabilization coefficients, i.e. the advective-diffusive term s_{AD} and the just advective term s_A . For the sake of clarity and to lighten the notation, we consider a two-dimensional scalar solution in this section (i.e., $d = 2$ and $\delta = 1$). In Section C.2 there is a sketch of proof for the formal CFL value for the 1D case in the case of a diffusive-dominant dynamics.

3.3.1 The local advective-diffusive stabilization term

For the definition of the coefficient s_{AD} in (3.28), we study a relaxed hyperbolic form of the parabolic equation (3.23). Let us consider the following relaxation by Cattaneo (we refer to [111] and its references for further details): let $0 < \varepsilon \ll 1$ be a relaxed time and consider variables v and w in $\Omega \times [0, T]$ such that

$$\partial_t v = \frac{1}{\varepsilon}(\partial_x u - v); \quad \partial_t w = \frac{1}{\varepsilon}(\partial_y u - w). \quad (3.31)$$

Relations (3.31) define the relaxations in the sense that $\partial_x u \rightarrow v$ and $\partial_y u \rightarrow w$ in the limit of a vanishing ε . Since the flux has to be computed along the manifold Γ_{ij}^n in the space-time continuum, let us consider solution u and all its first derivatives as *stationary solutions* with respect to a pseudo-time $t \in \mathbb{R}_+$. Thus, let $u(t; x, y, t) = [u, v, w]^T$ be the formal definition of the relaxed hyperbolic system with respect to pseudo-time t . It holds $\partial_t u = 0$. The conservative form problem (3.23) in quasi-linear form is

$$\partial_t u + \partial_x(Au) + \partial_y(Bu) + \partial_t(Cu) = f \quad \text{in } \mathbb{R}_+ \times \Omega(t) \times [0, T], \quad (3.32)$$

where A, B and C are 3×3 matrices (eventually involving the solution u among their components if the original problem is nonlinear) and the force term

$$f = [f, -v/\varepsilon, -w/\varepsilon]^T.$$

In particular, A and B always depend on the relaxation time ε and they are defined by the convection-diffusion term $\mathcal{F}(u, \nabla u)$ and C is always the identity matrix if the Cattaneo relaxation (3.31) is employed. In order to study the differential operator in (3.32), let us consider a vanishing force term, i.e. $f \equiv 0$. The presence of the pseudo-time t in (3.32) helps in treating the real time variable t as any other spatial variable x and y . When the force term in (3.32) is null, the problem is hyperbolic if the spectrum of matrix $\mathcal{A} = n_x A + n_y B + n_t C$ is real for any choice of real values n_x, n_y and n_t . If the hyperbolicity is ensured, the relaxed hyperbolic system has a planar wave solution propagating in the space-time continuum $\Omega \times [0, T]$. In particular, if $\mathbf{n}_{x,t} = [n_x, n_y, n_t]^T$ is a particular direction in the space-time continuum, the eigenvalues of \mathcal{A} define the speeds of propagation of the solution along the principal directions defined by the eigenvectors of \mathcal{A} . For this reason, in the perspective of an upwind stabilization, the local stabilization term s_{AD} in (3.28) is equal to the maximum speed of propagation of the wave, as it happens for the LLF flux approximation

for a generic hyperbolic problem of a propagating wave in the space continuum. Here we detail the previous analysis for the convection-diffusion problem with the convective field $\mathbf{a} = [a_x, a_y]^T$ and the diffusive term ν depending on space x and time t and eventually the solution u itself if a non-linearity leads the dynamics of the equation. In this case, the matrices of the quasi-linear problem (3.32) read

$$A = \begin{bmatrix} a_x & -\nu & 0 \\ -1/\varepsilon & 0 & 0 \\ 0 & 0 & 0 \end{bmatrix}, \quad B = \begin{bmatrix} a_y & 0 & -\nu \\ 0 & 0 & 0 \\ -1/\varepsilon & 0 & 0 \end{bmatrix}, \quad C = \begin{bmatrix} 1 & 0 & 0 \\ 0 & 1 & 0 \\ 0 & 0 & 1 \end{bmatrix}.$$

Consequently, the spectrum $\rho(\mathcal{A})$ of matrix \mathcal{A} is

$$\rho(\mathcal{A}) = \left\{ n_t; \frac{1}{2} \left[\sigma \pm \sqrt{\left(a_x^2 + \frac{4\nu}{\varepsilon} \right) n_x^2 + 2a_x a_y n_x n_y + \left(a_y^2 + \frac{4\nu}{\varepsilon} \right) n_y^2} \right] \right\}, \quad (3.33)$$

where $\sigma = (\mathbf{a} \cdot \mathbf{n} + 2n_t) / \sqrt{n_x^2 + n_y^2}$ and $\mathbf{n} = [n_x, n_y]^T$. Parameter σ is normalized with respect to the spatial directions in order to make spectrum $\rho(\mathcal{A})$ dimensionally consistent. The following proposition finally defines the advective-diffusive stabilization parameter.

Proposition 3.3.1. *For the advection-diffusion problem (3.1) with the convective field $\mathbf{a} = [a_x, a_y]^T$ and the diffusive term ν , the advection-diffusion stabilization coefficient s_{AD} is chosen to be the absolute value of the maximum of spectrum (3.33), i.e.,*

$$s_{AD} = \max |\rho(\mathcal{A})| = \frac{1}{2} \left| \sigma + \sqrt{\left(a_x^2 + \frac{4\nu}{\varepsilon} \right) n_x^2 + 2a_x a_y n_x n_y + \left(a_y^2 + \frac{4\nu}{\varepsilon} \right) n_y^2} \right|. \quad (3.34)$$

Since the spectrum $\rho(\mathcal{A}) \subset \mathbb{R}$ for any nonnegative ε , it yields the relaxed system (3.32) is always hyperbolic for any nonnegative ε .

3.3.2 The choice of the relaxation time

For the definition of the advective-diffusive stabilization term s_{AD} , we considered the relaxed hyperbolic system (3.32) deriving from the parabolic problem (3.23) through a relaxation time ε . If we were to solve the relaxed problem instead of the original one, the approximate solution would differ from the exact solution of two errors that are added together: the numerical error (typical of the scheme) and a relaxation error. For a linear problem, these errors have been investigated by Montecinos and Toro in [111]. The error $|u_{\text{hip}} - u|$ between the hyperbolized solution u_{hip} and the original solution u is $\mathcal{O}(\varepsilon)$ [83]. Thus, if $u_{\text{hip},h}$ is a numerical approximation of the exact relaxation solution u_{hip} , the error $|u_{\text{hip},h} - u_{\text{hip}}|$ is $\mathcal{O}(h_0^p)$, with p the order of the method (i.e., $p = 2$ in this thesis), and h_0 the maximum characteristic length of cells $\Omega_i(t)$'s. However, the goal is to choose a relaxation time ε such that the relaxation error is always dominated by or, at least, comparable to the numerical error, i.e. $\mathcal{O}(\varepsilon) \lesssim \mathcal{O}(h_0^p)$. The following theoretical result can help in fulfilling our task.

Proposition 3.3.2. *The solution u of the original parabolic problem (3.23) is approximated by a relaxed solution u_{hip} solving the relaxed problem (3.32) with accuracy p for all relaxation*

time ε and characteristic length cell h_0 satisfying

$$\frac{\mathcal{O}(\varepsilon)}{\mathcal{O}(h_0^p)} = \mathcal{O}\left(\frac{\varepsilon}{h_0^p}\right) = C_p \frac{\varepsilon}{h_0^p} = \mathcal{O}(1), \quad (3.35)$$

with

$$C_p = \frac{1 - 2^{-\frac{1}{2}}}{2^{p-\frac{1}{2}} - 1}.$$

The following proof of Proposition 3.3.2 was originally proposed in Section 2.4.1 of [80].

Proof. Since it holds $u_{\text{hip}} - u = \mathcal{O}(\varepsilon)$ and $u_{\text{hip},h} - u_{\text{hip}} = \mathcal{O}(h^p)$, for a generic mesh whose characteristic length h , we obtain

$$u_{\text{hip},h} - u = u_{\text{hip}} - u + \mathcal{O}(h^p), \quad (3.36)$$

which allows to relate the formulation error and the numerical error as

$$\mathcal{O}(h^r) = \mathcal{O}(\varepsilon) + \mathcal{O}(h^p), \quad (3.37)$$

where r is the order of accuracy by which the numerical scheme approximates the solution of the original AD problem. Note that the numerical error can be expressed as

$$\mathcal{O}(h^r) = \kappa h^r, \quad (3.38)$$

with κ depending on the problem to be solved but not on the mesh spacing h .

Let u_{hip,h_k} be the hyperbolic numerical solution referring to a mesh spacing h_k . Therefore, from (3.37) and (3.38), on two successive meshes characterized by cell lengths h_k and h_{k+1} , we obtain

$$\left(\frac{h_k}{h_{k+1}}\right)^r = \frac{\mathcal{O}(\varepsilon) + \mathcal{O}(h_k^p)}{\mathcal{O}(\varepsilon) + \mathcal{O}(h_{k+1}^p)}. \quad (3.39)$$

After some manipulations, it holds

$$\left(\frac{h_k}{h_{k+1}}\right)^r = \left(\frac{h_k}{h_{k+1}}\right)^p \alpha, \quad (3.40)$$

with

$$\alpha = \frac{\frac{\mathcal{O}(\varepsilon)}{\mathcal{O}(h_k^p)} + \mathcal{O}(1)}{\frac{\mathcal{O}(\varepsilon)}{\mathcal{O}(h_{k+1}^p)} + \mathcal{O}(1)}. \quad (3.41)$$

With no loss of generality, let us assume $h_k = 2h_{k+1}$. Taking the logarithm in (3.40), we obtain

$$r = p + \frac{\log \alpha}{\log 2}. \quad (3.42)$$

Let us now assume that given an expected order of accuracy p , we consider that the numerical scheme yields this accuracy if $r \geq p - 1/2$. Therefore, the order of accuracy for the AD problem attains the one of the hyperbolic problem when

$$-\frac{1}{2} < \frac{\log \alpha}{\log 2}. \quad (3.43)$$

Because of the monotonicity of the logarithm, the above expression is equivalent to

$$\frac{1}{\sqrt{2}} < \alpha, \quad (3.44)$$

which yields

$$\frac{1}{\sqrt{2}} \left(2^p \frac{\mathcal{O}(\varepsilon)}{\mathcal{O}(h_k^p)} + \mathcal{O}(1) \right) < \frac{\mathcal{O}(\varepsilon)}{h_k^p} + \mathcal{O}(1), \quad (3.45)$$

or

$$\frac{\mathcal{O}(\varepsilon)}{\mathcal{O}(h_k^p)} < \mathcal{O}(1) \left(\frac{1 - 2^{-1/2}}{2^{p-1/2} - 1} \right). \quad (3.46)$$

By hypothesis,

$$\frac{\mathcal{O}(\varepsilon)}{\mathcal{O}(h_k^p)} = \mathcal{O} \left(\frac{\varepsilon}{h_k^p} \right) = C \frac{\varepsilon}{h_k^p}, \quad (3.47)$$

with C to be determined. Moreover, it holds

$$C \frac{\varepsilon}{h_k^p} = \mathcal{O}(1), \quad (3.48)$$

or

$$C \varepsilon 2^{\bar{n}p} = \mathcal{O}(1), \quad (3.49)$$

noting that it is possible to set $h = 2^{-\bar{n}}$, where $\bar{n} = \log_2(1/h_0)$. From (3.46), for all $\bar{n} \geq 0$ we set

$$C \varepsilon \leq \frac{1}{2^{\bar{n}p}} \left(\frac{1 - 2^{-1/2}}{2^{p-1/2} - 1} \right) \leq \frac{1 - 2^{-1/2}}{2^{p-1/2} - 1}. \quad (3.50)$$

For convenience we take $C \leq C_{\max}/\varepsilon$, as to maintain order $\mathcal{O}(1)$. Thus, we have

$$C_{\max} := \varepsilon \frac{1 - 2^{-1/2}}{2^{p-1/2} - 1}. \quad (3.51)$$

This way, a sufficiency condition to maintain accuracy solving the AD problem for a given mesh of size h is given by

$$\frac{\varepsilon}{h^p} C_p = \mathcal{O}(1), \quad (3.52)$$

where $C_p := C_{\max}/\varepsilon$. □

As a consequence, there is the following corollary.

Corollary 3.3.1. *For a given mesh whose characteristic length is h_0 and a numerical method of order p for solving the hyperbolized problem (3.32) derived by the original parabolic problem (3.23), the optimal relaxation time ε_p is*

$$\varepsilon_p = \frac{\mathcal{O}(1)h_0^p}{C_p}. \quad (3.53)$$

We remark that, if a relaxation time ε is chosen to be less than or equal to ε_p , the numerical error dominates the relaxation error; on the contrary, if a relaxation time ε is chosen to be greater than the optimal value, the relaxation error dominates the numerical error. For this reason, in our simulation relaxation time $\varepsilon = \varepsilon_2/2$ is chosen.

3.3.3 The local advective stabilization term

In order to recover a stabilization term s_A by only considering the first order operator involved in the whole differential operator of the original problem, we can treat the equation to stabilize as a pure hyperbolic (namely just advective) problem. For this reason, the advective stabilization term s_A coincides with the maximum eigenvalue of the ALE Jacobian matrix in a spatial normal direction by excluding the diffusive component which acts on the diffusion from the advective-diffusive term $F(u, \nabla u)$ [41]. This matrix reads

$$A_{\tilde{\mathbf{n}}}^V = \sqrt{n_x^2 + n_y^2} \left[\frac{\partial F}{\partial u} \tilde{\mathbf{n}} - \mathbf{V} \cdot \tilde{\mathbf{n}} I \right], \quad (3.54)$$

where I is the identity tensor whose dimension is that one of the image space of the solution u and the unit vector $\tilde{\mathbf{n}}$ is the normalized projection of the space-time unit vector $\mathbf{n}_{x,t}$ along the spatial directions given by vector $[n_x, n_y]^T$, i.e.

$$\tilde{\mathbf{n}} = \frac{[n_x, n_y]^T}{\sqrt{n_x^2 + n_y^2}}.$$

By recalling that the recovered map \mathcal{M}_i is defined over $\bar{\mathcal{C}}$ with image in $\bar{\mathcal{C}}_i$, the space-time manifold Γ_{ij}^n , $j = 1, \dots, 4$, of the space-time cell \mathcal{C}_i can be described by only two of the three reference space-time variables (ξ, η, τ) ; i.e., by either couple (ξ, τ) , with $\eta = \bar{\eta}$, or couple (η, τ) , with $\xi = \bar{\xi}$; with $\bar{\xi}$ and $\bar{\eta}$ alternatively equal to 0 or 1, depending on the specific j -th space-time manifold Γ_{ij}^n . Let χ be the free variable (e.g. $\chi = \xi$) and $\bar{\kappa}$ be the constrained variable (e.g. $\bar{\kappa} = \eta$) for the specific manifold Γ_{ij}^n . Therefore, for a specific point $\tilde{\mathbf{x}}$ over Γ_{ij}^n it is possible to distinguish two directional vectors provided by the map \mathcal{M}_i

$$\mathbf{r}_\chi = \begin{bmatrix} x_\chi \\ y_\chi \\ 0 \end{bmatrix}_{\bar{\kappa}} \quad \text{and} \quad \mathbf{r}_\tau = \begin{bmatrix} x_\tau \\ y_\tau \\ \Delta t \end{bmatrix}_{\bar{\kappa}}.$$

The definitions of the directional vectors \mathbf{r}_χ and \mathbf{r}_τ allow to explicitly write the physical normal vector $\mathbf{n}_{x,t}$ on $\tilde{\mathbf{x}}$ as

$$\mathbf{n}_{x,t} = \frac{\mathbf{r}_\chi \wedge \mathbf{r}_\tau}{|\mathbf{r}_\chi \wedge \mathbf{r}_\tau|} \Big|_{\bar{\kappa}} = \frac{[\Delta t y_\chi, -\Delta t x_\chi, d_{\chi\tau}]^T}{\sqrt{\Delta t^2 y_\chi^2 + \Delta t^2 x_\chi^2 + d_{\chi\tau}^2}} \Big|_{\bar{\kappa}},$$

with $d_{\chi\tau} = x_\chi y_\tau - x_\tau y_\chi$. From now on we will omit the constraint variable $\bar{\kappa}$. It is now possible to write the unit vector $\tilde{\mathbf{n}}$ along the spatial directions and the velocity of the point as

$$\tilde{\mathbf{n}} = \frac{[y_\chi, -x_\chi]^T}{\sqrt{y_\chi^2 + x_\chi^2}} \quad \text{and} \quad \mathbf{V} = \frac{d\tilde{\mathbf{x}}}{dt} = \frac{[x_\tau, y_\tau]^T}{\Delta t}.$$

Consequently it holds

$$\mathbf{V} \cdot \tilde{\mathbf{n}} = \frac{-d_{\chi\tau}}{\Delta t \sqrt{y_\chi^2 + x_\chi^2}} = \frac{-n_t}{\sqrt{n_x^2 + n_y^2}}. \quad (3.55)$$

In the case of a linear problem the advective stabilization term reads

$$s_A = |a_x n_x + a_y n_y + n_t|. \quad (3.56)$$

The next proposition, through (3.55), allows to connect the advective-diffusive parameter s_{AD} with the advective parameter s_A in the limit of a vanishing diffusion parameter ν .

Proposition 3.3.3. *For linear problem (3.1), let the diffusion parameter ν go to zero, therefore the following limit holds*

$$\lim_{\nu \rightarrow 0} s_{AD} = \frac{1}{2} |\sigma + a_x n_x + a_y n_y| = |a_x n_x + a_y n_y + n_t| = s_A. \quad (3.57)$$

Proposition 3.3.3 confirms that, in the limit of small diffusion in the dynamics of linear problem (3.1), the two stabilization techniques coincide.

3.4 Numerical results

In this section we are going to present some numerical test cases in order to analyse the method.

Table 3.1 synthetically sums up the test cases that will be used for the different analyses. In particular, *test1* and *test2* (in lowercase letters) are the 1D tests and *TEST1* and *TEST2* (in capital letters) are the 2D test cases.

In the 1D tests, the foreground mesh is put in the middle between other two meshes composing the background mesh, and it deforms according to the deformation laws specified in the last row of Table 3.1. In the following, for *test1* we are not presenting a figure but only the rate of convergence. In Figure 3.5 three instants for *test2* simulation are showed; in particular, the red circle markers define the nodes of the moving foreground mesh which is in the middle between the other two meshes (in the background) whose nodes are marked by blue dots and x-symbols. The background meshes are always uniform while the foreground mesh is allowed to be displaced and deformed. The solution of *test2* is flat towards the boundaries of the computational domain and develops a moving front affected by a large spatial derivative; for this reason, the foreground mesh is set in order to follow the front. Finally we remark that, if h is the characteristic length of the cells in the background mesh, at the initial time $t = 0$ the foreground mesh is uniform with a characteristic length equal to $h/2$ in *test1* and $h/4$ for *test2*.

In *TEST1*, the foreground mesh is subjected to a deformation and rotation around its center of mass. We remark that in this case that the deformation velocity depends on the solution; in *TEST2*, the hyperbolic tangent in the exact solution describes a composed Gaussian bell whose maximum is originally located in the position $x = (-1, 0)$ and, after a time $T = \pi$, it computes a counterclockwise half rotation up to position $x = (1, 0)$ along the circumference of unit radius and centered in the origin of the axes. Due to the particular dynamics of the solution, we set a foreground mesh following the movement of the Gaussian bell. At the initial time, the foreground and background meshes in both 2D cases consist of squared cells whose sides have a length equal to h .

For all numerical tests, the time step Δt is set accordingly to (3.29) with CFL coefficient equal to 0.4. The reason of this value will be better explained in Section 3.4.2 where an empirical stability analysis is conducted.

Without reporting numerical evidences, we checked the scheme is free-stream preserving, i.e. it exactly solves a constant but nonzero solution.

3.4.1 Order of convergence

In this section we have a double goal. On one hand we want to numerically prove that the presented method is second order when an advective-diffusive LLF stabilization s_{AD} is employed. On the other hand, we want to compare this stabilization term with the local advective stabilization flux s_A . The study of the second order convergence is conducted on all test cases of Table 3.1. Finally, on the two mentioned 2D test cases the comparison of the performances for the flux approximations is carried out.

For quantifying the convergence rate, we considered the L^∞ - and L^2 -norms of the mismatch between the exact solution and the numerical solution at final time $t = T$. The errors are defined and approximated as

$$\begin{aligned} L^\infty\text{-err} &= \|u - u_{ex}\|_{L^\infty(\Omega)} = \operatorname{ess\,sup}_{x \in \Omega} |u(x, T) - u_{ex}(x, T)| \\ &\approx e_{L^\infty}^N = \max_{k=1, \dots, N} |u_k^M - u_{ex}(x_k, T)|; \end{aligned} \quad (3.58)$$

$$\begin{aligned} L^2\text{-err} &= \|u - u_{ex}\|_{L^2(\Omega)} = \sqrt{\int_{\Omega} (u(x, T) - u_{ex}(x, T))^2 \, d\Omega} \\ &\approx e_{L^2}^N [u - u_{ex}] = \sqrt{\frac{|\Omega| \sum_{k=1}^N (u_k^M - u_{ex}(x_k, T))^2}{N}}, \end{aligned} \quad (3.59)$$

and

$$\begin{aligned} |H^1|\text{-err} &= |u - u_{ex}|_{H^1(\Omega)} = \sqrt{\sum_{\alpha=1}^d \int_{\Omega} (\partial_{x_\alpha} u(x, T) - \partial_{x_\alpha} u_{ex}(x, T))^2 \, d\Omega} \\ &\approx \sqrt{\sum_{\alpha=1}^d (e_{L^2}^N [\partial_{x_\alpha} u - \partial_{x_\alpha} u_{ex}])^2}, \end{aligned} \quad (3.60)$$

respectively, where $N \approx |\Omega| h^{-1/d}$ is the number of cells such that any part of the of the domain is covered by one and only one cell at time T (with h the characteristic length of cells and $d = \dim(\Omega)$) and M is the maximum natural such that $T = M\Delta t$. Approximation (3.59) is valid only in the case of cells having approximately or exactly the same spacing. The error in H^1 -seminorm (3.60) gives a control on the convergence of the gradient of the recovered numerical solution. The convergence rate reads

$$L^p\text{-rate} = d \frac{\log(e_{L^p}^{N_1} / e_{L^p}^{N_2})}{\log(N_2 / N_1)}, \quad \text{for } p = 2, \infty, \quad (3.61)$$

for two different partition settings whose number of cells are N_1 and N_2 , respectively, with $N_1 < N_2$. The mesh refinement is performed by reducing the spacing (kept constant for any cell) and by preserving a layer of 4 cells both in background and foreground for the overlapping zone.

Table 3.2 sums up the convergence analysis for 1D test cases. In the last two columns there are the rates of convergence of the errors for both L^∞ and L^2 errors. From the analysis, the second order of the method is confirmed.

TABLE 3.1 – Summary scheme of test cases used in Sections 3.4.1 and 3.4.2. Rows *Diffusion* and *Advection* report the diffusion parameter and the advection field value(s), respectively. Rows *B.C.* and *I.C.* describe the boundary conditions and the initial conditions, respectively. The subsets defined in *fg mesh* row are those ones covered at initial time by the foreground mesh subjected to a motion equation with velocity V (last row).

	1D		2D	
	<i>test1</i>	<i>test2</i>	<i>TEST1</i>	<i>TEST2</i>
Ω	$(-1, 1)$	$(-1, 1)$	$(-\pi, \pi)^2$	$(-\pi, \pi)^2$
Diffusion	0.5	1	$6.37e-3$	$6.37e-3$
Advection	3	1	$[0.6, 0.8]^T$	$[0.6, 0.8]^T$
u_{ex}	$e^{-t} \sin(\pi(x-t))$	$\cos(\pi(t-1/2)) \tanh(10(x-t))$	$e^{-t} \cos(x) \sin(y)$	$-\tanh(2(x+\cos(t))^2 + 2(y-\sin(t))^2) +$ $-\cos(t) \cos(x) \sin(y)$
B.C.	periodic	Dirichlet: $u_{ex}(\pm 1, t)$	Dirichlet: $u_{ex}(x, y, t) _{\partial\Omega}$	Dirichlet: $u_{ex}(x, y, t) _{\partial\Omega}$
I.C.	$\sin(\pi x)$	0	$\cos(x) \sin(y)$	$-\tanh(2x^2 + 2(y-1)^2)$
T	0.25	0.5	1	π
fg mesh	$[-0.5, 0.25]$	$[-0.25, 0.25]$	$[-0.5, 0.5]^2$	$[-1.25, -0.75] \times [-0.25, 0.25]$
V	$2.5 + e^x$	$e^x \chi_{\{t \leq 0.25\}}(t) + \chi_{\{t > 0.25\}}(t)$	$[u(x, y, t) - y, u(x, y, t) + x]^T$	$[-y, x]^T$

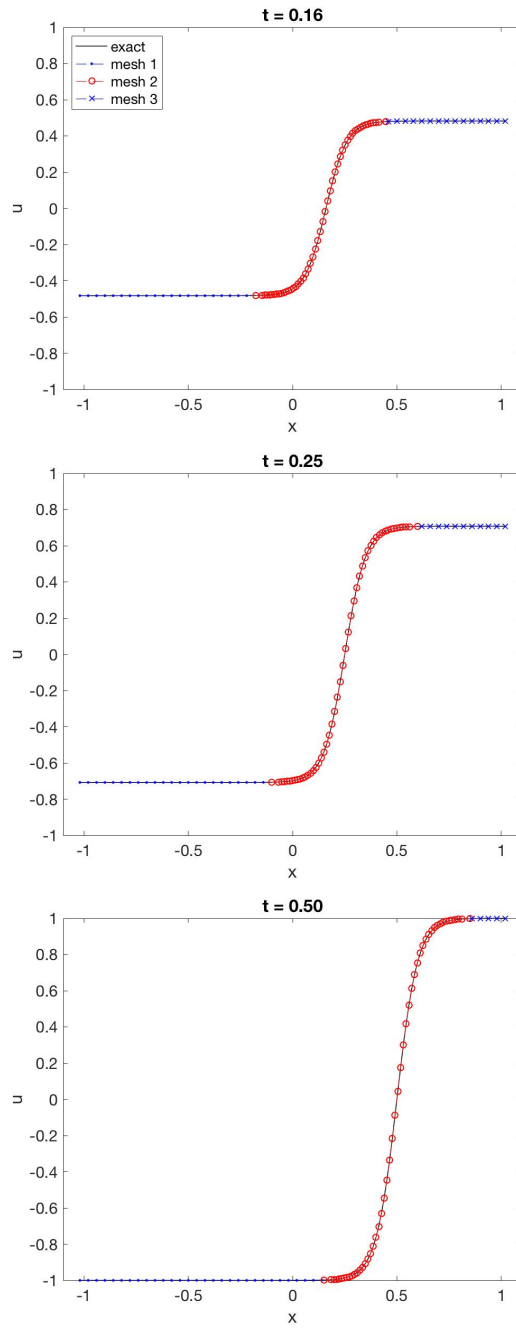


FIGURE 3.5 – Three time instants for the 1D test case *test2*. The circle markers define the nodes of the moving foreground mesh. The remaining dot and x markers are the nodes of the two background meshes.

TABLE 3.2 – Convergence analysis for 1D test cases *test1* and *test2*.

	T	h	L^∞ -err	L^2 -err	L^∞ -rate	L^2 -rate
<i>test1</i>	0.25	2.00e-2	1.2740e-3	1.3903e-3	0	0
		1.00e-2	2.5042e-4	2.9250e-4	2.37	2.79
		5.00e-3	5.6957e-5	6.6934e-5	2.15	2.14
		2.50e-3	1.3675e-5	1.6068e-5	2.06	2.06
<i>test2</i>	0.5	1.00e-2	9.2733e-4	6.3960e-4	0	0
		5.00e-3	1.1948e-4	1.0081e-4	2.88	2.60
		2.50e-3	2.1898e-5	1.6359e-5	2.49	2.67
		1.25e-3	5.6504e-6	2.8547e-6	1.96	2.44

TABLE 3.3 – Convergence analysis for 2D test cases *TEST1* and *TEST2*. Column labeled with h reports the smallest characteristic length among all cells.

	T	h	L^∞ -err		L^2 -err		L^∞ -rate		L^2 -rate	
			AD	A	AD	A	AD	A	AD	A
<i>TEST1</i>	1	3.00e-1	1.9012e-2	2.1887e-2	4.6211e-3	9.1724e-3	0	0	0	0
		1.50e-1	4.3829e-3	5.8280e-3	1.0854e-3	2.4464e-3	2.28	2.06	2.25	2.05
		7.50e-2	9.5837e-4	1.2096e-3	2.1323e-4	4.8789e-4	2.25	2.32	2.41	2.38
		3.75e-2	3.0646e-4	2.7571e-4	2.9265e-5	5.5269e-5	1.95	2.16	2.65	3.18
<i>TEST2</i>	π	3.00e-1	6.5375e-2	6.5375e-2	1.0682e-2	1.0682e-2	0	0	0	0
		2.25e-1	3.1934e-2	3.1598e-2	5.5980e-3	1.0043e-2	2.66	2.70	2.40	0.23
		1.50e-1	1.1276e-2	1.1276e-2	2.0116e-3	2.0116e-3	2.71	2.70	2.66	4.18
		1.13e-1	5.2093e-3	8.8807e-3	9.3905e-4	2.2073e-3	2.78	0.86	2.74	-0.33
		7.50e-2	2.4154e-3	3.6814e-3	3.9534e-4	8.6362e-4	1.94	2.22	2.19	2.37

In Table 3.3 we report the L^∞ - and L^2 -errors with their respective rate of convergence with respect to a local advective-diffusive (AD, white cells) and advective (A, grey cells) stabilization. We first remark that, for both cases, the errors relative to AD stabilization are slightly smaller with respect to the same errors with an A stabilization. The rate of convergence of the errors for an AD stabilization is at least 2. On the other hand, even though a second order of accuracy is also reached by employing an A stabilization, the convergence rate shows an irregular trend (especially for *TEST2*). For this reason we can state that an AD flux approximation allows to reach a more precise solution with a monotone trend for the rate of convergence with respect to the same solution with an A flux stabilization. Similar analysis follows from the convergence errors in H^1 -seminorm reported in Table 3.4.

3.4.2 Empirical analysis of stability condition

As already mentioned at the end of Section 3.2.4, the presence of a weak solution, found in the prediction step of the presented method and successively plugged into the flux of the finite volume scheme in the correction stage, makes a classical stability analysis not straightforward to be made. For this reason, we performed an empirical stability analysis by assuming that the right time step Δt allowing a stable computation is defined as in (3.29).

TABLE 3.4 – Convergence analysis for 2D test cases *TEST1* and *TEST2* in H^1 -seminorm.

T	h	$ H^1 $ -err		$ H^1 $ -rate		
		AD	A	AD	A	
<i>TEST1</i>	1	3.00e-1	3.3739e-2	5.0851e-2	0	0
		1.50e-1	7.4019e-3	1.4170e-2	2.36	1.99
		7.50e-2	1.5996e-3	3.0617e-3	2.26	2.27
		3.75e-2	3.9104e-4	4.5886e-4	2.06	2.77
<i>TEST2</i>	π	3.00e-1	1.2623e-1	1.2624e-1	0	0
		2.25e-1	6.7239e-2	8.1671e-2	2.34	1.70
		1.50e-1	2.5715e-2	2.5715e-2	2.50	2.92
		1.13e-1	1.2408e-2	1.7499e-2	2.62	1.38
		7.50e-2	6.3809e-3	8.5549e-3	1.87	1.81

TABLE 3.5 – Experimental stability analysis. For both tests, the reported CFL and Δt consist in the maximum CFL number and the maximum related time step Δt such that the method is stable. Labels A and AD underline the usage of an advective and advective-diffusive stabilization term for the LLF flux, respectively. The first column reports the space steps h used for the different simulations.

h	<i>TEST1</i>				<i>TEST2</i>			
	CFL		Δt		CFL		Δt	
	A	AD	A	AD	A	AD	A	AD
3.00e-1	0.55	0.95	2.06e-1	3.56e-1	0.75	0.95	2.81e-1	3.56e-1
1.50e-1	0.75	1.15	1.41e-1	2.16e-1	0.65	0.85	1.22e-1	1.59e-1
7.50e-2	0.75	0.95	7.03e-2	8.91e-2	0.55	0.75	5.16e-2	7.03e-2

On a given problem, once both background and foreground meshes are set, we considered a time step Δt starting from a CFL number equal to 0.1 and, by increasing this value of 0.05 each time, we look for the largest stable CFL. In particular, this process is executed on the same problem considering an approximated LLF flux employing once an advective-diffusive stabilization term s_{AD} and then with an advective stabilization term s_A .

The analysis is conducted on the 2D test cases presented in Table 3.1. In Figure 3.6 there are three time instants of both test cases.

In Table 3.5 there are the maximum CFL numbers and related maximum time steps Δt such that the method is stable. The time step Δt is computed by formula (3.29). By comparing the performances of a local advective (A) stabilization term against the same ones using a local advective-diffusive (AD) stabilization term, it is evident that an advective LLF flux always needs a smaller CFL with respect to an advective-diffusive LLF flux in order to stabilize the routine.

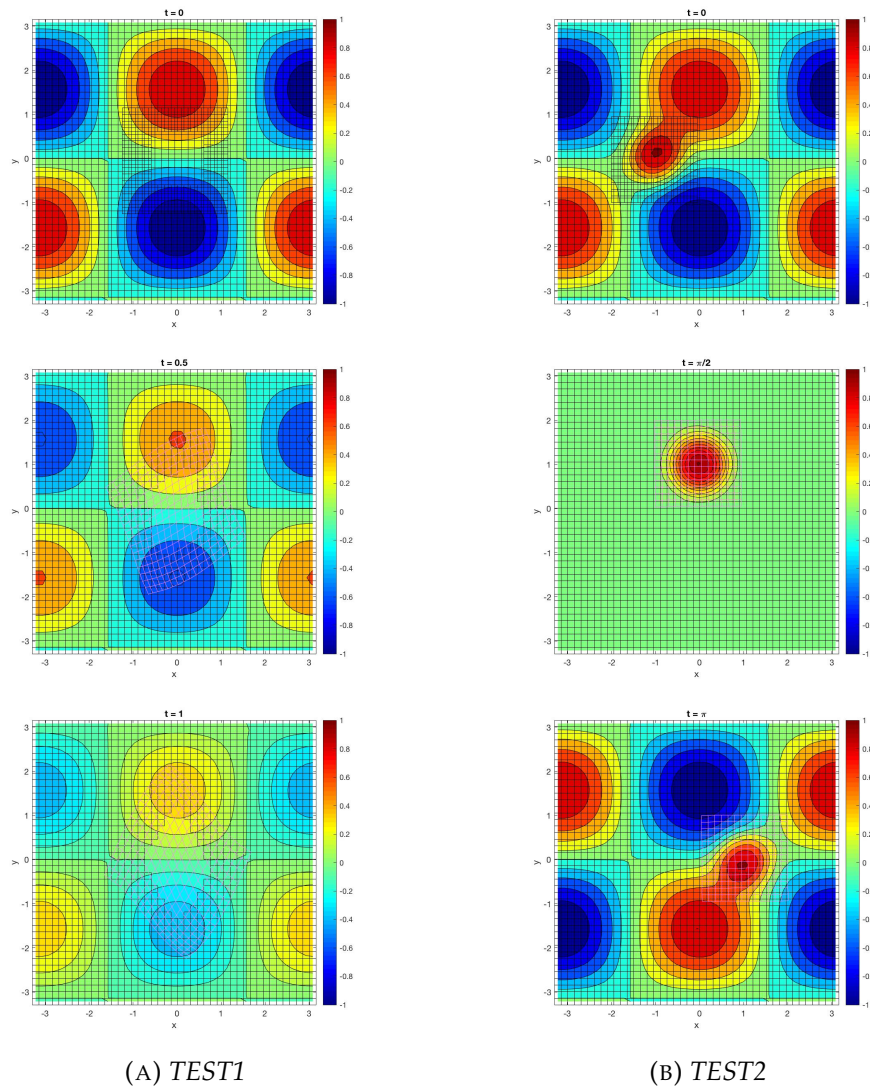


FIGURE 3.6 – Three time instants for test cases *TEST1* (a) and *TEST2* (b).

3.4.3 Relationship between the convective field and the foreground mesh velocity

From the theoretical explanation of the method, it does not emerge in any way an interaction between the speed of the foreground grid V and the intrinsic advective field a of the problem. In other words, there does not seem to be a limitation of the velocity of the mesh that is displaced and deformed in terms of stability of the method. The unique limitation of the mesh speed (see section 3.2.5) is due to the CFL condition with respect to the dimension of the single cell. In order to allow to the code to perform the automatic information transmission, the mesh speed is such that it does not allow a given fringe cell Ω_i^n in the foreground mesh to migrate beyond the boundaries of the stencil S_i centered on the cell itself in any time interval from t^n to t^{n+1} . As a matter of fact, if this process is not ensured, for those new born cells belonging to the background mesh at time t^{n+1} could not be able to recover the information from the polynomial interpolation. Consequently, the algorithm would incur a loss of information.

In this subsection we test on a numerical case that the stability is only given by the relative advective speed $a - V$ and the mesh velocity V does not affect the stability of the method in other ways. In particular, on the same linear test case, we will consider different possible movements of the foreground mesh by measuring, at final time $t = T$, the L^∞ - and L^2 -errors of the mismatch between the exact and the numerical solution. The tested case is named *TEST3* and it is summed up in Table 3.6 (top). The foreground mesh is either allowed not to move or to rigidly move in the parallel direction with respect to the abscissae axis. In particular, we consider three possibilities of movements, *P1*, *P2* and *P3*, reported and explained in Table 3.6 (bottom). We remark that test *P1* corresponds to a test case with a unique block mesh due to the position and the uniformity of the foreground mesh with respect to the background mesh. For this reason, tests *P2* and *P3* are compared with *P1*. In Figure 3.7 there are both the numerical solutions and the associated pointwise absolute values of the difference between the exact and numerical solution for the final time $T = 2$ for the configurations listed above. In particular, the configuration of the foreground mesh in Figure 3.7a (left) corresponds to the initial mesh configuration for tests *P2* and *P3* too. By visualizing the different plots of the errors, it is evident the movement of the foreground mesh introduces an error. As a matter of fact the errors of *P2* and *P3* are neither equal each other nor to the errors of *P1*. The quantitative differences among the different cases are reported in Table 3.7. Concerning test *P2*, the L^∞ -error is equal to the one of *P1*, even though the L^2 -error is the double. This distance between a steady and moving foreground mesh becomes slightly more evident at increasing of the mesh speed, as the last line of Table 3.7 shows. In any case, all the errors are comparable and this confirms that there is no relation between advective field and mesh velocity in terms of stability. The mesh velocity seems to affect the numerical solution only on the precision.

We conclude this subsection by analyzing the loss of information given by a very strong speed of the foreground mesh on the same test case. The foreground mesh is still located in the subset $[0.8, 1.2]^2$ at the initial time and moves rightwards with a speed equal to 4. This velocity, with the considered time step Δt , allows to the cells on the left side of the foreground mesh to overflow from the borders of their stencil from times t^n to t^{n+1} . In Figure 3.8 there is a comparison between the recovered numerical solution and the exact solution for $t = 0.84$ (which corresponds to that time when the right side of the moving mesh is fully aligned to the right side of the channel). There is no relation between the two solutions because the speed of the

TABLE 3.6 – On the top, features of *TEST3* are reported. On the bottom, there are the three considered movements of the foreground mesh.

<i>TEST3</i>	
Ω	$(0, 1) \times (0, 5)$
Diffusion	2e-3
Advection	$[1, 0]^T$
u_{ex}	$-\tanh(2(x-t)^2 + 5(y-1)^2) + e^{-t}(5x-x^2)(2y-y^2) + 1$
B.C.	Dirichlet: $u _{\partial\Omega} \equiv 0$
I.C.	$-\tanh(2x^2 + 5(y-1)^2) + (5x-x^2)(2y-y^2) + 1$
T	2
fg mesh	$[0.8, 1.2]^2$
V	$P1, P2, P3$

V

-
- P1* The foreground mesh is not moving for the whole period of the simulation.
-
- P2* The foreground has a constant velocity equal to the advective velocity for any time.
-
- P3* For half of the time the mesh moves with double the speed compared to the advective field and for the remaining half of the time the mesh moves with the same speed in modulus but in the opposite direction compared to the advective field.
-

TABLE 3.7 – Errors for *TEST3*. The errors refer to a characteristic length h equal to the cell of 2e-2 and a time $t = T = 2$.

	L^∞ -err	L^2 -err
<i>P1</i>	2.1554e-2	6.8500e-3
<i>P2</i>	2.1554e-2	4.8809e-3
<i>P3</i>	4.8809e-2	1.0864e-2

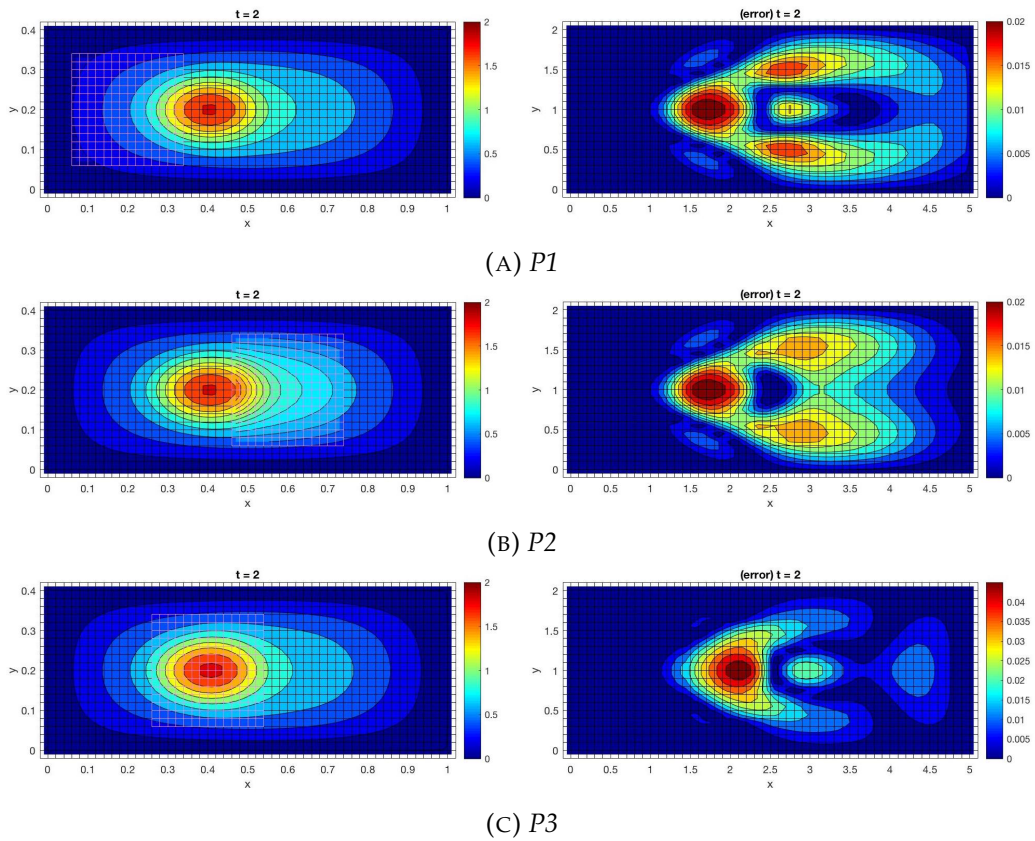


FIGURE 3.7 – The numerical solutions, on the left, at final time $t = 2$ of the three possibilities $P1$, $P2$ and $P3$ of foreground mesh movements for the $TEST3$. On the right there are the associated point-wise errors of the mismatch between the exact solution and the numerical solution.

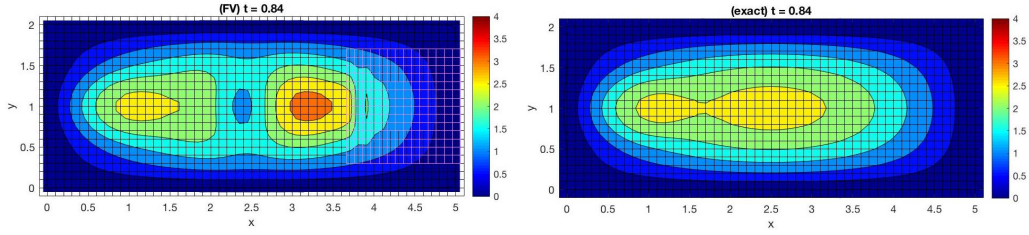


FIGURE 3.8 – Comparison between the numerical (left) and exact (right) solution of *TEST3* at time $t = 0.84$ for a moving foreground mesh traveling with a speed generating a loss of information.

foreground mesh is so fast that it does not allow the algorithm to assign the correct information about the background cells that arise in the wake of the foreground mesh itself.

3.4.4 Further topics

We conclude this section by presenting three test cases that show the potentiality of the method. Firstly, a *nonlinear advection-diffusion system* is solved; successively a *multimesh* setting of grids is considered for the already described *TEST2* (see Table 3.1); finally, we consider a test case with a *complex domain* in which the foreground mesh is employed in order to adapt its shape to the shape of the domain.

Nonlinear system

Let $\Omega = [-\pi, \pi]^2$ and $T = 0.5$ be the computational domain and the final time, respectively. Thus the problem is: *find* $\mathbf{u} : \Omega \times [0, T] \rightarrow \mathbb{R}^2$ *such that*:

$$\begin{cases} \partial_t \mathbf{u} + \nabla \cdot (\mathbf{u}\mathbf{u}^T) = \nu \Delta \mathbf{u} + \mathbf{f} & \text{in } \Omega \times [0, T] \\ \mathbf{u} \equiv \mathbf{u}_{ex} & \text{on } \partial\Omega \times [0, T], \\ \mathbf{u}(\mathbf{x}, 0) = \mathbf{u}_{ex}(\mathbf{x}, 0) & \text{in } \bar{\Omega} \times \{0\} \end{cases} \quad (3.62)$$

where the force term \mathbf{f} is chosen to have the exact solution

$$\mathbf{u}_{ex}(x, y, t) = e^{-t} \begin{bmatrix} \cos(x) \sin(y) \\ -\sin(x) \cos(y) \end{bmatrix}.$$

In problem (3.62), the diffusive term ν is equal to $5\pi \times 10^{-3}$ while the convective field is represented by the solution itself, thus the partial differential equation is nonlinear. For this problem, the convective-diffusive component \mathbf{F} is the matrix $\mathbf{u}\mathbf{u}^T - \nu \nabla \mathbf{u}$. The foreground mesh is originally located around the center of mass of the whole domain and it is allowed to rigidly counterclockwise rotate. In Figure 3.9 there are the two components of the numerical solution at final time $t = T$.

The error and convergence analysis is conducted as for the already presented linear test cases by comparing the performances of the flux discretization either with local advective-diffusive or just advective stabilization term. For this reason, Table 3.8 reports the L^∞ and L^2 errors and convergence rates by decreasing four times the characteristic length h of the cells. As already observed for the linear tests, also in this specific nonlinear case the errors of AD and A fluxes are similar even though an AD discretization is almost always more precise. Finally, we remark that both flux approximations have a second order discretization rate, as we expected *a priori*.

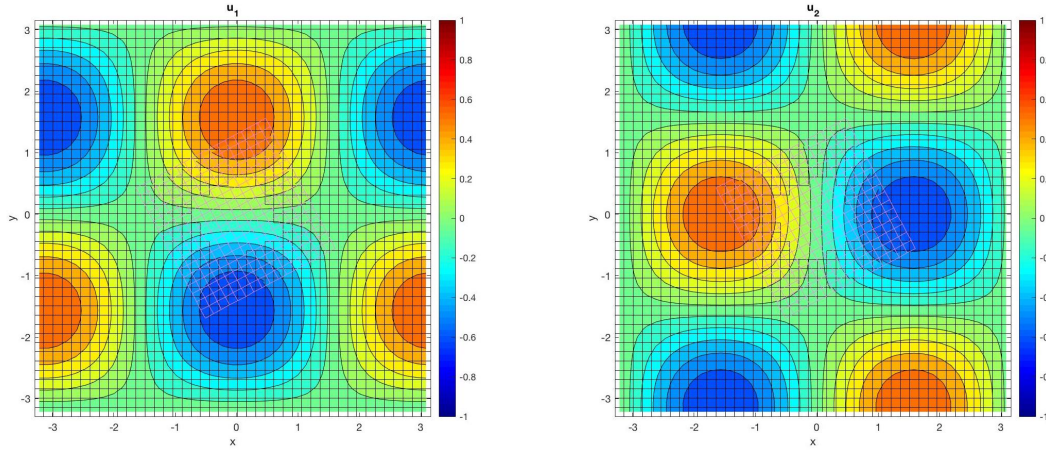


FIGURE 3.9 – Components of the solution of nonlinear test at time $t = T = 0.5$.

TABLE 3.8 – Convergence analysis of the nonlinear test case. The errors refer to time $t = T = 0.5$.

h	L^∞ -err		L^2 -err		L^∞ -rate		L^2 -rate	
	AD	A	AD	A	AD	A	AD	A
3.00e-1	2.3700e-2	2.01643e-2	5.2187e-3	4.9065e-3	0	0	0	0
1.50e-1	5.2138e-3	5.8552e-3	1.1061e-3	1.5086e-3	2.36	1.93	2.42	1.84
7.50e-2	2.4113e-3	2.4344e-3	2.4506e-4	5.7129e-4	1.15	1.33	1.30	1.44
3.75e-2	6.1828e-4	6.4658e-4	1.0332e-4	1.4322e-4	1.99	1.94	2.16	2.02

However, in H^1 -seminorm, the convergence error is second-order only when an AD stabilization parameter is used. In fact, as reported in Table 3.9, when an A flux is employed, the gradient converges at about first order.

Multimesh setting

The presented method can be easily extended to more than one foreground mesh. As a matter of fact, different meshes can be set with an independent movement and such that to exchange information with the background grid and with the other moving foreground meshes. Due to the possibility to move, the foreground meshes can overlap each other. Consequently, the hole will be present in the background as well as in some foreground grids by properly applying the same dynamics of the

TABLE 3.9 – Convergence analysis of the nonlinear test case in H^1 -seminorm.

h	$ H^1 $ -err		$ H^1 $ -rate	
	AD	A	AD	A
3.00e-1	4.2833e-2	4.0919e-2	0	0
1.50e-1	1.0336e-2	2.4094e-2	2.22	0.82
7.50e-2	5.2846e-3	1.3295e-2	2.00	0.82
3.75e-2	1.3233e-3	5.4676e-3	2.03	1.30

overlapping zone of Section 3.2.5 to the specific intermediate foreground mesh. In order to compare the performances of multimesh setting with two moving foreground meshes, we considered the presented case *TEST2* with a foreground mesh clockwise rotating around the origin (see Table 3.1) by adding a second foreground mesh. The new grid is originally located to subset $[-0.78, -0.18] \times [-0.62, -0.02]$ and horizontally moves on the right with a constant velocity $V_2 = [-0.8, 0]^T$ (see Figure 3.10). The new grid intercepts the original foreground mesh at the beginning and at the end of the simulation. For this reason, the original foreground mesh partially covers the new mesh by creating a new partial hole on it (see first and last rows in Figure 3.10b). Moreover a new hole is generated in the background. Since each foreground mesh is independent from the other, the holes in the background can be either connected (if the foreground grids overlap each other) or unconnected (if the foreground meshes are far enough to not overlap each other). Figure 3.10a refers to the solution where each grid is defined by squared grids whose cells have a characteristic length $h = 7.50e - 2$. The L^∞ - and L^2 -errors with respect to the exact solution are exactly the same reported in Table 3.3 (last row). This means that the new grid does not influence the performance of the method with respect to the previous grid setting.

Complex domains

An important application of chimera grids is the possibility to use meshes fitting the particular shape of the domain (which eventually evolves in time) by preserving a Cartesian background mesh. Here we present two test cases summed up in Table 3.10. For any positive time t , let the generic moving ball formally be

$$B_R(\rho_{\min}, \rho_{\max}; t) = \{(x, y) \in \mathbb{R}^2 : x = R(\rho, \theta) \cos(\theta), y = R(\rho, \theta) \sin(\theta) - 2t - \pi; \\ \text{with } (\rho, \theta) \in C, R : C \rightarrow \mathbb{R} \text{ and } C = [\rho_{\min}, \rho_{\max}] \times [0, 2\pi]\}.$$

For both test cases, the domain is the channel of dimensions $[-\pi, \pi] \times [-2\pi, 2\pi]$ from which the moving generalized ball $B(0, 0.5; t)$ is subtracted at any time $t \in [0, T]$. The ball vertically moves downwards with a constant velocity. In Figures 3.11a and 3.12a the numerical solutions at the initial and final time instants for the numerical tests are reported, respectively. In Figures 3.11b and 3.12b there is a focus on the grid settings. For the foreground meshes, a polar structured grids is employed. It fits the shape of the domain and moves as the domain evolves.

3.5 Conclusions of the chapter

We presented a second order finite volume scheme for unsteady advection-diffusion PDEs on overset grid. The scheme is based on an extension of the ADER method to advection-diffusion equations with compact data transmission conditions from the background to the foreground meshes and *vice versa*. We also introduced a new stabilization term for approximating the fluxes through a Local Lax-Friedrichs approach.

The numerical illustrations for linear and non-linear systems show that background and foreground moving meshes do not introduce spurious perturbation to the solution, uniformly reaching second order accuracy in space and time. In addition, we showed that the speed of the foreground mesh does not influence the stability of the method. Our results also show that the new LLF stabilization speed improves the precision and robustness of the numerical solution and allows a less restrictive CFL

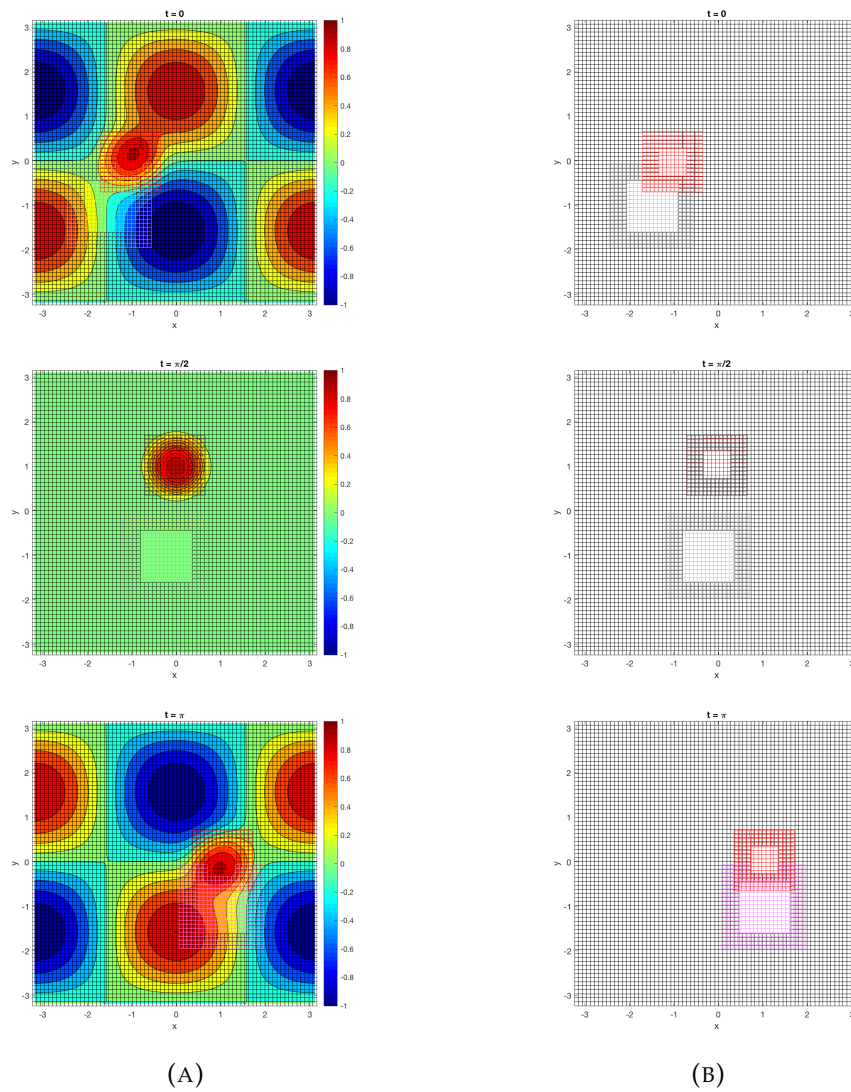


FIGURE 3.10 – On the left (a), the solution of *TEST2* for three time instants with a multimesh setting composed of two foreground meshes; on the right (b), for the same time instants, the configuration of the background and foreground grids.

TABLE 3.10 – Summary scheme of TEST4 and TEST5.

	TEST4	TEST5
Ω	$[-\pi, \pi] \times [-2\pi, 2\pi] / B_R(0, 0.5; t)$	$[-\pi, \pi] \times [-2\pi, 2\pi] / B_R(0, 0.5; t)$
$R(\rho, \theta)$	ρ	$\rho(1 + \sin(4\theta)) / 3$
Diffusion	0.05	0.1
Advection	$[0, -2]^T$	$[0, -5]^T$
$u_{ex}(x, y, t)$	$\exp[-x^2 - (y - 2t - \pi)^2 + 0.5](\cos(t) + 1)$	$0.01 \sin(x) \sin(y)[x^2 + (y - 2t - \pi)^2 - 0.5] \exp(-0.1t)$
B.C.	Dirichlet: $u_{ex}(x, y, t) _{\partial\Omega}$	Dirichlet: $u_{ex}(x, y, t) _{\partial\Omega}$
I.C.	$u_{ex}(x, y, 0)$	$u_{ex}(x, y, 0)$
T	$\pi/2$	π
fg mesh	$B(0.5, 1.5; 0)$	$B(0.5, 1.5; 0)$
V	$[0, -2]^T$	$[0, -2]^T$

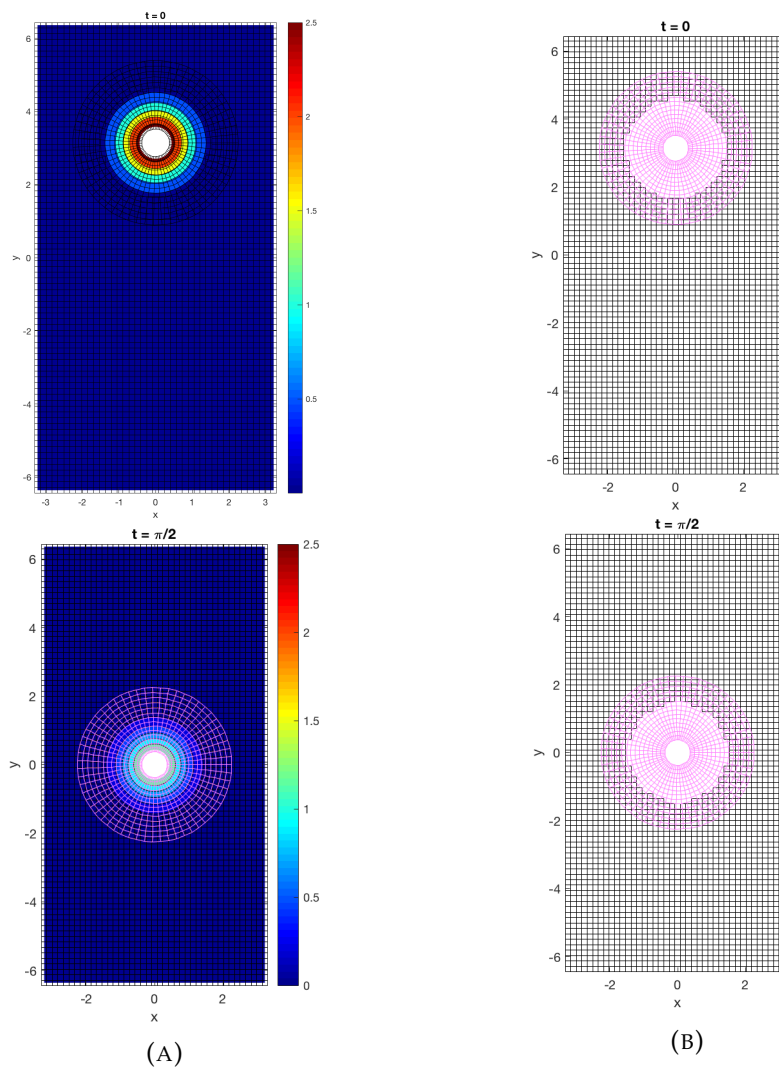


FIGURE 3.11 – On the left (a), the solution of *TEST4* for the initial and final time instants; on the right (b), for the same time instants, the background and foreground grids setting.

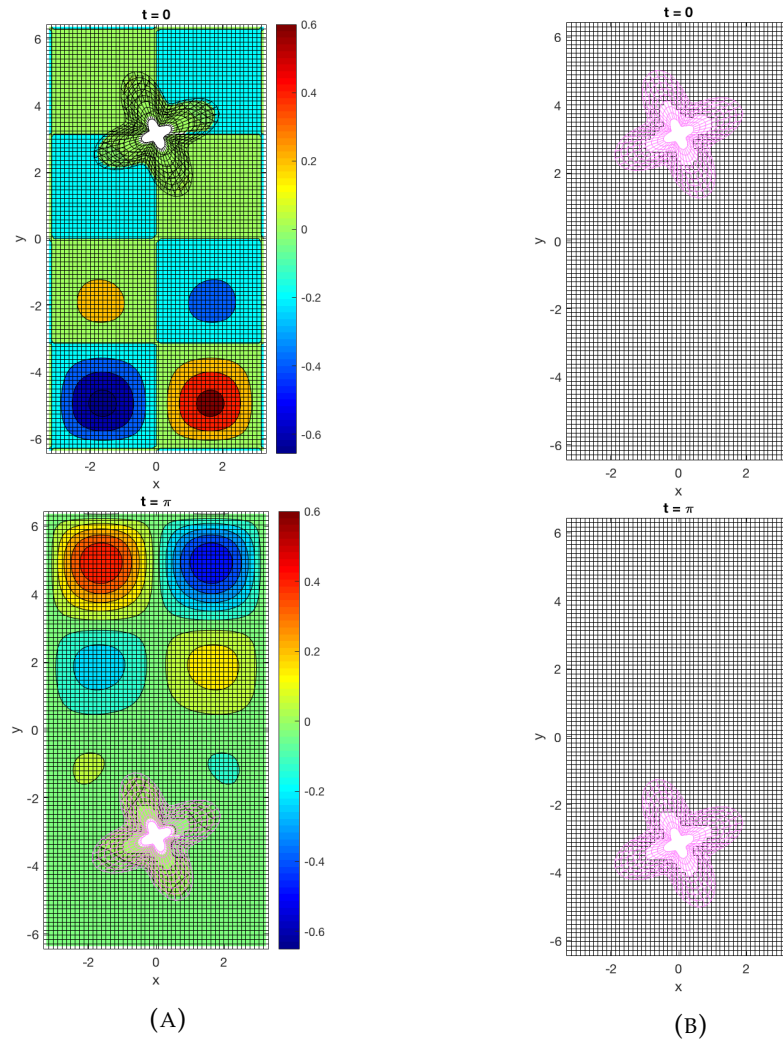


FIGURE 3.12 – On the left (a), the solution of *TEST5* for the initial and final time instants; on the right (b), for the same time instants, the background and foreground grids setting.

condition. Finally, it is shown that several foreground meshes, possibly overlapping and with independent displacements, can seamlessly be employed thanks to this approach.

Chapter 4

The incompressible Navier-Stokes equations

In this chapter, we propose a space-time Finite Volume (FV) scheme on Chimera grids. Our objective is to combine some aspects of an ALE approach, notably its flexibility with respect to grid displacement and deformation, to the multi-block discretization strategy of overset grids. In particular, special care is devoted to grid overlapping zones in order to devise a compact and accurate discretization stencil to exchange information between different mesh patches. The numerical solution of the incompressible Navier-Stokes equations follows a classical fractional method [33, 107] with a second-order accuracy in space and time.

The unsteady advection-diffusion equation is discretized through the ADER approach in the same spirit of the previous chapter and [18].

For the resolution of the Poisson equation in the projection step, we propose a hybrid FV method. On internal cells, a classical reconstruction of the gradient through the diamond formula [23, 36] is employed. On fringe cells, inspired by [93], the reconstruction of the gradient is performed by interpolating the data through an appropriate local minimization taking into account the geometry of the stencil. Special care is devoted to the definition of a fully conservative scheme in the limit of a no-shift overlapping configuration, namely when the background and foreground meshes coincide in the overlapping region.

Part of this chapter is in [21].

As for the previous chapter, the compact stencils on the fringe cells at the overlapping zone of the overset grid are built by following Algorithm 3.1 of the previous chapter. Consequently, the dynamics of the overlapping zone follows Section 3.2.5.

4.1 The governing equations

Let $\Omega(t) \subset \mathbb{R}^2$ be the computational domain, eventually evolving in time $t \in [0, T]$, with T positive real. We aim in studying the two-dimensional incompressible flow in the space-time domain $\Omega(t) \times (0, T)$ governed by the system

$$\rho \left(\frac{\partial \mathbf{u}}{\partial t} + (\mathbf{u} \cdot \nabla) \mathbf{u} \right) = -\nabla p + \mu \Delta \mathbf{u} \quad \text{in } \Omega(t) \times (0, T), \quad (4.1a)$$

$$\nabla \cdot \mathbf{u} = 0 \quad \text{in } \Omega(t) \times (0, T), \quad (4.1b)$$

$$\mathbf{u}(\mathbf{x}, 0) = \mathbf{u}_0(\mathbf{x}) \quad \text{in } \Omega(0) \times \{0\}, \quad (4.1c)$$

and completed with boundary conditions over $\partial\Omega(t) \times (0, T)$. In system (4.1), the unknowns are the velocity \mathbf{u} and the pressure p of the fluid of density ρ and dynamic viscosity μ . The initial condition is given by (4.1c) through the initial velocity \mathbf{u}_0 .

Sometimes, it is more convenient to study the nondimensionalized system of (4.1); in this case, through the incompressibility condition (4.1b), equations (4.1a) become

$$\frac{\partial \mathbf{u}}{\partial t} + \nabla \cdot (\mathbf{u}\mathbf{u}^T) = -\nabla p + \frac{1}{\text{Re}} \Delta \mathbf{u} \quad \text{in } \Omega(t) \times (0, T), \quad (4.2)$$

where $\text{Re} = \rho u_\infty L / \mu$ is the Reynolds number, with u_∞ the characteristic velocity of the fluid and L the characteristic length of either the physical domain or the obstacle, if it is present.

The domain $\Omega(t)$ is discretized with an overset mesh whose background and foreground partitions are \mathcal{T}_{bg} and \mathcal{T}_{fg} , respectively. For the sake of simplicity we consider only one foreground mesh even though it is possible to extend the method by employing several foreground meshes. The cells of the foreground partition define a subset Ω_{fg} of the physical domain. The foreground mesh of coordinates \mathbf{X} are allowed to move and deform accordingly to the motion equation

$$\frac{d\mathbf{X}}{dt} = \mathbf{V} \quad \text{in } (0, T), \quad (4.3)$$

which is a Cauchy problem of initial condition $\mathbf{X}|_{t=0} = \mathbf{X}_0(\mathbf{x})$. In problem (4.3) the force term is the mesh velocity $\mathbf{V}(\mathbf{x}, t; \mathbf{u}, p)$, eventually dependent on the fluid velocity and pressure¹. The motion equation (4.3) can be imposed regardless of the physics described by system (4.1). However, when studying fluid-structure interaction phenomena, the foreground mesh is employed in order to easily take into account the generic shape of the solid body. Consequently, the computational domain $\Omega(t)$ defines the fluid domain and part of the boundary of the foreground subdomain Ω_{fg} discretizes the boundary Γ_s of the solid, i.e., $\Gamma_s \subset \partial\Omega_{\text{fg}}$ (see Figure 4.1). Along the boundary Γ_s the interaction between the fluid and the solid takes place and it mathematically reads

$$\mathbf{u} = \mathbf{u}_B \quad \text{on } \Gamma_s(t) \times (0, T), \quad (4.4)$$

where \mathbf{u}_B is the velocity of the solid body. Thus, the mesh velocity \mathbf{V} has to coincide with the velocity \mathbf{u}_B of the body on the boundary Γ_s of the solid:

$$\mathbf{V}|_{\Gamma_s} \equiv \mathbf{u}_B. \quad (4.5)$$

Consequently, the dynamics of motion and deformation of the foreground mesh in (4.3) is led by condition (4.5).

4.2 The numerical method

The Navier-Stokes equations (4.1) are discretized using a Finite Volume (FV) scheme with the collocated cell-centered variables (\mathbf{u}, p) . Let the whole time interval $(0, T)$ be subdivided into N sub-intervals (t^n, t^{n+1}) , $n = 1, \dots, N-1$, of length Δt . For a given variable $\phi(\mathbf{x}, t)$, we indicate its evaluation at discrete time t^n with ϕ^n . A fractional step method is used to evaluate the solution in time. In order to improve the pressure smoothness and avoid some odd-even oscillation phenomena, the face-centered velocity

$$\mathbf{U} = (\mathbf{u})_{\text{fc}} \quad (4.6)$$

1. In that case systems (4.1) and (4.3) are coupled.

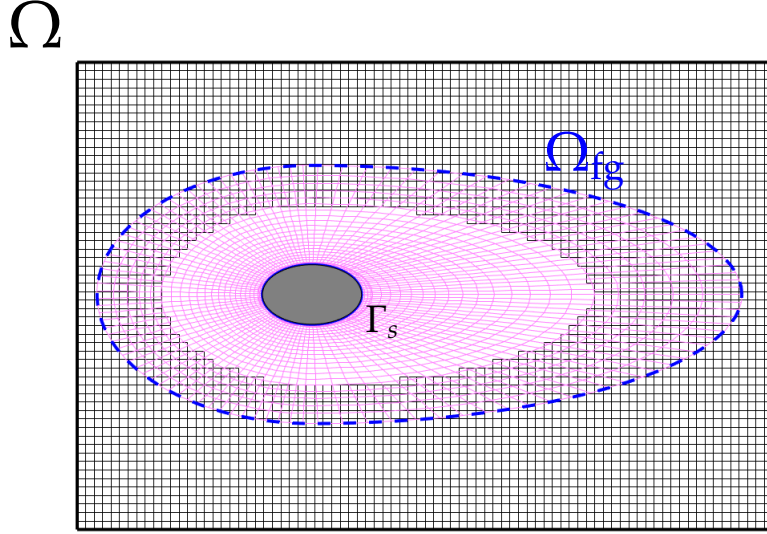


FIGURE 4.1 – Sketch of the mesh configuration. The computational (i.e. fluid) domain contains the solid body whose boundary is Γ_s . The foreground mesh (in blue) defines the foreground subdomain Ω_{fg} whose boundary is the union of an external (dashed line) and internal (continuous line) boundary. Consequently, the internal foreground boundary coincides with the solid body boundary.

is introduced as presented by Mittal *et al.* [79]. The symbol $(\cdot)_{fc}$ is a discrete operator computing the face-centered value of the cell-centered input and it will be explained later in this chapter.

Based on the predictor-projection-correction non incremental Chorin-Temam scheme² [33, 107], the first step (predictor step) evaluates an intermediate velocity \mathbf{u}^* obtained by the resolution of an unsteady convection-diffusion equation

$$\begin{cases} \frac{\partial \mathbf{u}^*}{\partial t} + \nabla \cdot (\mathbf{u}^* (\mathbf{U}^n)^T) - \frac{1}{\text{Re}} \Delta \mathbf{u}^* = \mathbf{0} & \text{in } \Omega(t) \times (t^n, t^{n+1}) \\ \mathbf{u}^* = \mathbf{u}^n & \text{in } \Omega^n \times \{t^n\} \end{cases}, \quad (4.7)$$

which will be numerically solved as explained in the next subsection.

The intermediate velocity \mathbf{u}^* solving problem (4.7) is not divergence free. Thus the predicted field \mathbf{u}^* is projected onto a divergence free space through the pressure. As a matter of fact, by computing the divergence of equation

$$\frac{\mathbf{u}^{n+1} - \mathbf{u}^*}{\Delta t} = -\nabla p^{n+1} \quad \text{in } \Omega(t) \times (t^n, t^{n+1}) \quad (4.8)$$

and applying the divergence condition (4.1b) on the velocity fluid \mathbf{u}^{n+1} , we obtain the Poisson equation for the pressure

$$\Delta \psi^{n+1} = -\nabla \cdot \mathbf{u}^* \quad \text{in } \Omega^{n+1}, \quad (4.9)$$

2. For more information, the reader is referred to the Appendix D.

with $\psi = \Delta t p$, by defining the projection step³. Problem (4.9) refers to the cell-centered velocity field and pressure. Thus, by employing the face-centered intermediate velocity $\mathbf{U}^* = (\mathbf{u}^*)_{\text{fc}}$, problem (4.9) turns into

$$\Delta \psi^{n+1} = -\nabla \cdot \mathbf{U}^* \quad \text{in } \Omega^{n+1}, \quad (4.10)$$

which is numerically solved as explained in Section 4.3.

The velocity fields \mathbf{u}^{n+1} and \mathbf{U}^{n+1} at the cell-centers and face-centers, respectively, are finally corrected through equation (4.8) as

$$\mathbf{u}^{n+1} = \mathbf{u}^* - \nabla \psi^{n+1}, \quad (4.11a)$$

$$\mathbf{U}^{n+1} = \mathbf{U}^* - (\nabla \psi^{n+1})_{\text{fc}}, \quad (4.11b)$$

which conclude the numerical routine within the time sub-interval from t^n to t^{n+1} .

4.2.1 The predictor solution

The predictor equation (4.7) for the intermediate velocity \mathbf{u}^* is solved via the ADER scheme for AD problems on overset grid presented in Chapter 3. Here the method is briefly summed up.

Local space-time Galerkin predictor

The component-wise problem to be solved is: find $q_k : \mathcal{C}_i^n \rightarrow \mathbb{R}$, $k = 1, 2$, such that

$$\begin{cases} \partial_t q_k + \nabla \cdot \mathbf{F}(q_k, \nabla q_k) = 0 & \text{in } \mathcal{C}_i^n \\ q_k = \Pi_i u_k^n & \text{on } \Omega_i^n \end{cases}, \quad (4.12)$$

where $\mathbf{F}(q_k, \nabla q_k) = \mathbf{q}q_k - \nabla q_k / \text{Re}$ is the convective-diffusive term⁴.

Remark 4.2.1. At this stage, the face-centered velocity \mathbf{U} is not required as originally indicated in problem (4.7).

In order to discretize problem (4.12), let $\mathcal{M}_i : \hat{\mathcal{C}} \rightarrow \mathcal{C}_i^n$ be a map from the reference space-time cell $\hat{\mathcal{C}} = (0, 1)^3$ to the local space-time cell $\mathcal{C}_i^n = \Omega_i(t) \times [t^n, t^{n+1}]$. The Jacobian J of the map and its inverse J^{-1} are written in (3.10) and (3.11), respectively. In particular, through the spatial restriction J_s^{-1} of the inverse Jacobian (3.12), the problem in the reference domain reads^{5,6}

$$\partial_\tau q_k + \Delta t \mathcal{F}^\flat(\hat{\nabla} q_k) + \Delta t J_s^{-T} \hat{\nabla} \cdot \mathcal{F}^\sharp(q_k, \hat{\nabla} q_k) = 0 \quad \text{in } \hat{\mathcal{C}}, \quad (4.13)$$

with

$$\mathcal{F}^\flat(\hat{\nabla} q_k) = \begin{bmatrix} \hat{\xi}_t \\ \hat{\eta}_t \end{bmatrix} \cdot \hat{\nabla} q_k; \quad \mathcal{F}^\sharp(q_k, \hat{\nabla} q_k) = \mathbf{F}(q_k, J_s^{-T} \hat{\nabla} q_k) = \begin{bmatrix} \mathcal{F}_\xi^\sharp \\ \mathcal{F}_\eta^\sharp \end{bmatrix}.$$

3. For the boundary conditions of problem (4.9), see Section D.1.

4. The initial value datum $\Pi_i u_k^n$ refers to the $\mathcal{P}_2(E_i^n)$ -interpolation, with $E_i^n = \Omega_i^n \cup \bigcup_{j \in \mathcal{S}_i^n} \Omega_j^n$ the set of cells composing the stencil \mathcal{S}_i^n at time t^n .

5. Because of the transformation, it holds

$$\partial_t q_k = \frac{\partial_\tau q_k}{\Delta t} + \mathcal{F}^\flat(\hat{\nabla} q_k); \quad \text{and} \quad \nabla = J_s^{-T} \hat{\nabla}.$$

6. The hat differential operators refer to the reference space variables $\hat{\xi}$ and $\hat{\eta}$ in the reference space-time cell $\hat{\mathcal{C}}$. In particular, $\hat{\nabla} = [\partial_{\hat{\xi}}, \partial_{\hat{\eta}}]^T$.

In order to weaken the problem (4.13), we introduce the following functional space

$$\Theta = \left\{ v \in L^2(\hat{\mathcal{C}}) : (0, 1)^2 \ni (\xi, \tau) \mapsto v(\xi, \eta, \tau) \in H^1((0, 1)) \right\}$$

as finite energy functions of $L^2(\hat{\mathcal{C}})$ associating Sobolev functions in $H^1((0, 1))$ for any fixed reference space couple (ξ, τ) . Finally, for our purposes, it is identified Θ as a test functional space and a trial functional space Q_k is defined as

$$Q_k = \left\{ v \in H^1(\hat{\mathcal{C}}) : v(\xi, \eta, 0) = \Pi_i u_k^n(x(\xi, \eta, 0), y(\xi, \eta, 0), t^n) \wedge J^{-1} \begin{bmatrix} \hat{\nabla} v \\ \partial_\tau v \end{bmatrix} \in L^2(\hat{\mathcal{C}}; \mathbb{R}^3) \right\}, \quad (4.14)$$

By multiplying left and right side of (4.13) by a generic test function θ in Θ and by integrating over the reference space-time cell $\hat{\mathcal{C}}$, the weak problem reads⁷: find $q_k \in Q_k$ such that

$$[\theta, q_k]_1 - \langle \partial_\tau \theta, q_k \rangle + \Delta t \langle \theta, \mathcal{F}^\flat(\hat{\nabla} q_k) \rangle + \Delta t \langle \theta, J_s^{-T} \hat{\nabla} \cdot \mathcal{F}^\sharp(q_k, \hat{\nabla} q_k) \rangle = [\theta, \Pi_i u_k^n]_0 \quad (4.15)$$

$\forall \theta \in \Theta$. Problem (4.15) is discretized via finite elements employing a Lagrangian polynomial basis over the 27 Gauss-Legendre quadrature points introduced in Section 3.2.2. Finally, the arising nonlinear problem is linearized through a fixed-point strategy.

The space-time finite volume scheme

Once the local predictor solution q_k is computed in each space-time cells \mathcal{C}^n , we can perform the ADER correction stage. First, we rewrite the convective-diffusive equation (4.7) in divergence form. Let $F_{\mathbf{U}^n}(u_k^*, \nabla u_k^*) = \mathbf{U}^n u_k^* - \nabla u_k^* / \text{Re}$, with $k = 1, 2$, be the convective-diffusion term associated to the component-wise equation (4.7); let $\nabla_{x,t} = [\nabla, \partial_t]^T$ be the space-time differential operator and, finally, let $\mathcal{U}_k = [F_{\mathbf{U}^n}(u_k^*, \nabla u_k^*), u_k^*]^T$, $k = 1, 2$, be the k -component of the space-time solution, thus problem (4.7) can be rewritten as: for any $k = 1, 2$,

$$\nabla_{x,t} \cdot \mathcal{U}_k = 0 \quad \text{in } \Omega(t) \times (0, T). \quad (4.16)$$

The objective is to find a finite volume solution for the above equation, where the finite volume is the space-time cell \mathcal{C}_i^n , whose boundary is 3.24. By integrating equation (4.16) over \mathcal{C}_i^n and by applying the divergence theorem to the left side, we obtain

$$\oint_{\partial \mathcal{C}_i^n} \mathcal{U}_k^n \cdot \mathbf{n}_{x,t} \, d\Gamma = 0, \quad (4.17)$$

with $\mathbf{n}_{x,t} = [n_x, n_t]^T = [n_x, n_y, n_t]^T$ being the normal unit vector to the boundary $\partial \mathcal{C}_i^n$ of the cell. Let $\bar{u}_{k,i}^{*,n}$ be the spatial average solution u_k^* cell-centered in the space cell Ω_i^n at time t^n , i.e.,

$$\bar{u}_{k,i}^{*,n} = \frac{1}{|\Omega_i^n|} \int_{\Omega_i^n} u_k^*(x, y, t^n) \, dx \, dy, \quad (4.18)$$

7. As for the previous chapter, for any function $f, g \in \Theta$, the following notation is assumed:

$$\langle f, g \rangle = \int_{\hat{\mathcal{C}}} f g \, d\hat{\xi}; \quad [f, g]_\tau = \int_0^1 \int_0^1 f(\xi, \eta, \tau) g(\xi, \eta, \tau) \, d\xi \, d\eta.$$

Though (4.18), equation (4.17) explicitly is

$$-|\Omega_i^n|\bar{u}_{k,i}^{*,n} + |\Omega_i^{n+1}|\bar{u}_{k,i}^{*,n+1} + \sum_{j=1}^4 \int_{\Gamma_{ij}^n} \mathbf{u}_k \cdot \mathbf{n}_{x,t} \, d\Gamma = 0, \quad (4.19)$$

where the unknown is the average solution $\bar{u}_{k,i}^{*,n+1}$ at time t^{n+1} , while the last term of the left hand side is the space-time flux along the space-time sides $\bigcup_{j=1}^4 \Gamma_{ij}^n$. Scheme (4.19) is the space-time Finite Volume scheme.

Remark 4.2.2. Scheme (4.19) is still exact.

In order to solve (4.19), the integral function of the space-time flux is approximated through a Local Lax-Friedrichs (LLF) approach:

$$[\mathbf{u}_k \cdot \mathbf{n}_{x,t}]_{\Gamma_{ij}^n} \approx \Phi(q_{k,j}^+, q_{k,j}^-) = \frac{1}{2}(\mathbf{u}_{k,j}^+ + \mathbf{u}_{k,j}^-) \cdot \mathbf{n}_{x,t} - \frac{s}{2}(q_{k,j}^+ - q_{k,j}^-), \quad (4.20)$$

where $\mathbf{u}_{k,j}^+ = \mathbf{u}_{k,j}(q_{k,j}^+)$ and $\mathbf{u}_{k,j}^- = \mathbf{u}_{k,j}(q_{k,j}^-)$ are the space-time solution of (4.16) computed by solutions $q_{k,j}^+$ and $q_{k,j}^-$, which represent the local predictor solutions outside and inside the cell, respectively, with respect to the space-time side Γ_{ij}^n . The term s is the local stabilization coefficient depending on the face-centered velocity \mathbf{U}^n considered constant over the space-time side Γ_{ij}^n . It reads

$$s = \frac{1}{2} \left| \mathbf{U}^n \cdot \mathbf{n}_x + 2n_t + \sqrt{\left[(U_x^n)^2 + \frac{4}{\varepsilon \text{Re}} \right] n_x^2 + 2U_x^n U_y^n n_x n_y + \left[(U_y^n)^2 + \frac{4}{\varepsilon \text{Re}} \right] n_y^2} \right|, \quad (4.21)$$

where ε is the optimal relaxation parameter (i.e., $\varepsilon = \varepsilon_2/2$, see Section 3.3.2).

Equation (4.19) with the flux approximation (4.20) closes the correction stage of the ADER method. At the end of this stage, the cell-centered k -th component of the solution $u_{k,i}^{*,n+1}$ is found over any cell Ω_i^{n+1} at time t^{n+1} .

4.3 The pressure equation

The second step of the fractional step method is the projection step defined by the Poisson equation (4.10) for pressure $\psi^{n+1} = \Delta t p^{n+1}$ at time t^{n+1} on the Chimera configuration for the domain Ω^{n+1} . In this section, in order to lighten the notation, the reference to time t^{n+1} is omitted for all involved variables and quantities. Let the stencil \mathcal{S}_i centered on cell Ω_i be decomposed in $\mathcal{S}_i = \mathcal{S}_i^+ \cup \mathcal{S}_i^\times$, with \mathcal{S}_i^+ of cells sharing either one or no edge with Ω_i and \mathcal{S}_i^\times the remaining cells sharing only one vertex of Ω_i . The proposed scheme for (4.10) is a spatial FV approach. Thus, by integrating over the space cell Ω_i , whose boundary is $\partial\Omega_i = \bigcup_{j \in \mathcal{S}_i^+} \gamma_{ij}$, and by applying the divergence theorem both to the left and right hand sides, the problem exactly reads

$$\sum_{j \in \mathcal{S}_i^+} \int_{\gamma_{ij}} \nabla \psi \cdot \mathbf{n}_{ij} \, d\gamma = \sum_{j \in \mathcal{S}_i^+} \int_{\gamma_{ij}} \mathbf{u}^* \cdot \mathbf{n}_{ij} \, d\gamma, \quad (4.22)$$

with \mathbf{n}_{ij} the unit outer normal to side γ_{ij} . The integrals in (4.22) are approximated as

$$\sum_{j \in \mathcal{S}_i^+} |\gamma_{ij}| [\nabla \psi \cdot \mathbf{n}]_{ij} = \sum_{j \in \mathcal{S}_i^+} |\gamma_{ij}| \mathbf{u}_{ij}^* \cdot \mathbf{n}_{ij}, \quad (4.23)$$

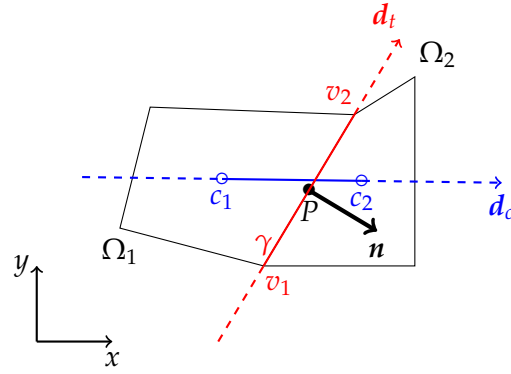


FIGURE 4.2 – Sketch of two internal cells Ω_1 and Ω_2 sharing the edge γ .

where $|\gamma_{ij}|$ is the length of side γ_{ij} . In order to achieve the Poisson algebraic system for problem (4.23), the approximation of the face-centered normal divergence term $[\nabla\psi \cdot \mathbf{n}]_{ij}$ along γ_{ij} is needed. For this reason, two different strategies are adopted with respect to the position of the spatial cell Ω_i : if the cell is not *fringe*, namely it is not at the boundary of the overlapping interface of its partition, the approximation is performed through a geometric reconstruction, otherwise, an approach involving Taylor expansion is employed.

4.3.1 The geometric reconstruction

By considering Figure 4.2, let us consider two internal cells Ω_1 and Ω_2 in the same partition and sharing the edge γ of normal \mathbf{n} . Let P be the face-center of γ . Moreover, let c_1 and c_2 be the cell-centers of the two cells and v_1 and v_2 be the extremes of edge γ . These points define the unit direction vectors \mathbf{d}_c (of the centers) and \mathbf{d}_t (tangent), respectively. The objective is to approximate the normal gradient $[\nabla\psi \cdot \mathbf{n}]_P$, applied on P , assumed to be constant over γ . It is approximated via the *diamond formula* [23, 36] accordingly to the following theorem.

Theorem 4.3.1 (Diamond formula). *In the configuration of Figure 4.2 and under the hypothesis that the normal gradient $\nabla\psi \cdot \mathbf{n}$ is constant all over the shared edge γ , the following approximated formula holds:*

$$[\nabla\psi \cdot \mathbf{n}]_P \approx \frac{1}{\mathbf{d}_c \cdot \mathbf{n}} \left(\frac{\psi_{c_2} - \psi_{c_1}}{|c_2 - c_1|} - \frac{\psi_{v_2} - \psi_{v_1}}{|\gamma|} \mathbf{d}_c \cdot \mathbf{d}_t \right). \quad (4.24)$$

Proof. Despite the value of the gradient $\nabla\psi_P$ is unknown, its projection over the non canonical basis $\{\mathbf{d}_c, \mathbf{d}_t\}$ for \mathbb{R}^2 can be approximated as

$$\nabla\psi \cdot \mathbf{d}_c \approx \frac{\psi_{c_2} - \psi_{c_1}}{|c_2 - c_1|} \quad \text{and} \quad \nabla\psi \cdot \mathbf{d}_t \approx \frac{\psi_{v_2} - \psi_{v_1}}{|\gamma|}, \quad (4.25)$$

respectively. By considering the notation of Figure 4.3, let α be the angle between directions \mathbf{n} and \mathbf{d}_c , therefore $\cos \alpha = \mathbf{d}_c \cdot \mathbf{n}$. Let us identify with \overline{PQ} the unknown quantity $\nabla\psi_P \cdot \mathbf{n}$ to be found. It is true that $\overline{PR} = \nabla\psi_P \cdot \mathbf{d}_c / \cos \alpha$ and $\overline{QR} =$

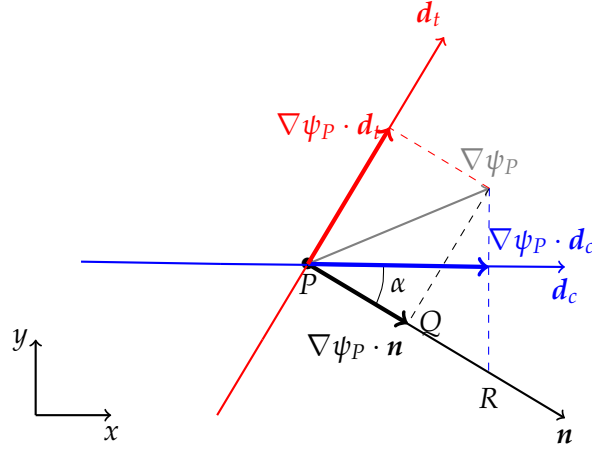


FIGURE 4.3 – Zoom of unit directions \mathbf{d}_c , \mathbf{d}_t and \mathbf{n} over the face-center P .

$(\tan \alpha) \nabla \psi_P \cdot \mathbf{d}_t$, therefore:

$$\begin{aligned} \overline{PQ} &= \overline{PR} - \overline{QR} = \frac{1}{\cos \alpha} \left(\nabla \psi_P \cdot \mathbf{d}_c - \nabla \psi_P \cdot \mathbf{d}_t \sin \alpha \right) \\ &= \frac{1}{\mathbf{d}_c \cdot \mathbf{n}} \left[\nabla \psi_P \cdot \mathbf{d}_c - (\nabla \psi_P \cdot \mathbf{d}_t)(\mathbf{d}_c \cdot \mathbf{d}_t) \right], \end{aligned} \quad (4.26)$$

which is equivalent to formula (4.24). □

In the above approximation, due to the cell-centered nature of the scheme, an approximation of the vertex-centered quantities ψ_{v_1} and ψ_{v_2} are necessary. In particular, they have to be expressed as function of some cell-centered quantities of the unknown pressure ψ . Let us study this approximation for vertex v_1 ; the extension to vertex v_2 trivially follows. Let $\tilde{\mathcal{S}}_{v_1}$ be the substencil of indexes of those cells sharing vertex v_1 . For internal cells, the cardinality of substencil $\tilde{\mathcal{S}}_{v_1}$ is equal to 4. Thus, let $\tilde{E}_{v_1} = \bigcup_{j \in \tilde{\mathcal{S}}_{v_1}} \Omega_j$ be the subdomain composed of cells sharing the vertex v_1 . Finally, let $\tilde{\Pi}_{v_1} \phi$ be the polynomial interpolation of a given function $\phi \in C^2(\tilde{E}_{v_1})$, whose knowledge is available to the cell-centers, by employing the bilinear basis of the polynomial space function $\mathcal{Q}_1^0 = \text{span}\{1, x, y, xy\}$. In particular, it holds that

$$\tilde{\Pi}_{v_1} \psi(x, y) = \alpha_{v_1,1} + \alpha_{v_1,2}x + \alpha_{v_1,3}y + \alpha_{v_1,4}xy = \mathbf{z}^T \boldsymbol{\alpha}_{v_1},$$

with $\mathbf{z} = [1, x, y, xy]^T$ and the unknown polynomial coefficients collected in vector $\boldsymbol{\alpha}_{v_1}$. The polynomial coefficients are looked for by imposing that the polynomial equals the pressure at the cell-centers of the substencil (i.e., $\tilde{\Pi}_{v_1} \psi(x_j, y_j) \equiv \psi_j$ for any j in $\tilde{\mathcal{S}}_{v_1}$). This yields the resolution of linear system $A_{v_1} \boldsymbol{\alpha}_{v_1} = \boldsymbol{\psi}_{v_1}$, where the row space of $A_{v_1} \in \mathbb{R}^{4 \times 4}$ is defined by the coordinates in \mathbf{z}_j and vector $\boldsymbol{\psi}_{v_1}$ collects the cell-centered values ψ_j , with $j \in \tilde{\mathcal{S}}_{v_1}$. Finally we approximate as follows:

$$\psi_{v_1} \approx \tilde{\Pi}_{v_1} \psi(x_{v_1}, y_{v_1}) = \mathbf{z}_{v_1}^T \boldsymbol{\alpha}_{v_1} = \mathbf{z}_{v_1}^T A_{v_1}^{-1} \boldsymbol{\psi}_{v_1}, \quad (4.27)$$

that only depends on cell-centered values of ψ . This allows to finally define the i -th line of system for problem (4.23). The scheme for internal cells reads

$$\sum_{j \in \mathcal{S}_i^+} \frac{|\gamma_{ij}|}{\mathbf{d}_{c_{ij}} \cdot \mathbf{n}_{ij}} \left(\frac{\psi_j - \psi_i}{|\mathbf{c}_j - \mathbf{c}_i|} - \frac{\mathbf{z}_{v_{2j}}^T A_{v_{2j}}^{-1} \boldsymbol{\psi}_{v_{2j}} - \mathbf{z}_{v_{1j}}^T A_{v_{1j}}^{-1} \boldsymbol{\psi}_{v_{1j}}}{|\gamma_{ij}|} \mathbf{d}_{c_{ij}} \cdot \mathbf{d}_{v_{ij}} \right) = \sum_{j \in \mathcal{S}_i^+} |\gamma_{ij}| \mathbf{U}_{ij}^* \cdot \mathbf{n}_{ij}, \quad (4.28)$$

where the unknowns are the cell-centered values of ψ .

4.3.2 Truncation error and stencil at fringe cells

For the fringe cells, the diamond formula (4.24) for approximating the normal gradient in (4.22) is more complicated. In fact there exists at least one edge for which the second center \mathbf{c}_2 falls in the other partition. Thus, in a generic configuration, it could be happen that the center direction \mathbf{d}_c tends to be parallel to the tangent direction \mathbf{d}_t , implying a vanishing term $\mathbf{d}_c \cdot \mathbf{n}$. The approach that we adopt exploits the analytic information stored in any stencil \mathcal{S}_i centered on cell Ω_i . Let $\mathcal{R}_i = \mathcal{S}_i \cup \{i\}$ be the increased stencil which includes also the index i . Let P be the generic face-centered point on which the pressure gradient needs to be approximated. In the sequel we provide the gradient approximation along the x -direction; the approximation along y similarly follows. For any j in \mathcal{R}_i , the Taylor polynomial expansion of ψ_j with respect to the face-centered value ψ_P truncated to the second-order terms is

$$\psi_j = \psi_P + h_j^x \partial_x \psi_P + h_j^y \partial_y \psi_P + h_j^x h_j^y \partial_{xy}^2 \psi_P + \frac{1}{2} (h_j^x)^2 \partial_{xx}^2 \psi_P + \frac{1}{2} (h_j^y)^2 \partial_{yy}^2 \psi_P + \mathcal{O}(H_j^3), \quad (4.29)$$

with $h_j^x = x_j - x_P$, $h_j^y = y_j - y_P$ and $H_j = \max\{|h_j^x|, |h_j^y|\}$. As done in the previous subsection, the objective is to represent the face-centered gradient as dependent on the cell-centered quantity in the stencil, i.e.,

$$\partial_x \psi_P = \sum_{j \in \mathcal{R}_i} \beta_{s_P(j)}^x \psi_j, \quad (4.30)$$

with coefficients $\beta_{s_P(j)}^x$ to be found. The discrete function $s_P : \mathcal{R}_i \rightarrow \{1, \dots, m\}$, with $m = |\mathcal{R}_i|$ being the cardinality of the enlarged stencil, sorts the indexes in \mathcal{R}_i in increasing order. By plugging the Taylor truncated expansion (4.29) in (4.30), it holds:

$$\begin{aligned} \partial_x \psi_P &= \left(\sum_{j \in \mathcal{R}_i} \beta_{s_P(j)}^x \right) \psi_P + \left(\sum_{j \in \mathcal{R}_i} \beta_{s_P(j)}^x h_j^x \right) \partial_x \psi_P + \left(\sum_{j \in \mathcal{R}_i} \beta_{s_P(j)}^y h_j^y \right) \partial_y \psi_P \\ &+ \left(\sum_{j \in \mathcal{R}_i} \beta_{s_P(j)}^x h_j^x h_j^y \right) \partial_{xy}^2 \psi_P + \left(\sum_{j \in \mathcal{R}_i} \frac{1}{2} \beta_{s_P(j)}^x (h_j^x)^2 \right) \partial_{xx}^2 \psi_P \\ &+ \left(\sum_{j \in \mathcal{R}_i} \frac{1}{2} \beta_{s_P(j)}^x (h_j^y)^2 \right) \partial_{yy}^2 \psi_P + \mathcal{O} \left(\max_{j \in \mathcal{R}_i} H_j^3 \right). \end{aligned} \quad (4.31)$$

Since the right side of (4.31) is the approximation of the x -derivative of ψ_p , the condition on the coefficients $\beta_{s_p(j)}^x$ are

$$\begin{aligned} \sum_{j \in \mathcal{R}_i} \beta_{s_p(j)}^x &= 0; & \sum_{j \in \mathcal{R}_i} \beta_{s_p(j)}^x h_j^x &= 1; & \sum_{j \in \mathcal{R}_i} \beta_{s_p(j)}^x h_j^y &= 0; \\ \sum_{j \in \mathcal{R}_i} \beta_{s_p(j)}^x h_j^x h_j^y &= 0; & \sum_{j \in \mathcal{R}_i} \frac{1}{2} \beta_{s_p(j)}^x (h_j^x)^2 &= 0; & \sum_{j \in \mathcal{R}_i} \frac{1}{2} \beta_{s_p(j)}^x (h_j^y)^2 &= 0; \end{aligned} \quad (4.32)$$

which can be synthesized in the linear system $M\beta^x = \mathbf{b}^x$, with $M \in \mathbb{R}^{6 \times m}$, $\beta^x \in \mathbb{R}^m$, $\mathbf{b}^x \in \mathbb{R}^6$. Similar considerations can be assumed for the approximation of the y -derivative⁸. For this reason, let us consider the generic system

$$M\beta = \mathbf{b}. \quad (4.33)$$

Inspired by [93], for a general value of m , system (4.33) is solved by minimizing a Lagrangian function under the constraints defined by a convex function $\mathcal{H} : \mathbb{R}^m \rightarrow \mathbb{R}$. Let $\lambda \in \mathbb{R}^v$ be a vector of Lagrangian multipliers. Moreover let $\mathcal{L} : \mathbb{R}^m \times \mathbb{R}^v \rightarrow \mathbb{R}$ be the Lagrangian function to be minimized defined as

$$\mathcal{L}(\beta, \lambda) = \mathcal{H}(\beta) - \lambda^T (M\beta - \mathbf{b}). \quad (4.34)$$

To minimize this function means to find the stationary point (β, λ) such that

$$\begin{cases} \frac{\partial \mathcal{L}}{\partial \beta} = \mathbf{0} \\ \frac{\partial \mathcal{L}}{\partial \lambda} = \mathbf{0} \end{cases} \iff \begin{cases} \frac{\partial \mathcal{H}}{\partial \beta} - M^T \lambda = \mathbf{0} \\ M\beta = \mathbf{b} \end{cases}. \quad (4.35)$$

Let $C \in \mathbb{R}^{4 \times m}$ be the sub-matrix relative to the second-order constraints. Two cases are distinguished:

$m \leq 10$: The convex function is $\mathcal{H}(\beta) = 1/2\beta^T[(1-\delta)C^T C + \delta G]\beta$, with $v = 6$, consequently the local system to be solved is

$$\begin{bmatrix} [(1-\delta)C^T C + \delta G] & -M^T \\ M & O \end{bmatrix} \begin{bmatrix} \beta \\ \lambda \end{bmatrix} = \begin{bmatrix} \mathbf{0} \\ \mathbf{b} \end{bmatrix}, \quad (4.36)$$

where O is the null matrix in $\mathbb{R}^{6 \times 6}$. This choice of the convex function $\mathcal{H}(\beta)$ is such that the discretization coefficients minimize the second-order truncation error encoded in matrix M and their L^2 -norm is penalized by coefficient δ (which is put equal to 0.01 in the presented test cases) in that region of the stencil indicated by matrix $G \in \mathbb{R}^{m \times m}$, as it will be later discussed.

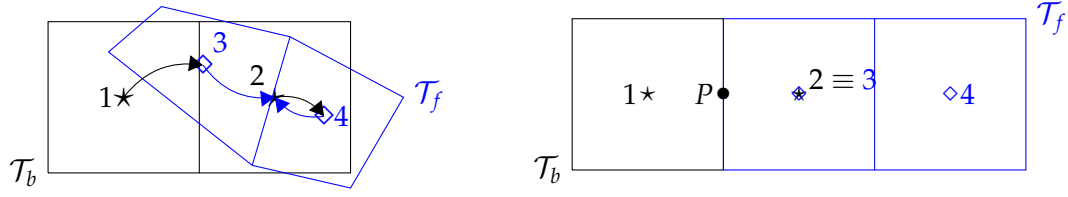
$m > 10$: The convex function reads $\mathcal{H}(\beta) = 1/2\beta^T \beta$ and $v = 10$. Thus the local minimization system is

$$\begin{bmatrix} I & -\tilde{M}^T \\ \tilde{M} & O \end{bmatrix} \begin{bmatrix} \beta \\ \mathbf{0} \end{bmatrix} = \begin{bmatrix} \mathbf{0} \\ \mathbf{b} \end{bmatrix}, \quad (4.37)$$

8. In this case, with respect to constraints (4.32), there is

$$\sum_{j \in \mathcal{R}_i} \beta_{s_p(j)}^y h_j^x = 0 \quad \text{and} \quad \sum_{j \in \mathcal{R}_i} \beta_{s_p(j)}^y h_j^y = 1.$$

Nothing changes for the other conditions.



(A) In this configuration it holds: $a_{bf}(\{1,2\}) = \{3,4\}$ while $a_{fb}(\{3,4\}) = \{2\}$.

(B) No-shift configuration. It holds: $a_{bf}(2) = 3 = a_{fb}^{-1}(2)$, $a_{fb}(3) = 2 = a_{bf}^{-1}(3)$ and $\Omega_2 \equiv \Omega_3$.

FIGURE 4.4 – Sketch of overlapping configurations. Black cells $\{1,2\}$ belong to the background partitions, blue cells $\{3,4\}$ to the foreground. The star symbols (\star) and the diamond symbols (\diamond) represent the cell-centers for cells in the background and in the foreground, respectively.

with $\tilde{M} = \begin{bmatrix} M \\ C \end{bmatrix}$ and I is the identity matrix in $\mathbb{R}^{10 \times 10}$. In this case the coefficients satisfy 10 second-order accuracy constraints while their norm is minimized.

Finally, the scheme for the fringe cells is

$$\sum_{j \in \mathcal{S}_i^+} |\gamma_{ij}| \sum_{l \in \mathcal{R}_i} (\beta_{s_{ij}(l)}^x n_{x,ij} + \beta_{s_{ij}(l)}^y n_{y,ij}) \psi_l = \sum_{j \in \mathcal{S}_i^+} |\gamma_{ij}| \mathbf{u}_{ij}^* \cdot \mathbf{n}_{ij}, \quad (4.38)$$

where the unknowns are the cell-centered values of ψ .

One goal for numerically solving the pressure problem is to have the same scheme for fringe and internal cells in the limit of a perfect no-shift overlapping between the background and foreground meshes. This allows to properly control the fluxes exiting from the background and entering in the foreground (and *vice versa*) and, consequently, to have a conservative scheme at least in this limit condition.

Let \mathcal{O} be the set of indexes for cells in the overlapping zone. It is possible to separate this set in two subsets \mathcal{O}_b and \mathcal{O}_f for the background and foreground, respectively, such that $\mathcal{O} = \mathcal{O}_b \cup \mathcal{O}_f$ and $\mathcal{O}_b \cap \mathcal{O}_f = \emptyset$. Moreover, let $a_{bf} : \mathcal{O}_b \rightarrow \mathcal{O}_f$ (and $a_{fb} : \mathcal{O}_f \rightarrow \mathcal{O}_b$) be the function associating the closest background (foreground) overlapping cell to a given foreground (background) overlapping cell, i.e., for any $i \in \mathcal{O}_b$ (and $j \in \mathcal{O}_f$)

$$a_{bf}(i) = \arg \min_{j \in \mathcal{O}_f} |\mathbf{x}_i - \mathbf{x}_j| \quad \left(\text{and } a_{fb}(j) = \arg \min_{i \in \mathcal{O}_b} |\mathbf{x}_j - \mathbf{x}_i| \right). \quad (4.39)$$

In a general overlapping configuration, it holds that $a_{fb}^{-1} \neq a_{bf}$ and $a_{bf}^{-1} \neq a_{fb}$, as it is showed in Figure 4.4a. Through the association functions it is possible to formalize the no-shift overlapping limit configuration.

Definition 4.3.1 (No-shift overlapping configuration). *The overlapping configuration is said to be no-shift when it holds both*

$$a_{bf} = a_{fb}^{-1} \quad \text{or} \quad a_{fb} = a_{bf}^{-1}; \quad (4.40a)$$

$$\forall i \in \mathcal{O}_b \quad \exists ! j = a_{bf}(i) \in \mathcal{O}_f \quad \text{such that} \quad i = a_{fb}(j) \quad \text{and} \quad \overline{\Omega_i} \cap \overline{\Omega_j} = \overline{\Omega_k}, \quad \text{with } k = i, j. \quad (4.40b)$$

The limit of no-shift condition takes place when all overlapping cells in the background perfectly coincide with all overlapping foreground cells in the foreground with a one-to-one match defined by the associations functions (an example is sketched in Figure 4.4b).

Let us consider a fringe cell Ω_i in a no-shift overlapping configuration for uniform Cartesian meshes of characteristic length h and let us suppose to compute the gradient at the face-center P of the side after which there is cell Ω_j not belonging to the same partition of Ω_i (as in Figure 4.4b for cells Ω_3 , fringe, and Ω_1 , internal). If the diamond formula (4.24) is used in this case, the tangential contribution vanishes because $\mathbf{d}_c \cdot \mathbf{d}_t = 0$, consequently, the diamond formula corresponds to the minimization of the Lagrangian functional associated to problem (4.33) fulfilling the second-order constraints (4.32) with coefficients: $\beta_{s_{ij}(i)} = -\beta_{s_{ij}(j)} = -1/h$ and $\beta_{s_{ij}(k)} = 0$ for any $k \in \mathcal{R}_i / \{i, j\}$. This means that, in the view of the problem defined by (4.36), the diamond formula is minimizing the L^2 -norm of the local parameters only in those cells of the stencil sufficiently far from the face-center point P (where the value of the local coefficients is set to 0). Consequently, all the information for the reconstruction of the gradient is recovered from the closest cells to P . This concept is encoded in matrix G defined as a diagonal matrix $G = \text{diag}(g_{s_{ij}(k)})_{k \in \mathcal{R}_i}$, with the diagonal components defined as

$$g_{s_{ij}(k)} = \begin{cases} 1; & k \neq \arg \min_{l \in \mathcal{R}_i} |\mathbf{x}_l - \mathbf{x}_P| \\ 0; & \text{otherwise} \end{cases}. \quad (4.41)$$

With this definition, in the considered overlapping configuration, components g_k assume value 1 only for $k \neq i, j$ (thus for all cells whose centers do not minimize the distance with the face-center P) and the solution of problem (4.36) can be proved to provide $\beta_{s_{ij}(i)} = -\beta_{s_{ij}(j)} = -1/h$ and $\beta_{s_{ij}(k)} = 0$ for any $k \in \mathcal{R}_i / \{i, j\}$, as defined by the diamond formula. When matrix G is put equal to the identity, the L^∞ -norm is penalized all over the stencil [93]. In the simulations of this work, matrix G with coefficients defined by (4.41) is used for any overlapping configuration, allowing to have a unique scheme for internal and fringe cells in the limit of the no-shift overlapping condition.

4.4 The face-center discrete operators on overset grids

Accordingly to the Chorin-Temam scheme presented at the beginning of Section 4.2, the face-centered values of the velocity and pressure gradient are needed. These computations take again into account either the internal or fringe position of the cell. When the intermediate velocity \mathbf{u}^* is computed at the end of the predictor step (4.7), its face-centered counterpart \mathbf{U}^* becomes the force term for the pressure equation (4.10). If the edge is shared by two cells of the same partition, the face-centered approximation is the mean of the \mathcal{P}_2 -interpolations evaluated on the face-center by using both the stencils of the two involved cells. On the contrary, when the side only belongs to one cell (because it is fringe), the approximation is still the evaluation of the polynomial interpolation on the face-center but just considering the hybrid stencil of the cell.

In the last step (4.11b) of the fractional step, the face-centered gradient pressure is used to correct the new face-centered velocity. For fringe cells, the face-centered approximation still exploits the local coefficients explained in the Section 4.3.2. For internal cells, through the diamond formula (4.24), it is possible to approximate the

directional derivatives on the face-center along the center and tangential directions. In particular they read

$$\partial_{d_c} \psi \approx \frac{\psi_{c_2} - \psi_{c_1}}{|\mathbf{c}_2 - \mathbf{c}_1|} \quad \text{and} \quad \partial_{d_t} \psi \approx \frac{\psi_{v_2} - \psi_{v_1}}{|\boldsymbol{\gamma}|}, \quad (4.42)$$

respectively, where $\partial_{\mathbf{d}} \psi = \nabla \psi \cdot \mathbf{d}$ is the directional derivative of ψ along direction \mathbf{d} . Consequently it holds

$$\begin{bmatrix} d_{c,x} & d_{c,y} \\ d_{t,x} & d_{t,y} \end{bmatrix} \begin{bmatrix} \partial_x \psi \\ \partial_y \psi \end{bmatrix} = \begin{bmatrix} \partial_{d_c} \psi \\ \partial_{d_t} \psi \end{bmatrix} \quad (4.43)$$

which can be compactly written in an algebraic form as $D(\nabla \psi)_{fc} = \mathbf{w}$. By solving the local face-centered system (4.43), correction (4.11b) is finally performed.

4.5 Numerical results

The first subsection 4.5.1 is devoted to the numerical solution of a generic Poisson problem. In Section 4.5.2 the performances of the algorithm with respect to the order of grid convergence is presented. In Sections 4.5.3 and 4.5.4 validations of physical data for simulations of *lid driven cavity* and *flows around cylinders*, respectively, compared to the literature are presented.

4.5.1 Poisson equation

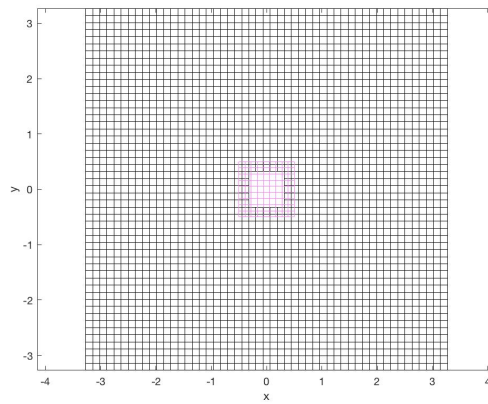
Let the Poisson problem be: *find* $u : \Omega \rightarrow \mathbb{R}$ *such that*

$$-\Delta u = f \quad \text{in } \Omega \quad (4.44)$$

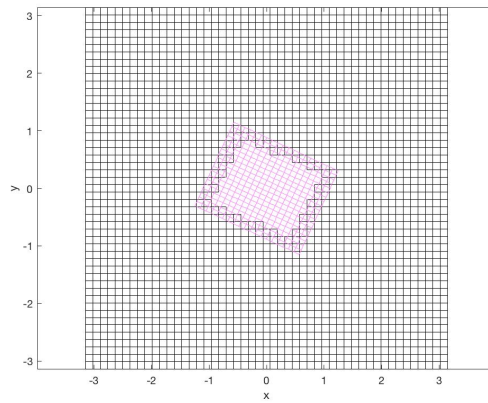
completed with adequate boundary conditions. In particular, for problem (4.44), the force term f is such that the exact solution $u_{ex}(x, y)$ is $\sin(x^2 + y^2)$, with $\Omega = (-\pi, \pi)^2$. Dirichlet boundary conditions are considered (i.e., $u|_{\partial\Omega} = u_{ex}|_{\partial\Omega}$). Three chimera configurations in Figure 4.5 are considered. In Table 4.1, The L^2 -errors and the convergences for the three configurations are reported. The convergence is definitely 2 and the error depends on the configuration of the overlapping zone. In Figure 4.6, there are the color-plots of the solution over the three different configurations. In Figure 4.7, there are depicted the pointwise errors of the numerical solution with respect to the exact solution. It is evident that the overlapping zone does not contribute to increase the error which is smaller at the overlapping than in other places of the computational domain.

4.5.2 Order of convergence

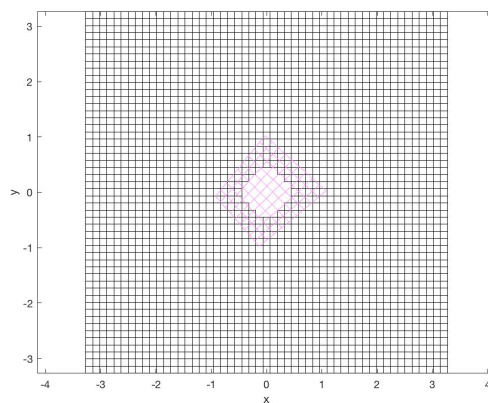
For measuring the order of convergence of the method we computed the L^2 -norm of the mismatch between the numerical solutions (both velocity and pressure) and the exact ones (\mathbf{u}_{ex}, p_{ex}) for the Taylor-Green vortices at $\text{Re} = 100$ in the computational domain $\Omega = (-\pi, \pi)^2$ at final time $T = 1$. In particular, the foreground mesh originally covers the subdomain $(-0.76, 0.76)^2$; it is composed of cells of the same characteristic dimension h of cells in the background and it rigidly counterclockwise rotates around the origin of axes accordingly to the mesh velocity $\mathbf{V} = 1/2[-y, x]^T$. At the boundaries, the numerical velocity is imposed to be equal to the exact solution. In order to measure the space-time order of convergence, the time step Δt is chosen by respecting the CFL condition; in particular, since at the boundaries the



(A) The square



(B) The rectangle



(C) The irregular quadrilateral

FIGURE 4.5 – Three different chimera-meshes for the computational domain $\Omega = (-\pi, \pi)^2$. The background mesh is in black, the foreground mesh in pink.

TABLE 4.1 – Errors and convergence rate in L^2 -norm for the Poisson equation of solution $\sin(x^2y^2)$ with respect to the over-set configurations of Figure 4.5. In the first column there is the total number N of cells.

	N	L^2 -err	L^2 -rate
Square	2401	3.1100e-2	-
	9537	7.3000e-3	2.10
	37873	2.0000e-3	1.88
Rectangle	2451	2.5400e-2	-
	10287	8.5000e-3	1.53
	42153	2.3000e-3	1.85
Quadrilateral	2443	4.000e-2	-
	9853	7.1000e-3	2.48
	39511	1.7000e-3	2.06

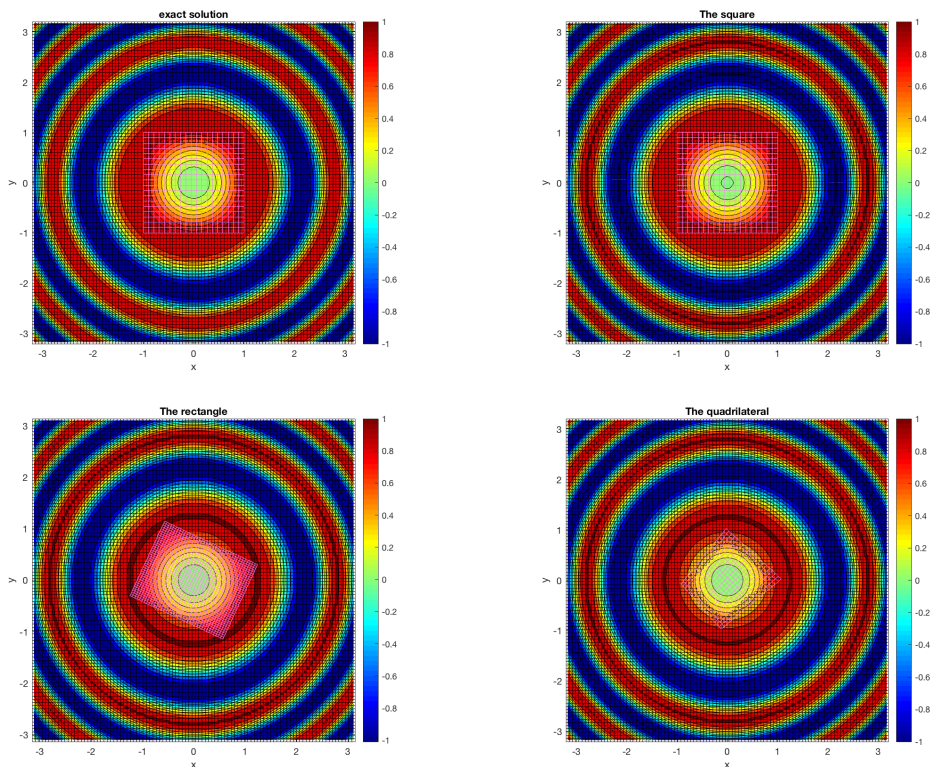


FIGURE 4.6 – Solution of the Poisson problem for the different configurations. The northwest picture is the exact solution over the first configuration (the square).

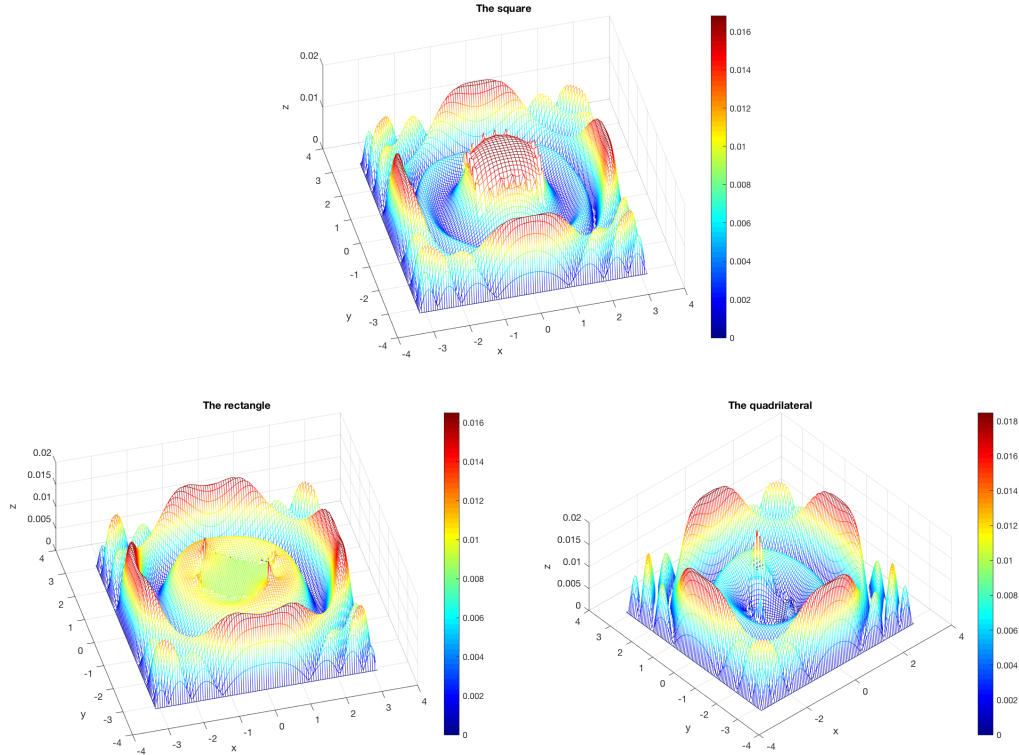


FIGURE 4.7 – Pointwise errors of the divergence of the Poisson problem for the different configurations.

maximum velocity is 1, we set $\Delta t = \text{CFL } h / u_\infty$, with $\text{CFL} = 0.4$ and $u_\infty = 1$. Despite the overset configuration is changing due to the rotation of the foreground mesh, the convergence rate for the velocity and the pressure is around 2.50 for the velocity and slightly smaller than 2 for the pressure, as showed in Table 4.2.

4.5.3 The lid driven cavity

In this section we study a lid driven cavity flow at $\text{Re} = 1000$. At the initial time the fluid has zero velocity inside the cavity $\Omega = (0, 1)^2$. No-slip boundary conditions (i.e., $\mathbf{u} \equiv \mathbf{0}$) are strongly imposed on all sides of the cavity with exception to the upper boundary where velocity is constant and equal to $[-1, 0]^T$. A steady foreground mesh occupies the subdomain $(0.21, 0.79)^2$. Both the background and the foreground meshes are uniform and Cartesian, with a characteristic length

TABLE 4.2 – Convergence analysis for Taylor-Green Vortices in $(-\pi, \pi)^2$ at final time $T = 1$.

h	L^2 -error		convergence rate	
	velocity	pressure	velocity	pressure
1.57e-1	2.7636e-5	2.0345e-3	-	-
1.05e-1	8.4817e-6	9.4667e-4	2.95	1.91
7.85e-2	3.8148e-6	6.9023e-4	2.79	1.11
6.28e-2	2.1021e-6	4.8696e-4	2.68	1.57
5.24e-2	1.3363e-6	3.4589e-4	2.49	1.88

TABLE 4.3 – Comparison on the primary vortex for the lid driven cavity: maximum stream-function Ψ_{\max} , vorticity ω and location of the topological point. The reference into brackets indicates the used methodology.

	Ψ_{\max}	ω	x	y
Present	0.1171	1.9721	0.4687	0.5625
Bruneau [27]	0.1179	2.0508	0.4687	0.5625
Bruneau [27] (Upwind)	0.1180	2.0549	0.4687	0.5625
Bruneau [27] (Kawamura [66])	0.1179	2.0557	0.4687	0.5625
Bruneau [27] (Quickest [72])	0.1150	1.9910	0.4687	0.5625
Ghia [46]	0.1179	2.0497	0.4687	0.5625

$h = 1/128$. Moreover the overlapping configuration is no-shift. We are interested in the steady solution. This solution is reached when the L^2 -norm of the difference between the velocity at two consecutive times t^n and t^{n+1} is less than 10^{-10} . Figure 4.8 shows the streamlines at the steady state. The solution presents a main vortex and two minor vortexes located towards the lower corners of the cavity. The main vortex originates from the upper boundary and moves to the region discretized by the foreground mesh. In order to quantitatively measure this movement, we consider the geometrical topological point where the stream-function⁹ Ψ is maximized. Before the steady condition, this topological point moves from the background to the foreground by passing through the overlapping zone. Table 4.3 resumes the comparison of the maximum stream-function Ψ_{\max} and its location. Along the topological point, also the value of the vorticity¹⁰ ω is reported. All data from the literature for the comparison consider a discretization grid of 128×128 . The validation confirms that the presence of the foreground mesh does not influence the performance of the simulation. The results are in good agreement with reference ones. No perturbations to the numerical solution are induced by the foreground mesh in the case of no-shift overlapping condition.

9. A stream-function $\Psi(x, y, t)$ of a 2D incompressible flow field \mathbf{u} over a line $\gamma \subset \Omega$ formally reads

$$\Psi = \int_{\gamma} (u_x \, dy - u_y \, dx).$$

Consequently it holds that

$$u_x = \frac{\partial \Psi}{\partial y} \quad \text{and} \quad u_y = -\frac{\partial \Psi}{\partial x}.$$

The stream-function can be also derived as solution of the Poisson equation with the vorticity ω as force term as

$$\Delta \Psi = -\omega.$$

10. The vorticity field ω is the curl of the velocity field \mathbf{u} :

$$\omega = \nabla \wedge \mathbf{u}.$$

In a two-dimensional flow the vorticity is always zero along x and y . Thus it is considered scalar and defined as

$$\omega = \frac{\partial u_y}{\partial x} - \frac{\partial u_x}{\partial y}.$$

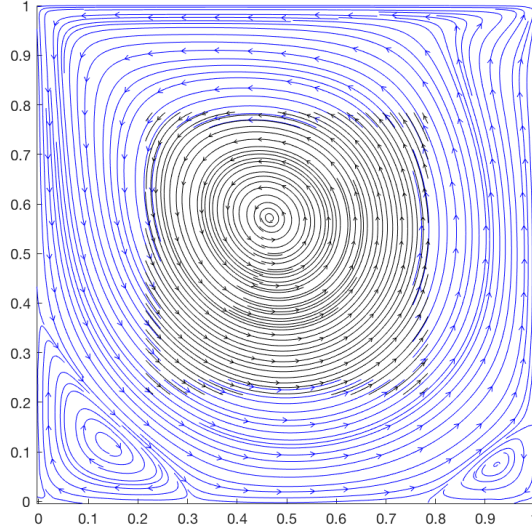


FIGURE 4.8 – Steady streamlines for the lid driven cavity test: blue for the background and black for the foreground.

4.5.4 The cylinders

In this section the method is validated by studying the flow around a cylinder that can be steady or moving. Let \mathbf{u}_∞ be the fluid velocity at the inlet boundary of the computational domain. Moreover we recall that \mathbf{u}_B is the body velocity (namely of the cylinder). Let the dimensionless stress tensor $\mathbb{T}(\mathbf{u}, p)$ be defined as

$$\mathbb{T}(\mathbf{u}, p) = -pI + \frac{1}{\text{Re}}(\nabla\mathbf{u} + \nabla\mathbf{u}^T), \quad (4.45)$$

with I the 2×2 identity tensor. The fluid dynamics force \mathbf{F}_f and torque M_f exerted by the fluid on the cylinder are

$$\mathbf{F}_f = \oint_{\partial\Omega_B} \mathbb{T}(\mathbf{u}, p)\mathbf{n}_B \, d\gamma_B, \quad (4.46a)$$

$$M_f = \oint_{\partial\Omega_B} \mathbf{r}_B \wedge \mathbb{T}(\mathbf{u}, p)\mathbf{n}_B \, d\gamma_B, \quad (4.46b)$$

where \mathbf{n}_B is the unit outer normal to the cylinder and \mathbf{r}_B is the position of any point along the boundary $\partial\Omega_B$ of the cylinder. We define the aerodynamics coefficients as $\mathbf{C} = 2\mathbf{F}_f / (\rho u_\infty^2 D)$, with D the diameter of the cylinder. Finally, let the drag C_D and lift C_L coefficients be $C_D = \mathbf{C} \cdot \mathbf{e}_x$ and $C_L = \mathbf{C} \cdot \mathbf{e}_y$, respectively, with $\{\mathbf{e}_x, \mathbf{e}_y\}$ the canonical basis for \mathbb{R}^2 .

The geometrical setting in this section is the same for all test cases. For this reason we study the grid convergence on one case and we consider the same set of back- and foreground meshes for all the other test cases. This zero test case simulates the flow around a steady cylinder at $\text{Re} = 550$ with an inlet fluid velocity $\mathbf{u}_\infty = [1, 0]^T$. The center of the cylinder is located in the origin of the axis and is $8D$ far from the inlet boundary, $16D$ from the outlet boundary and $8D$ from any of the upper and lower boundary of the channel. At the boundaries, at the inlet a constant velocity \mathbf{u}_∞ is imposed, there are no-reflecting conditions at the outlet [64] and streamline conditions (i.e., $v = 0$ and $\partial_y u = 0$) on the other two boundaries. Since the analytic solution for this case is not available, we compute the drag coefficient evolution in

TABLE 4.4 – Features of the five considered Chimera meshes for the convergence grid study. The number of cells in background and foreground are N_b and N_f , respectively, whose sum is N . Label N_B refers to the number of cells around the cylinder.

	Background		Foreground				N
	h	N_b	$\min(h)$	$\max(h)$	N_f	N_B	
<i>Grid1</i>	4.00e-1	2604	2.14e-2	4.00e-1	2686	80	5290
<i>Grid2</i>	3.00e-1	4510	1.11e-2	3.00e-1	4554	100	9044
<i>Grid3</i>	3.00e-1	4510	7.90e-3	3.00e-1	7848	110	12358
<i>Grid4</i>	2.00e-1	10004	7.90e-3	2.00e-1	7194	110	17198
<i>Grid5</i>	1.00e-1	39204	6.90e-3	1.00e-1	18183	210	57387

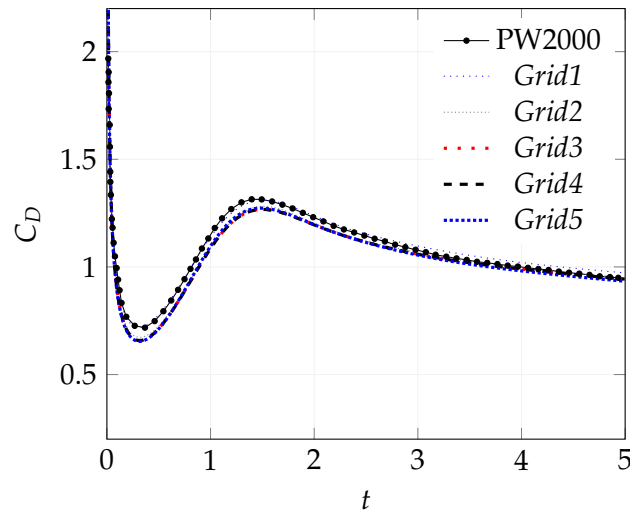
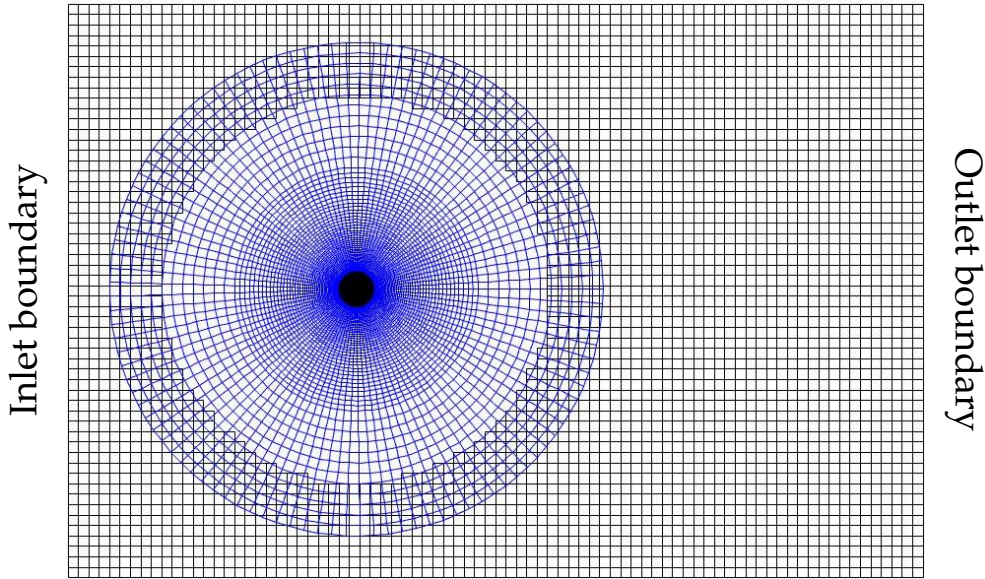


FIGURE 4.9 – Drag coefficient for the zero test case (steady cylinder at $Re = 550$). The comparison is also validated with the drag coefficient from Ploumhans and Winckelmans (PW2000) [91].

the time window $[0, 5]$ for five different Chimera grid configurations, summarized in Table 4.4. *Grid1* is the coarsest grid and *Grid5* is the finest one. In particular, *Grid3* is an intermediate configuration between *Grid2* and *Grid4*. In fact it mixes the background characteristics of *Grid2* with the foreground ones of *Grid4*. The drag coefficients from the different overset configurations are also compared with the one by Ploumhans and Winckelmans [91] for the same test case. Figure 4.9 shows the comparison. All curves match the one from the literature and, from the second to the last configuration, the drag coefficient is the same. For this reason we use the Chimera mesh *Grid3* (in Figure 4.10) because, among all the meshes, it allows a good compromise between computational times and numerical results.

Steady cylinder

Let us consider the same configuration of the zero test case for a Reynolds number $Re = 200$. In particular we study the asymptotic regime (long time integration). For this test case the validation with literature is performed for the average drag coefficient and the Strouhal number $S_t = f_v D / u_\infty$, with f_v the frequency of vortex

FIGURE 4.10 – Chimera configuration of *Grid3*.TABLE 4.5 – Comparison for the average drag coefficient C_D and the Strouhal number S_t for the steady cylinder at $Re = 200$.

	C_D	S_t
Present	1.3430	0.1979
Bergmann [17]	1.3900	0.1999
Bergmann Iollo [20]	1.3500	0.1980
Bergmann <i>et al.</i> [19]	1.4000	-
Braza <i>et al.</i> [26]	1.4000	0.2000
He <i>et al.</i> [56]	1.3560	0.1978
Henderson [57]	1.3412	0.1971

shedding. The comparison in Table 4.5 shows that the results obtained with the presented scheme match the results of the literature. In Figure 4.11 there are the plots of the drag and lift coefficients for the whole time period of integration.

Impulsively started cylinders

We now consider the impulsively started cylinders, namely test cases for which $\mathbf{u}_B \neq \mathbf{0}$ and $\mathbf{u}_\infty = \mathbf{0}$. In this case no reflecting conditions are imposed also on the inlet boundary. At the initial time the cylinder is horizontally shifted of $5D$ towards the outlet boundary with respect to the steady test cases. For the whole time interval of integration a constant velocity $\mathbf{u}_\infty = [-1, 0]^T$ is imposed to the cylinder.

In these conditions, at $Re = 550$ we expect a similar situation with the zero test case. Thus we compute the drag coefficient by comparing it to both the one of the steady case and the one from the literature provided by Ploumhans and Winckelmans [91] as previously done. The comparison is plotted in Figure 4.12. The curves for the steady and moving cases are very similar and comparable with the reference literature data. The similarity of the two test cases is also evident from the color plots of the pressure at time $t = 5$ in Figure 4.13.

As for the steady test cases, we also considered the impulsively started cylinder at $Re = 200$. By analysing the comparison in Figure 4.14 of the drag coefficient and data

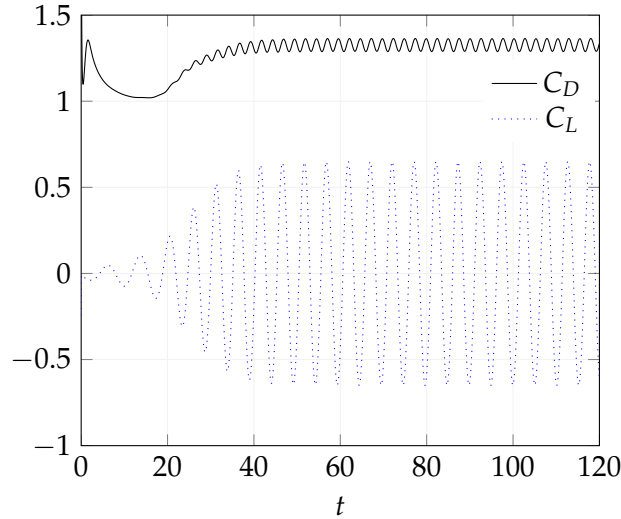


FIGURE 4.11 – Drag and lift coefficients for the steady cylinder at $\text{Re} = 200$.

from the literature by Koumoutsakos and Leonard (KL1995) [69] and Bergmann *et al.* (BHI2014) [19], there is a good agreement with the previous studies.

Impulsively started then stopped cylinders

With the same boundary conditions of the previous subsection, we also consider test cases where the cylinder is impulsively starting its movement and at a given time t_0 it stops. For this subsection we consider a viscous-dominant flow at $\text{Re} = 40$ and a convective-dominant flow at $\text{Re} = 550$. For the former case the stopping time $t_0 = 5$, while in the latter case the cylinder is stopped at $t_0 = 2.5$. For both cases, before stopping, the cylinder has a constant velocity $\mathbf{u}_B = [-1, 0]^T$. Figures 4.15 and 4.16 show the plot of the evolution of the drag coefficient compared with data from literature provided by Koumoutsakos and Leonard [69] and Bergmann *et al.* [19] for both test cases. Also in this case present data match the previous studies.

With the same accuracy, evaluated against the test cases of Bergmann *et al.* [19], the validated data though the presented method require the mesh to be composed of a number of cells from 1 to 2 orders of magnitude less. As a matter of fact, if the degrees of freedom in [19] and [20] are $\sim 10^6$ and $\sim 10^5$, respectively, the overset grid exploits $\sim 10^4$ spatial cells.

4.6 Sedimentation of a cylinder

The last test case analyses the sedimentation of a cylinder in a cavity. In order to validate the computed data with the proposed method, we set the same configuration by Coquerelle and Cottet [35], Bergmann *et al.* [19] and Bergmann and Iollo [20]. The cavity is defined by the vertical channel $[0, 2] \times [0, 6]$ with a two-dimensional cylinder, with its center of mass originally located in $(1, 4)$, falling subjected to the gravity up to the lower boundary. The cylinder radius is $r = 0.125$ with a density $\rho_s = 1.5$. The viscosity and the density of the bounding fluid are $\nu = 0.01$ and $\rho_f = 1.0$, respectively. The gravity has a modulus $g = -980$. The cylinder moves

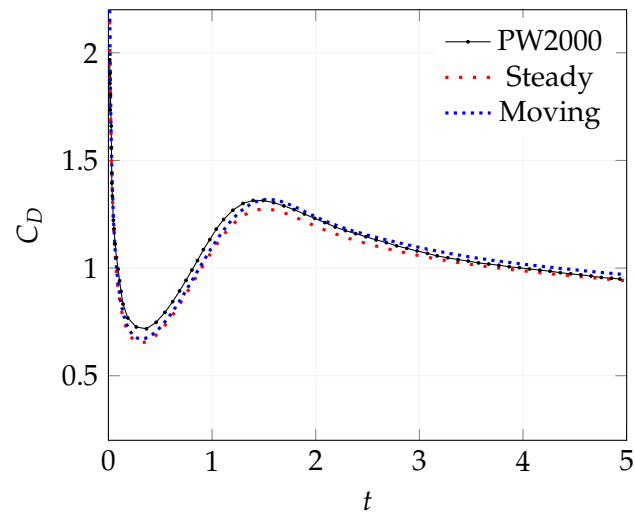
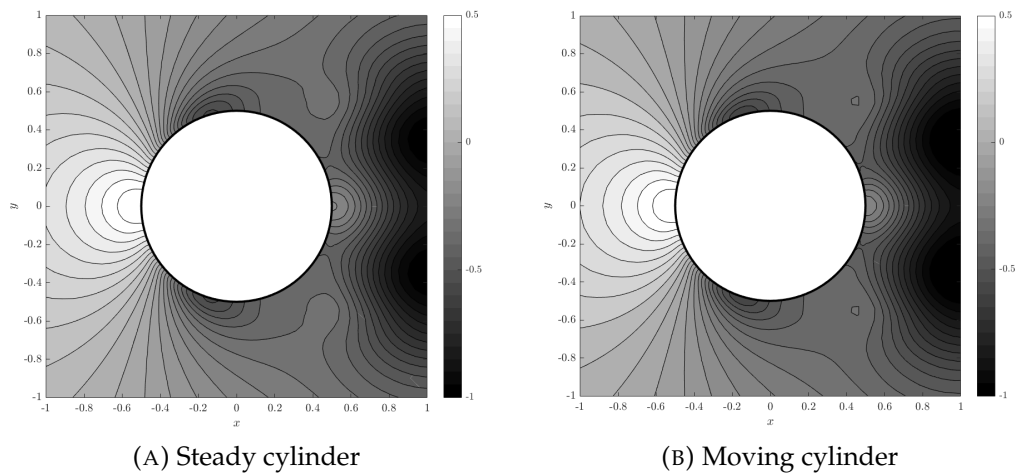


FIGURE 4.12 – Comparison of drag coefficient between the steady and impulsively started cylinder at $Re = 550$. Both are compared with the results by Ploumhans and Winckelmans (PW2000) [91].



(A) Steady cylinder

(B) Moving cylinder

FIGURE 4.13 – Pressure at $t = 5$ for steady and impulsively moving cylinders at $Re = 550$.

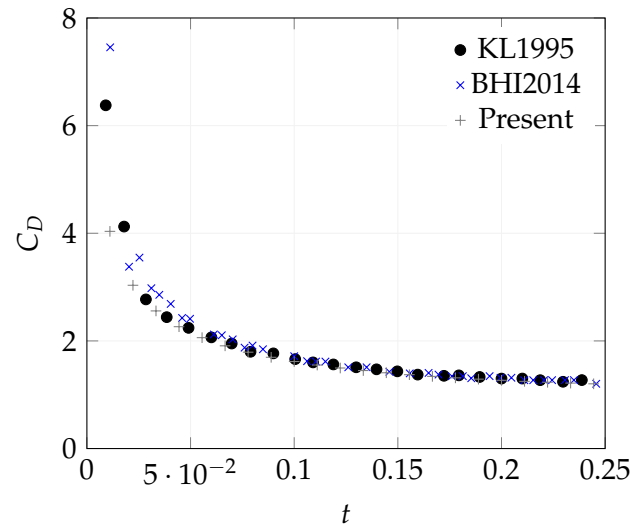


FIGURE 4.14 – Comparison of the evolution of the drag coefficient up to $t = 0.25$ for the impulsively started cylinder at $Re = 200$ with data by Koumoutsakos and Leonard (KL1995) [69] and Bergmann *et al.* (BHI2014) [19].

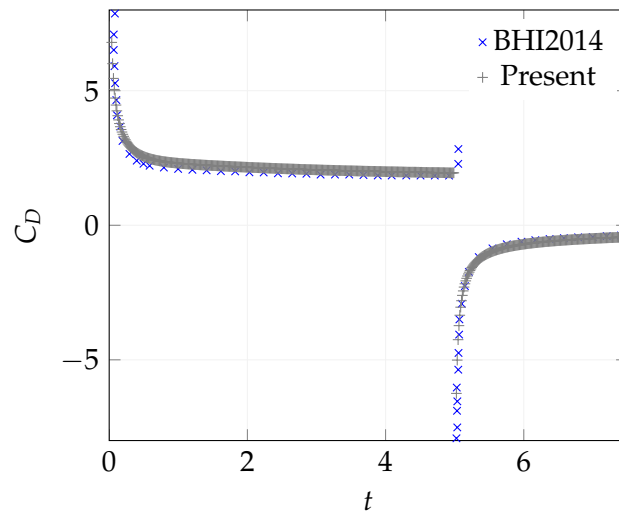


FIGURE 4.15 – Comparison of the evolution of the drag coefficient up to $t = 7.5$ for the impulsively started and then stopped cylinder at $Re = 40$ with data by Bergmann *et al.* (BHI2014) [19].

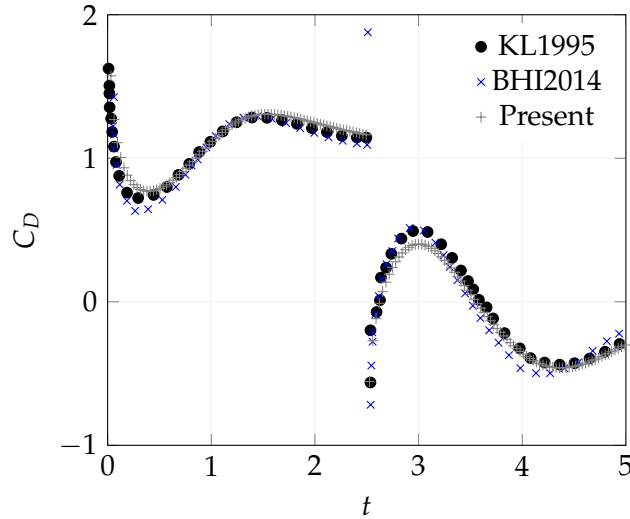


FIGURE 4.16 – Comparison of the evolution of the drag coefficient up to $t = 5$ for the impulsively started and then stopped cylinder at $Re = 550$ with data by Koumoutsakos and Leonard (KL1995) [69] and Bergmann *et al.* (BHI2014) [19].

accordingly to

$$\mathbf{u}_B = \mathbf{V} + \boldsymbol{\Omega} \wedge (\mathbf{x} - \mathbf{x}_G), \quad (4.47a)$$

$$m_B \dot{\mathbf{V}} = -\mathbf{F}_f + \tilde{m} \mathbf{g}, \quad (4.47b)$$

$$J_B \dot{\boldsymbol{\Omega}} = M_f, \quad (4.47c)$$

where \mathbf{V} and $\boldsymbol{\Omega}$ are the translation and rotational velocities, respectively, and \mathbf{x}_G is the center of the cylinder; in the translation equation (4.47b) $m_B = \pi r^2 \rho_s$ is the cylinder mass while $\tilde{m} = \pi r^2 (\rho_s - \rho_f)$ is the difference of fluid and cylinder masses after the Archimedes' law; in the rotational equation (4.47c) the cylinder inertia is denoted by $J_B = \pi r^4 \rho_s$; finally \mathbf{F}_f and M_f are the fluid dynamics forces and torque defined in (4.46), respectively.

The background mesh is uniform and Cartesian with cells of size $h = 5 \times 10^{-2}$. The foreground mesh fits the cylinder shape with the characteristic lengths of the cell varying from 1.4×10^{-3} to 5×10^{-2} . The time step is $\Delta t = \min(h)/20$. Since we are interested in simulating the cylinder up to the lower boundary, there exists a time t_0 after which the foreground mesh overcomes the physical boundaries of the cavity, as showed in Figure 4.17. In order to manage the part of the foreground mesh exceeding the physical domain, we extend the computational domain as $\tilde{\Omega} = (0, 2) \times (-1, 2)$ such that the foreground mesh is always fully contained. Thus, the exceeding region is discretized by a part of the background and, for any time $t > t_0$, by a part of the foreground mesh. Consequently, also the hole in the background will overcome the physical boundary after t_0 . In the whole computational domain a fluid-solid single flow is considered by modeling a solid material in the extended part (i.e., for any $y < 0$). This single flow is computed via a penalization method [4]. With this approach the entire system is considered as a porous medium with a variable discontinuous permeability K . In particular, the extended domain simulates an impermeable body with a very low permeability (i.e., $K \ll 1$). In this case, the

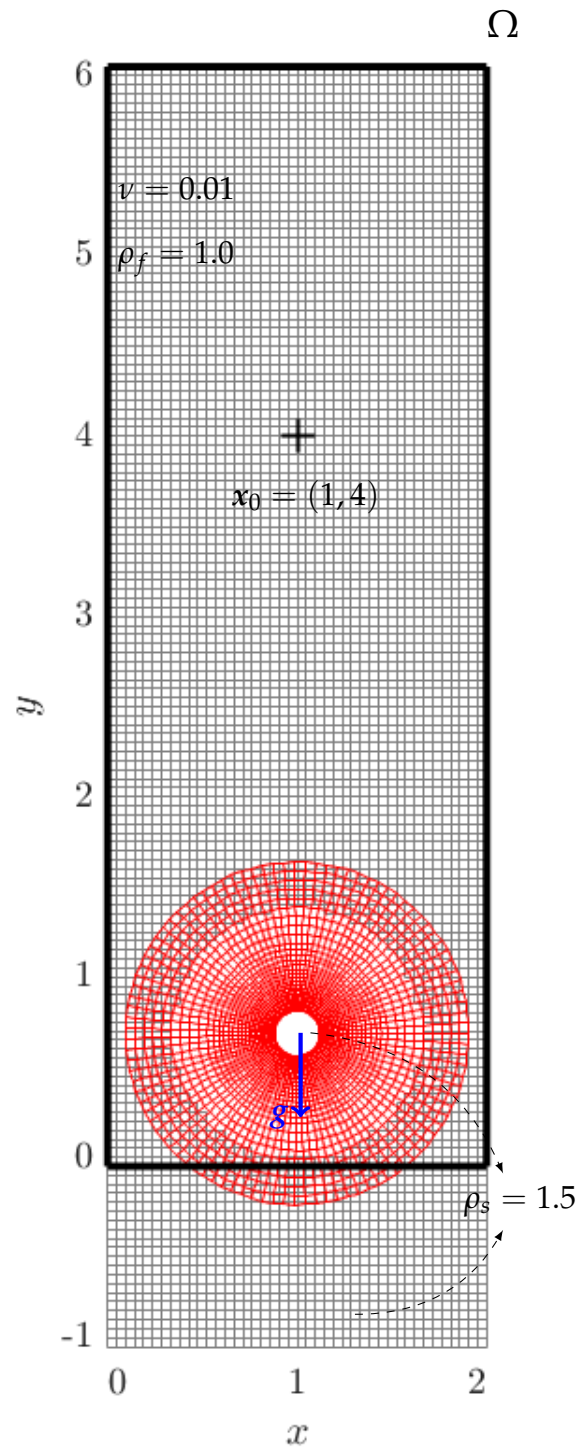


FIGURE 4.17 – Chimera configuration for the sedimentation cylinder.

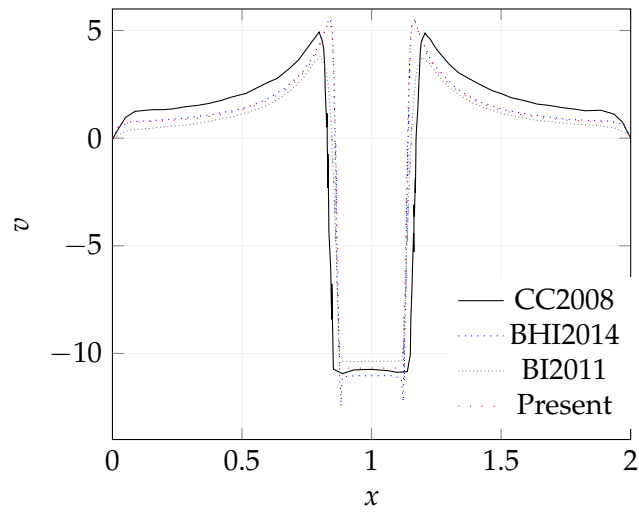


FIGURE 4.18 – Comparison of the vertical velocity v on a horizontal cut through the center of the cylinder at time $t = 0.1$ for the sedimentation test case with data by Coquerelle and Cottet (CC2008) [35], Bergmann *et al.* (BHI2014) [19] and Bergmann and Iollo (BI2011) [20].

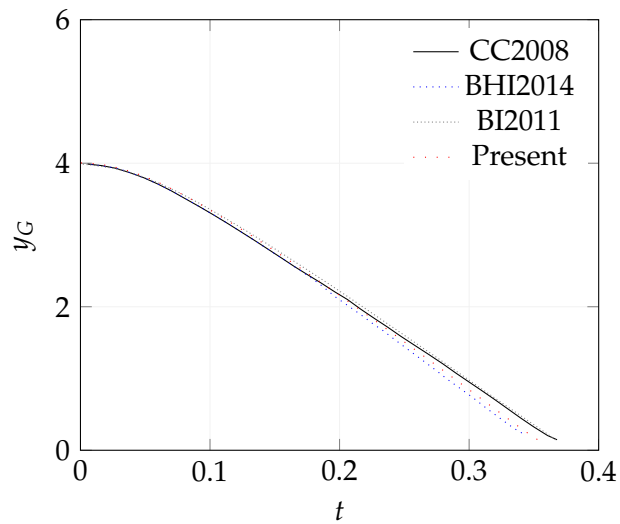


FIGURE 4.19 – Comparison of the evolution of the vertical position y_G of the center of the cylinder for the sedimentation test case with data by Coquerelle and Cottet (CC2008) [35], Bergmann *et al.* (BHI2014) [19] and Bergmann and Iollo (BI2011) [20].

considered equation in place of (4.2) reads

$$\frac{\partial \mathbf{u}}{\partial t} + \nabla \cdot (\mathbf{u}\mathbf{u}^T) = -\nabla p + \frac{1}{\text{Re}} \Delta \mathbf{u} + \frac{\chi_W}{K} (\mathbf{u}_W - \mathbf{u}), \quad (4.48)$$

where \mathbf{u}_W is the velocity of the wall, zero in our case, and χ_W is the characteristic function defined as

$$\chi_W = \begin{cases} 1, & \text{in the wall} \\ 0, & \text{elsewhere} \end{cases}. \quad (4.49)$$

In the limit of $K \rightarrow 0$, equation (4.48) tends to the Navier-Stokes equation (4.2) [4]. In this test case $K = 10^{-8}$. Despite in principle the penalization method can be used also for the cylinder, we remark that in this case we use it only for managing the extended part of the computational domain. In particular, we consider the solid below the wall having the same density of the cylinder (i.e., $\rho_s = 1.5$). Since the new reaction term in (4.48) affects the velocity, with respect to the fractional Chorin-Temam method, it is included in the predictor solution (4.7). Thus, it implies the ADER scheme to consider a reaction stiff source term [59]. In particular, for the local space-time Galerkin solution, a pseudo-mass term arises as

$$\frac{\Delta t}{K} \langle \theta_m, \chi_W |_{\hat{\xi}_l} \theta_l \rangle \hat{q}_{k,l} \quad (4.50)$$

for $m, l = 1, \dots, 27$, with $\chi_W |_{\hat{\xi}_l} = \chi_W(x(\hat{\xi}_l), y(\hat{\xi}_l))$ is the characteristic function composed with the spatial components of the reference map \mathcal{M}_i along the l -th tensor Gauss-Legendre quadrature point. Successively, for the fixed-point problem, at the iteration r , this reaction term (4.50) yields an unknown component as

$$\frac{\Delta t}{K} \langle \theta_m, \chi_W |_{\hat{\xi}_l} \theta_l \rangle \hat{q}_{k,l}^{r+1}.$$

During the ADER correction step (4.16), the penalization term is just added at the left hand side of the space-time divergence form as

$$\nabla_{x,t} \cdot \mathbf{u}_k + \frac{\chi_W}{K} u_k = 0. \quad (4.51)$$

In order to write the FV scheme, by integrating the above expression in the physical space-time slab \mathcal{C}_i^n , the method becomes

$$-|\Omega_i^n| \bar{u}_{k,i}^{*,n} + |\Omega_i^{n+1}| \bar{u}_{k,i}^{*,n+1} + \sum_{j=1}^4 \iint_{\Gamma_{ij}^n} \mathbf{u}_k \cdot \mathbf{n}_{x,t} \, d\Gamma + \iiint_{\mathcal{C}_i^n} \frac{\chi_W}{K} u_k \, d\mathcal{C} = 0. \quad (4.52)$$

Scheme (4.52) is not affected in the space-time fluxes by the new reaction term. For this reason, the procedure of the method remains the same as explained in Section 4.2.1.

Figures 4.18 and 4.19 show the validation for the vertical velocity on the horizontal line cutting the cylinder along the center and the evolution of the height of the cylinder, respectively. Present data present good agreement with all the ones from the literature. In particular it is possible to remark a closer match with the curves by Bergmann *et al.* [19]; indeed both the present method and the method used in that paper are second-order accurate. Also in this case it is possible to remark the sensible

decreasing of degrees of freedom needed by the numerical solution through the presented method with respect to the ones from the literature. In fact if the overset grid is composed of 9267 cells (i.e., 5964 in the background and 3663 in the foreground), grids employed in [35], [19] and [20] use about 3×10^6 , 8×10^5 and 2×10^6 cells.

4.7 Conclusions of the chapter

We presented a FV scheme that is second-order accurate in space and time for the solution of the incompressible Navier-Stokes equations with moving meshes. The method is based on the Chorin-Temam fractional step method. The predictor velocity is solved through an extension of the ADER method for a nonlinear convective-diffusive system on a Chimera mesh with a compact data transmission condition for fringe cells, i.e., those cells devoted to the communication between the different meshes of the overset grid. The projection step exploits a FV hybrid method for the reconstruction of the pressure gradient. In particular a geometric approach is used for internal cells and a weighted expansion is employed for expressing the gradient along the fringe cells. We proved that the approaches for internal and fringe cells are the same in the limit of a no-shift overlapping condition. This result is achieved by properly minimizing a convex function for the local coefficients allowing to take into account both the second-order truncation of the solution and the distribution of data in the local stencil.

The numerical results showed that the movement of the mesh does not introduce spurious oscillation to the numerical solution of the problem and that second-order accuracy is preserved in both space and time. In order to test the method, a wide range of canonical cases is exposed. Their validation confirms that the obtained data match the ones from the literature. In particular, results for tests where the exact solution is not available are always closer to the ones obtained by second-order methods. Moreover, at equal accuracy, the total number of cells for the overset grid (namely the degrees of freedom) is reduced by up to two orders of magnitude compared to the ones from the cited literature. With the sedimentation test case, we introduced a reaction term which is not present *a priori* in the original equation. In particular, we mixed the adapted ADER method for Chimera meshes with a penalization method in order not to cut part of the foreground mesh that overcomes the physical boundaries of the domain. This application highlights the versatility of the proposed method even in proximity of boundaries defined on other mesh blocks.

Chapter 5

Reduced and Hyper-reduced ADER method

The Model Order Reduction (MOR) is a numerical approach aiming at decreasing the computational cost for the recovery of a numerical parameter-dependent solution associated to a system of partial differential equations. It consists in a training stage (*offline stage*) where a relevant amount of information regarding the high-fidelity solution is stored and processed in order to allow a cheap computation step (*online stage*) for the computation of a new solution with a new set of values for the parameter.

Among the several reduced order models (such as Reduced Basis [11, 92], Proper Generalized Decomposition [31], Hierarchical Model Reduction [85], . . .), one of the most used is the Proper Orthogonal Decomposition (POD) [102, 22]. Accordingly to this approach, a proper amount of information of high-fidelity solutions deriving by the same problem for different parameter settings is stored in order to hierarchically define a subspace where to finally project the reduced solution for a new parameter setting in the online step. In particular, in the offline stage, the redundant information is discarded and the relevant one is used in order to successively reduce the computational cost in the online step.

In general, for solution of PDEs, the parameter setting (defining the geometry information as well as the boundary condition or the diffusion parameter, for example) affects the solution itself (e.g., by changing the support compact, or the features of a shock wave, discontinuity contact, etc.).

In this chapter, we propose a reduced model in a Domain Decomposition (DD) frame. This means that only in a certain region of the domain the reduction is applied while in the remaining part the High-Fidelity Model (HFM) is still employed for recovering the numerical solution. The domain decomposition is automatically defined by the overset composition of the meshes.

A preliminary first reduction based on the ADER method is proposed. In addition, also a hyper-reduction [44, 43, 52] is defined for a cheap computation of the matrices defining the algebraic counterparts of the scheme.

For the sake of simplicity and with no loss of generality, we present the method by analyzing the linear and nonlinear convection-diffusion problem defined by the problem: *find* $u : \Omega(t) \times (0, T) \rightarrow \mathbb{R}$ such that:

$$\partial_t u + \nabla \cdot F(u, \nabla u) = f \quad \Omega(t; z) \times (0, T) \quad (5.1)$$

properly closed with boundary and initial conditions. Problem (5.1) depends on a

parameter $z \in Z \subset \mathbb{R}$ (eventually time-dependent) defining the evolution of the domain $\Omega(t)$ in time. For this reason, the problem is coupled with the Cauchy problem

$$\begin{cases} \dot{\mathbf{X}} = \mathbf{V}(\mathbf{x}, t; u; z) & \text{in } (0, T) \\ \mathbf{X}(0) = \mathbf{X}_0 \end{cases} \quad (5.2)$$

which defines the movement of the foreground mesh employed for discretizing the space around the deforming subset of the physical domain.

5.1 Reduced-order model based on ADER approach

Inspired by ADER method explained in Chapter 3, this section is devoted in modeling a reduced-order model for ADER method. As for the full approach, first the reduction is applied to the prediction finite element step, successively the reduced correction stage is explained.

5.1.1 The prediction stage

Let the time interval $(0, T)$ be subdivided into intervals (t^n, t^{n+1}) . The prediction problem reads: *find* $q : \Omega(t) \times (t^n, t^{n+1}) \rightarrow \mathbb{R}$ such that:

$$\begin{cases} \partial_t q + \nabla \cdot \mathbf{F}(q, \nabla q) = f & \text{in } \Omega(t) \times (t^n, t^{n+1}) \\ q = u^n & \text{in } \Omega^n \end{cases}, \quad (5.3)$$

where u^n is the just computed solution at time t^n . The space-time cylinder $\Omega(t) \times (t^n, t^{n+1})$ is named \mathcal{B} . Accordingly with the notation in the previous chapters, its discretization is $\mathcal{B} = \bigcup_{i=1}^N \mathcal{C}_i^n$, with $\mathcal{C}_i^n = \Omega_i(t) \times (t^n, t^{n+1})$. Let $V_M = \text{span}\{\Phi_m\}_{m=1}^M$ be the reduced space defined by M modal function $\Phi_m(\mathbf{x}, t)$ for any (\mathbf{x}, t) in \mathcal{B} . The modal function are found during the offline stage of the reduced order model. The objective is to find a projection of the solution over the reduced space. It means to find a reduced solution

$$q(\mathbf{x}, t; z) = \sum_{m=1}^M a_m^n(z) \Phi_m(\mathbf{x}, t), \quad (5.4)$$

where coefficients $\{a_m^n(z)\}_{m=1}^M$, referring to time sub-interval (t^n, t^{n+1}) , are found in the online stage.

Since the modal function in V_M are computed from the ADER prediction stage, it is possible to state the inclusion $V_M \subset X$, with

$$X = \left\{ v : \mathcal{B} \rightarrow \mathbb{R} : (v|_{\mathcal{C}_i^n} \circ \mathcal{M}_i|_z) \in \Theta \quad \forall i = 1, \dots, N \right\} \quad (5.5)$$

functional space of functions whose restriction to any space-time cell \mathcal{C}_i^n in \mathcal{B} belongs to

$$\Theta = \left\{ v \in L^2(\hat{\mathcal{C}}) : (0, 1)^2 \ni (\xi, \eta) \mapsto v(\xi, \eta, \tau) \in H^1((0, 1)) \right\}, \quad (5.6)$$

which is the functional solution space of local solutions from the high-fidelity method. Space (5.6) is introduced in 3.2.2 and it is the natural space where to find the high-fidelity weak solution of problem (5.1) restricted to the space-time \mathcal{C}_i^n .

Remark 5.1.1. Functions in space X (and consequently in subspace V_M) are potentially discontinuous in space.

Remark 5.1.2. For different instances of the parameter $z \in Z$, the union of the prediction solutions over any space-time cell belongs to space (5.5).

It is now possible to weaken (5.3) as follows: find $q \in V_M$ such that $q|_{t=t^n} = u^n$ and

$$\int_{\mathcal{B}} \Phi(\partial_t q + \nabla \cdot F(q, \nabla q) - f) \, d\mathcal{B} = 0 \quad \forall \Phi \in X. \quad (5.7)$$

Since the reduction is applied only on a decomposition of the domain defined by the foreground mesh, it holds a mutually disjoint condition such that $\mathcal{C}_i^n \cap \mathcal{C}_j^n = \emptyset$ for any $i \neq j$. Consequently weak form (5.7) can be exactly written as

$$\sum_{i=1}^N \left(\int_{\mathcal{C}_i^n} \Phi \partial_t q \, d\mathcal{C} + \int_{\mathcal{C}_i^n} \Phi \nabla \cdot F(q, \nabla q) \, d\mathcal{C} - \int_{\mathcal{C}_i^n} \Phi f \, d\mathcal{C} \right) = 0 \quad \forall \Phi \in X. \quad (5.8)$$

Concerning the first left hand side of (5.8), it holds $\Phi \partial_t q = \partial_t(\Phi q) - \partial_t \Phi q$. Moreover, due to both Reynolds' transport theorem and the first fundamental integral calculus theorem we have

$$\begin{aligned} \int_{\mathcal{C}_i^n} \partial_t(\Phi q) \, d\mathcal{C} &= \int_{t^n}^{t^{n+1}} \int_{\Omega_i(t)} \partial_t(\Phi q) \, d\Omega \, dt \\ &= \int_{t^n}^{t^{n+1}} \left(\frac{d}{dt} \int_{\Omega_i(t)} \Phi q \, d\Omega - \oint_{\partial\Omega_i(t)} \Phi q \mathbf{V} \cdot \bar{\mathbf{n}}_i \, d\gamma \right) dt \\ &= \int_{\Omega_i^{n+1}} \Phi q \, d\Omega - \int_{\Omega_i^n} \Phi q \, d\Omega - \sum_{j=1}^4 \int_{\Gamma_{ij}^n} \Phi q \mathbf{V}_{ij} \cdot \bar{\mathbf{n}}_{ij} \, d\Gamma, \end{aligned} \quad (5.9)$$

with the boundary of the space time cell

$$\partial\mathcal{C}_i^n = \Omega_i^n \cup \Omega_i^{n+1} \cup \bigcup_{j=1}^4 \Gamma_{ij}^n$$

whose space-time manifold $\bigcup_{j=1}^4 \Gamma_{ij}^n$ deformation velocity and spatial unit normal are \mathbf{V}_{ij} and $\bar{\mathbf{n}}_{ij}$, respectively. Let

$$F_\chi = \sum_{m=1}^M F_{\chi,m} \Phi_m \quad (5.10)$$

be the χ -component of the advective-diffusive term F projected onto V_M , with $\chi = x, y$. By taking the generic test function Φ in the reduced space and by plugging (5.4),

(5.10) and (5.9) into the analytic weak form (5.8), its algebraic counterpart reads¹

$$\begin{aligned} \sum_{i=1}^N \left[\left(\int_{\Omega_i^{n+1}} \Phi_l \Phi_m \, d\Omega - \sum_{j=1}^4 \int_{\Gamma_{ij}^n} \Phi_l \Phi_m \mathbf{V}_{ij} \cdot \bar{\mathbf{n}}_{ij} \, d\Gamma - \int_{\mathcal{C}_i^n} \partial_t \Phi_l \Phi_m \, d\mathcal{C} \right) a_m^n \right. \\ \left. + \int_{\mathcal{C}_i^n} \Phi_l \partial_x \Phi_m \, d\mathcal{C} F_{x,m} + \int_{\mathcal{C}_i^n} \Phi_l \partial_y \Phi_m \, d\mathcal{C} F_{y,m} \right. \\ \left. - \int_{\mathcal{C}_i^n} \Phi_l f \, d\mathcal{C} - \int_{\Omega_i^n} \Phi_l u^n \, d\Omega \right] = 0 \quad \forall l = 1, \dots, M. \end{aligned} \quad (5.11)$$

By defining the matrices and vectors

$$\begin{aligned} [M^1]_{lm} &= \sum_{i=1}^N \int_{\Omega_i^{n+1}} \Phi_l \Phi_m \, d\Omega; & [A]_{lm} &= \sum_{i=1}^N \sum_{j=1}^4 \int_{\Gamma_{ij}^n} \Phi_l \Phi_m \mathbf{V}_{ij} \cdot \bar{\mathbf{n}}_{ij} \, d\Gamma; \\ [K_t]_{lm} &= \sum_{i=1}^N \int_{\mathcal{C}_i^n} \partial_t \Phi_l \Phi_m \, d\mathcal{C}; & [K_\chi]_{lm} &= \sum_{i=1}^N \int_{\mathcal{C}_i^n} \Phi_l \partial_\chi \Phi_m \, d\mathcal{C}; \\ [\mathbf{a}^n]_m &= a_m^n; & [\mathbf{F}_\chi]_m &= F_{\chi,m} = \sum_{i=1}^N \int_{\mathcal{C}_i^n} F_\chi \Phi_m \, d\mathcal{C}; \\ [\mathbf{f}]_l &= \sum_{i=1}^N \int_{\mathcal{C}_i^n} \Phi_l f \, d\mathcal{C}; & [\mathbf{u}_{old}]_l &= \sum_{i=1}^N \int_{\Omega_i^n} \Phi_l u^n \, d\Omega; \end{aligned} \quad (5.12)$$

for any $l, m = 1, \dots, M$ and $\chi = x, y$, scheme (5.11) becomes

$$(\mathbf{M}^1 - \mathbf{A} - \mathbf{K}_t) \mathbf{a}^n + \mathbf{K}_x \mathbf{F}_x + \mathbf{K}_y \mathbf{F}_y = \mathbf{f} + \mathbf{u}_{old}. \quad (5.13)$$

In the above algebraic problem the advective-diffusive components \mathbf{F}_x and \mathbf{F}_y are implicitly defined by the unknown coefficients \mathbf{a}^n . Thus, it is solved via a fixed point iteration approach as for the high-fidelity method.

5.1.2 The correction step

Once the predictor solution (5.4) is found through (5.13), the corrected ADER solution $u^{n+1} : \Omega^{n+1} \rightarrow \mathbb{R}$ as well is found as usual (see Section 3.2.4).

In view of model reduction and hyper-reduction that also concerns the correction stage of ADER, it is necessary to define a reduced representation also for the corrected solution. In particular, let the functional space

$$\mathcal{U}_L = \text{span}\{\Psi_l\}_{l=1}^L \subset H^1(\Omega(t)) \quad \forall t \in (0, T)$$

be defined by corrected modal basis functions $\Psi_l(\mathbf{x})$ on $\Omega(t)$, with t in $(0, T)$. The corrected modal basis are computed in the offline stage as for the previously introduced reduced modal basis $\Phi_m(\mathbf{x}, t)$. Consequently, the projection of the corrected solution over the space reads

$$u(\mathbf{x}, t; z) = \sum_{l=1}^L \alpha_l(t; z) \Psi_l(\mathbf{x}(t)). \quad (5.14)$$

1. The Einstein's notation on repeated index m is used.

Let \mathbf{u} be the discrete counterpart of (5.14) defined over any cell (thus $\mathbf{u} \in \mathbb{R}^N$). Therefore, at time t^{n+1} , the representation (5.14) algebraically is $\mathbf{u} = [\Psi]\boldsymbol{\alpha}$, with matrix of basis $[\Psi] \in \mathbb{R}^{N \times L}$ and coefficient vector $\boldsymbol{\alpha} \in \mathbb{R}^L$.

In view of a model reduction and hyper-reduction, in principle it is possible to define a reduced scheme of the correction stage of ADER. However, in this chapter we just project the corrected solution onto the corrected reduced space \mathcal{U}_L . In particular, the l -th corrected coefficient

$$\alpha_l = \int_{\Omega^{n+1}} u \Psi_l \, d\Omega \quad (5.15)$$

is the L^2 -projection of the solution u along the l -th basis component Ψ_l . By introducing the quadrature integration matrix $W \in \mathbb{R}^{N \times N}$ associated to the spatial configuration Ω^{n+1} , the corrected coefficient (5.15) is approximated as $\alpha_l \simeq \Psi_l^T W \mathbf{u}$, with Ψ_l the l -th column of $[\Psi]$. Therefore it holds $\boldsymbol{\alpha} = [\Psi]^T W \mathbf{u}$. In order to be coherent with the presented theory, in the numerical validation, instead of the corrected solution u , we consider its projection $\mathcal{P}_{\mathcal{U}_L} u$ which algebraically is

$$\mathcal{P}_{\mathcal{U}_L} \mathbf{u} = [\Psi]\boldsymbol{\alpha} = [\Psi][\Psi]^T W \mathbf{u}. \quad (5.16)$$

Remark 5.1.3. *By abuse of notation, the projector functional $\mathcal{P}_{\mathcal{U}_L} : L^2(\Omega^{n+1}) \rightarrow \mathcal{U}_L$ for solution u is confused with its algebraic counterpart as written in (5.16).*

Remark 5.1.4. *There is a substantial difference in the properties of the coefficients $\{a_m^n\}_{m=1}^M$ projecting the predicted solution onto V_M and those in (5.15) projecting the corrected solution onto \mathcal{U}_L . As a matter of fact, the former do not have a point-wise dependence on the time instant between t^n and t^{n+1} , for any $n > 0$. Rather they depend on the time step Δt defining the time dimension of \mathcal{B} . Instead, the second indexes strictly depend on the time instant on which the solution of the problem is evaluated.*

5.1.3 Domain decomposition approach

As mentioned in the previous subsection, the proposed reduced model is built in a domain decomposition frame. In particular, the reduction is applied to the moving subdomain defined by the partition of the foreground mesh and a high-fidelity (HF) ADER approach is used for recovering the numerical solution in the remaining subdomain defined by the background mesh. Thus, the exchange of information is managed as explained in Section 3.2.5, even though the information are reduced in foreground and HF in background. We remark that both the reduced and HF subdomains change accordingly to the parameter z . Consequently, for a different values of z , for the same confined region of the space in Ω , the recovered information could be either reduced or high-fidelity with respect to the specific deformation of the domain.

The proposed reduced method in Sections 5.1.1 and 5.1.2 is an attempt to model ADER method over a macro-cell defined by the foreground mesh. In particular, the HFM is employed in the micro-cells \mathcal{C}_i^n and Ω_i^n , while the ROM is defined over the macro-cell identified by the moving or deforming foreground mesh. Consequently, the global domain is decomposed in regions in order to isolate specific solutions features accordingly to the deformation itself. In this context, the overset grid not only easily discretizes the deforming space with respect to its geometrical variations but also defines the zone of the high-fidelity and reduced numerical solution.

5.2 Proper Orthogonal Decomposition

In the offline stage, the ADER scheme provides a database of N_s snapshots for both predictor and corrector high-fidelity solutions collected at different time instances, for different input parameters as well as for different mesh configurations. Let $g^b = g(\mathbf{x}, t_{k(b)}; z_{j(b)})$ be the b -th snapshot for any node \mathbf{x} in (sub)domain $E \subseteq \bar{\mathcal{B}}$ at time instance $t_{k(b)}$ and for parameter assuming value $z_{j(b)}$.

The basis functions Y_r (with Y_r being either Φ_r or Ψ_r), $r = 1, \dots, R$ (with R the dimension of the reduced space, namely M for the predictor basis and L for the corrected basis) are computed by POD in order to represent the solution snapshots at best. In particular, the subspace $\mathcal{Y} = \text{span}\{Y_r\}_{r=1}^R$ (with \mathcal{Y} coinciding with V_M or \mathcal{U}_L) is the subspace of rank R minimizing the difference between the snapshots and their projection onto the subspace itself, in the least-square sense. Formally, the projection onto the subspace \mathcal{Y} is defined by the projector functional $\mathcal{P}_{\mathcal{Y}} : L^2(E) \rightarrow \mathcal{Y}$ such that

$$L^2(E) \ni g \mapsto \mathcal{P}_{\mathcal{Y}}g = \sum_{r=1}^R \int_E g Y_r \, dE Y_r \in \mathcal{Y}. \quad (5.17)$$

The basis functions Y_r are the solution of the optimization problem

$$\begin{aligned} & \underset{Y_1, \dots, Y_R}{\text{minimize}} && \sum_{b=1}^{N_s} \int_E (g^b - \mathcal{P}_{\mathcal{Y}}g^b)^2 \, dE \\ & \text{subject to} && \int_E Y_\mu Y_\nu \, dE = \delta_{\mu\nu} \quad \forall \mu, \nu = 1, \dots, R. \end{aligned} \quad (5.18)$$

In order to numerically solve the POD problem (5.17), let the snapshots and the basis functions be stored in matrices

$$G = \begin{bmatrix} g^1(\mathbf{x}_1) & g^2(\mathbf{x}_1) & \cdots & g^{N_s}(\mathbf{x}_1) \\ g^1(\mathbf{x}_2) & g^2(\mathbf{x}_2) & \cdots & g^{N_s}(\mathbf{x}_2) \\ \vdots & \vdots & \ddots & \vdots \\ g^1(\mathbf{x}_{N_x}) & g^2(\mathbf{x}_{N_x}) & \cdots & g^{N_s}(\mathbf{x}_{N_x}) \end{bmatrix} \in \mathbb{R}^{N_x \times N_s} \quad (5.19)$$

and

$$[Y] = \begin{bmatrix} Y_1(\mathbf{x}_1) & Y_2(\mathbf{x}_1) & \cdots & Y_R(\mathbf{x}_1) \\ Y_1(\mathbf{x}_2) & Y_2(\mathbf{x}_2) & \cdots & Y_R(\mathbf{x}_2) \\ \vdots & \vdots & \ddots & \vdots \\ Y_1(\mathbf{x}_{N_x}) & Y_2(\mathbf{x}_{N_x}) & \cdots & Y_R(\mathbf{x}_{N_x}) \end{bmatrix} \in \mathbb{R}^{N_x \times R}, \quad (5.20)$$

respectively, with N_x the number of quadrature points in E . Moreover, let $W \in \mathbb{R}^{N_x \times N_x}$ be the symmetric positive definite matrix of weights for a quadrature rule integration. Thus problem (5.17) is rewritten as

$$\begin{aligned} & \underset{[Y]}{\text{minimize}} && \|G - [Y][Y]^T W G\|_{F_W}^2 \\ & \text{subject to} && [Y]^T W [Y] = I, \end{aligned} \quad (5.21)$$

where, for a generic matrix A , $\|A\|_{F_W}^2 := \text{tr}(A^T W A)$ is the Frobenius' norm associated to the scalar product defined by W . By defining matrix $\hat{G} = (W^{\frac{1}{2}})^T G$, with $W = W^{\frac{1}{2}}(W^{\frac{1}{2}})^T$ the Cholesky decomposition of weight matrix W , its truncated SVD reads $\hat{G} \simeq U_R \Sigma_R V_R^T$. Due to the Eckart-Young theorem [42], problem (5.21) is solved

by

$$[Y] = (W^{\frac{1}{2}})^{-T} U_R. \quad (5.22)$$

5.3 Hyper-reduction

For the resolution of problem (5.13), matrices as well as convective-diffusive components, force term and previous solution vectors in (5.12) have to be computed. Let $E \subseteq \bar{\mathcal{B}}$ be a subset of the space-time cylinder $\mathcal{B} = \Omega(t) \times (t^n, t^{n+1})$ (in particular, it could be the cylinder \mathcal{B} itself, or the lower base Ω^n or the upper base Ω^{n+1} or the union of all the space-time manifolds Γ_{ij}^n). Moreover, let $\mathcal{T}_E = \{E_i\}_{i=1}^{N_E}$ be a partition of set E such that $E = \bigcup_{i=1}^{N_E} E_i$, with $E_i \cap E_j = \emptyset$ for any $i \neq j$. All the algebraic components in (5.12) can be defined in an abstract form from the following functionals $\mathcal{H}_E^z : V_M \times V_M \rightarrow \mathbb{R}$ such that

$$V_M \times V_M \ni (f, g) \mapsto \mathcal{H}_E^z[f, g] := \sum_{i=1}^{N_E} \int_{E_i} \delta_1 f \delta_2 g \, dE \in \mathbb{R}, \quad (5.23)$$

and $\mathcal{P}_{V_M, m} : L^2(\mathcal{B}) \rightarrow \mathbb{R}$, for any $m = 1, \dots, M$ defined as

$$L^2(\mathcal{B}) \ni h \mapsto \mathcal{P}_{V_M, m} h := \int_{\mathcal{B}} h \Phi_m \, d\mathcal{C} \in \mathbb{R}. \quad (5.24)$$

For functional (5.23), the local operators δ_1 and δ_2 represent any derivative up to the first order among the identity I and ∂_t, ∂_x or ∂_y . The derivative in time is always possible to perform for functions in V_M since any map \mathcal{M}_i is always continuous in time. In addition, since the functional \mathcal{H}_E^z is defined as sum of integrals over any cell E_i , the derivatives in space have sense because functions in V_M are discontinuous over E but their restriction over the single cell E_i , for any $i = 1, \dots, N_E$, is regular enough for first order space derivatives. Functionals in (5.24) represent the projection of any function in $L^2(\mathcal{B})$ along the m -th basis component of V_M .

Remark 5.3.1. Functional \mathcal{H}_E^z depends on the configuration of the space and, eventually, time of set E . The configuration is led by the value of the parameter z .

For the sake of simplicity, we present the hyper-reduction over functional \mathcal{H}_E^z ; the hyper-reduction for projectors (5.24) easily follows. Let $\hat{E} \subseteq \bar{\mathcal{C}}$ such that $\mathcal{M}_i(\hat{E}) \equiv E_i$. For the reference cell \hat{E} it is possible to define N_{int} quadrature nodes $\{\hat{x}_j\}_{j=1}^{N_{int}}$ associated to weights $\{\omega_j\}_{j=1}^{N_{int}}$. Since functional \mathcal{H}_E^z takes input in V_M , its computation for any $f, g \in V_M$ is totally described by the computation over the basis components Φ_l and Φ_m , for any couple $l, m = 1, \dots, M$. Therefore, at discrete level, it holds

$$\begin{aligned} \mathcal{H}_E^z[\Phi_l, \Phi_m] &= \sum_{i=1}^{N_E} \int_{E_i} \delta_1 \Phi_l \delta_2 \Phi_m \, dE = \sum_{i=1}^{N_E} \int_{\hat{E}} (\delta_1 \Phi_l \circ \mathcal{M}_i) (\delta_2 \Phi_m \circ \mathcal{M}_i) D_z^i \, d\hat{E} \\ &\simeq \sum_{i=1}^{N_E} \sum_{j=1}^{N_{int}} \omega_j (\delta_1 \Phi_l \circ \mathcal{M}_i)_j (\delta_2 \Phi_m \circ \mathcal{M}_i)_j D_{z,j}^i \end{aligned} \quad (5.25)$$

where $(\delta_1 \Phi_l \circ \mathcal{M}_i)_j = (\delta_1 \Phi_l \circ \mathcal{M}_i)(\hat{x}_j)$ and $(\delta_2 \Phi_m \circ \mathcal{M}_i)_j = (\delta_2 \Phi_m \circ \mathcal{M}_i)(\hat{x}_j)$. Integral (5.25) is performed over the reference cell \hat{E} through map \mathcal{M}_i for two reasons: this numerically simplifies the computation of the integral via a quadrature rule

TABLE 5.1 – Characteristics of the generator functional \mathcal{H}_E^z for the hyper-reduction with respect to matrices in (5.12). Numbers N and N_{edges} are the total number of cells and the total number of edges, respectively. For matrix A , the definition of the metric D_z^i depends on the integration domain Γ_{ij}^n . Vector \mathbf{n}_{ij} is the unit outward normal to manifold edge Γ_{ij}^n . Physical variable χ can be either x or y .

	E_i	δ_1	δ_2	D_z^i	\hat{E}	N_E	N_{int}
M^1	Ω_i^{n+1}	I	I	$ x_{\xi}y_{\eta} - x_{\eta}y_{\xi} _{\tau=1}$	$(0, 1)^2$	N	9
A	Γ_{ij}^n	I	I	$ \text{Cof}(J)\mathbf{n}_{ij} $	$(0, 1)^2$	N_{edges}	9
K_t	\mathcal{C}_i^n	∂_t	I	$ \det J_i $	$(0, 1)^3$	N	27
K_{χ}	\mathcal{C}_i^n	I	∂_{χ}	$ \det J_i $	$(0, 1)^3$	N	27

and because in the prediction step of ADER approach usually the snapshots are collected with respect to the reference system (ξ, η, τ) ; consequently the reduced basis spanning V_M from the offline stage is still defined over the reference cell. Consequently, the geometrical information of the integral over E_i is stored in the generic metric component² D_z^i which depends on the particular configuration of E , i.e. on the specific value of the parameter z . Table (5.1) resumes all the characteristics of the generator functional \mathcal{H}_E^z . Regarding the m -th projector functional $\mathcal{P}_{V_M, m}$, for vectors \mathcal{F}_{χ} , \mathbf{f} and \mathbf{u}_{old} , the input functions are F_{χ} , f and u^n , respectively. The total number of quadrature points for computing the projector outputs is NN_{int} , with $N_{int} = 27$.

The total number of quadrature nodes is $N_E N_{int}$. The goal in the hyper-reduction stage is to find a number $N_{hr} \ll N_E N_{int}$ of quadrature points among all in order to alleviate the computational costs for assembling matrices and vectors. Thus, a new set of weights needs to be found. Let $\{\tilde{\omega}_j^i\}_{j=1}^{N_{int}}$ be the set of new weights such that only N_{hr} among them are strictly positive with the remaining ones assuming value 0. Moreover, let

$$c_{j,k}^{(l,m),i} = (\delta_1 \Phi_l \circ \mathcal{M}_i)_j (\delta_2 \Phi_m \circ \mathcal{M}_i)_j D_{z_k, j}^i$$

be the integrating discretized function associated to cell E_i over the quadrature node \hat{x}_j in the configuration given by the k -th parameter z in the dataset for the couple of basis function Φ_l and Φ_m , for $l, m = 1, \dots, M$, $i = 1, \dots, N_E$, $j = 1, \dots, N_{int}$ and $k = 1, \dots, N_z$. Inspired by [95], the new quadrature points and weights are determined simultaneously in the offline stage by approximating the hyper-reduction system

$$C\tilde{\omega} \simeq \mathbf{d}, \quad (5.26)$$

2. For example, if E_i is the space-time cell \mathcal{C}_i^n , the metric component is given by the absolute value of the determinant of the Jacobian tensor associated to the transformation map \mathcal{M}_i .

with

$$C = \begin{bmatrix} C^{1,1} \\ C^{2,1} \\ \vdots \\ C^{M,1} \\ C^{1,2} \\ \vdots \\ C^{1,M} \\ \vdots \\ C^{MM} \end{bmatrix} \in \mathbb{R}^{M^2 N_z \times N_E N_{int}},$$

whose blocks are

$$C^{l,m} = \begin{bmatrix} c_{1,1}^{(l,m),1} & \cdots & c_{N_{int},1}^{(l,m),1} & c_{1,1}^{(l,m),2} & \cdots & c_{N_{int},1}^{(l,m),2} & \cdots & c_{1,1}^{(l,m),N_E} & \cdots & c_{N_{int},1}^{(l,m),N_E} \\ c_{1,2}^{(l,m),1} & \cdots & c_{N_{int},2}^{(l,m),1} & c_{1,2}^{(l,m),2} & \cdots & c_{N_{int},2}^{(l,m),2} & \cdots & c_{1,2}^{(l,m),N_E} & \cdots & c_{N_{int},2}^{(l,m),N_E} \\ \vdots & \ddots & \vdots & \vdots & \ddots & \vdots & \ddots & \vdots & \ddots & \vdots \\ c_{1,N_s}^{(l,m),1} & \cdots & c_{N_{int},N_s}^{(l,m),1} & c_{1,N_s}^{(l,m),2} & \cdots & c_{N_{int},N_s}^{(l,m),2} & \cdots & c_{1,N_s}^{(l,m),N_E} & \cdots & c_{N_{int},N_s}^{(l,m),N_E} \end{bmatrix} \in \mathbb{R}^{N_z \times N_E \cdot N_{int}},$$

$$\tilde{\omega} = [\tilde{\omega}_1^1, \cdots, \tilde{\omega}_{N_{int}}^1, \cdots, \tilde{\omega}_1^{N_E}, \cdots, \tilde{\omega}_{N_{int}}^{N_E}]^T \in \mathbb{R}^{N_E N_{int}}$$

and

$$d = \begin{bmatrix} d^{1,1} \\ d^{2,1} \\ \vdots \\ d^{M,1} \\ d^{1,2} \\ \vdots \\ d^{1,M} \\ \vdots \\ d^{MM} \end{bmatrix} \in \mathbb{R}^{M^2 N_z},$$

whose components are

$$d^{l,m} = [\mathcal{H}_E^{z_1}[\Phi_l, \Phi_m], \cdots, \mathcal{H}_E^{z_{N_z}}[\Phi_l, \Phi_m]]^T \in \mathbb{R}^{N_z}.$$

The quadrature weights have to be non-negative and approximate system (5.26). Thus they are looked in the set $\Lambda = \{\omega \in \mathbb{R}_+^{N_E N_{int}} : \|C\omega - d\|_2 \leq \epsilon \|d\|_2\}$, depending on a certain fixed tolerance ϵ , such that

$$\tilde{\omega} = \arg \min_{\omega \in \Lambda} \|\omega\|_0, \quad (5.27)$$

with $\|\cdot\|_0$ the ℓ_0 -pseudo-norm. Problem (5.27) is NP-hard. For this reason it is replaced by the non-negative least square minimization problem

$$\tilde{\omega} = \arg \min_{\omega \in \mathbb{R}_+^{N_E N_{int}}} \|C\omega - d\|_2^2. \quad (5.28)$$

Problem (5.28) is solved through the algorithm explained in Section 3 of Chapter 23 of [71]. This algorithm promotes the sparsity in the solution and terminates when the stopping criterion $\|C\tilde{\omega} - d\|_2 \leq \epsilon \|d\|_2$ is fulfilled. The accuracy of the integral

tends to be the one provided by the full integration as the hyper-reduction tolerance ϵ vanishes. Once the new weights $\tilde{\omega}$ are found, the new quadrature nodes are the ones corresponding to the nonzero new weights.

When the solution of hyper-reduction problem (5.26) is approximated, the full weight matrix W involved in the computation of integrals is replaced by the hyper-reduced weight matrix \tilde{W} provided by the new weights $\tilde{\omega}$.

Remark 5.3.2. *The approximated integral by using all quadrature nodes as in (5.25) strictly depends on the metric of the integral, thus on the specific configuration in space and time of integration domain E . The hyper-reduction stage allows to define a subset of quadrature points and weights for any admissible configuration as stored in the dataset of snapshots.*

Remark 5.3.3. *As for the full model, also for the reduced model of ADER, in the prediction stage, there are matrices that can be pre-computed once for all and others for which this is not possible. Matrices in (5.12) depend on the deformation at any time. Thus, they have to be computed at each time instance. The hyper-reduction stage outlines a strategy for accelerating and alleviating the computation.*

5.4 Numerical results

In this section we present a linear and a nonlinear test case for numerically validating the reduced and hyper-reduced ADER algorithm. For both test cases, the evolving domain is

$$\Omega(t; z) = (-\pi, \pi) \times (-2\pi, 2\pi) / \left\{ (x, y) \in \mathbb{R}^2 : x^2 + (y + zt)^2 < 0.5^2 \right\}, \quad (5.29)$$

representing a vertical channel with a removed vertically moving circle of radius 0.5 moving in time $t \in (0, 1.5)$ whose velocity is the parameter $z \in Z = [-2, 2]$. In particular, the motion equation for the foreground mesh has a velocity force term

$$\mathbf{V} = [0, z]^T.$$

At time $t = 0$ the circle has center in the origin of axes, successively it can move along y -axis towards $-\infty$ if $z < 0$ or $+\infty$ if $z > 0$. Around the removed circle, a polar grid with radius from 0.5 to 1.5 is built. It represents the foreground moving mesh. On the background a Cartesian grid discretizes the remaining zones of the channel. Both the background and foreground meshes are composed of cells whose size is approximately $h_0 = 1.5 \times 10^{-1}$ (for example, see Figures 5.1 or 5.6). For both test cases, the dataset is composed of predicted and corrected high-fidelity solution any $5\Delta t$ ($\Delta t = \text{CFL}h_0/\|\boldsymbol{\beta}\|$, with $\text{CFL} = 0.4$ and $\boldsymbol{\beta}$ being the advective field) for time velocities $z \in \{-2 + 0.5k\}_{k=0}^8$ (consequently $N_z = 9$).

The accuracy of the ROM with respect to the HFM is evaluated by measuring the mismatch between the reduced solution and the high-fidelity solution accordingly to the relative space-time error:

$$\text{Error} = \sqrt{\frac{\int_0^T \int_{\Omega(t)} (u_{\text{HFM}} - u_{\text{ROM}})^2 \, d\Omega \, dt}{\int_0^T \int_{\Omega(t)} u_{\text{HFM}}^2 \, d\Omega \, dt}}. \quad (5.30)$$

For both linear and nonlinear test cases, the total number of cells composing the foreground mesh is $N_{fg} = 767$. Thus, since for the prediction step the number of quadrature points into any cell is $N_{int} = 27$, the problem reduces from $N_{fg}N_{int} =$

20709 DOFs to M DOFs. Regarding the corrected solution, if it is composed of 767 DOFs in the HFM, it is described by L DOFs after the projection over \mathcal{U}_L .

5.4.1 Linear test case

The linear test case is characterized by an advective-diffusive term

$$F(u; \nabla u) = \beta u - \nu \nabla u,$$

where the advective field $\beta = [1, 1]^T$ and the diffusive term $\nu = 5 \times 10^{-2}$. The force term f of the equation is such that the exact solution of the problem is

$$u_{ex}(x, y, t; z) = \exp(-x^2 - (y + zt)^2 + 0.5^2) + \cos(x - 0.5t) \sin(y - 0.5t).$$

On the boundaries of the domain and at the origin of time, the numerical solution is imposed to be the exact solution.

For this test case, three ROM solutions are recovered for three different definition of parameter z :

- *in-sample velocity*: constant velocity $z \equiv 1$, which is a value of the parameter z already stored in the dataset and used to build the reduced basis with the other values of z ;
- *out-of-sample velocity*: constant velocity $z \equiv 0.8$ which is a value of parameter z not characterizing the solutions stored in the dataset;
- *variable velocity*: variable velocity $z(t) = 2 \cos(4t)$; this test case evaluates the method not considering a constant velocity but a variable velocity whose absolute value is always in $Z = (-2, 2)$.

In figure 5.1 there are the high-fidelity solutions at final time $t = 1.5$ for some values of cylinder velocity z . For the same time instance, the output of the ROM solutions are in Figure 5.2.

For both in-sample and out-of-sample reconstruction, no hyper-reduction is used. For the last case, i.e. for the variable velocity, both only reduced and hyper-reduced numerical solutions are defined. In Figure 5.3 there are reported the reduced coefficients for the prediction step as functions of time. We remark that these coefficients do not refer to the specific time instance t^n but to all times in $[t^n, t^{n+1})$. In Figure 5.4 the plots of the errors between the reduced and hyper-reduced solutions are reported. After the 6th mode the errors are less than 0.25%. For the hyper-reduction, in Table 5.2 the number of quadrature points used for the different integrals are reported. With respect to Figure 5.5 which depicts the percentage ratio between the number N_{hr} of hyper-reduced quadrature points and the total number of quadrature points $N_E N_{int}$, for the variable velocity, from the 8th mode, the error is around 0.25% for both reduced and hyper-reduced methods. These results is obtained despite the values of the numbers of quadrature points reduce to less than 111 for $E = \Omega$, 230 for $E = \cup_{ij} \Gamma_{ij}^n$ and 332 for $E = \mathcal{B}$ with respect to the total numbers of quadrature points reported in Table 5.2.

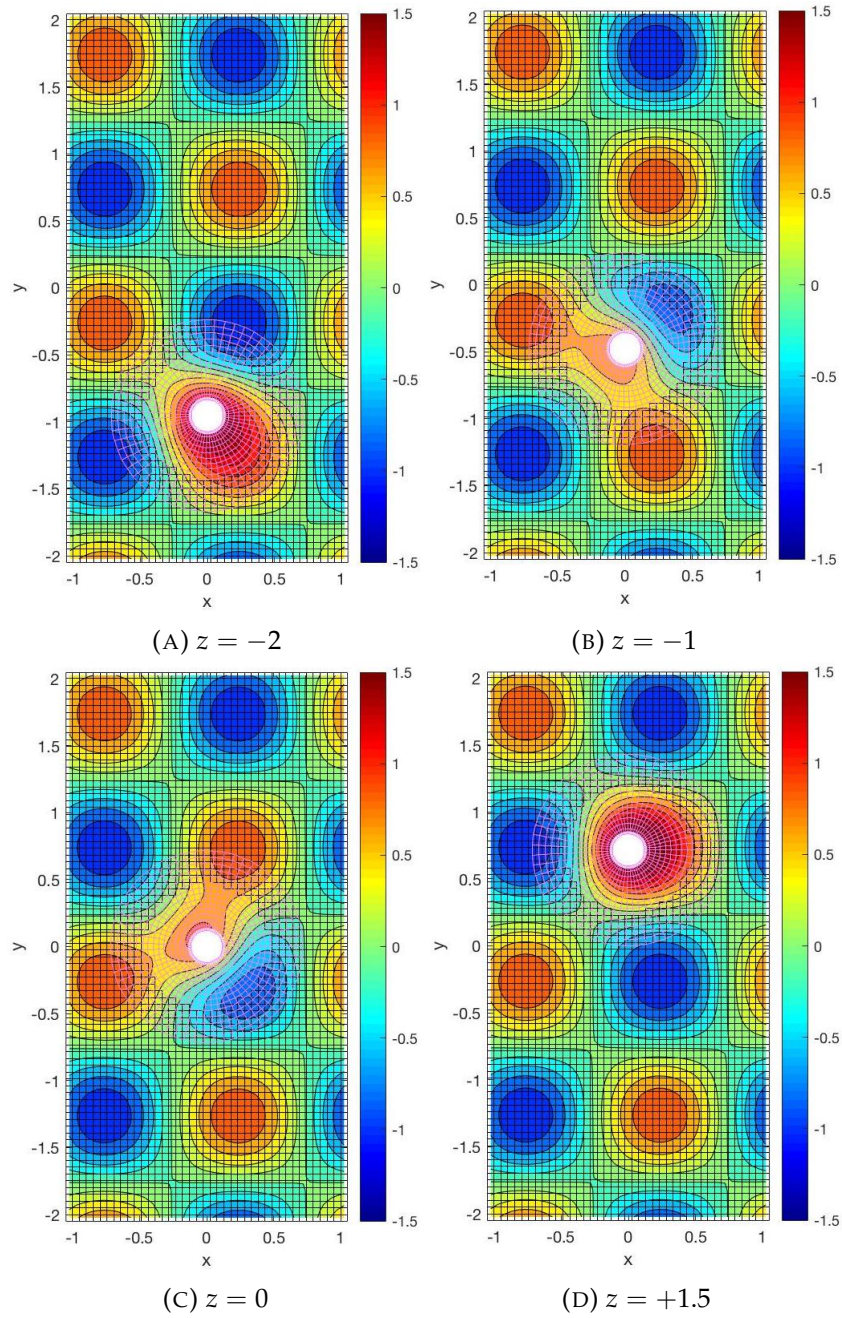
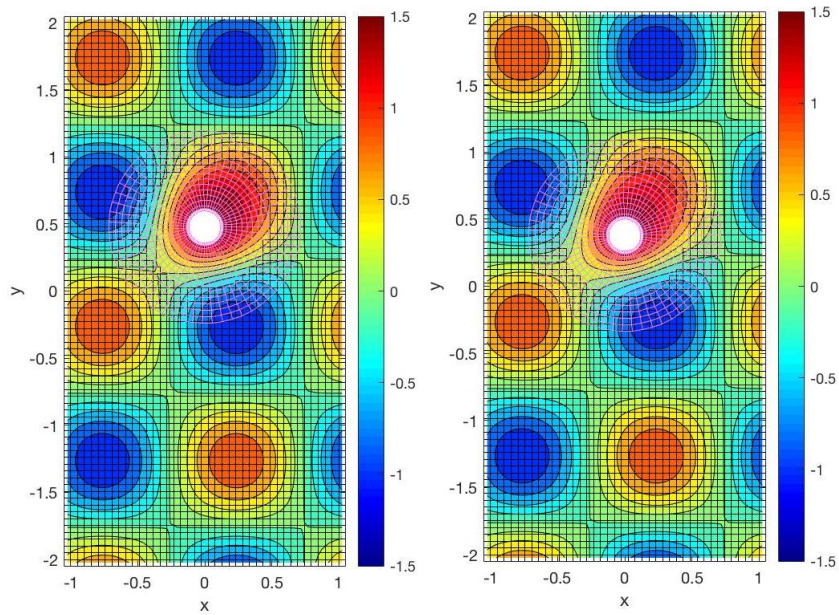
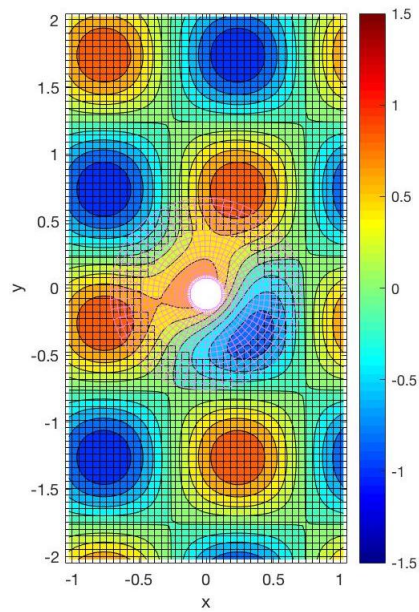


FIGURE 5.1 – High-fidelity solution at time $t = 1.5$ for the linear test case for some instances of cylinder velocity z .

TABLE 5.2 – Total number $N_E N_{int}$ of quadrature points with respect to the domain integration E .

E	N_E	N_{int}	$N_E N_{int}$
Ω	767	9	6903
$\cup_{ij} \Gamma_{ij}^n$	1594	9	14346
\mathcal{B}	767	27	20709

(A) In-sample, $z = +1$ (B) Out-of-sample, $z = +0.8$ (C) Variable velocity, $z(t) = 2 \cos(4t)$ FIGURE 5.2 – ROM solutions at time $t = 1.5$ for the linear test case.

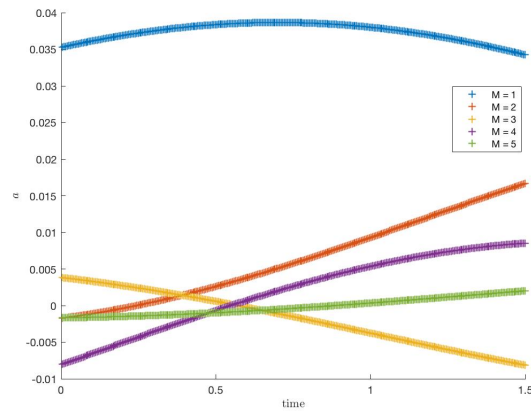
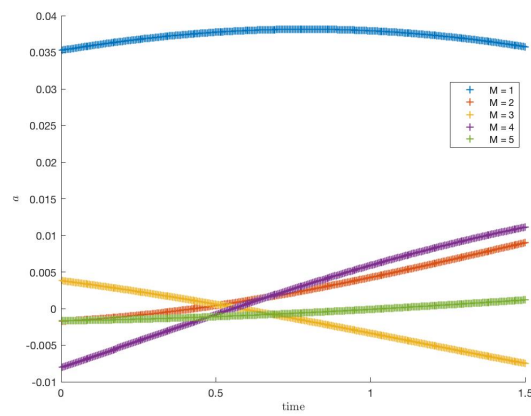
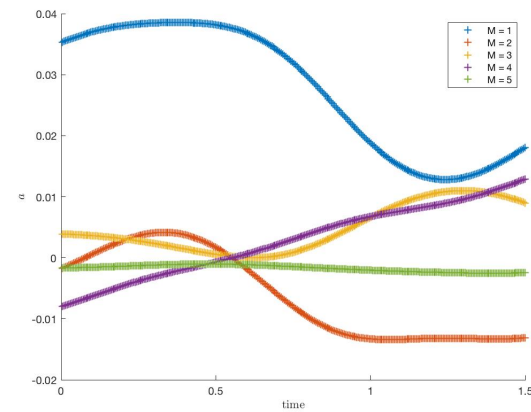
(A) In-sample, $z = +1$ (B) Out-of-sample, $z = +0.8$ (C) Variable velocity, $z(t) = 2 \cos(4t)$

FIGURE 5.3 – Evolution of the first five reduction coefficients for the in-sample, out-of-sample and variable velocity reconstruction. These coefficients do not refer to the specific time instance t^n but to all times in $[t^n, t^{n+1})$.

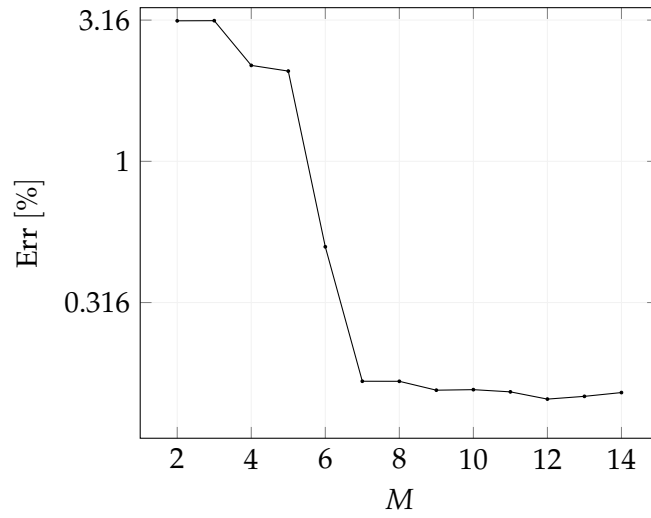
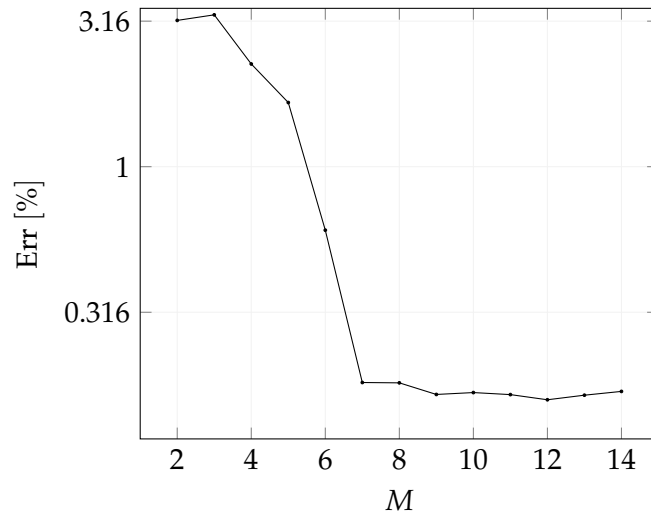
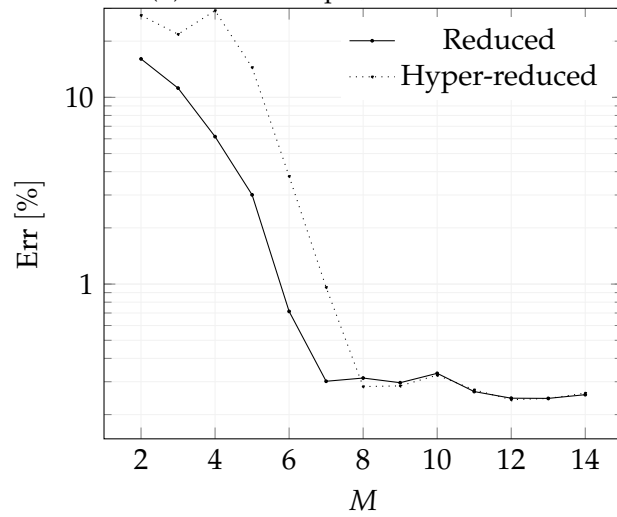
(A) In-sample, $z = +1$ (B) Out-of-sample, $z = +0.8$ (C) Variable velocity, $z(t) = 2 \cos(4t)$

FIGURE 5.4 – Error analysis for the linear test case. Both in-sample and out-of-sample reconstructions are only reduced. For the last case, the errors refer to the reduced and hyper-reduced numerical solutions.

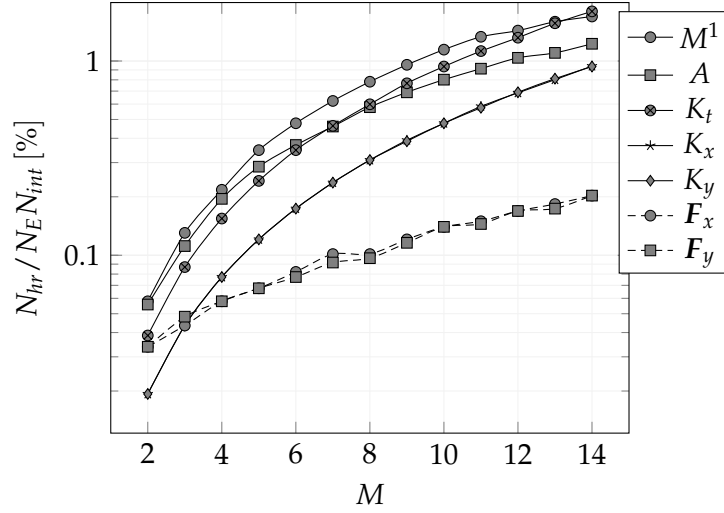


FIGURE 5.5 – Percentage analysis of $N_{hr}/(N_E N_{int})$ as function of the number of modes for the linear test case. The reference number of integration points is reported in the last column of Table 5.2.

5.4.2 Nonlinear test case

The nonlinear test case formally reads

$$\begin{cases} \partial_t u + \nabla \cdot F(u, \nabla u) = 1 & \text{in } \Omega(t) \times (0, T) \\ u \equiv 0 & \text{on } \Gamma_D \times (0, T) \\ u = z & \text{on } \Gamma_B(t) \times (0, T) \\ \nabla u \cdot \mathbf{n} = 0 & \text{on } \Gamma_N \times (0, T) \\ u = u_0(\mathbf{x}) & \text{in } \Omega(0) \times \{0\} \end{cases}$$

where the final time $T = 1.5$ and the domain $\Omega(t; z)$ is the same as the previous linear test case. Boundary surfaces Γ_N and $\Gamma_B(t)$ are the bottom of the channel and the surface of the moving cylinder, respectively; consequently $\Gamma_N = \partial\Omega(t)/(\Gamma_N \cup \Gamma_B(t))$. As for the previous test case, the dynamics of the moving cylinder is led by the vertical velocity $z \in Z = [-2, 2]$. The convection-diffusion term is defined as

$$F(u, \nabla u) = \begin{bmatrix} 0 \\ -z \end{bmatrix} \tanh(u) u - \nu \nabla u,$$

with $\nu = 5 \times 10^{-2}$. Because of the hyperbolic tangent of the solution in the convective part, the equation is nonlinear. Finally, the initial condition is

$$u_0(x, y) = \frac{1}{2\pi^3} (y - 2\pi)(x^2 - \pi^2).$$

This test case is particularly affected by the parameter z . As a matter of fact, it defines the value of the solution at the boundary $\Gamma_B(t)$ and it modulates the convective component along the y direction. Moreover, when the cylinder does not move, i.e. when $z \equiv 0$, the convective component in F vanishes and the problem turns into a linear heat equation on a non-evolving domain closed with mixed homogeneous Dirichlet - Neumann conditions. Consequently, the parameter z also defines the nature of the local operator and, consequently, of the equation itself. We remark that, for this test case (as for the previous one), the most relevant dynamics is around the

moving cylinder because of the strong boundary condition imposed on its surface.

In Figure 5.6 the high-fidelity solution at final time $t = 1.5$ for some instances of the cylinder velocity z are reported. Figure 5.7 depicts the considered ROM solutions at final time $t = 1.5$.

The ROM and HR solution is recovered in the following cases:

- *in-sample velocity*: constant velocity $z \equiv 1$, which is a solution stored in the dataset in the offline stage;
- *variable velocity*: quadratically variable velocity $z(t) = 8t^2/9$; in this case the values of the velocity go from a minimum of 0 to the maximum value 2 (i.e. all the possible positive velocities stored in the dataset).

In Figure 5.6 the high-fidelity solution at final time $t = 1.5$ for some instances of the cylinder velocity z are reported. Figure 5.7 depicts the considered ROM solutions at final time $t = 1.5$.

For the in-sample reconstruction, the hyper-reduction is not applied. On the contrary, a comparison between the reduced and the hyper-reduced techniques is performed for the test case with a variable velocity. The plots of the first five reduced coefficients for the two test cases are in Figure 5.8. The errors of the two test cases are plotted in Figure 5.9. With respect to the linear test case, for both nonlinear tests the errors start around a value of 35% but at the 14th mode they are slightly larger than 1%, despite of the nonlinear dynamics governing the problem. Since the used overset mesh is the same of the previous linear test case, information regarding the total number of quadrature points in Table 5.2 is valid also for the nonlinear problem. After the 4th mode, the errors of the reduced and hyper-reduced mode for the variable velocity are almost the same even though the number of quadrature points for the hyper-reduced solution is less than 2% with respect to the total number of quadrature points. In particular, for hyper-reduced solution with 14 modes (corresponding to the maximum percentage of used quadrature points), when $E = \Omega$ the number of quadrature points reduces from 6903 to 118, when $E = \bigcup_{ij} \Gamma_{ij}^n$ it reduces from 14346 to 244 and when $E = \mathcal{B}$ from 20709 to 352. The hyper-reduction seems to not affect the error with respect to the just reduced solution.

5.5 Conclusions and future perspectives of the chapter

We presented a former reduced and hyper-reduced formulation for ADER based on a Proper Orthogonal Decomposition approach in a domain decomposition frame over an overset grid. In particular, on several parameter settings for a linear and nonlinear test cases, we analyzed the mismatch between the high-fidelity solution and the reduced/hyper-reduced numerical solution. No spurious oscillations are observed due to the movement of the foreground mesh over the background mesh. For the presented test cases, the reduction in terms of degrees of freedom goes from $\mathcal{O}(10^5)$ to $\mathcal{O}(1) \sim \mathcal{O}(10)$, with no significant loss in the precision of the solution. Moreover, the hyper-reduction training in the offline stage allows to compute the matrices involved in the algebraic counterpart of the scheme by using less than the 2% of the total number of quadrature points by not affecting the computed errors.

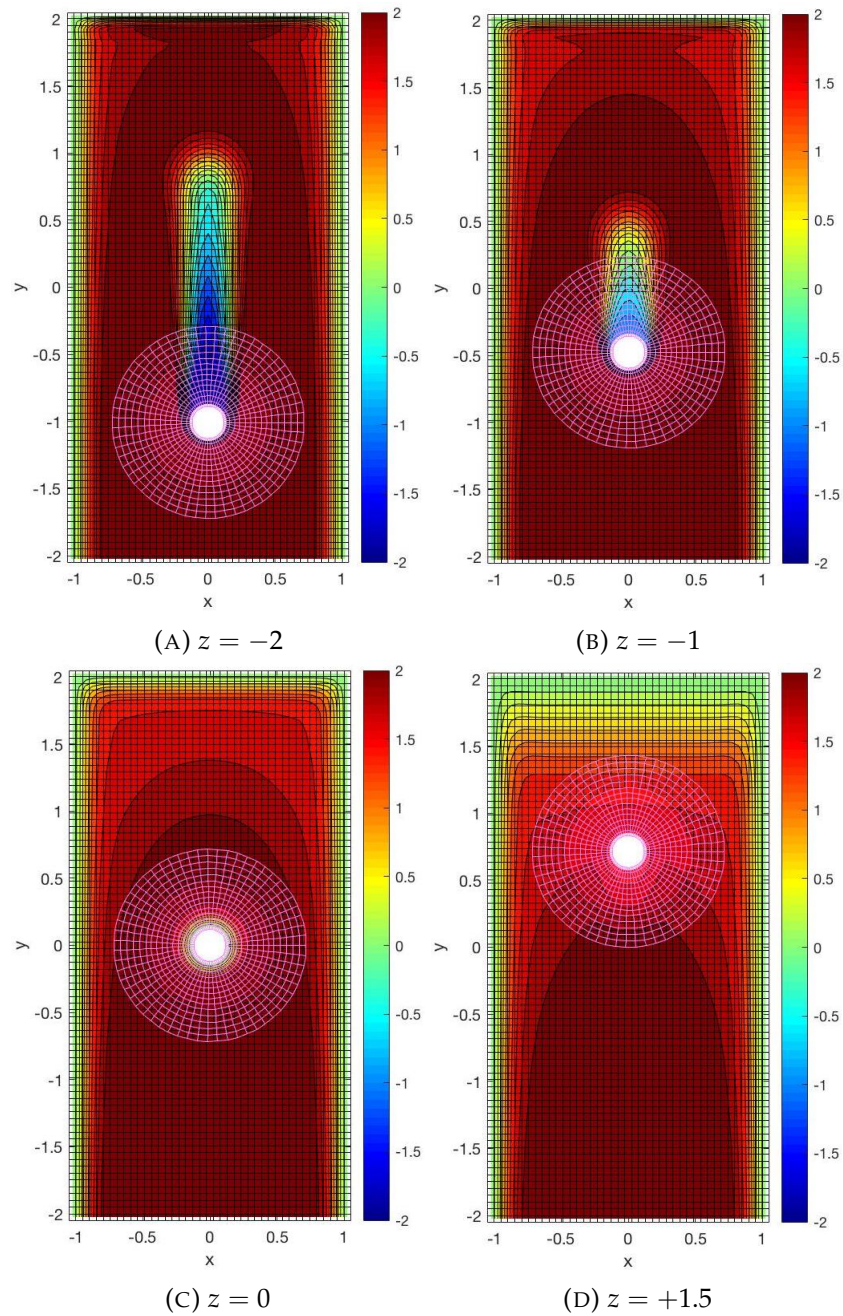


FIGURE 5.6 – High-fidelity solution at time $t = 1.5$ for the nonlinear test case for some instances of cylinder velocity z .

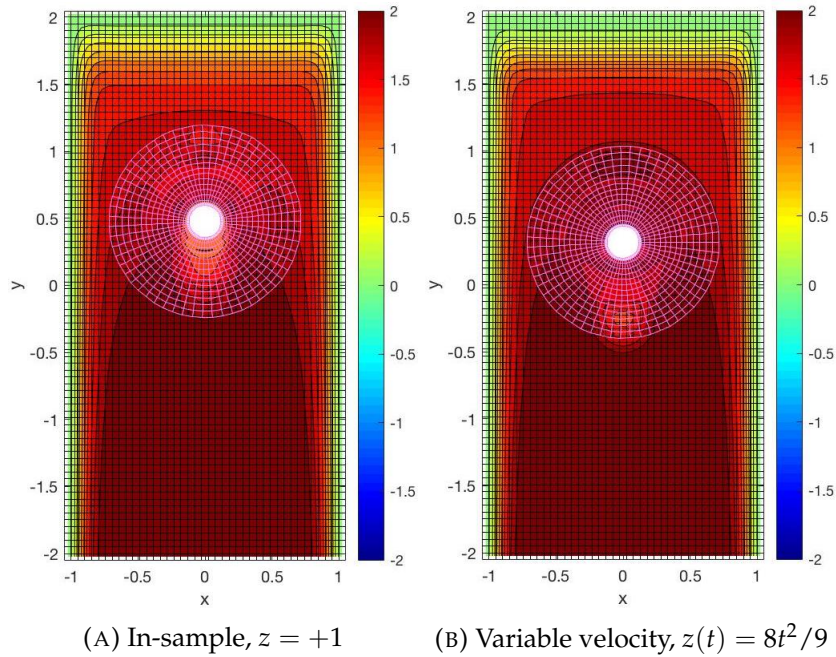


FIGURE 5.7 – ROM solutions at time $t = 1.5$ for the nonlinear test case.

Future investigations will extend the integration of the scheme to incompressible flows. Moreover, since the nature of the prediction reduced parameters do not depend on the time instance but rather on the time-dimension of the space-time cylinder \mathcal{B} , future perspectives address on using a larger time step in the online stage with respect to the one used in the offline stage in order to enhance the computational times.

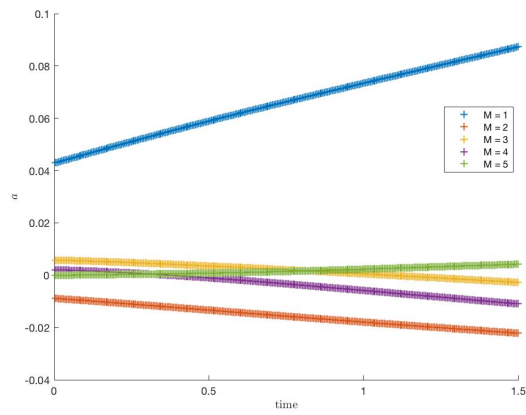
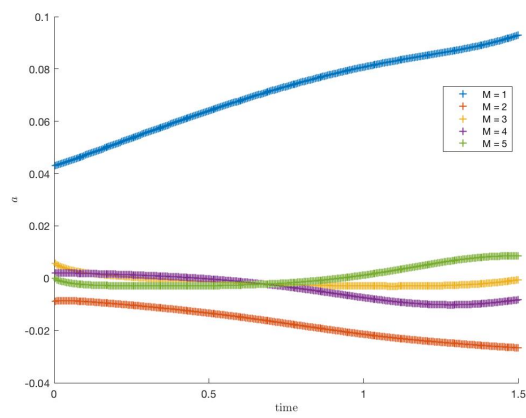
(A) In-sample, $z = +1$ (B) Variable velocity, $z(t) = 8t^2/9$

FIGURE 5.8 – Evolution of the first five reduction coefficients for the in-sample and variable velocity reconstructions. These coefficients do not refer to the specific time instance t^n but to all times in $[t^n, t^{n+1})$.

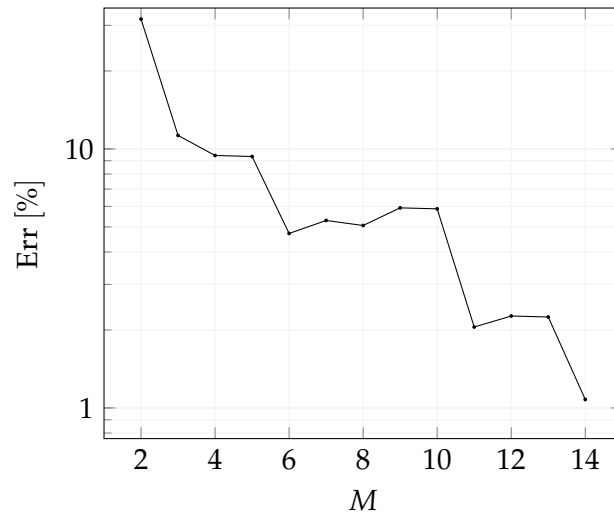
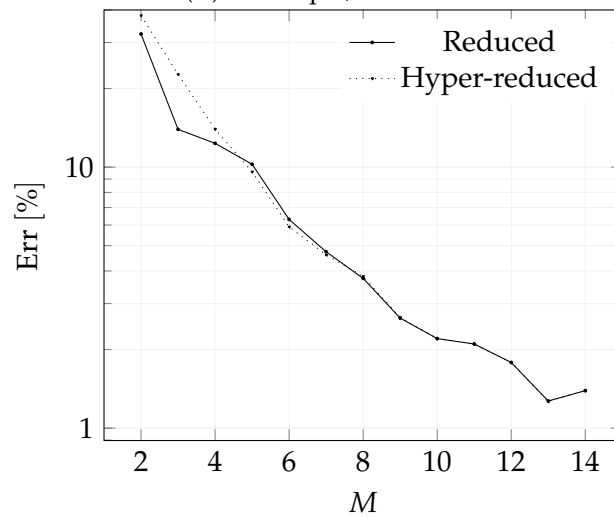
(A) In-sample, $z = +1$ (B) Variable velocity, $z(t) = 8t^2/9$

FIGURE 5.9 – Error analysis for the nonlinear test case. The in-sample reconstruction is only reduced. For the other case, the errors refer to the reduced and hyper-reduced numerical solutions.

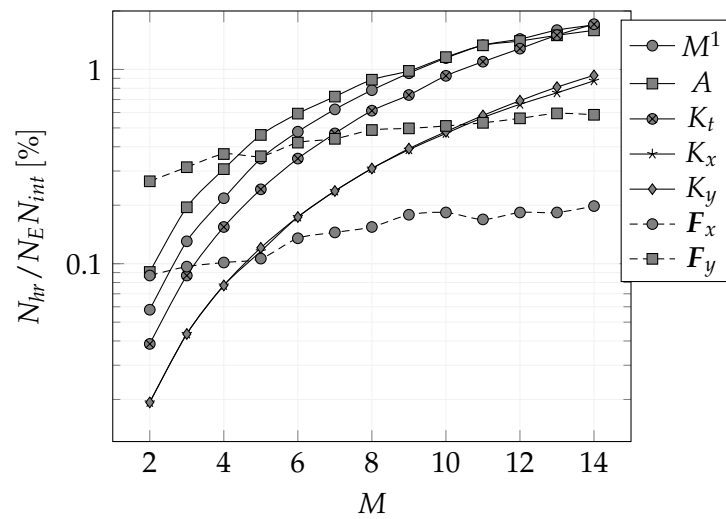


FIGURE 5.10 – Percentage analysis of $N_{hr} / (N_E N_{int})$ as function of the number of modes for the nonlinear test case. The reference number of integration points is reported in the last column of Table 5.2.

Conclusions

In this thesis we aim to formulate a method for the numerical solution of the incompressible Navier-Stokes equations over complex domains discretized through overset grids.

After some preliminary results in one dimension in Chapter 2, in Chapter 3 we presented a second-order finite volume scheme for unsteady advection-diffusion PDEs on overset grid. The scheme is based on an extension of the ADER method to advection-diffusion equations with compact data transmission conditions from the background to the foreground meshes and *vice versa*. During the prediction step, ADER method is able to recover the numerical solution via a free-mesh approach. For this reason any active cell (namely no hole cells) are undistinguished with respect to their location far or at the overlapping interface. Successively, due to the definition of a compact stencil at the interface, i.e. a hybrid minimal set of cells belonging to different mesh blocks that surround the fringe cell, the corrected solution at the overlapping interface does not need to be interpolated through a subsequent interpolation step.

We also introduced a new stabilization term for approximating the fluxes through a Local Lax-Friedrichs approach. It takes into account both the convective and the diffusive components of the local differential operator and it is obtained by properly relaxing the original problem by turning it into a hyperbolic system. Thus, we introduced a relaxation parameter for which when it is taken smaller than a given constant dependent on the suited order of accuracy of the scheme, it introduces an error which is dominated by the numerical error.

The numerical illustrations for linear and non-linear systems show that background and foreground moving meshes do not introduce spurious perturbation to the solution, uniformly reaching second order accuracy in space and time. In addition, we showed that the speed of the foreground mesh does not influence the stability of the method. Our results also show that the new LLF stabilization speed improves the precision and robustness of the numerical solution and allows a less restrictive CFL condition. Finally, it is shown that several foreground meshes, possibly overlapping and with independent displacements, can seamlessly be employed thanks to this approach.

In Chapter 4 we presented a FV scheme that is second-order accurate in space and time for the solution of the incompressible Navier-Stokes equations with moving meshes. The method is based on the Chorin-Temam fractional step method. The predictor velocity is solved through an extension of the ADER method for a nonlinear convective-diffusive system on a Chimera mesh with a compact data transmission condition for fringe cells, as previously discussed.

The projection step exploits a FV hybrid method for the reconstruction of the pressure gradient. In particular a geometric approach is used for internal cells and a weighted expansion is employed for expressing the gradient along the fringe cells. We proved that the approaches for internal and fringe cells are the same in the limit

of a no-shift overlapping condition, i.e. when the overlapping between two blocks is perfectly aligned for any cell. This result is achieved by properly minimizing a convex function for the local coefficients allowing to take into account both the second-order truncation of the solution and the distribution of data in the local stencil. As previously remarked for the convection-diffusion problem, also for the Poisson equation arising the projection step, an interpolation step is skipped because the discretization itself of the gradient is able to take into account the overlapping configuration.

Also in this case, the numerical results showed that the movement of the mesh does not introduce spurious oscillation to the numerical solution of the problem and that second-order accuracy is preserved in both space and time. In order to test the method, a wide range of canonical cases is exposed. Their validation confirms that the obtained data match the ones from the literature. In particular, results for tests where the exact solution is not available are always closer to the ones obtained by second-order methods. Moreover, at equal accuracy, the total number of cells for the overset grid (namely the degrees of freedom) is reduced by up to two orders of magnitude compared to the ones from the cited literature.

With the sedimentation test case, we introduced a reaction term which is not present *a priori* in the original equation. In particular, we mixed the adapted ADER method for Chimera meshes with a penalization method in order not to cut part of the foreground mesh that overcomes the physical boundaries of the domain. This application highlights the versatility of the proposed method even in proximity of boundaries defined on other mesh blocks.

Finally, in the last Chapter 5 we presented a reduced and hyper-reduced formulation for ADER based on a Proper Orthogonal Decomposition approach in a domain decomposition frame over an overset grid. In particular, on several parameter settings for a linear and nonlinear test cases, we analyzed the mismatch between the high-fidelity solution and the reduced/hyper-reduced numerical solution. No spurious oscillations are observed due to the movement of the foreground mesh over the background mesh. In addition, the solution seems to be not affected by the domain decomposition approach for which the solution is reduced in foreground but still high-fidelity in background.

The reduced ADER formulation gives the opportunity to re-define the method with respect to a macro-cell geometrically outlined by the foreground mesh. In particular, the classical Galerkin projection of ADER is substituted by a projection on particular *broken space*, whose functions are locally continuous in space.

On the other hand, this new reformulation mandatory obliges to compute all the matrices involved in the algebraic counterpart at any time instance. In order to enlighten the consequent computational costs, a hyper-reduction is introduced. Through a training process, it allows to drastically decrease the number of quadrature point over which the integrals are discretized regardless of the evolution of the domain; in other words, the offline hyper-reduction step finds a fixed small set of quadrature points onto which discretize the integrals for any admissible movement of the domain.

For the presented test cases, the reduction in terms of degrees of freedom goes from $\mathcal{O}(10^5)$ to $\mathcal{O}(1) \sim \mathcal{O}(10)$. Moreover, the hyper-reduction training in the offline stage allows to compute the matrices involved in the algebraic counterpart of the scheme by using less than the 2% of the total number of quadrature points by not affecting the computed errors.

Future perspectives

One crucial aspect of the method is the local interpolation of the corrected solution at current time t^n used for the recovery of the predicted solution over the space-time cell $\Omega_i(t) \times (t^n, t^{n+1})$. For hyperbolic equations whose solution eventually present shock waves or large gradients in specific regions of the computational domain a CWENO interpolation is used. For (linear and nonlinear) convection-diffusion equations, due to the non-vanishing diffusion parameter, a simpler interpolation in \mathcal{P}_2 is adopted, i.e. polynomials of degree 2 are employed. However, even for diffusive problems, especially in the presence of nonlinear PDEs, sometimes the solutions may exhibit local characteristics that would be badly represented by simple polynomials of order 2. Since CWENO polynomials for overset grids in one dimension have been shown to describe solutions with large gradients well, also at the overlapping zone, possible extensions could be made in multiple dimensions. This might be possible, moreover, from the fact that a compact stencil was also defined at the overlap interfaces, i.e., for the fringe cells.

As often pointed out in the different chapters, a difference between the contents of this thesis and the state of the art is in the definition of a compact stencil, even at the overlapping interface. This operation facilitates the exchange of information along the fringe cells. In some cases, as for the Poisson equation, it has also allowed to encode already in the gradient approximation the particular geometric configuration of superposition. However for now the search for a compact frontier stencil is only well achieved when the size of the fringe cell is comparable to the cells on the other partition. The compact stencil composition algorithm is essentially based on a minimization of the Euclidean distance of the cell centers in a certain proximity. In the future, some other criteria (for example on more appropriate Euclidean minimization or on the definition of proximity itself) could allow to relax the hypothesis of the comparable aspect ratio among the overlapping cells of different blocks.

The issue of the stability of the scheme remains an open problem in the thesis. The proposed method is definitively explicit and in fact a CFL condition is necessary for the method to remain stable. Through a suitable relaxation of the original problem, we have exhibited a new stabilization term that is more efficient and less restrictive in terms of the definition of the time step Δt . However, its validation remains only numerical. Even in the simplest linear cases, because of the prediction-correction nature of ADER a classical stability analysis remains tricky. In this direction, it should be found a closed formula that links the time step with the imposed convective field with respect to the linear or nonlinear characteristics of the differential problem and the operator characterizing it as well as the features of the chimera mesh.

Such knowledge of the time step would also not only better characterize the properties of the scheme but also help find alternative solutions to the current foreground grid velocity constraint. As a matter of fact, from times t^n to t^{n+1} , the deformation of the grid has to ensure that the region of hole cells turning into active cells is a slice whose length along the deformation direction is at most equal to the aspect ratio of the background cells. Otherwise a loss of information on the new active cells could be incurred. Perhaps other approaches could allow a larger deformation for the grid at equal time step Δt .

The approximation of the gradient operator at the superposition interface, used for the solution of the Poisson problem in the projection step for the incompressible Navier-Stokes equations, showed that, at least in the no-shift configuration, the diamond formula and the analytical approach based on Taylor developments coincided. The necessity to define hybrid methods on chimera grids that are globally conservative at least in trivial configurations is one of the open topics within the scientific community using overset grids. Our proposed hybrid method defines some new directions on the search for such solutions. Further future studies may allow us to refine these techniques and probably find computationally cheap schemes that are at least globally conservative. In fact, the current state of the art proposes schemes with this property that are almost impossible to be applied in 3D and in any case very computationally expensive.

Regarding the reduction and the hyper-reduction, in the future some extensions to incompressible flows problems can be studied by properly extending the reduction to the projection step interesting the Poisson problem for the pressure and by adequately taking into account not known *a priori* overlapping configurations. Moreover the extension to whole blocks could be considered in order to reduce the computational costs also on the background mesh. For now this is not possible because of the change of the hole in background dominated by the movement of the grid in foreground. Therefore, the way the problem is formulated, finding a reduced space defined on the background domain that both includes zones that may or may not exist with respect to the (admissible) grid movement is not possible. Perhaps, further techniques could be taken into account. For example by defining another training offline stage allowing to identify some cells or regions susceptible to the movement over which to evaluate the information as well as to compute the integrals defined by the scheme. This could be done in the same spirit of the offline training stage for finding the small set of nodes for reducing the computational cost of integration via quadrature rule for any admissible movement of the grid.

Some AMR approaches could optimize the number of degrees of freedom in those sub-regions of the space where the solution is essentially free from high gradients and, in general, far enough from the overlapping region. Finally, the extensions to three-dimensional flows as well as the parallelization of the computations can be envisaged.

The extension to the 3D case should inherit the same characteristics of the 2D with respect to the overlapping configuration enrolled either in the different passages of ADER or in the discretization of the local differential operators. In particular, the definition of three-dimensional compact stencil at the interface is needed. Since the algorithm for the definition of a compact stencil is defined on a general Euclidean minimization, the extension should be easily achieved. Moreover the ADER approach, in both the prediction and correction step, can be easily extended to the 3D. Concerning the incompressible Navier-Stokes equations, a problem could be represented by the automatic encoding of the overlapping geometric features for the discretization of the gradient operator. As a matter of fact, more analysis could be conducted in order to prove a generalization of the presented approach to three dimensions.

The presented numerical validations do not consider any parallel computation.

The translation to parallel computations needs to be take into account some considerations. If the ADER method in its predictor step is embarrassingly parallel (because of the restriction of the original problem to the single space-time cell), in the corrector step the partitioning processes on different processors is not a trivial matter. In fact, for evolving domains and especially when the movement of the mesh is not known *a priori*, the partitioning could be defined at any time instance. This creates some open questions on how to manage these processes. Similar considerations apply also to the discretization of other differential operators (e.g. gradient approximation).

Appendix A

The CWENO polynomial

A.1 The non overlapping stencil

The notation of this appendix follows the one introduced in Chapter 2.

Let us consider the basis for $\mathcal{P}_2(\mathcal{S}_j)$ of the polynomial with zero mean over the central cell Ω_j : $\langle 1, x - x_j, [(x - x_j)^2 - h_j^2/12] \rangle$. The optimal polynomial is described as the linear combination of the element of the basis: $P_{\text{opt}}(x) = a[(x - x_j)^2 - h_j^2/12] + b(x - x_j) + c$. Thus the goal is to look for the polynomial coefficients a , b and c . By imposing the WENO condition (2.2), we easily find that $c = U_j$ and

$$\begin{cases} \frac{1}{2} \left[(x_{j-1} - x_j)^2 + \frac{h_{j-1}^2 - h_j^2}{12} \right] a + (x_{j-1} - x_j)b = U_{j-1} - U_j \\ \frac{1}{2} \left[(x_{j+1} - x_j)^2 + \frac{h_{j+1}^2 - h_j^2}{12} \right] a + (x_{j+1} - x_j)b = U_{j+1} - U_j \end{cases} .$$

By recalling that, in the non overlapping configuration, $x_{j-1} - x_j = -(h_{j-1} + h_j)/2$ and $x_{j+1} - x_j = (h_{j+1} - h_j)$, we can rewrite the above system by multiplying the first and the second line by $-1/(x_{j-1} - x_j)$ and $1/(x_{j+1} - x_j)$, respectively:

$$\begin{cases} \frac{1}{6}(2h_{j-1} + h_j)a - b = -\frac{U_j - U_{j-1}}{x_j - x_{j-1}} \\ \frac{1}{6}(2h_{j+1} + h_j)a - b = \frac{U_{j+1} - U_j}{x_{j+1} - x_j} \end{cases} . \quad (\text{A.1})$$

This allows to find that a and b are exactly the polynomial coefficients p_x and p_{xx} , respectively, presented in the section 2.1.1.

Concerning the linear polynomials P_1 and P_2 , they are both represented by choosing the basis $\langle 1, x - x_j \rangle$. In particular, for the former we impose it matches the cell averages U_{j-1} and U_j , for the latter we impose it matches the cell averages U_j and U_{j+1} . For P_1 , it writes as $P_1(x) = a_1(x - x_j) + b_1$. Its polynomial coefficients solve the system

$$\begin{cases} (x_{j-1} - x_j)a_1 + b_1 = U_{j-1} \\ b_1 = U_j \end{cases} ,$$

therefore, $a_1 = U[j - 1, j]$ and $b_1 = U_j$. Following the same for P_2 , it writes as $P_2(x) = a_2(x - x_j) + b_2$, with $a_2 = U[j, j + 1]$ and $b_2 = U_j$. We remark that, for these polynomials, the topology of the overlapping of the stencil does not influence their definition. For this reason, even in the presence of an overlapping, their definitions do not change.

Since it holds that $P_{\text{opt}} = \sum_{\gamma=0}^2 \alpha_\gamma P_\gamma$, we can find the central polynomial P_0 .

A.2 The overlapping stencil

Let the stencil \mathcal{S}_j be composed of two overlapping cells, i.e. $|\Omega_j \cap \Omega_{j+1}| \neq 0$. In this case, for the research of the polynomial, any consideration up to (A.1) in the previous subsection can be replaced. In this configuration the followings hold: $x_{j-1} - x_j = -(h_{j-1} + h_j)/2$ and $x_{j+1} - x_j = (h_{j+1} + h_j)/2 - \sigma$, where the corrector term σ is the measure of the overlapping zone, i.e. $\sigma = |\Omega_j \cap \Omega_{j+1}| = x_j + h_j/2 - x_{j+1} + h_{j+1}/2$. By defining the term

$$\tilde{\sigma}_{j,j+1} = \frac{\sigma[3\sigma - (h_{j+1} + 2h_j)]}{3(h_{j+1} + h_j - 2\sigma)},$$

it can be easily proven that the polynomial coefficients for P_{opt} are

$$p_x = \frac{(h_j + 2h_{j+1} + 6\tilde{\sigma}_{j,j+1})U[j-1, j] + (h_j + 2h_{j-1})U[j, j+1]}{2(h_{j-1} + h_j + h_{j+1} + 3\tilde{\sigma}_{j,j+1})},$$

$$p_{xx} = \frac{3(2h_j + h_{j-1} + h_{j+1} - 2\sigma)U[j-1, j+1]}{2(h_{j-1} + h_j + h_{j+1} + 3\tilde{\sigma}_{j,j+1})}.$$

All the other ingredients involved in the CWENO reconstruction are the same as in the non overlapping configuration.

If the overlapping involves the cells Ω_{j-1} and Ω_j , the corrector term is defined as $\sigma = |\Omega_{j-1} \cap \Omega_j|$. Consequently the lumped corrector term reads:

$$\tilde{\sigma}_{j-1,j} = \frac{\sigma[3\sigma - (h_{j-1} + 2h_j)]}{3(h_{j-1} + h_j - 2\sigma)}.$$

Therefore, the polynomial coefficients for the optimal polynomial in this configuration are

$$p_x = \frac{(2h_{j+1} - h_j)U[j-1, j] + (2h_{j-1} + h_j + 6\tilde{\sigma}_{j-1,j})U[j, j+1]}{2(h_{j-1} + h_j + h_{j+1} + 3\tilde{\sigma}_{j-1,j})},$$

$$p_{xx} = \frac{3(h_{j-1} + 2h_j + h_{j+1} - 2\sigma)U[j-1, j+1]}{2(h_{j-1} + h_j + h_{j+1} + 3\tilde{\sigma}_{j-1,j})}.$$

Appendix B

ADER approach for the 1D advection equation

B.1 The research of the Galerkin predictor solution

Let $\hat{\Omega} = (0, 1)^2$ be the reference space-time domain in which the predictor solution is referred to and looked for. The nodes and the Lagrangian basis are the following:

$$\begin{aligned}\zeta_1 &= (0, 0); & \theta_1(\zeta, \tau) &= 2\zeta^2 + 2\zeta\tau + 2\tau^2 - 3\zeta - 3\tau + 1; \\ \zeta_2 &= (1/2, 0); & \theta_2(\zeta, \tau) &= -4\zeta^2 - 2\tau^2 + 4\zeta + \tau; \\ \zeta_3 &= (1, 0); & \theta_3(\zeta, \tau) &= 2\zeta^2 - 2\zeta\tau + 2\tau^2 - \zeta - \tau; \\ \zeta_4 &= (0, 1/2); & \theta_4(\zeta, \tau) &= -2\zeta\tau - 2\tau^2 + 3\tau; \\ \zeta_5 &= (1/2, 1); & \theta_5(\zeta, \tau) &= 2\tau^2 - \tau; \\ \zeta_6 &= (1, 1/2); & \theta_6(\zeta, \tau) &= 2\zeta\tau^2 - 2\tau^2 + \tau.\end{aligned}$$

Recalling that the matrices K and M are defined as:

$$K_{ij} = \int_{\hat{\Omega}} \partial_\tau \theta_i \theta_j \, d\zeta \, d\tau; \quad M_{ij} = \int_{\hat{\Omega}} \theta_i \theta_j \, d\zeta \, d\tau,$$

their sub-matrices are:

$$\begin{aligned}K^{10} &= \frac{1}{6} \begin{bmatrix} -1 & -2 & 1 \\ 2 & -3 & 2 \\ 1 & -2 & -1 \end{bmatrix}; & K^{11} &= \frac{1}{6} \begin{bmatrix} 1 & 2 & -1 \\ -2 & 3 & -2 \\ -1 & 2 & 1 \end{bmatrix}; \\ M^{10} &= \frac{1}{180} \begin{bmatrix} -19 & 34 & -9 \\ -1 & -4 & -1 \\ -9 & 34 & -19 \end{bmatrix}; & M^{11} &= \frac{1}{180} \begin{bmatrix} 44 & 6 & 4 \\ 6 & 24 & 6 \\ 4 & 6 & 4 \end{bmatrix}.\end{aligned}$$

B.2 Constants in Rusanov flux

In this section we formally derive the constants involved in the integration of the flux approximated through the numerical model by Rusanov.

Let us suppose to want to find the constants for the right side $\partial C_{j,j+1}^n$ of the space-time cell C_j^n . Since $\partial C_{j,j+1}^n$ is a segment in the space-time, the generic point $\tilde{x}_{j,j+1} \in$

$\partial C_{j,j+1}^n$ can be parametrized as:

$$\begin{cases} \tilde{x}_{j,j+1}(\tau) = \beta_1(\tau)X_{j,j+1}^n + \beta_2(\tau)X_{j,j+1}^{n+1} \\ t = t^n + \Delta t \tau \end{cases} . \quad (\text{B.1})$$

In the above parametric system, the first line is (2.28), therefore β_1 and β_2 are the basis functions mapping $\tau \in [0, 1]$ in $\tilde{x}_{j,j+1}$. For Pythagoras' theorem, it holds $|\partial C_{j,j+1}| = \sqrt{(\Delta t)^2 + (\Delta X_{j,j+1}^n)^2}$ and the unit-norm outward vector to the that side is $\mathbf{n}_{j,j+1} = [\Delta t, -\Delta X_{j,j+1}^n]^T / |\partial C_{j,j+1}^n|$. Consequently:

$$\int_{\partial C_{j,j+1}^n} \tilde{\mathbf{u}} \cdot \mathbf{n}_{j,j+1} \, d\gamma = \int_0^1 |\partial C_{j,j+1}^n| [\tilde{\mathbf{u}} \cdot \mathbf{n}_{j,j+1}]_{\xi=1} \, d\tau.$$

By considering relation (2.34), the two addenda explicitly are:

$$\begin{aligned} (\mathbf{u}_{j,j+1}^+ + \mathbf{u}_{j,j+1}^-) \cdot \mathbf{n}_{j,j+1} &= \frac{u_{j,j+1}^+ + u_{j,j+1}^-}{|\partial C_{j,j+1}^n|} (\Delta t - \Delta X_{j,j+1}^n); \\ s \equiv A_n^V(u) &= \Delta t \left(\frac{\partial u}{\partial x} n - V n \right) = \Delta t \left(1 - \frac{d\tilde{x}_{j,j+1}}{dt} \right) \\ &= \Delta t \left(1 - \frac{\partial \tilde{x}_{j,j+1}}{\partial \tau} \frac{\partial \tau}{\partial t} \right) = \Delta t \left(1 - \frac{\Delta X_{j,j+1}^n}{\Delta t} \right), \end{aligned}$$

with $n = [\mathbf{n}_{j,j+1}]_x / |[\mathbf{n}_{j,j+1}]_x| \equiv +1$. Therefore, the Rusanov flux writes:

$$\begin{aligned} \tilde{\mathbf{u}}_{j,j+1}^n \cdot \mathbf{n}_{j,j+1} &= \frac{1}{2} \left[\frac{\Delta t - \Delta X_{j,j+1}^n}{|\partial C_{j,j+1}^n|} - \Delta t \left(1 - \frac{\Delta X_{j,j+1}^n}{\Delta t} \right) \right] u_{j,j+1}^+ \\ &\quad + \frac{1}{2} \left[\frac{\Delta t - \Delta X_{j,j+1}^n}{|\partial C_{j,j+1}^n|} + \Delta t \left(1 - \frac{\Delta X_{j,j+1}^n}{\Delta t} \right) \right] u_{j,j+1}^-. \end{aligned}$$

Consequently the integral of the flux is:

$$\int_{\partial C_{j,j+1}^n} \tilde{\mathbf{u}}_{j,j+1}^n \cdot \mathbf{n}_{j,j+1} \, d\gamma = \frac{1}{2} a_{j,j+1} \int_0^1 u_{j,j+1}^+ |_{\xi^*} \, d\tau + \frac{1}{2} b_{j,j+1} \int_0^1 u_{j,j+1}^- |_{\xi^*} \, d\tau,$$

with ξ^* such that $x(\xi^*, \tau) = \tilde{x}_{j,j+1}(\tau)$ for any $\tau \in [0, 1]$ and

$$\begin{aligned} a_{j,j+1} &= (1 - |\partial C_{j,j+1}^n|)(\Delta t - \Delta X_{j,j+1}^n), \\ b_{j,j+1} &= (1 + |\partial C_{j,j+1}^n|)(\Delta t - \Delta X_{j,j+1}^n). \end{aligned}$$

The same reasoning can be done for the space-time side $\partial C_{j-1,j}$. The integral flux is exactly the same but the constants are:

$$\begin{aligned} a_{j-1,j} &= (1 - |\partial C_{j,j+1}^n|)(-\Delta t + \Delta X_{j,j+1}^n), \\ b_{j-1,j} &= (1 + |\partial C_{j,j+1}^n|)(-\Delta t + \Delta X_{j,j+1}^n). \end{aligned}$$

Appendix C

The ADER approach for the advection-diffusion problem

C.1 The Galerkin predictor

The inverse of the Jacobian matrix in (3.11) formally is

$$J^{-1} = \frac{d\boldsymbol{\zeta}}{d\mathbf{x}} = \begin{bmatrix} \zeta_x & \zeta_y & \zeta_t \\ \eta_x & \eta_y & \eta_t \\ 0 & 0 & 1/\Delta t \end{bmatrix} = \frac{1}{\Delta t d_{\zeta\eta}} \begin{bmatrix} \Delta t y_\eta & -\Delta t x_\eta & d_{\eta\tau} \\ -\Delta t y_\zeta & \Delta t x_\zeta & -d_{\zeta\tau} \\ 0 & 0 & d_{\zeta\eta} \end{bmatrix}, \quad (\text{C.1})$$

with $d_{\alpha\beta} = x_\alpha y_\beta - x_\beta y_\alpha$, $\alpha, \beta = \zeta, \eta, \tau$.

From the weak formulation (3.14), matrices not involving the derivatives of map \mathcal{M}_i , i.e. $[\theta_k, \theta_l]_1$ and $\langle \partial_\tau \theta_k, \theta_l \rangle$, are exactly computed once for all. All the remaining matrices $\langle \theta_k, (\zeta_x \partial_\zeta + \eta_x \partial_\eta) \theta_l \rangle$ and $\langle \theta_k, (\zeta_x \partial_\zeta + \eta_x \partial_\eta) \theta_l \rangle$ are computed by numerically integrating by quadrature rule. The components of these matrices can be resumed in the following two forms: $\langle \theta_k, \rho \partial_\alpha \theta_l \rangle$, with $\alpha = \zeta, \eta$ and $\rho : \hat{\mathcal{C}} \rightarrow \mathbb{R}$ any function in (C.1). By using the discrete map index (3.6) over indexes $k = \mathfrak{m}(a, b, c)$ and $l = \mathfrak{m}(a', b', c')$ and the tensor representation (3.7), they formally read

$$\langle \theta_k, \rho \partial_\zeta \theta_l \rangle = \begin{cases} \omega_k^{3D} \rho(\hat{\boldsymbol{\zeta}}_k) (\theta_{a'}^\zeta(\hat{\boldsymbol{\zeta}}_a))', & \text{when } l = \mathfrak{m}(a', b, c) \quad \forall a' = 1, 2, 3 \\ 0 & \text{otherwise} \end{cases}$$

and

$$\langle \theta_k, \rho \partial_\eta \theta_l \rangle = \begin{cases} \omega_k^{3D} \rho(\hat{\boldsymbol{\zeta}}_k) (\theta_{b'}^\eta(\hat{\boldsymbol{\eta}}_b))', & \text{when } l = \mathfrak{m}(a, b', c) \quad \forall b' = 1, 2, 3 \\ 0 & \text{otherwise} \end{cases},$$

where $\omega_k^{3D} = \omega_a \omega_b \omega_c$ is the 3D quadrature weight from the single direction Gauss-Legendre weights $\{\omega_1, \omega_2, \omega_3\} = \{5/18, 4/9, 5/18\}$ and $\hat{\boldsymbol{\zeta}}_k = (\hat{\zeta}_a, \hat{\eta}_b, \hat{\tau}_c)$ is the k -th 3D quadrature node.

The cofactor matrix $\text{Cof}(J)$ of the Jacobian matrix J is

$$\text{Cof}(J) = \begin{bmatrix} \Delta t y_\eta & -\Delta t y_\zeta & 0 \\ -\Delta t x_\eta & \Delta t x_\zeta & 0 \\ d_{\eta\tau} & -d_{\zeta\tau} & d_{\zeta\eta} \end{bmatrix}.$$

C.2 Time step Δt in the limit of large diffusion

The assumption for the time step Δt in (3.29) could appear too simple and does not take into account the possibility of a large diffusion (i.e. $\mathcal{O}(v) > \mathcal{O}(|a|)$). It can be justified by the presence of the stabilization parameter s_{AD} presented in (3.34) through the right relaxation parameter ε_p introduced in Corollary 3.3.1. Despite of the simplistic definition of the time step, the diffusion (also in the limit of a diffusive-dominant dynamics) is recovered by the stabilization term s_{AD} . Here it is provided a sketch of proof for this statement in the 1D case.

Let us start saying that a classical stabilization analysis is complicated because of the FEM-predictor solution in the space-time flux (3.28). Let us assume the convective-diffusive term to be linear, i.e. $F(u, u_x) = au - vu_x$. By approximating the integrals in the scheme (3.27) through the rectangle formula¹, at the first order in space and in time it holds²

$$-hU^n + hU^{n+1} + \Delta t(\Phi_l + \Phi_r) = 0.$$

Since the space-time cell normal edge is $\mathbf{n}_{x,t} = [\pm\Delta t, \mp ch]^T / \sqrt{\Delta t^2 + c^2 h^2}$, where we assume the deformation of the cell to be smaller than or equal to the characteristic length h of the mesh (i.e. $0 < c \leq 1$), it is possible to sum the scheme up as follows

$$-hU^n + hU^{n+1} + \Delta t C_1 \bar{U}_x + \Delta t C_2 \bar{U} - \frac{1}{2} \Delta t s_{AD} C_q = 0, \quad (\text{C.2})$$

where \bar{U}_x , \bar{U} and C_q take into account the contribution of the space derivatives, the solution and the FEM-predictor solution q in the fluxes (3.28), respectively. These quantities are assumed finite. Accordingly to the definition in (3.29) and in the limit of a diffusive-dominant dynamics, it holds:

$$\Delta t C_1 \sim \frac{\text{CFL}^2 h v}{a \sqrt{\text{CFL}^2 + a^2 c^2}}, \quad (\text{C.3a})$$

$$\Delta t C_2 \sim \frac{c \text{CFL}}{\sqrt{\text{CFL}^2 + a^2 c^2}}, \quad (\text{C.3b})$$

$$\Delta t s_{AD} \sim \frac{1}{2} \text{CFL} h^2 (\text{CFL}^2 + a^2 c^2) |a \text{CFL} h + 4c^2 h^2 - 4\text{CFL} c h^2 + \kappa \text{CFL}^2 v^{1/2}|, \quad (\text{C.3c})$$

where constant κ takes into account the constants of the optimal relaxation parameter of Corollary 3.3.1. By plugging (C.3) into (C.2) there is a possibility to properly define a CFL condition in order to ensure the stability of the scheme for any initial value problem³.

With this sketch of proof we want to communicate that the stabilization parameter takes into account the diffusive parameter. A formal stability analysis is cumbersome for more dimensions and for more complicated mesh deformations. Thus, this justifies the empirical numerical analysis for a proper CFL value in Section 3.4.2.

1. In one dimension the rectangle formula reads:

$$\int_a^b f(x) dx \approx \frac{a+b}{2} f\left(\frac{a+b}{2}\right).$$

2. Here the dependence of the formulation on the i -th cell is omitted.

3. Here this computation it is not performed.

Appendix D

Chorin-Temam method

Consider a generic differential problems of type: *find* $w : \Omega \times \mathbb{R}_+ \rightarrow \mathbb{R}^{d_2}$, with $\Omega \subset \mathbb{R}^{d_1}$ ($d_1, d_2 = 1, 2, 3$) such that

$$\partial_t w + L_1 w + L_2 w = f \quad \text{in } \Omega \times \mathbb{R}_+,$$

properly closed with additional conditions and with L_1 and L_2 representing two differential operators. A fractional step method consists in the idea of splitting the time advancing from t^n to $t^{n+1} = t^n + \Delta t$ in two sub-problems each one accounting one differential operator:

$$\begin{aligned} \frac{\tilde{w}^{n+1} - w^n}{\Delta t} + L_1 \tilde{w}^{n+1} &= 0, \\ \frac{w^{n+1} - \tilde{w}^{n+1}}{\Delta t} + L_2 w^{n+1} &= 0, \end{aligned}$$

with \tilde{w} an auxiliary intermediate solution. Among the fractional step method there is a class of methods called projection methods.

Concerning the Navier-Stokes equations, Chorin-Temam method is a projection step for looking for the fluid and pressure velocity. In particular it consists of two major steps:

$$\begin{aligned} \frac{\tilde{\mathbf{u}} - \mathbf{u}^n}{\Delta t} - \frac{1}{\text{Re}} \Delta \tilde{\mathbf{u}} + (\tilde{\mathbf{u}} \cdot \nabla) \tilde{\mathbf{u}} &= \mathbf{0}, \quad (\text{Step 1}) \\ \begin{cases} \frac{\mathbf{u}^{n+1} - \tilde{\mathbf{u}}}{\Delta t} + \nabla p^{n+1} = \mathbf{0}, \\ \nabla \cdot \mathbf{u}^{n+1} = 0, \end{cases} & \quad (\text{Step 2}) \end{aligned}$$

The two sub-problems require suitable boundary conditions. Step 1 is an advection-diffusion problem for the intermediate velocity $\tilde{\mathbf{u}}$ and inherits the same boundary conditions imposed for the original Navier-Stokes problem. On the other hand, problem of Step 2 is not diffusive and the trace $\mathbf{u}|_{\partial\Omega}$ of the solution is not defined. It is possible to prove that the only information defined on the solution is its normal component $[\mathbf{u} \cdot \mathbf{n}]_{\partial\Omega}$. Thus, if the original problem is closed through fully homogeneous Dirichlet boundary conditions, problem of Step 2 is well posed if when $\mathbf{u} \cdot \mathbf{n} = \mathbf{0}$ over $\partial\Omega$ is imposed. This mismatch on the boundary conditions of the final velocity contributes to the splitting error associated to the fractional step approach. Step 1 is usually defined the prediction step because the solving velocity $\tilde{\mathbf{u}}$ does not fulfill the continuity equation (i.e. it is not free-divergent). Step 2 is called projection step because of the projection of the final velocity on a free-divergent functional space. Let $H_{div}(\Omega) := \{\mathbf{v} \in H^1(\Omega)^d : \nabla \cdot \mathbf{v} = 0\}$. Let Step 2 be weakened for any

$\boldsymbol{v} \in H_{div,0} := \{\boldsymbol{w} \in H_{div} : [\boldsymbol{w} \cdot \boldsymbol{n}]_{\partial\Omega} = 0\}$, thus

$$\int_{\Omega} \frac{\boldsymbol{u}^{n+1} - \tilde{\boldsymbol{u}}}{\Delta t} \cdot \boldsymbol{v} \, d\Omega = - \int_{\Omega} \nabla p^{n+1} \cdot \boldsymbol{v} \, d\Omega = \int_{\Omega} p^{n+1} \nabla \cdot \boldsymbol{v} \, d\Omega = 0.$$

Consequently,

$$\int_{\Omega} \boldsymbol{u}^{n+1} \cdot \boldsymbol{v} \, d\Omega = \int_{\Omega} \tilde{\boldsymbol{u}} \cdot \boldsymbol{v} \, d\Omega.$$

This means that the final velocity \boldsymbol{u} is the orthogonal projection of $\tilde{\boldsymbol{u}}$ onto the subspace $H_{div,0}$. This is a direct consequence of the Helmholtz's decomposition theorem:

Theorem D.0.1 (Helmholtz's decomposition theorem). *Let $\Omega \subset \mathbb{R}^d$ be a simply connected domain. For any $\boldsymbol{v} \in H^1(\Omega)^d$ there exists a unique decomposition into a solenoidal (divergence-free) and an irrotational (curl-free) part such that*

$$\boldsymbol{v} = \boldsymbol{w} + \nabla\phi,$$

with $\boldsymbol{w} \in H_{div,0}(\Omega)$ and $\phi \in H^1(\Omega)$.

From the projection step of Chorin-Temam method, the decomposition reads

$$\tilde{\boldsymbol{u}} = \boldsymbol{u}^{n+1} + \Delta t \nabla p^{n+1},$$

with \boldsymbol{u}^{n+1} and p^{n+1} defining the solenoidal and irrotational parts, respectively. Finally, by applying the divergence operator to Step 2, the Poisson problem for the pressure of (4.9) arises.

D.1 Poisson equation with fully homogeneous Neumann conditions

Let us suppose to have Dirichlet boundary condition along the whole boundary $\partial\Omega$ for the velocity \boldsymbol{u} . Since both the the intermediate and corrected velocities share the same boundary conditions, by applying the scalar product with respect to the unit outward normal at the boundary at Step 2, the arising boundary condition for the Poisson pressure problem reads is

$$\nabla p^{n+1} \cdot \boldsymbol{n} = 0,$$

which is a fully homogeneous Neumann condition. Let $\psi = \Delta t p^{n+1}$, the following problem has to be solved:

$$\begin{cases} -\Delta\psi = f & \text{in } \Omega \\ \nabla\psi \cdot \boldsymbol{n} = 0 & \text{on } \partial\Omega \end{cases} \quad (\text{D.1})$$

with f a proper force term. Because of the boundary conditions, problem (D.1) has not a unique solution. In particular, if ψ solves (D.1), also $\psi + c$ solves (D.1) for any real c . Consequently, if the algebraic FV counterpart of the problem is $K\boldsymbol{\psi} = \boldsymbol{f}$, the stiffness matrix K has a nontrivial kernel. For this reason, in the code, the zero mean solution solving (D.1) is found. We define $V = \{v \in H^1(\Omega) : [\nabla v \cdot \boldsymbol{n}]_{\partial\Omega} = 0\}$ and the energy functional $\mathcal{J} : V \rightarrow \mathbb{R}$ associated to the problem formally written as

$$\mathcal{J}(v) = \frac{1}{2} \int_{\Omega} \nabla v \cdot \nabla v \, d\Omega - \int_{\Omega} f v \, d\Omega.$$

For our goal, the looked solution ψ is the minimizer of the following problem

$$\begin{aligned} & \underset{v \in V}{\text{minimize}} && \mathcal{J}(v) \\ & \text{subject to} && \int_{\Omega} v \, d\Omega = 0. \end{aligned} \tag{D.2}$$

Let the associated Lagrangian functional $\mathcal{L} : V \times \mathbb{R} \rightarrow \mathbb{R}$ be

$$\mathcal{L}(v, \lambda) = \mathcal{J}(v) + \lambda \mathcal{I}(v),$$

with $\mathcal{I}(v) = \int_{\Omega} v \, d\Omega$ the constraint. In order to solve the optimization problem (D.2), the following system is solved¹

$$\begin{cases} \frac{D\mathcal{L}[w]}{Dv} = 0 & \forall w \in V \\ \frac{\partial \mathcal{L}}{\partial \lambda} = 0 \end{cases} \Rightarrow \begin{cases} \int_{\Omega} \nabla v \cdot \nabla w \, d\Omega - \int_{\Omega} f w \, d\Omega + \lambda \int_{\Omega} w \, d\Omega = 0 & \forall w \in V \\ \int_{\Omega} v \, d\Omega = 0 \end{cases}.$$

Due to the zero normal derivative at the boundary of functions in V , the first line of the system turns into

$$\int_{\Omega} (-\Delta v - f + \lambda) w \, d\Omega = 0 \quad \forall w \in V,$$

In particular, by choosing $w \equiv 1$, we recover a FV problem associated to the algebraic counterpart

$$\begin{bmatrix} K & \boldsymbol{\omega} \\ \boldsymbol{\omega}^T & 0 \end{bmatrix} \begin{bmatrix} \boldsymbol{\psi} \\ \lambda \end{bmatrix} = \begin{bmatrix} \boldsymbol{f} \\ 0 \end{bmatrix},$$

with $\omega_i = |\Omega_i|$ the measure of cell Ω_i . Finally, the above problem is solved.

1. By definition:

$$\frac{D\mathcal{L}[w]}{Dv} = \lim_{\delta \rightarrow 0} \frac{\mathcal{L}(v + \delta w, \lambda) - \mathcal{L}(v, \lambda)}{\delta} \quad \forall w \in V.$$

Bibliography

- [1] Remi Abgrall, Héloïse Beaugendre, and Cécile Dobrzynski. « An immersed boundary method using unstructured anisotropic mesh adaptation combined with level-sets and penalization techniques ». In: *Journal of Computational Physics* 257 (2014), pp. 83–101.
- [2] Daniel M Anderson, Geoffrey B McFadden, and Adam A Wheeler. « Diffuse-interface methods in fluid mechanics ». In: *Annual review of fluid mechanics* 30.1 (1998), pp. 139–165.
- [3] Ph Angot and Jean-Paul Caltagirone. « Natural convection through periodic porous media ». In: *International Heat Transfer Conference Digital Library*. Begel House Inc. 1990.
- [4] Philippe Angot, Charles-Henri Bruneau, and Pierre Fabrie. « A penalization method to take into account obstacles in incompressible viscous flows ». In: *Numerische Mathematik* 81.4 (1999), pp. 497–520.
- [5] Philippe Angot and JP Caltagirone. *New Graphical and Computational Architecture Concept for Numerical Simulation of Supercomputers*. CERFACS, 1990.
- [6] E Arquis, JP Caltagirone, et al. « Sur les conditions hydrodynamiques au voisinage d’une interface milieu fluide-milieu poreux: application la convection naturelle ». In: *CR Acad. Sci. Paris II* 299 (1984), pp. 1–4.
- [7] E Atta. « Component-adaptive grid interfacing ». In: *19th Aerospace Sciences Meeting*. 1981, p. 382.
- [8] Jeffrey W Banks, William D Henshaw, and Björn Sjögreen. « A stable FSI algorithm for light rigid bodies in compressible flow ». In: *Journal of Computational Physics* 245 (2013), pp. 399–430.
- [9] Jeffrey W Banks, Donald W Schwendeman, Ashwana K Kapila, and William D Henshaw. « A high-resolution Godunov method for compressible multi-material flow on overlapping grids ». In: *Journal of Computational Physics* 223.1 (2007), pp. 262–297.
- [10] Jeffrey W Banks, William D Henshaw, Ashwana K Kapila, and Donald W Schwendeman. « An added-mass partition algorithm for fluid–structure interactions of compressible fluids and nonlinear solids ». In: *Journal of Computational Physics* 305 (2016), pp. 1037–1064.
- [11] Maxime Barrault, Yvon Maday, Ngoc Cuong Nguyen, and Anthony T Patera. « An ‘empirical interpolation’ method: application to efficient reduced-basis discretization of partial differential equations ». In: *Comptes Rendus Mathématique* 339.9 (2004), pp. 667–672.
- [12] Matania Ben-Artzi and Joseph Falcovitz. « A second-order Godunov-type scheme for compressible fluid dynamics ». In: *Journal of Computational Physics* 55.1 (1984), pp. 1–32.

- [13] J Benek, J Steger, and F Carroll Dougherty. « A flexible grid embedding technique with application to the Euler equations ». In: *6th computational fluid dynamics conference Danvers*. 1983, p. 1944.
- [14] Jk Benek, P Buning, and J Steger. « A 3-D chimera grid embedding technique ». In: *7th Computational Physics Conference*. 1985, p. 1523.
- [15] Marsha Berger and Michael Aftosmis. « Aspects (and aspect ratios) of Cartesian mesh methods ». In: *Sixteenth International Conference on Numerical Methods in Fluid Dynamics*. Springer. 1998, pp. 1–12.
- [16] Marsha J Berger and Joseph Oliger. « Adaptive mesh refinement for hyperbolic partial differential equations ». In: *Journal of computational Physics* 53.3 (1984), pp. 484–512.
- [17] Michel Bergmann. « Optimisation aérodynamique par réduction de modele POD et contrôle optimal. Application au sillage laminaire d'un cylindre circulaire ». In: *Institut National Polytechnique de Lorraine* (2004).
- [18] Michel Bergmann, Michele Giuliano Carlino, and Angelo Iollo. « Second order scheme for unsteady advection-diffusion on moving overset grids with a compact transmission condition ». working paper or preprint. Jan. 2021. URL: <https://hal.inria.fr/hal-03119830>.
- [19] Michel Bergmann, Jessica Hovnanian, and Angelo Iollo. « An accurate cartesian method for incompressible flows with moving boundaries ». In: *Communications in Computational Physics* 15.5 (2014), pp. 1266–1290.
- [20] Michel Bergmann and Angelo Iollo. « Modeling and simulation of fish-like swimming ». In: *Journal of Computational Physics* 230.2 (2011), pp. 329–348.
- [21] Michel Bergmann, Michele Giuliano Carlino, Angelo Iollo, and Haysam Telib. *ADER scheme for incompressible Navier-Stokes equations on Overset grids with a compact transmission condition*. Research Report RR-9414. Inria & Labri, Univ. Bordeaux ; Optimad, June 2021, p. 32. URL: <https://hal.inria.fr/hal-03263417>.
- [22] Gal Berkooz, Philip Holmes, and John L Lumley. « The proper orthogonal decomposition in the analysis of turbulent flows ». In: *Annual review of fluid mechanics* 25.1 (1993), pp. 539–575.
- [23] Enrico Bertolazzi and Gianmarco Manzini. « A cell-centered second-order accurate finite volume method for convection–diffusion problems on unstructured meshes ». In: *Mathematical Models and Methods in Applied Sciences* 14.08 (2004), pp. 1235–1260.
- [24] Walter Boscheri and Michael Dumbser. « Arbitrary-Lagrangian-Eulerian one-step WENO finite volume schemes on unstructured triangular meshes ». In: *Communications in Computational Physics* 14.5 (2013), pp. 1174–1206.
- [25] A Bourgeade, Ph Le Floch, and PA Raviart. « An asymptotic expansion for the solution of the generalized Riemann problem. Part 2: Application to the equations of gas dynamics ». In: *Annales de l'Institut Henri Poincaré C, Analyse non linéaire*. Vol. 6. 6. Elsevier. 1989, pp. 437–480.
- [26] M Braza, PHHM Chassaing, and H Ha Minh. « Numerical study and physical analysis of the pressure and velocity fields in the near wake of a circular cylinder ». In: *Journal of fluid mechanics* 165 (1986), pp. 79–130.
- [27] Charles-Henri Bruneau and Mazen Saad. « The 2D lid-driven cavity problem revisited ». In: *Computers & fluids* 35.3 (2006), pp. 326–348.

- [28] Saray Busto, Simone Chiocchetti, Michael Dumbser, Elena Gaburro, and Ilya Peshkov. « High order ADER schemes for continuum mechanics ». In: *Frontiers in Physics* 8 (2020), p. 32.
- [29] Cristóbal E Castro and Eleuterio F Toro. « Solvers for the high-order Riemann problem for hyperbolic balance laws ». In: *Journal of Computational Physics* 227.4 (2008), pp. 2481–2513.
- [30] G Chesshire and William D Henshaw. « Composite overlapping meshes for the solution of partial differential equations ». In: *Journal of Computational Physics* 90.1 (1990), pp. 1–64.
- [31] Francisco Chinesta, Roland Keunings, and Adrien Leygue. *The proper generalized decomposition for advanced numerical simulations: a primer*. Springer Science & Business Media, 2013.
- [32] Ing-Tsau Chiu and Robert Meakin. « On automating domain connectivity for overset grids ». In: *33rd Aerospace Sciences Meeting and Exhibit*. 1995, p. 854.
- [33] Alexandre Joel Chorin. « Numerical solution of the Navier-Stokes equations ». In: *Mathematics of computation* 22.104 (1968), pp. 745–762.
- [34] D Keith Clarke, MD Salas, and HA Hassan. « Euler calculations for multielement airfoils using Cartesian grids ». In: *AIAA journal* 24.3 (1986), pp. 353–358.
- [35] Mathieu Coquerelle and G-H Cottet. « A vortex level set method for the two-way coupling of an incompressible fluid with colliding rigid bodies ». In: *Journal of Computational Physics* 227.21 (2008), pp. 9121–9137.
- [36] Yves Coudière, Jean-Paul Vila, and Philippe Villedieu. « Convergence rate of a finite volume scheme for a two dimensional convection-diffusion problem ». In: *ESAIM: Mathematical Modelling and Numerical Analysis* 33.3 (1999), pp. 493–516.
- [37] Darren De Zeeuw and Kenneth G Powell. « An adaptively-refined Cartesian mesh solver for the Euler equations ». In: (1991).
- [38] Michael Dumbser, Cedric Enaux, and Eleuterio F Toro. « Finite volume schemes of very high order of accuracy for stiff hyperbolic balance laws ». In: *Journal of Computational Physics* 227.8 (2008), pp. 3971–4001.
- [39] Michael Dumbser and Martin Käser. « Arbitrary high order non-oscillatory finite volume schemes on unstructured meshes for linear hyperbolic systems ». In: *Journal of Computational Physics* 221.2 (2007), pp. 693–723.
- [40] Michael Dumbser, Dinshaw S Balsara, Eleuterio F Toro, and Claus-Dieter Munz. « A unified framework for the construction of one-step finite volume and discontinuous Galerkin schemes on unstructured meshes ». In: *Journal of Computational Physics* 227.18 (2008), pp. 8209–8253.
- [41] Michael Dumbser, Walter Boscheri, Matteo Semplice, and Giovanni Russo. « Central weighted ENO schemes for hyperbolic conservation laws on fixed and moving unstructured meshes ». In: *SIAM Journal on Scientific Computing* 39.6 (2017), A2564–A2591.
- [42] Carl Eckart and Gale Young. « The approximation of one matrix by another of lower rank ». In: *Psychometrika* 1.3 (1936), pp. 211–218.

- [43] Charbel Farhat, Todd Chapman, and Philip Avery. « Structure-preserving, stability, and accuracy properties of the energy-conserving sampling and weighting method for the hyper reduction of nonlinear finite element dynamic models ». In: *International journal for numerical methods in engineering* 102.5 (2015), pp. 1077–1110.
- [44] Charbel Farhat, Philip Avery, Todd Chapman, and Julien Cortial. « Dimensional reduction of nonlinear finite element dynamic models with finite rotations and energy-based mesh sampling and weighting for computational efficiency ». In: *International Journal for Numerical Methods in Engineering* 98.9 (2014), pp. 625–662.
- [45] Ronald P Fedkiw, Tariq Aslam, Barry Merriman, and Stanley Osher. « A non-oscillatory Eulerian approach to interfaces in multimaterial flows (the ghost fluid method) ». In: *Journal of computational physics* 152.2 (1999), pp. 457–492.
- [46] UKNG Ghia, Kirti N Ghia, and CT Shin. « High-Re solutions for incompressible flow using the Navier-Stokes equations and a multigrid method ». In: *Journal of computational physics* 48.3 (1982), pp. 387–411.
- [47] Frederic Gibou, Ronald P Fedkiw, Li-Tien Cheng, and Myungjoo Kang. « A second-order-accurate symmetric discretization of the Poisson equation on irregular domains ». In: *Journal of Computational Physics* 176.1 (2002), pp. 205–227.
- [48] Roland Glowinski, Tsorng-Whay Pan, and Jacques Periaux. « A fictitious domain method for Dirichlet problem and applications ». In: *Computer Methods in Applied Mechanics and Engineering* 111.3-4 (1994), pp. 283–303.
- [49] SK Godunov. « A finite difference method for the computation of discontinuous solutions of the equations of fluid dynamics. » In: *Sbornik: Mathematics* 47.8-9 (1959), pp. 357–393.
- [50] So K Godunov, AV Zabrodin, M Ia Ivanov, AN Kraiko, and GP Prokopov. « Numerical solution of multidimensional problems of gas dynamics ». In: *Moscow Izdatel Nauka* (1976).
- [51] D Goldstein, R Handler, and L Sirovich. « Modeling a no-slip flow boundary with an external force field ». In: *Journal of computational physics* 105.2 (1993), pp. 354–366.
- [52] Sebastian Grimberg, Charbel Farhat, Radek Tezaur, and Charbel Bou-Mosleh. « Mesh sampling and weighting for the hyperreduction of nonlinear Petrov–Galerkin reduced-order models with local reduced-order bases ». In: *International Journal for Numerical Methods in Engineering* 122.7 (2021), pp. 1846–1874.
- [53] Joel Guerrero. « Overset composite grids for the simulation of complex moving geometries ». In: *DICAT, University of Genoa, Italy* (2006).
- [54] Francis H Harlow. *NUMERICAL METHODS FOR FLUID DYNAMICS, AN ANNOTATED BIBLIOGRAPHY*. Tech. rep. Los Alamos Scientific Lab., N. Mex., 1969.
- [55] Ami Harten, Bjorn Engquist, Stanley Osher, and Sukumar R Chakravarthy. « Uniformly high order accurate essentially non-oscillatory schemes, III ». In: *Upwind and high-resolution schemes*. Springer, 1987, pp. 218–290.

- [56] J-W He, R Glowinski, R Metcalfe, A Nordlander, and J Periaux. « Active control and drag optimization for flow past a circular cylinder: I. Oscillatory cylinder rotation ». In: *Journal of Computational Physics* 163.1 (2000), pp. 83–117.
- [57] Ronald D Henderson. « Details of the drag curve near the onset of vortex shedding ». In: *Physics of Fluids* 7.9 (1995), pp. 2102–2104.
- [58] William D Henshaw. « On multigrid for overlapping grids ». In: *SIAM Journal on Scientific Computing* 26.5 (2005), pp. 1547–1572.
- [59] Arturo Hidalgo and Michael Dumbser. « ADER schemes for nonlinear systems of stiff advection–diffusion–reaction equations ». In: *Journal of Scientific Computing* 48.1-3 (2011), pp. 173–189.
- [60] CW Hirt. « An arbitrary Lagrangian-Eulerian method for incompressible flows ». In: *Proceedings of the Second International Conference on Numerical Methods in Fluid Dynamics*. 1970.
- [61] Cyrill W Hirt, Anthony A Amsden, and JL Cook. « An arbitrary Lagrangian-Eulerian computing method for all flow speeds ». In: *Journal of computational physics* 14.3 (1974), pp. 227–253.
- [62] G Houzeaux, JC Cajas, Marco Discacciati, B Eguzkitza, A Gargallo-Peiró, M Rivero, and M Vázquez. « Domain decomposition methods for domain composition purpose: chimera, overset, gluing and sliding mesh methods ». In: *Archives of Computational Methods in Engineering* 24.4 (2017), pp. 1033–1070.
- [63] Guang-Shan Jiang and Chi-Wang Shu. « Efficient implementation of weighted ENO schemes ». In: *Journal of computational physics* 126.1 (1996), pp. 202–228.
- [64] G Jin and M Braza. « A nonreflecting outlet boundary condition for incompressible unsteady Navier-Stokes calculations ». In: *Journal of computational physics* 107.2 (1993), pp. 239–253.
- [65] Kai-Hsiung Kao and Meng-Sing Liou. « Advance in overset grid schemes-From Chimera to DRAGON grids ». In: *AIAA journal* 33.10 (1995), pp. 1809–1815.
- [66] Tetuya Kawamura, Hideo Takami, and Kunio Kuwahara. « New higher-order upwind scheme for incompressible Navier-Stokes equations ». In: *Ninth International Conference on Numerical Methods in Fluid Dynamics*. Springer. 1985, pp. 291–295.
- [67] Oliver Kolb. « On the full and global accuracy of a compact third order WENO scheme ». In: *SIAM Journal on Numerical Analysis* 52.5 (2014), pp. 2335–2355.
- [68] VP Kolgan. « Application of the minimum-derivative principle in the construction of finite-difference schemes for numerical analysis of discontinuous solutions in gas dynamics ». In: *Uchenye Zapiski TsAGI [Sci. Notes Central Inst. Aerodyn]* 3.6 (1972), pp. 68–77.
- [69] Petros Koumoutsakos and A Leonard. « High-resolution simulations of the flow around an impulsively started cylinder using vortex methods ». In: *Journal of Fluid Mechanics* 296 (1995), pp. 1–38.
- [70] Barbro Kreiss. « Construction of a curvilinear grid ». In: *SIAM Journal on Scientific and Statistical Computing* 4.2 (1983), pp. 270–279.
- [71] Charles L Lawson and Richard J Hanson. *Solving least squares problems*. SIAM, 1995.

- [72] BP Leonard. « The ULTIMATE conservative difference scheme applied to unsteady one-dimensional advection ». In: *Computer methods in applied mechanics and engineering* 88.1 (1991), pp. 17–74.
- [73] Doron Levy, Gabriella Puppo, and Giovanni Russo. « Central WENO schemes for hyperbolic systems of conservation laws ». In: *ESAIM: Mathematical Modelling and Numerical Analysis* 33.3 (1999), pp. 547–571.
- [74] Meng-Sing Liou and Yao Zheng. « A novel approach of three-dimensional hybrid grid methodology: Part 2. Flow solution ». In: *Computer methods in applied mechanics and engineering* 192.37-38 (2003), pp. 4173–4193.
- [75] RL Meakin. « Chapter 11: Composite overset structured grids ». In: *Handbook of grid generation*, JF Thompson, BK Soni and NP Weatherill. CRC (1999).
- [76] F Meng, JW Banks, WD Henshaw, and DW Schwendeman. « Fourth-order accurate fractional-step IMEX schemes for the incompressible Navier–Stokes equations on moving overlapping grids ». In: *Computer Methods in Applied Mechanics and Engineering* 366 (2020), p. 113040.
- [77] Ketan Mittal, Som Dutta, and Paul Fischer. « Nonconforming Schwarz-spectral element methods for incompressible flow ». In: *Computers & Fluids* 191 (2019), p. 104237.
- [78] Rajat Mittal and Gianluca Iaccarino. « Immersed boundary methods ». In: *Annu. Rev. Fluid Mech.* 37 (2005), pp. 239–261.
- [79] Rajat Mittal, Haibo Dong, Meliha Bozkurttas, FM Najjar, Abel Vargas, and Alfred Von Loebbecke. « A versatile sharp interface immersed boundary method for incompressible flows with complex boundaries ». In: *Journal of computational physics* 227.10 (2008), pp. 4825–4852.
- [80] Gino Ignacio Montecinos. « Numerical methods for advection-diffusion-reaction equations and medical applications ». PhD thesis. University of Trento, 2014.
- [81] YOUNG MOON and Meng-Sing Liou. « Conservative treatment of boundary interfaces for overlaid grids and multi-level grid adaptations ». In: *9th Computational Fluid Dynamics Conference*. 1989, p. 1980.
- [82] W Mulder, S Osher, and James A Sethian. « Computing interface motion in compressible gas dynamics ». In: *Journal of computational physics* 100.2 (1992), pp. 209–228.
- [83] Gabriel B Nagy, Omar E Ortiz, and Oscar A Reula. « The behavior of hyperbolic heat equations’s solutions near their parabolic limits ». In: *Journal of Mathematical Physics* 35.8 (1994), pp. 4334–4356.
- [84] Stanley Osher and Fred Solomon. « Upwind difference schemes for hyperbolic systems of conservation laws ». In: *Mathematics of computation* 38.158 (1982), pp. 339–374.
- [85] Simona Perotto, Alexandre Ern, and Alessandro Veneziani. « Hierarchical local model reduction for elliptic problems: a domain decomposition approach ». In: *Multiscale Modeling & Simulation* 8.4 (2010), pp. 1102–1127.
- [86] Charles S Peskin. « Numerical analysis of blood flow in the heart ». In: *Journal of computational physics* 25.3 (1977), pp. 220–252.
- [87] Charles S Peskin. « The fluid dynamics of heart valves: experimental, theoretical, and computational methods ». In: *Annual review of fluid mechanics* 14.1 (1982), pp. 235–259.

- [88] Charles S Peskin. « The immersed boundary method ». In: *Acta numerica* 11 (2002), pp. 479–517.
- [89] Charles Samuel Peskin. *Flow patterns around heart valves: a digital computer method for solving the equations of motion*. Yeshiva University, 1972.
- [90] N Anders Petersson. « Hole-cutting for three-dimensional overlapping grids ». In: *SIAM Journal on Scientific Computing* 21.2 (1999), pp. 646–665.
- [91] P Ploumhans and GS Winckelmans. « Vortex methods for high-resolution simulations of viscous flow past bluff bodies of general geometry ». In: *Journal of Computational Physics* 165.2 (2000), pp. 354–406.
- [92] Alfio Quarteroni, Andrea Manzoni, and Federico Negri. *Reduced basis methods for partial differential equations: an introduction*. Vol. 92. Springer, 2015.
- [93] Alice Raeli, Michel Bergmann, and Angelo Iollo. « A finite-difference method for the variable coefficient Poisson equation on hierarchical Cartesian meshes ». In: *Journal of computational Physics* 355 (2018), pp. 59–77.
- [94] Man Mohan Rai. « A conservative treatment of zonal boundaries for Euler equation calculations ». In: *Journal of Computational Physics* 62.2 (1986), pp. 472–503.
- [95] Sébastien Riffaud, Michel Bergmann, Charbel Farhat, Sebastian Grimberg, and Angelo Iollo. « The DGDD method for reduced-order modeling of conservation laws ». In: *Journal of Computational Physics* 437 (2021), p. 110336.
- [96] EM Saiki and S Biringen. « Numerical simulation of a cylinder in uniform flow: application of a virtual boundary method ». In: *Journal of computational physics* 123.2 (1996), pp. 450–465.
- [97] Ruben Scardovelli and Stéphane Zaleski. « Direct numerical simulation of free-surface and interfacial flow ». In: *Annual review of fluid mechanics* 31.1 (1999), pp. 567–603.
- [98] DW Schwendeman, AK Kapila, and WD Henshaw. « A study of detonation diffraction and failure for a model of compressible two-phase reactive flow ». In: *Combustion Theory and Modelling* 14.3 (2010), pp. 331–366.
- [99] Matteo Semplice, Armando Coco, and Giovanni Russo. « Adaptive mesh refinement for hyperbolic systems based on third-order compact WENO reconstruction ». In: *Journal of Scientific Computing* 66.2 (2016), pp. 692–724.
- [100] Ashesh Sharma, Shreyas Ananthan, Jayanarayanan Sitaraman, Stephen Thomas, and Michael A Sprague. « Overset meshes for incompressible flows: On preserving accuracy of underlying discretizations ». In: *Journal of Computational Physics* 428 (2021), p. 109987.
- [101] Chi-Wang Shu. « Essentially non-oscillatory and weighted essentially non-oscillatory schemes for hyperbolic conservation laws ». In: *Advanced numerical approximation of nonlinear hyperbolic equations*. Springer, 1998, pp. 325–432.
- [102] Lawrence Sirovich. « Turbulence and the dynamics of coherent structures. III. Dynamics and scaling ». In: *Quarterly of Applied mathematics* 45.3 (1987), pp. 583–590.
- [103] Göran Starius. « Composite mesh difference methods for elliptic boundary value problems ». In: *Numerische Mathematik* 28.2 (1977), pp. 243–258.
- [104] Göran Starius. « Constructing orthogonal curvilinear meshes by solving initial value problems ». In: *Numerische Mathematik* 28.1 (1977), pp. 25–48.

- [105] Göran Starius. « On composite mesh difference methods for hyperbolic differential equations ». In: *Numerische Mathematik* 35.3 (1980), pp. 241–255.
- [106] Mark Sussman, Peter Smereka, and Stanley Osher. « A level set approach for computing solutions to incompressible two-phase flow ». In: *Journal of Computational physics* 114.1 (1994), pp. 146–159.
- [107] Roger Temam. « Sur l’approximation de la solution des équations de Navier-Stokes par la méthode des pas fractionnaires (II) ». In: *Archive for rational mechanics and analysis* 33.5 (1969), pp. 377–385.
- [108] Vladimir A Titarev and Eleuterio F Toro. « ADER: Arbitrary high order Godunov approach ». In: *Journal of Scientific Computing* 17.1-4 (2002), pp. 609–618.
- [109] Vladimir A Titarev and Eleuterio F Toro. « ADER schemes for three-dimensional non-linear hyperbolic systems ». In: *Journal of Computational Physics* 204.2 (2005), pp. 715–736.
- [110] EF Toro and VA Titarev. « Solution of the generalized Riemann problem for advection–reaction equations ». In: *Proceedings of the Royal Society of London. Series A: Mathematical, Physical and Engineering Sciences* 458.2018 (2002), pp. 271–281.
- [111] Eleuterio F Toro and Gino I Montecinos. « Advection-diffusion-reaction equations: hyperbolization and high-order ADER discretizations ». In: *SIAM Journal on Scientific Computing* 36.5 (2014), A2423–A2457.
- [112] Eleuterio F Toro and Vladimir A Titarev. « Derivative Riemann solvers for systems of conservation laws and ADER methods ». In: *Journal of Computational Physics* 212.1 (2006), pp. 150–165.
- [113] John G Trulio. *Theory and Structure of the AFTON Codes*. Tech. rep. NORTRONICS NEWBURY PARK CA, 1966.
- [114] Holavanahalli S Udaykumar, Wei Shyy, and Madhukar M Rao. « Elafint: a mixed Eulerian–Lagrangian method for fluid flows with complex and moving boundaries ». In: *International journal for numerical methods in fluids* 22.8 (1996), pp. 691–712.
- [115] Bram Van Leer. « On the relation between the upwind-differencing schemes of Godunov, Engquist–Osher and Roe ». In: *SIAM Journal on Scientific and Statistical Computing* 5.1 (1984), pp. 1–20.
- [116] E Volkov. « The method of composite meshes ». In: *Automatic Programming, Numerical Methods and Functional Analysis* 96.96 (1970), p. 145.
- [117] ZJ Wang. « A fully conservative interface algorithm for overlapped grids ». In: *Journal of Computational Physics* 122.1 (1995), pp. 96–106.
- [118] Jeff A Wright and Wei Shyy. « A pressure-based composite grid method for the Navier-Stokes equations ». In: *Journal of computational physics* 107.2 (1993), pp. 225–238.
- [119] Tao Ye, Rajat Mittal, HS Udaykumar, and Wei Shyy. « An accurate Cartesian grid method for viscous incompressible flows with complex immersed boundaries ». In: *Journal of computational physics* 156.2 (1999), pp. 209–240.